Clays and Opals on Mars:

Implications for Water-Rock Interactions Through Time

by

Vivian Zheng Sun

B.S., California Institute of Technology, 2012

Sc. M., Brown University, 2014

A dissertation submitted in partial fulfillment of the requirements

for the degree of Doctor of Philosophy in the Program of

Earth, Environmental, and Planetary Sciences at Brown University

Providence, Rhode Island

May 2017

This dissertation by Vivian Zheng Sun is accepted in its present form by the Department of Earth, Environmental, and Planetary Science as satisfying the dissertation requirement for the Doctor of Philosophy.

Date _____ _____

Ralph E. Milliken, Brown University, Advisor

Recommended to the Graduate Council

Date _____ _____

John F. Mustard, Brown University, Reader

Date _____ _____

James M. Russell, Brown University, Reader

Date _____ _____

Carle M. Pieters, Brown University, Reader

Date _____ _____

Steve W. Ruff, Arizona State University, Reader

Approved by the Graduate Council

Date _____ _____

Andrew G. Campbell, Dean of the Graduate School

VIVIAN Z. SUN

Box 1846, 324 Brook Street, Brown University, Providence, RI 02912
vivian.z.sun@gmail.com
http://planetary.brown.edu/grad_pages/Sun/index.html

EDUCATION

BROWN UNIVERSITY, Providence RI

Doctor of Philosophy in Earth, Environmental, and Planetary Sciences 2017

Master of Science in Geological Sciences 2014

CALIFORNIA INSTITUTE OF TECHNOLOGY, Pasadena CA

Bachelor of Science with Honors in Planetary Science 2012

RESEARCH EXPERIENCE

BROWN UNIVERSITY, Dept. Earth, Environmental, and Planetary Sciences, Providence RI

Graduate Student

Advisor: Prof. Ralph E. Milliken 2012 – Present

Dissertation: Clays and Opals on Mars: Implications for Water-Rock Interactions Through Time

JET PROPULSION LABORATORY, Pasadena CA

Research Intern

Advisor: Dr. Leslie Tamppari Summer 2011

Project: Inferring Wind Directions from Dust Devil Tracks and Wind Streaks in the North Polar Region of Mars

CALIFORNIA INSTITUTE OF TECHNOLOGY, Div. Geological and Planetary Sciences, Pasadena CA

Research Assistant

- *Advisor:* Prof. Judith Cohen Spring 2011
  Task: Assisted with preparing and cataloging Hamburg/ESO survey results
- *Advisors:* Prof. Andrew Ingersoll & Dr. Shawn Ewald Summer 2010
  Project: Analyzing the Behaviors and Life Cycles of Jovian Vortices Using Cassini Data, with a Focus on Polar Regions
- *Advisors:* Prof. Joseph Kirschvink & Dr. Timothy Raub Summer 2009
  Project: Understanding the North American Permian-Triassic Mass Extinction Record: Isotopic Study of Quinn River Formation, Nevada

TEACHING EXPERIENCE

BROWN UNIVERSITY, Dept. Earth, Environmental, and Planetary Sciences, Providence RI

Teaching Assistant

- GEOL 1240 - Stratigraphy and Sedimentation Fall 2014

CALIFORNIA INSTITUTE OF TECHNOLOGY, Div. Geological and Planetary Sciences, Pasadena CA
Teaching Assistant

- Ge 10 - Frontiers in Geological and Planetary Sciences — Spring 2012
- Ay 1 - The Evolving Universe — Spring 2011

RELATED EXPERIENCE

Mars Science Laboratory (MSL) Participating Science Collaborator	2012 – Present
External Reviewer for Mars Data Analysis Program	2017
Reviewer for Icarus	2016
JPL Planetary Science Summer School	August, 2015
Impact Cratering Short Course and Field School, Sudbury, Ontario	October, 2013
USGS Photogrammetric Processing of Planetary Stereo Imagery, Flagstaff, AZ	September, 2013

HONORS AND AWARDS

Lunar and Planetary Institute Career Development Award	2017
Brown University Dissertation Fellowship	2017
American Geophysical Union (AGU) Student Travel Grant Recipient	2016
SETI Institute Lunar and Planetary Science Conference Travel Grant Recipient	2016
Geological Society of America Northeastern Section Student Travel Grant	2014, 2015
NASA Group Achievement Award MSL Science Operations Team	2013, 2015
Brown University First Year Fellowship	2012
Hugh F. and Andy Lou Colvin SURF Fellow	2010

PROFESSIONAL AFFILIATIONS

American Geophysical Union
Geological Society of America

PUBLICATIONS

Sun, V.Z., Milliken, R.E., Robertson, K.M., Ruff, S.W., and Farmer, J.D., *Mineralogy and Chemistry of Opal-Rich Samples from Mars Analog Sites and Implications for Rover Observations.* In preparation.

Sun, V.Z., Milliken, R.E., and Robertson, K.M., *Distinguishing Opal Types and Water Distributions from Near-Infrared Spectroscopy for Applications to Mars.* In preparation.

Sun, V.Z., Milliken, R.E., and Robertson, K.M., *Constraining the Hydration Behavior of Opaline Silica at Mars-Relevant Conditions from Laboratory Experiments.* In preparation.

Sun, V.Z., and Milliken, R.E., *Hydrated Silica on Mars: Geologic Settings and Orbital Evidence for Opal Maturity and Seasonal Cycling of Water with the Atmosphere.* In preparation.

MacKenzie, S.M., Caswell, T.E., Phillips-Lander, C.M., Stavros, E.N., Hofgartner, J.D., **Sun, V.Z.**, Powell, K.E., Steuer, C.J., O'Rourke, J.G., Dhaliwal, J.K., Leung, C.W.S., Petro, E.M., Wynne, J.J., Phan, S., Crismani, M., Krishnamurthy, A., John, K.K., DeBruin, K., Budney, C.J., and Mitchell, K.L. (2016), THEO *Concept Mission: Testing the Habitability of Enceladus's Ocean.* Advances in Space Research, 58, 1117-1137, doi:10.1016/j.asr.2016.05.037.

Sun, V.Z., and Milliken, R.E. (2015), *Ancient and recent clay formation on Mars as revealed from a global survey of hydrous minerals in crater central peaks.* Journal of Geophysical Research - Planets, 120, 2293-2332, doi: 10.1002/2015JE004918.

Sun, V.Z., and Milliken, R.E. (2014), *The geology and mineralogy of Ritchey crater, Mars: Evidence for post-Noachian clay formation.* Journal of Geophysical Research - Planets, 119, 810–836, doi: 10.1002/2013JE004602.

ABSTRACTS (* denotes oral presentations)

***Sun, V.Z.**, Milliken, R.E., and Robertson, K.M. (2017), *Opals on Mars: Geologic Settings and Orbital Evidence for Seasonal Cycling of Water with the Atmosphere*. Lunar and Planetary Science Conference 48, #1715.

Sun, V.Z. and Milliken, R.E. (2016), *An overview of orbital detections of hydrated silica and silica-rich rocks on Mars* (Invited). AGU Fall Meeting 2016, #127599.

McAdam, A., Knudson, C.A., Sutter, B., Andrejkovicova, S.C., Archer, P.D., Franz, H.B., Eigenbrode, J.L., Morris, R.V., Ming, D.W., **Sun, V.Z.**, Milliken, R.E., Wilhelm, M.B., Mahaffy, P.R., Navarro-Gonzalez, R. (2016), *Laboratory evolved gas analyses of Si-rich amorphous materials: Implications for analyses of Si-rich amorphous material in Gale Crater by the Mars Science Laboratory Sample Analysis at Mars Instrument.* AGU Fall Meeting 2016, #169004.

***Sun, V.Z.**, Milliken, R.E., and Robertson, K.M. (2016), *Relating opaline silica hydration and maturity to geologic settings on Mars*. Goldschmidt Conference 2016, #1330.

***Sun, V.Z.**, Milliken, R.E., and Robertson, K.M. (2016), *Hydrated silica on Mars: Relating geologic setting to degree of hydration, crystallinity, and maturity through coupled orbital and laboratory studies*. Lunar and Planetary Science Conference 47, #2416.

Sun, V.Z., Milliken, R.E., Robertson, K.M., Ruff, S.W., and Farmer, J.D. (2016), *Spectral characterization and mineralogy/chemistry of opaline silica samples from diverse Mars analog sites.* Lunar and Planetary Science Conference 47, #2071.

John, K.K., Wynne, J.J., Powell, K.E., MacKenzie, S.M., Caswell, T., Stavros, E.N., Crismani, M., DeBruin, K., Dhaliwal, J., Hofgartner, J., Krishnamurthy, A., Phillips-Lander, C., Leung, C., O'Rourke, J., Petro, E., Phan, S., Steuer, C., **Sun, V.**, Budney, C., and Mitchell, K. (2016), *THEO mission concept: Testing the Habitability of Enceladus' Ocean*. Lunar and Planetary Science Conference 47, #1277.

MacKenzie, S., Caswell, T., Crismani, M., DeBruin, K., Dhaliwal, J., Hofgartner, J., Krishnamurthy, A., John, K., Phillips-Lander, C., Leung, C., O'Rourke, J., Petro, E., Phan, S., Powell, K., Stavros, E.N., Steuer, C., **Sun, V.**, Wynne, J., Budney, C., and Mitchell, K. (2016), *THEO: Testing the Habitability of Enceladus' Ocean*. American Astronomical Society, DPS meeting #47, ID 312.24.

***Sun, V.Z.** and Milliken, R.E. (2015), *Ancient and recent clay formation on Mars as revealed from a global survey of hydrated minerals in crater central peaks*. 2015 GSA Annual Meeting, #265182.

Sun, V.Z. and Milliken, R.E. (2015), *Hydrated silica as a mineralogical marker for Hesperian Mars: Constraining environmental conditions from orbital and laboratory data.* Lunar and Planetary Science Conference 46, #2157.

***Sun, V.Z.** and Milliken, R.E. (2015), *Understanding ancient and recent clay formation on Mars from a global survey of crater central peaks*. Lunar and Planetary Science Conference 46,

#1652.

*__Sun, V.Z.__ and Milliken, R.E. (2014), *Recent periods of clay and hydrated silica formation at Martian central peaks.* 2014 GSA Annual Meeting, #246594.

__Sun, V.Z.__ and Milliken, R.E. (2014), *The timing and distribution of clay and hydrated mineral formation in Martian central peaks*. 8th International Conference on Mars, #1362.

__Sun, V.Z.__ and Milliken, R.E. (2014), *Origin of clay minerals in Martian central peaks: Evidence for post-Noachian clay formation.* Lunar and Planetary Science Conference 45, #1523.

__Sun, V.Z.__ and Milliken, R.E. (2013), *Geologic and mineralogical mapping to determine the origin of clay minerals in Ritchey Crater, Mars.* Lunar and Planetary Science Conference 44, #2675.

ACKNOWLEDGEMENTS

I would not be where I am today if it were not for the help and support of many, many wonderful people in the DEEPS department, the planetary community, and my family.

First and foremost, I thank my advisor Ralph Milliken, for contributing the most to my growth as a scientist. Ralph is an incredible teacher with an eye for details, and he has been a generous mentor who I can always look to for advice. He constantly encourages me to think about my research in different ways and to put my work in a big picture context. I will always respect and value his critical thinking and can only hope that I've acquired a fraction of it.

I would also like to thank the members of my committee. Jack Mustard was my point of contact when I was first thinking of applying to Brown for graduate school and has been welcoming and supportive ever since. Jim Russell always leads great Sed Strat field trips and brings a terrestrial perspective to my work. Thank you both for being on my committees and for your support since my first year as a graduate student. Carle Pieters, thank you for your contagious excitement for all things spectroscopy, and for hosting Spectroscopy Group Chat meetings during my first few years at Brown which helped introduce me to so many new spectroscopy topics. Steve Ruff, thank you for serving as my outside reader and for collecting all those opal samples with Ralph. Your feedback has been invaluable, and I appreciate you taking the time to read my dissertation.

The DEEPS department and the faculty are among the best in the world. They are dedicated to science and teaching, so thank you all, especially Pete Schultz, Don Forsyth, Alberto Saal, and Steve Parman for teaching informative classes that have helped broaden

my knowledge outside of my research. An extra thank you to Jim Head and Yan Liang for serving on my prelims committee and for helping to make the examination much less scary than what I was expecting. I also owe a big thanks to the administrative and technical staff, including Pat Davey, Anne Cote, Bill Collins, Karen Leap-Canis, Dave Blair, Gloria Correra, and Lisa Sheehan, who all are always so helpful and allow the department to run so efficiently.

Many others have helped me along through grad school. Shuai Li and Kevin Robertson, thank you for welcoming me into the research group five years ago. Kevin, I will sorely miss your expertise in the lab and am forever grateful for your patience in helping me set up the same experiment five times because I kept forgetting what goes where. Shuai, thanks for being the older graduate student figure in the group and lending an ear when I needed advice. You always have something encouraging to say to me and have been a great friend. Hannah Kaplan, I still remember when you came in as a first year and now you're the organics expert! Thanks for being my work buddy and for keeping me company in the lab space. Rachel Sheppard, thank you for being a lively presence on the third floor and for sharing your enthusiasm for everything. I'm going to miss our D&D sessions, so thank you as well to Ted, Alyssa Pascuzzo, and Parker. To Elizabeth Fisher, Brendan Anzures, and Yazhou Yang, welcome to the research group! I'm sad to be leaving, but I wish you all the best for the rest of your time at Brown and beyond.

Rebecca Greenberger, you have always been kind to me and I remember how you were the one to introduce me to working with CRISM data. I appreciate all your moral support throughout the years and your advice for navigating this last hectic year especially. Stephanie Quintana Bouchey, thank you for being my writing buddy and general defense

buddy; you've helped make to make my past few months more manageable. Tess Caswell, thank you as always for your friendship, coffee breaks, and chats since our first year at Brown. Thanks also to the rest of the planetary cohort: Terik Daly, Kevin Cannon, David Weiss, and Noah Hammond – I can't believe the last five years have passed by so quickly. And to anyone I missed in the planetary group and in DEEPS, thank you all for your kindness and friendliness; you've all helped me along in one way or another. Kirit Karkare and Shamili Allam, it's hard to believe how fast time flies and that we've been friends ever since our undergrad years at Tech. Thanks for sticking with me through thick and thin.

Most of all, I thank my family. Mom, Dad, Grandma, thank you for raising me, loving me, and giving me all the opportunities to succeed. You've taught me how to keep things in perspective and find happiness in life. And thank you Franz for your support through all these years, but especially during these last five years of graduate school. I hope to subject you to my ramblings about silica, spectra, and CRISM for many more years to come.

TABLE OF CONTENTS

CHAPTER 1:

Fe/Mg Clays and Hydrated Silica as Markers of Aqueous Environments on Mars

Vivian Z. Sun

Department of Earth, Environmental, and Planetary Sciences, Brown University,

Providence, RI 02912, USA

1. Introduction

The surface of Mars hosts an impressive array of hydrous minerals that is yet unprecedented on planetary bodies other than Earth. The collective assemblage of these minerals – phyllosilicates, sulfates, carbonates, zeolites, and hydrated silica – points to a pervasive history of aqueous alteration and their association with distinct localities and strata suggests diverse environments that varied in pH and water/rock ratio [e.g., Murchie et al., 2009]. Of these mineral groups, Fe/Mg clays and hydrated silica comprise many of the hydrous detections on Mars and are seen at orbital, rover, and meteorite scales of observation. Beyond indicating previous presence of water, both mineral classes also bear unique attributes that allow for the interpretation of environmental conditions such as pH and aqueous activity. Identification of these minerals and correlation with their geologic and stratigraphic contexts can thus yield significant insights into the nature of aqueous environments on Mars through time. The objective of this dissertation is therefore to determine the spatial and temporal distribution of Fe/Mg clays and hydrated silica formation as a means of understanding the extent of aqueous conditions throughout Mars' history.

2. Fe/Mg Clays

Fe/Mg smectites and chlorites are the most prevalent mineral group identified on Mars, and are considered evidence for widespread aqueous alteration at neutral-to-alkaline pH conditions. These clays have been proposed to form from many scenarios, including surface alteration on a "warm and wet" Mars [Bibring et al., 2006], subsurface alteration under "colder and drier" surface conditions [Ehlmann et al., 2011], and

volcanic or impact hydrothermalism [Newson, 1980; Rathbun and Squyres, 2002]. Regardless of formation mechanism, these clays are commonly interpreted as the remnants of widespread alteration during the Noachian, indicating that habitable conditions may have been restricted to the early periods of Mars' history. Much of this interpretation is attributed to clay detections associated with impact craters that are assumed to excavate and uplift these clay-bearing materials from depth. Clays associated with central peaks in particular are assumed to represent ancient alteration products that have since been buried at depth within the crust.

However, several recent studies of individual craters have combined analyses of mineralogy and high-resolution geomorphology and stratigraphy to determine that some of these clays could have formed authigenically post-impact. The clays in these craters – Holden [Tornabene et al., 2009], Toro [Marzo et al., 2010], Majuro [Mangold et al., 2012], and Ritchey [Sun and Milliken, 2014] – are associated with impact melt units or putative hydrothermal vents that postdate the impact event. Importantly, these craters are Hesperian in age, suggesting that more recent clay-forming and habitable conditions could have existed on Mars during the Hesperian or Amazonian. These detailed studies demonstrate the need to correlate high-resolution spectroscopy and imagery to properly constrain the periods of clay formation on Mars.

The distinction between Fe/Mg smectites and chlorites is also important to make, and one that is possible using near-infrared (NIR) reflectance spectra from the high-resolution CRISM (Compact Reconnaissance Imaging Spectrometer for Mars) dataset. Previous observations of crater ejecta suggest that chlorite occurrences increase with the inferred excavation depth from the martian crust [Carter et al., 2013]. On Earth,

conversion of smectite to chlorite at depth is commonly recognized as a diagenetic process that requires the presence of water and heat over time [Chang et al., 1986; Inoue et al., 1991; Środoń, 1999]. A detailed study of uplifted clays at central peaks of craters is well-poised to address if this is the case within Mars' crust. If so, observations of increasing chlorite with depth would suggest either crustal fluids enabling diagenesis or surface conditions changing to favor formation of smectites rather than chlorites over time.

Regarding Fe/Mg clays, this dissertation therefore aims to address the following questions based on mineralogic, geomorphologic, and stratigraphic study:

1) Of Fe/Mg clay detections at central peaks, what is the distribution of excavated materials versus detrital or authigenic clays that were emplaced post-impact?
2) Based on these geomorphologic interpretations, what is the timeline for clay formation on Mars and what are the implications for habitability through time?
3) What is the extent and distribution of clay type – smectite versus chlorite – with depth in the Martian crust, and what are the implications for diagenetic processes?

3. Hydrated Silica

Hydrated silica is the most recent phase to be detected at all available scales of observation on Mars, encompassing orbital spectroscopic data in the NIR [e.g., Milliken et al., 2008] and thermal wavelengths [Bandfield, 2008], *in situ* rover observations from Spirit [Squyres et al., 2008; Ruff et al., 2011] and Curiosity [Morris et al., 2016; Rampe et al., 2017], and high-resolution analyses of the Nakhla meteorite [Lee et al., 2015]. Though the terms "hydrated silica" and "opaline silica" are often used interchangeably in

the Martian literature, this dissertation defines "hydrated silica" as a family of silica polymorphs with the chemical formula $SiO_2 \cdot nH_2O$ bearing more than 1 wt% water [Jones and Segnit, 1971]. The structures of these phases are amorphous to microcrystalline, allowing water to exist within structural imperfections and bonded to surfaces, in contrast to the crystalline structures of nominally anhydrous silica phases such as quartz, cristobalite, and tridymite. Hydrated silica subclasses can be defined in order of increasing structural order and correspondingly decreasing water content: silica-rich glasses from volcanic or impact processes, opal-A, opal-CT, opal-C, and microcrystalline quartz (see also **Chapters 3, 4 and Appendix A**).

Unlike Fe/Mg clays, which typically form at specific neutral-to-alkaline pH conditions, hydrated silica can form under acidic and neutral-to-alkaline conditions [Krauskopf, 1956] and is found in a variety of geologic settings on Earth, such as soils [e.g., Tokashiki and Wada, 1975], marine environments [e.g., Kastner et al., 1977], hot spring sinters [e.g., Jones and Renaut, 2003], and residues, rinds, and coatings in fumarolic environments [e.g., Morris et al., 2000; Rodgers et al., 2002; Lynne et al., 2006; Minitti et al., 2007; Chemtob et al., 2010]. However, opals are unique in that opal crystallinity increases with increasing aqueous alteration, thus opal type (A/CT/C) can serve as a gauge for the extent of aqueous activity [Siever, 1962; Kastner et al., 1977; Williams and Crerar, 1985]. Opals therefore offer a mechanism for evaluating the intensity of aqueous alteration in martian environments, since hydrated silica is so widespread across the planet. Opals are also excellent materials for preserving biomarkers [Cady and Farmer, 1996; Konhauser et al., 2003], and it has been noted that immature opals tend to offer better preservation quality as more mature opals result from

further aqueous processing that may overprint the original biomarkers [e.g., Jones and Renaut, 2003; Campbell et al., 2015].

However, while opals have been detected on Mars from orbital NIR spectra, it has so far proved difficult to distinguish the types of opal present, although more general silica groups (e.g., opals versus quartz) can be distinguished [Rice et al., 2013]. Opals are also associated with diverse settings on Mars and hypotheses for their formation on Mars vary from hydrothermal alteration [Skok et al., 2010] to precipitation [Ruff et al., 2011; Bandfield et al., 2013] to acidic leaching [Squyres et al., 2008]. Due to hydrated silica's ubiquity, it is also necessary to study the mineralogical and geological contexts of opal-forming sites to determine past environmental conditions.

The second part of this dissertation focuses on the opaline silica family and the means by which we can determine characteristics of its formation environments on Earth and Mars. This work coordinates spectral, mineralogical, and geomorphic analyses of terrestrial opal samples and orbital detections of martian hydrated silica to answer the following questions:

1) Do opal-forming environments have unique mineralogical and chemical traits that allow us to distinguish environmental conditions (e.g., pH, redox, water/rock ratios) and formation mechanism (e.g., leaching, precipitation)?
2) Can different opal types (A/CT/C) be distinguished only using NIR spectroscopy, currently the most effective technique used to detect opals on a global scale on Mars?

3) How does opal hydration, and therefore its spectral features, change when measured at Mars-like atmospheric conditions of pressure, temperature, and relative humidity?
4) Is there evidence for different types of opal on Mars in orbital CRISM data? If so, what kinds of environments do they represent and what do they imply for the longevity of water in Mars' past?

4. Dissertation Structure

Chapter 2 focuses on assessing the hydrous mineralogy of martian crater central peaks and determine whether these materials were authigenic, detrital, or uplifted from crustal depths. Clays in central peaks were previously assumed to represent uplifted ancient materials and have contributed to the paradigm of clay formation, and therefore possibly habitable conditions, during the Noachian era (>3.7 Ga) [Bibring et al., 2006; Mustard et al., 2008]. This work tests that hypothesis by combining detailed mineralogical and geomorphological study of 633 central peaks to determine the origins of their hydrous minerals. Our study finds that 35% of central peak clays do not occur in uplifted material and many Fe/Mg clays and hydrated silica are found in putative impact melt deposits that may suggest post-impact authigenic formation of these hydrous minerals. We also observe that uplifted clays become increasingly more chloritic with depth, implying diagenetic processes and fluids in the crust. Overall, these results suggest that clay formation was widespread during the Noachian, but could have occurred as recently as the Amazonian within some impact craters. Chapter 2 was published in the *Journal of Geophysical Research – Planets* in December 2015 [Sun and Milliken, 2015].

A serendipitous outcome of this work was the observation of two distinct hydrated silica spectra at Elorza Crater, detected in two different geologic contexts only four kilometers apart within the same CRISM image **(Figure 1)**. Other hydrated silica spectra across Mars show similar variability, though none thus far seem to be as stunning as this archetypical example at Elorza. Several variables could be contributing to these spectral differences: opal type, opal hydration, type of host material (e.g., bedrock versus unconsolidated material), and possibly atmospheric conditions. The remaining dissertation chapters are largely dedicated to unraveling what these spectral variations represent and the implications for hydrated silica-forming environments and the duration of aqueous conditions on Mars.

Chapter 3 comprises a terrestrial analog study of 135 opal-bearing samples from acidic fumarole and acidic and neutral-alkaline sinter sites in Hawaii, Yellowstone National Park, and New Zealand. This chapter determines if there are diagnostic chemical or mineralogical characteristics that may reflect formation pH or mechanism (e.g., precipitation versus leaching) in these opal-rich environments. This work supports interpretations of rover data from Spirit and Curiosity and determines if additional information such as geologic context and micro/macro-scale features are necessary to assess the nature of opal-forming environments. In particular, high Ti content has previously been attributed to acid-sulfate leaching at Gusev Crater [Squyres et al., 2008] and possibly Gale Crater [Morris et al., 2016; Rampe et al., 2017]. Our results show that opal formed from acidic-leached basalt is accompanied by kaolinite, jarosite, while opals from hot spring sinters have fewer accessory minerals – generally calcite and halite at neutral-alkaline sites and kaolinite at more acidic sites. Chemical data, however, are more

difficult to interpret as few distinctions are observed between the chemistry of acidic versus neutral-alkaline sites. Ti and Mn show some correlation with environmental pH, but there is significant overlap between unaltered and acid-leached Hawaiian samples, and Ti content in sinters can range as high as 0.5 wt% in our samples or up to 0.9 wt% in previous work [Preston et al., 2008; Ruff et al., 2011]. These values overlap with the TiO_2 range observed from rovers [Squyres et al., 2008], demonstrating that high Ti levels are not uniquely associated with acid-leached basalt.

Chapter 4 focuses on determining if the different opal types (e.g., A versus CT) can be distinguished using NIR spectra alone, as this is the primary dataset used to detect hydrated silica on a global scale on Mars. Identifying the opal types present on Mars carries many implications for water longevity [Tosca and Knoll, 2009] and biopreservation [Campbell et al., 2015]. This work develops spectral parameters to characterize opal's 1.4, 1.9, and 2.2 μm features [e.g., Rice et al., 2013] for the samples described in Chapter 3. Band position, depth, area, and Gaussian fits were used to quantify variations in these hydration features, which are each composed of a short-wavelength absorption (indicative of structural H_2O or SiOH) and a long-wavelength absorption (indicative of H-bonding effects from adsorbed or multiple H_2O layers). We find that opal-A and opal-CT can be distinguished solely from their 1.4 and 2.2 μm absorptions, which allows for application to CRISM data as these features are not obscured by atmospheric absorptions at ~2 μm. In particular, opal-A has shorter 1.4 μm band positions and higher values for the ratio of the 2.26/2.21 μm band depths or Gaussian amplitudes. These parameters work equally well for powder and rock chip samples, and can identify opal-rich materials with >80% opal. A new and key result from

this work is that opal-CT tends to adsorb H_2O in multiple layers, whereas opal-A adsorbs more H_2O as a monolayer bonded to SiOH.

Chapter 5 investigates opal hydration and spectra at Mars-like atmospheric conditions. Opals are likely to appear spectrally different when subject to Mars' drier and colder atmosphere [Bishop and Pieters, 1995], and furthermore opal-A and opal-CT have different H_2O adsorption properties that may influence their spectra in Mars' lower H_2O atmosphere. In this chapter we perform hydration and dehydration experiments on opals at Mars-like pressure, temperature, and relative humidity and monitor spectra changes at 1.4, 1.9, 2.2, and 3 μm using the parameters defined in Chapter 4. From measurements at low pressures, we find that opal-A and opal-CT are still spectrally distinguishable at martian conditions, particularly with the position of the 1.4 μm feature occurring at 1.37-1.41 μm for opal-A and at 1.41-1.45 μm for opal-CT. These 1.4 μm band positions coincide with the full range of values observed in orbital CRISM detections of hydrated silica on Mars [Smith et al., 2013]. Low temperature experiments also show that opal-A and opal-CT may have different hydration behaviors on Mars. Opal-A readily hydrates at -85°C and 100% relative humidity and dehydrates at -55°C and 15% relative humidity and show observable variations in the 2.26/2.21 μm band depth ratio over timescales as short as a few hours. This suggests that despite slow kinetics at low temperatures, martian opal-A are capable of water exchange with the atmosphere and, importantly, that these effects are observable in CRISM data. Another observation is that opal-CT develops ice-like spectra at temperatures below -45°C due to its greater population of multilayer H2O, suggesting that martian opal-CT should exhibit ice-like features, particularly at 3 μm, in CRISM data.

Chapter 6 applies the results from Chapters 3-5 to hydrated silica detections from orbital CRISM data to document the geologic settings of martian opals and determine the opal types present. Hydrated silica detections on Mars are found in almost every type of observed geologic setting: bedrock outcrops, sedimentary deposits, volcanic or hydrothermal settings, eolian or unconsolidated deposits, and in impact craters [e.g., Milliken et al., 2008; Bandfield, 2008; Ehlmann et al., 2009; Skok et al., 2010]. These detections also vary in the shape and position of the 1.4 and 2.2 μm features, similar to what was observed in laboratory measurements from Chapters 4 and 5. We find that hydrated silica associated with bedrock units are spectrally distinct from silica in unconsolidated or periglacial deposits. Based on the position of the 1.4 μm feature and comparison with laboratory measurements, bedrock silica appears consistent with opal-A while unconsolidated silica is more consistent with opal-CT. This could reflect differences in exposure age between the two geologic settings or indicate slow opal maturation facilitated by the particulate nature of these unconsolidated deposits.

We also observe temporal variations in the ratio of the 2.26/2.21 μm absorptions, which may result from H_2O exchange between opals and a seasonally changing atmosphere. Laboratory experiments from Chapter 5 show that this is a kinetically feasible process, although much work remains to guarantee the robustness of these observations for the 2.2 μm feature. However, if valid, these results may represent the first evidence for H_2O exchange between a specific mineral and the martian atmosphere and support hypotheses of hydrated minerals helping to regulate diurnal and seasonal variations in atmospheric water content. Overall, our results are consistent with previous observations of more mature silica phases on Mars [Smith et al., 2013; Morris et al.,

2016] and suggest that some opals record prolonged or intense periods of aqueous alteration and may play a role in present-day atmospheric water cycling. However, given the complexities of opal's spectral variations and geologic contexts, caution and further work is still needed to determine how to best interpret hydrated silica detections to make valid inferences about paleoenvironments on Mars.

Finally, **Chapter 7** provides a synthesis of Chapters 2-6 and summarizes the major contributions of this dissertation as well as future work and directions. Orbital observations of both Fe/Mg clays and hydrated silica, supported by laboratory measurements and experiments in the case of the latter, show that aqueous processes may have been more extensive than previously thought [e.g., Tosca and Knoll, 2009]. Although martian clays and opals generally still seem to be geochemically immature, both mineral groups show evidence for diagenetic alteration. Fe/Mg smectites appear to have converted to chlorite at depth in the martian crust based on central peak observations, and opal-CT is observed in unconsolidated materials in contrast with opal-A in bedrock units. However, much work remains to understand other aspects of these aqueous environments, such as pH and water-to-rock ratios, and will likely require documentation of complete mineral assemblages and detailed correlation with stratigraphy and geomorphology.

References

Bandfield, J. L. (2008), High-silica deposits of an aqueous origin in western Hellas Basin, Mars, *Geophysical Research Letters*, *35*(12), doi:10.1029/2008GL033807.

Bandfield, J. L., E. S. Amador, and N. H. Thomas (2013), Extensive hydrated silica materials in western Hellas Basin, Mars, *Icarus*, *226*(2), 1489–1498, doi:10.1016/j.icarus.2013.08.005.

Bibring, J.-P. et al. (2006), Global Mineralogical and Aqueous Mars History Derived from OMEGA/Mars Express Data, *Science*, *312*(5772), 400–404, doi:10.1126/science.1122659.

Bishop, J. L., and C. M. Pieters (1995), Low-temperature and low atmospheric pressure infrared reflectance spectroscopy of Mars soil analog materials, *J. Geophys. Res.*, *100*(E3), 5369–5379, doi:10.1029/94JE03331.

Cady, S. L., and J. D. Farmer (1996), Fossilization processes in siliceous thermal springs: trends in preservation along thermal gradients, *Ciba Found. Symp.*, *202*, 150-170; discussion 170-173.

Campbell, K. A., B. Y. Lynne, K. M. Handley, S. Jordan, J. D. Farmer, D. M. Guido, F. Foucher, S. Turner, and R. S. Perry (2015), Tracing Biosignature Preservation of Geothermally Silicified Microbial Textures into the Geological Record, *Astrobiology*, *15*(10), 858–882, doi:10.1089/ast.2015.1307.

Carter, J., F. Poulet, J.-P. Bibring, N. Mangold, and S. Murchie (2013), Hydrous minerals on Mars as seen by the CRISM and OMEGA imaging spectrometers: Updated global view, *J. Geophys. Res. Planets*, *118*(4), 831–858, doi:10.1029/2012JE004145.

Chang, H. K., F. T. MacKenzie, and J. Schoonmaker (1986), Comparisons between the diagenesis of dioctahedral and trioctahedral smectite, Brazilian offshore basins, *Clays and Clay Minerals*, *34*(4), 407–423.

Chemtob, S. M., B. L. Jolliff, G. R. Rossman, J. M. Eiler, and R. E. Arvidson (2010), Silica coatings in the Ka'u Desert, Hawaii, a Mars analog terrain: A micromorphological, spectral, chemical, and isotopic study, *J. Geophys. Res.*, *115*(E4), E04001, doi:10.1029/2009JE003473.

Ehlmann, B. L. et al. (2009), Identification of hydrated silicate minerals on Mars using MRO-CRISM: Geologic context near Nili Fossae and implications for aqueous alteration, *Journal of Geophysical Research: Planets*, *114*, E00D08, doi:10.1029/2009JE003339.

Ehlmann, B. L., J. F. Mustard, S. L. Murchie, J.-P. Bibring, A. Meunier, A. A. Fraeman, and Y. Langevin (2011), Subsurface water and clay mineral formation during the early history of Mars, *Nature*, *479*(7371), 53–60, doi:10.1038/nature10582.

Inoue, A., M. Utada, and K. Wakita (1992), Smectite-to-illite conversion in natural hydrothermal systems, *Applied Clay Science*, *7*(1–3), 131–145, doi:10.1016/0169-1317(92)90035-L.

Jones, B., and R. W. Renaut (2003), Hot spring and geyser sinters: the integrated product of precipitation, replacement, and deposition, *Can. J. Earth Sci.*, *40*(11), 1549–1569, doi:10.1139/e03-078.

Jones, J. B., and E. R. Segnit (1971), The nature of opal I. nomenclature and constituent phases, *Journal of the Geological Society of Australia*, *18*(1), 57–68, doi:10.1080/00167617108728743.

Kastner, M., J. B. Keene, and J. M. Gieskes (1977), Diagenesis of siliceous oozes—I. Chemical controls on the rate of opal-A to opal-CT transformation—an experimental

study, *Geochimica et Cosmochimica Acta*, *41*(8), 1041–1059, doi:10.1016/0016-7037(77)90099-0.

Konhauser, K. O., B. Jones, A.-L. Reysenbach, and R. W. Renaut (2003), Hot spring sinters: keys to understanding Earth's earliest life forms, *Can. J. Earth Sci.*, *40*(11), 1713–1724, doi:10.1139/e03-059.

Krauskopf, K. B. (1956), Dissolution and precipitation of silica at low temperatures, *Geochimica et Cosmochimica Acta*, *10*(1), 1–26, doi:10.1016/0016-7037(56)90009-6.

Lee, M. R., I. MacLaren, S. M. L. Andersson, A. Kovács, T. Tomkinson, D. F. Mark, and C. L. Smith (2015), Opal-A in the Nakhla meteorite: A tracer of ephemeral liquid water in the Amazonian crust of Mars, *Meteorit Planet Sci*, *50*(8), 1362–1377, doi:10.1111/maps.12471.

Lynne, B. Y., K. A. Campbell, R. S. Perry, P. R. L. Browne, and J. N. Moore (2006), Acceleration of sinter diagenesis in an active fumarole, Taupo volcanic zone, New Zealand, *Geology*, *34*(9), 749–752, doi:10.1130/G22523.1.

Mangold, N., J. Carter, F. Poulet, E. Dehouck, V. Ansan, and D. Loizeau (2012), Late Hesperian aqueous alteration at Majuro crater, Mars, *Planetary and Space Science*, *72*(1), 18–30, doi:10.1016/j.pss.2012.03.014.

Marzo, G. A., A. F. Davila, L. L. Tornabene, J. M. Dohm, A. G. Fairén, C. Gross, T. Kneissl, J. L. Bishop, T. L. Roush, and C. P. McKay (2010), Evidence for Hesperian impact-induced hydrothermalism on Mars, *Icarus*, *208*(2), 667–683, doi:10.1016/j.icarus.2010.03.013.

Milliken, R. E. et al. (2008), Opaline silica in young deposits on Mars, *Geology*, *36*(11), 847–850, doi:10.1130/G24967A.1.

Minitti, M. E., C. M. Weitz, M. D. Lane, and J. L. Bishop (2007), Morphology, chemistry, and spectral properties of Hawaiian rock coatings and implications for Mars, *J. Geophys. Res.*, *112*(E5), E05015, doi:10.1029/2006JE002839.

Morris, R. V. et al. (2000), Mineralogy, composition, and alteration of Mars Pathfinder rocks and soils: Evidence from multispectral, elemental, and magnetic data on terrestrial analogue, SNC meteorite, and Pathfinder samples, *J. Geophys. Res.*, *105*(E1), 1757–1817, doi:10.1029/1999JE001059.

Morris, R. V. et al. (2016), Silicic volcanism on Mars evidenced by tridymite in high-SiO2 sedimentary rock at Gale crater, *PNAS*, *113*(26), 7071–7076, doi:10.1073/pnas.1607098113.

Murchie, S. L. et al. (2009), Compact Reconnaissance Imaging Spectrometer for Mars investigation and data set from the Mars Reconnaissance Orbiter's primary science phase, *Journal of Geophysical Research: Planets*, *114*, E00D07, doi:10.1029/2009JE003344.

Mustard, J. F. et al. (2008), Hydrated silicate minerals on Mars observed by the Mars Reconnaissance Orbiter CRISM instrument, *Nature*, *454*(7202), 305–309, doi:10.1038/nature07097.

Newsom, H. E. (1980), Hydrothermal alteration of impact melt sheets with implications for Mars, *Icarus*, *44*(1), 207–216, doi:10.1016/0019-1035(80)90066-4.

Preston, L. J., G. K. Benedix, M. J. Genge, and M. A. Sephton (2008), A multidisciplinary study of silica sinter deposits with applications to silica identification and detection of fossil life on Mars, *Icarus*, *198*(2), 331–350, doi:10.1016/j.icarus.2008.08.006.

Rampe et al., E. B. (2017), Mineralogical trends in mudstone deposits from the Murray formation, Gale crater, Mars, *in revision at Earth and Planetary Science Letters*.

Rathbun, J. A., and S. W. Squyres (2002), Hydrothermal Systems Associated with Martian Impact Craters, *Icarus*, *157*(2), 362–372, doi:10.1006/icar.2002.6838.

Rice, M. S., E. A. Cloutis, J. F. Bell III, D. L. Bish, B. H. Horgan, S. A. Mertzman, M. A. Craig, R. W. Renaut, B. Gautason, and B. Mountain (2013), Reflectance spectra diversity of silica-rich materials: Sensitivity to environment and implications for detections on Mars, *Icarus*, *223*(1), 499–533, doi:10.1016/j.icarus.2012.09.021.

Rodgers, K. A., K. L. Cook, P. R. L. Browne, and K. A. Campbell (2002), The mineralogy, texture and significance of silica derived from alteration by steam condensate in three New Zealand geothermal fields, *Clay Minerals*, *37*(2), 299–322, doi:10.1180/0009855023720035.

Ruff, S. W. et al. (2011), Characteristics, distribution, origin, and significance of opaline silica observed by the Spirit rover in Gusev crater, Mars, *Journal of Geophysical Research: Planets*, *116*(E7), n/a–n/a, doi:10.1029/2010JE003767.

Siever, R. (1962), Silica Solubility, 0°-200° C., and the Diagenesis of Siliceous Sediments, *The Journal of Geology*, *70*(2), 127–150.

Skok, J. R., J. F. Mustard, B. L. Ehlmann, R. E. Milliken, and S. L. Murchie (2010), Silica deposits in the Nili Patera caldera on the Syrtis Major volcanic complex on Mars, *Nature Geosci*, *3*(12), 838–841, doi:10.1038/ngeo990.

Smith, M. R., J. L. Bandfield, E. A. Cloutis, and M. S. Rice (2013), Hydrated silica on mars: combined analysis with near-infrared and thermal-infrared spectroscopy, *Icarus*, doi:10.1016/j.icarus.2013.01.024.

Squyres, S. W. et al. (2008), Detection of Silica-Rich Deposits on Mars, *Science*, *320*(5879), 1063–1067, doi:10.1126/science.1155429.

Środoń, J. (1999), Nature of Mixed-Layer Clays and Mechanisms of Their Formation and Alteration, *Annual Review of Earth and Planetary Sciences*, *27*(1), 19–53, doi:10.1146/annurev.earth.27.1.19.

Sun, V. Z., and R. E. Milliken (2014), The geology and mineralogy of Ritchey crater, Mars: Evidence for post-Noachian clay formation, *J. Geophys. Res. Planets*, *119*(4), 2013JE004602, doi:10.1002/2013JE004602.

Sun, V. Z., and R. E. Milliken (2015), Ancient and recent clay formation on Mars as revealed from a global survey of hydrous minerals in crater central peaks, *J. Geophys. Res. Planets*, *120*(12), 2015JE004918, doi:10.1002/2015JE004918.

Tokashiki, Y., and K. Wada (1975), Weathering implications of the mineralogy of clay fractions of two Ando soils, Kyushu, *Geoderma*, *14*(1), 47–62, doi:10.1016/0016-7061(75)90012-9.

Tornabene, L. L., G. R. Osinski, and McEwen, A. S. (2009), Parautochthonous Megabreccias and Possible Evidence of Impact-Induced Hydrothermal Alteration in Holden Crater, Mars., *Lunar Planet. Sci. XL*, Abstract 1766.

Tosca, N. J., and A. H. Knoll (2009), Juvenile chemical sediments and the long term persistence of water at the surface of Mars, *Earth and Planetary Science Letters*, *286*(3–4), 379–386, doi:10.1016/j.epsl.2009.07.004.

Williams, L. A., and D. A. Crerar (1985), Silica Diagenesis, II. General Mechanisms, *Journal of Sedimentary Research*, *55*(3).

Figures

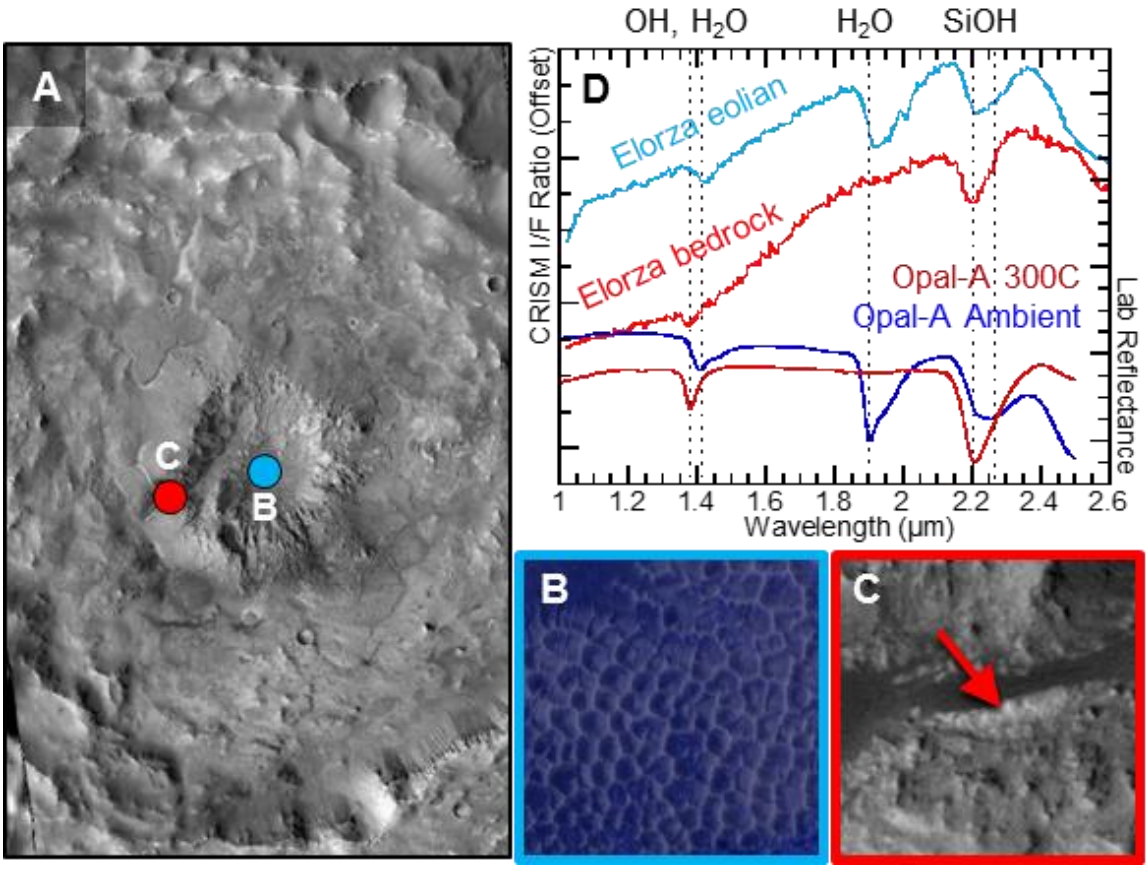

Figure 1. A) Elorza Crater hosts B) hydrated and/or opal-CT silica in eolian deposits and C) dehydrated and/or opal-A silica in bedrock, both within the same CRISM image (FRT00008236).

CHAPTER 2:

Ancient and Recent Clay Formation on Mars as Revealed from a Global Survey of Hydrous Minerals in Crater Central Peaks

Vivian Z. Sun

and

Ralph E. Milliken

Department of Earth, Environmental, and Planetary Sciences, Brown University,

Providence, RI 02912, USA

Published in its current form in:

Journal of Geophysical Research - Planets

doi:10.1002/2015JE004918.

Abstract

Clay minerals on Mars have commonly been interpreted as the remnants of pervasive water-rock interaction during the Noachian period (>3.7 Ga). This history has been partly inferred by observations of clays in central peaks of impact craters, which often are presumed uplifted from depth. However, combined mineralogical and morphological analyses of individual craters have shown that some central peak clays may represent post-impact, possibly authigenic processes. Here we present a global survey of 633 central peaks to assess their hydrous minerals and the prevalence of uplifted, detrital, and authigenic clays. Central peak regions are examined using high-resolution CRISM and HiRISE data to identify hydrous minerals and place their detections in a stratigraphic and geologic context. We find that many occurrences of Fe/Mg clays and hydrated silica are associated with potential impact melt deposits. Over 35% of central peak clays are not associated with uplifted rocks, thus caution must be used when inferring deeper crustal compositions from surface mineralogy of central peaks. Uplifted clay-bearing rocks suggest the martian crust hosts clays to depths of at least 7 km. We also observe evidence for increasing chloritization with depth, implying the presence of fluids in the upper portions of the crust. Our observations are consistent with widespread Noachian/Early Hesperian clay formation, but a number of central peak clays are also suggestive of clay formation during the Amazonian. These results broadly support current paradigms of Mars' aqueous history while adding insight to global crustal and diagenetic processes associated with clay mineral formation and stability.

1. Introduction

Hydrous minerals can record evidence of past aqueous and atmospheric conditions and are now recognized as important components of the martian crust. Diverse minerals such as phyllosilicates, sulfates, hydrated silica, carbonates, and zeolites have been detected from orbit using visible-near infrared (VIS-NIR) reflectance spectroscopy [e.g., Bibring et al., 2006; Murchie et al., 2009], and their presence suggests a rich history of alteration and water-rock interaction in different environments on Mars. Of these hydrous phases, Fe/Mg-bearing phyllosilicates are the most prevalent and occur in 89% of exposures exhibiting hydrous minerals [Carter et al., 2013]. These clay minerals, hereafter referred to simply as "clays", can form from the interaction of liquid water and rock or via direct precipitation under neutral to alkaline conditions, and thus may preserve evidence of past environmental conditions. Such clay-forming conditions could have existed at the surface of a "warm and wet" Mars [Poulet et al., 2005; Bibring et al., 2006], in the deeper subsurface under a colder and drier climate [Ehlmann et al., 2011b], in volcanic [Farmer, 1996] or impact-induced hydrothermal environments [Newsom, 1980; Allen et al., 1982; Rathbun and Squyres, 2002], or in aqueous depositional environments that allow for in situ formation (e.g., neoformation) [Milliken and Bish, 2010; Bristow and Milliken, 2011; Vaniman et al., 2014].

The observed hydrous minerals are spatially and stratigraphically associated with the major martian geologic units and epochs. Terrains corresponding to the earliest period, the Noachian (≥3.7 Ga based on Hartmann and Neukum [2001]), are characterized by an abundance of Fe/Mg clays, particularly in the ancient southern highlands [Bibring et al., 2006; Mustard et al., 2008]. In contrast, younger Hesperian

(3.1-3.7 Ga) and Amazonian (≤3.1 Ga) terrains are marked by a relative paucity or absence of clay minerals [Poulet et al., 2005; Bibring et al., 2006; Murchie et al., 2009; Arvidson et al., 2014]. Because clay minerals may be indicative of habitable conditions, these observations could suggest that the best prospects for habitability on Mars existed very early in the planet's history, during the Noachian. In the model of Bibring et al. [2006], subsequent times saw a global transition towards the cold and arid climate that typifies Mars today, resulting in conditions that are not conducive to widespread clay formation at or near the surface. This paradigm of decreasing availability of liquid water and the desiccation of Mars is further supported by independent observations of widespread valley networks that formed during the Noachian and largely ceased by the early Hesperian [Carr, 1996; Fassett and Head, 2008]. However, to fully explore these concepts and to understand whether or not mineralogy can be used as a marker for global climatic and atmospheric evolution, it is first necessary to place individual mineral detections in their proper geologic context and, ultimately, in a relative or absolute chronology.

Impact craters are crucial to this investigation as they can probe subsurface mineralogy, host environments that form clays, and are also basins for detrital and eolian materials. In this study we examine globally distributed craters on Mars that exhibit central peak structures, with a focus on determining the geologic context of hydrous minerals observed in these locations. Our goals are to assess the presence, diversity, and distribution of hydrous minerals in these environments and to ascertain whether these minerals occur in deep-seated, uplifted rocks or if they are instead the result of younger, near-surface processes. Understanding the proper stratigraphic context of hydrous

minerals in crater environments and the relative ages of the deposits that host these minerals will allow us to place better constraints on the vertical distribution of hydrous minerals in the martian crust, as well as the timing and duration of clay forming conditions on Mars.

2. Background

2.1 Clay Minerals in Craters

Impact craters are ubiquitous landforms in the ancient crust of Mars that expose subsurface materials and allow us to probe crustal compositions using orbitally-acquired VIS-NIR reflectance spectra. Observations of clays in crater environments have been crucial in establishing the Noachian period (>3.7 Ga) as the primary time of clay formation, with over 50% of all clay minerals found in crater settings [Ehlmann et al., 2011b; Carter et al., 2013]. The majority of clay detections are in the Noachian southern highlands, where they have been interpreted as excavated and uplifted materials due to their spatial association with crater walls, central peaks, and ejecta blankets [Bibring et al., 2006; Mustard et al., 2008; Loizeau et al., 2012; Quantin et al., 2012]. In particular, uplifted central peak materials are generally inferred to originate from crustal depths as great as 10% of the crater diameter [Ivanov et al., 1982; Grieve and Pilkington, 1996]. Shallower strata may also be incorporated into the central structure via listric faulting during the crater modification stage. However, the bulk of central peak material (particularly in the upper/higher portion) likely originates from depth and this is supported by numerous examples from the terrestrial impact crater literature [e.g., Grieve and Pilkington, 1996]. Clays at central peaks are therefore often hypothesized to

represent either buried Noachian surface alteration products [Bibring et al., 2006; Mustard et al., 2008] or clays formed via deep-seated subsurface alteration [Ehlmann et al., 2011b]. Despite this common presumption that central peak clays are generally Noachian in age, detailed studies have identified younger and possibly authigenic clays in the central peaks of several Hesperian impact craters. These Hesperian or Amazonian clays are proposed to have formed in a hydrothermal system at Toro crater [Marzo et al., 2010] and an alluvial fan in Majuro crater [Mangold et al., 2012b], or in association with impact melt in the case of Ritchey crater [Sun and Milliken, 2014], suggesting that post-Noachian clay formation was possible in impact systems. The possibility that central peak clays may represent near-surface (and perhaps more recent) formation rather than uplifted Noachian crust highlights the need to examine the geologic context of central peak clays in more detail.

Various mechanisms are capable of emplacing clays within craters and, by extension, at central peaks. In addition to excavation and uplift, authigenic formation and fluvial or eolian transport are other processes that could produce clay mineral signatures in impact craters. Each emplacement mechanism has distinct implications for the origin (crustal or otherwise) and formation age of the clay-bearing units. Impact-generated authigenic alteration has been associated with a number of impacts on Earth, either through local post-impact chemical weathering or hydrothermal systems hosted within impact crater lakes [Osinski et al., 2013]. Impact events may also facilitate post-impact alteration by producing impact glass and by fragmenting materials, increasing susceptibility to chemical weathering. On Mars, authigenic clay formation has been invoked for several Hesperian craters where clays occur in units that were emplaced after

the impact event and whose origin could not be attributed to fluvial or eolian deposition. These clays may have formed in hydrothermal systems in the case of Toro crater [Marzo et al., 2010] or in lower-temperature environments such as clays in Majuro crater [Mangold et al., 2012b]. Potentially fine-grained and/or glassy impact-related products, such as the injected melt veins observed at Holden crater [Tornabene et al., 2009] and impact melt at the central peak of Ritchey crater [Sun and Milliken, 2014], could also undergo in situ alteration to clay minerals in the near-surface environment. The stratigraphic position of these impact-related clay-bearing units dictates that they must have been deposited and/or formed after the impact event, which is in contrast to clays in ejected or uplifted rocks that may predate an impact event. In the case of possible post-impact authigenic clays, the age of the host crater can be used to constrain the oldest formation age of the clays and thus local water-rock interaction.

Exogenous (detrital) clays could have been fluvially transported from an external source region to a crater and may occur in alluvial fan or delta deposits, as in the case of clay-rich deposits at Holden crater [Grant et al., 2008; Milliken and Bish, 2010], Jezero crater [Ehlmann et al., 2008a], and Terby crater [Ansan et al., 2011]. The origin of these clays can be traced in a source-to-sink scenario [e.g., Milliken and Bish, 2010; Goudge et al., 2015] and fluvial systems likely sample a different portion of the crust than centrally uplifted materials. In such cases the fluvial activity must postdate the host crater that is incised, but the detrital clays could have formed at any time before fluvial transport. A similar reasoning can be applied to wind-transported clays [Loizeau et al., 2007] that may occur in loess or other eolian deposits, which may have an untraceable provenance but must have formed prior to their deposition in the crater. However, there is a significant

caveat in that clays found in fluvial or eolian deposits could also have formed authigenically, as suggested for mudstones studied by the Curiosity rover in Gale crater [Vaniman et al., 2014; Bristow et al., 2015], inferred ancient lakebeds in Columbus crater [Wray et al., 2011], wind-blown sandstones in Gale crater [Milliken et al., 2014], and altered ash or wind-blown deposits at Mawrth Vallis [Loizeau et al., 2007; Wray et al., 2008; Bishop et al., 2008]. Authigenesis is difficult to discount in many cases as it is effectively impossible to conclusively prove or disprove this formation mechanism using orbital data alone. If such clays are truly authigenic, then their formation must postdate the impact event.

The complex range of possible formation scenarios and ages for clays and other hydrous minerals detected in central peak regions emphasizes the need to examine these units in greater detail. Uplifted clays can inform us of deep crustal compositions, burial history, diagenetic processes, and ancient water availability, whereas detrital and authigenic clays may provide insight into more recent fluvial activity and local or regional water-rock interaction. Authigenic clays are particularly intriguing as they may indicate habitable environments after the early period of presumed widespread clay formation during the Noachian. Distinguishing between uplifted, detrital, and possible authigenic minerals requires detailed correlation of high-resolution reflectance spectroscopy with visible imagery to discern which geomorphologic units actually host the hydrous minerals observed within each crater. Many of the key geologic and stratigraphic observations needed for such discrimination can only be resolved in high-resolution data.

2.2 This Study

In this paper we present a detailed study of individual central peak regions from a comprehensive global survey of craters, with a focus on the implications for clay formation on Mars. This work builds upon the methodology and results of our previous case study of Ritchey crater [Sun and Milliken, 2014] and addresses several key questions:

1. What proportion of clay occurrences in central peak regions truly represents uplifted crust rather than materials emplaced within the crater after the impact event?
2. What is the extent and distribution of clay type with depth in the martian crust and what does this imply for clay-forming conditions and processes?
3. How common are examples of post-Noachian clays in central peak regions and what is their geologic context?

This work aims to bridge the gap between global surveys of hydrous minerals [Murchie et al., 2009; Ehlmann et al., 2011b; Carter et al., 2013; Pan et al., 2015] and higher-resolution, detailed geomorphologic studies of individual craters [e.g., Marzo et al., 2010; Michalski and Niles, 2010; Mangold et al., 2012b; Sun and Milliken, 2014]. We assess whether hydrous minerals in crater central peaks represent uplifted crustal materials, detrital sediments, or potential authigenic phases. Lastly, we constrain the formation ages of the deposits that host these minerals. We document all hydrous minerals detected at central peak regions to better understand the diversity of past aqueous environments, but we focus on clay minerals in particular due to their pervasiveness and commonly inferred Noachian origin. An important motivation for this

work is establishing a taxonomic scheme by which hydrous minerals in central peak regions can be objectively classified into geologic contexts **(Section 3.4)**. Although we focus on uplifted and impact melt-related clays in our Discussion, we stress that it is important to consider all the possible geologic contexts that may host hydrous minerals in central peak regions. In this context, it is our hope that these results may help constrain future studies that examine the mineralogy of central peaks (e.g., with CRISM or OMEGA) but that lack sufficient image data (e.g., HiRISE) to resolve the details of their origins.

We describe our methods in **Section 3**, which consists of a description of the datasets used **(Section 3.1)**, selection of the global central peak population **(Section 3.2)**, mineral identification techniques **(Section 3.3)**, our classification scheme for the geologic contexts of hydrous minerals **(Section 3.4)**, crater count age dating methods **(Section 3.5)**, and an acknowledgement of the observational biases and caveats to be considered in our results **(Section 3.6)**. The results are presented in several sections, starting with a description of the hydrous minerals detected at central peaks **(Section 4)**, followed by a description of the geologic contexts of each hydrous mineral group **(Section 5)** and the ages of host craters **(Section 6)**. We also discuss the results of our study relative to those of previous global studies **(Section 7)**. Finally, we discuss the apparent distribution of hydrous minerals within the crust **(Section 8.1),** how clay mineralogy varies with depth **(Section 8.2)**, and implications for the timing and duration of clay-forming conditions on Mars **(Section 8.3)**.

3. Methods

Analysis at each crater first consists of identification of hydrous minerals in the central peak region **(Section 3.3)** using all available CRISM data. If hydrous minerals are detected, we extend our CRISM analysis to the entire crater interior to better constrain our interpretations. We then determine the geologic contexts of the hydrous minerals in order to infer relative ages and potential emplacement mechanisms **(Section 3.4)**. Craters whose central peak regions bear hydrous minerals are then age-dated using crater counts, thus constraining the formation ages of the deposits that host hydrous minerals **(Section 3.5)**. We also document other crater features that may help with the interpretation of the central peak observations, including the type of central structure (e.g., peak, pit, summit pit, peak ring), target geologic unit [Tanaka et al., 2014], the presence of alluvial landforms or fluvial features, and crater degradation state [Mangold et al., 2012a]. A flowchart of this analysis procedure is presented in **Figure 1**.

3.1 CTX, HiRISE, and CRISM Datasets

Assessing potential origins of hydrous phases requires correlating mineralogy from high-resolution spectral data with geomorphologic units defined in high-resolution images. We used data acquired by a suite of instruments on the Mars Reconnaissance Orbiter (MRO): Compact Reconnaissance Imaging Spectrometer for Mars (CRISM) spectral data, Context Camera (CTX) images, and High Resolution Imaging Science Experiment (HiRISE) images.

CRISM ‘targeted’ observations provide hyperspectral reflectance data at the highest spectral and spatial resolution currently available for Mars at VIS-NIR

wavelengths. The instrument's two detectors acquire reflected solar radiation from 0.36-3.92 μm over 544 channels at a sampling of 6.55 nm/channel, which is sufficient for resolving the narrow absorption features characteristic of many hydrous minerals. In this study we used data from the L detector, which spans the 1.0-3.92 μm wavelength region. We primarily use data in the 1.0-2.6 μm range, which captures diagnostic vibration absorptions associated with the presence of H_2O and/or OH. CRISM images are ~10 km wide, with spatial resolution ranging from ~15-19 m/pixel for Full Resolution Targeted (FRT) observations to ~38 m/pixel for Half Resolution Long/Short (HRL/HRS) observations [Murchie et al., 2007].

CRISM data were processed in ENVI using the CRISM Analysis Toolkit v6.6, where we applied standard corrections for viewing geometry and atmospheric gas absorptions. Photometric corrections were performed by dividing the data cubes by the cosine of the solar incidence angle. Atmospheric effects were removed using the volcano scan method, which divides each observed spectrum by a scaled atmospheric transmission spectrum derived from observations at the base and top of Olympus Mons [McGuire et al., 2009]. The data are then processed to reduce vertical striping effects and spectral spikes [Parente, 2008] and each processed image cube is then map-projected. Standard CRISM spectral summary parameter maps [Pelkey et al., 2007] were also generated and map-projected to guide mineral identification.

CTX images are obtained in 30 km wide swaths at a resolution of 5-6.5 m/pixel, giving almost global coverage at moderate resolution and providing context for smaller HiRISE and targeted CRISM images [Malin et al., 2007]. Geomorphologic units and fluvial features can generally be distinguished at CTX resolution, but the stratigraphic

relations between units are not always readily discernable without higher-resolution imagery [e.g., Tornabene et al., 2009]. We used CTX imagery for general context and crater counts and HiRISE imagery for detailed study of geomorphology and stratigraphic relationships within central peak regions. HiRISE images are acquired from a red channel (0.57-0.83 μm) in 6 km wide swaths at 0.25-0.50 cm/pixel resolution, with a central 1.2 km wide swath providing additional data from a blue-green (0.4-0.58 μm) and a near-infrared (0.79-1.1 μm) channel [McEwen et al., 2007]. Although these multispectral bands are not sufficient to provide unique mineral identifications, this central false-color portion of the image can highlight spectral variability that is likely associated with mineralogical variability.

3.2 Selection of Craters for Study

Craters that bear a discernable central structure and that have both CRISM and HiRISE coverage over at least a portion of their central region were included in our study. While we do not explicitly impose a cutoff crater size, factors such as degradation of larger craters and observational biases **(Section 3.6)** result in our survey spanning craters from 5 to 216 km in diameter. Although central structures can appear as peaks, pits, summit pits, and peak rings, we group and categorize them all as 'central peaks' for the sake of brevity in this work. Central peaks are also sometimes referred to as 'central uplifts' in the literature, but we avoid using this term so as not to impose a presumption on the origin or stratigraphic position of hydrous minerals located in these regions. We define a crater's 'central peak region' as residing within the innermost 50% of the crater diameter and whose structures are discernable at the resolution of MOLA topography.

For smaller craters whose central structures are not resolvable from MOLA, inferences on the type of central structure are made from visible imagery. Our criteria omit filled-in, flat-floored basins as well as heavily mantled craters at high latitudes. We also disregard craters that are already documented as having central structures likely obscured by infill, which includes craters such as Gale, Crommelin, Nicholson, and Becquerel (termed 'overfilled' in the classification scheme of Grotzinger and Milliken [2012]), as well as potential paleolakes such as Jezero [Goudge et al., 2015]. This study utilized CRISM images (version TRR3) released before February 12, 2014. To conduct a comprehensive global survey and to avoid bias that could result from selecting a smaller 'representative' population of craters, we chose to study *all* craters that met the aforementioned criteria. This amounted to a total of 633 central peak regions **(Figure 2)**, which we note is but a subset (21.5%) of the entire catalog of 2,997 craters with visible central structures on Mars [Barlow and Bradley, 2000].

3.3 CRISM Mineral Identification

Hydrous minerals are identified from diagnostic vibrational absorptions in the 1.0-2.6 μm wavelength range of CRISM data. We focus on minerals that have been previously documented on Mars, such as Fe/Mg/Al smectites, chlorites, hydrated silica, carbonates, zeolites, and sulfates [Ehlmann et al., 2009; Murchie et al., 2009]. CRISM spectral summary products, particularly the BD1900, BD2210, D2300, BD2350, and SINDEX parameters [Pelkey et al., 2007], were first examined to locate regions that were likely to host hydrous minerals. The BD1900 parameter highlights a non-unique 1.9 μm H_2O absorption that could indicate any of the previously mentioned hydrous minerals,

depending on the absorption center and shape. The BD2210 parameter indicates a 2.2 μm absorption due to Al-OH or Si-OH vibrations from aluminous clays or hydrated silica respectively, whereas the D2300 parameter measures a drop in reflectance values at ~2.3 μm that is often attributable to Fe/Mg-OH vibrations in clays. Finally, the BD2350 parameter highlights some chlorites that have a complex absorption feature centered at 2.35 μm, and the SINDEX parameter can indicate hydrated sulfates. The diagnostic absorptions particular to each hydrous mineral group are discussed in further detail in their respective sections in **Section 4**, and a more detailed overview of CRISM spectral parameters is provided in Pelkey et al. [2007]. Recent work by Viviano-Beck et al. [2014] discusses new and improved CRISM spectral parameters that are likely more sensitive to detection of certain minerals, but these were not available at the start of this work and were not adopted mid-way for consistency. However, our study only used the spectral parameters as a guide and our detailed analysis of CRISM images and spectra allows for a much more nuanced interpretation of mineralogy, thus we consider it to be fully representative of hydrous minerals in central peak regions.

Regions highlighted in the spectral summary parameters were manually inspected to confirm the presence or absence of hydrous minerals. Regions of interest (ROIs) were defined from the parameter maps as well as from distinctly colored regions in CRISM false-color images, where clays and hydrated silica often appear blue-green in tone when NIR wavelengths of 2.5295, 1.5066, and 1.0800 μm are viewed in the red, green, and blue color channels, respectively. We note that intriguing color tones observed in the false-color RGB composites are not always highlighted in the spectral parameter maps. Our examination of these pixels therefore provides a more detailed level of analysis than

what is gained by looking only at 'positive' detections in the spectral parameter maps. The ROI spectra were then divided by the mean spectrum of a 'bland' background region to enhance spectral features by suppressing residual atmospheric effects and instrumental noise. This ratio method can sometimes induce spectral slopes on the ratio spectra, as it depends on the choice of the background (denominator spectrum) and emphasizes mineralogical differences between the ROI and background pixels. Each ROI ratio spectrum was then manually inspected for diagnostic absorption features and compared to laboratory spectra from the Reflectance Experiment LABoratory (RELAB) and CRISM [Murchie et al., 2007] spectral libraries to identify specific minerals. Individual ROIs (as small as tens to hundreds of pixels) that exhibit similar absorption features and absorption strengths were then combined into larger ROIs that may total up to thousands of pixels. This procedure produces cleaner spectra by averaging over a larger ROI while minimizing effects due to noisy pixels, shadows, and false positives identified from the smaller individual ROIs. By starting with small ROIs and only averaging spectrally similar ROIs we reduce the potential for accidentally missing regions of distinct mineralogy during the averaging process. We applied these procedures to all available CRISM data over each central peak region to maximize spatial coverage, and we reinforced hydrous mineral detections by examining multiple CRISM observations. Overlapping images were also assessed to reduce the chance of overlooking weak mineral signatures due to unfavorable atmospheric or instrument conditions at the time of data acquisition.

We classified hydrous mineral detections into the following groups: Fe/Mg smectite (including potential mixed-layer chlorite/smectite [e.g., Milliken and Bish, 2010;

Milliken et al., 2010; 2011]), chlorite, hydrated/opaline silica, zeolite, sulfate, Al-phyllosilicates, and unidentified hydrous phases (bearing only a non-unique 1.9 μm H_2O absorption) **(Table 1)**. Where possible, we corroborate our detections with previously published literature on hydrous minerals in craters from large surveys [e.g., Carter et al., 2010; Quantin et al., 2012; Pan et al., 2015] or individual crater studies [e.g., Marzo et al., 2010; Michalski and Niles, 2010; Mangold et al., 2012b] **(Appendix B)**. Hydrous minerals such as serpentine, carbonate, prehnite, and pumpellyite can be diagnostic of certain environments and/or conditions, but spectra of these minerals have absorptions at similar wavelengths to those of some Fe/Mg smectites and chlorites, making their unique identification difficult if they occur in mixtures of clay minerals. We did not definitively identify serpentine, carbonate, prehnite, or pumpellyite in our survey of central peak regions, though we discuss possible occurrences of these minerals in the results sections for Fe/Mg smectite and chlorite detections **(Sections 4.2 and 4.3)**.

3.4 Determination of Hydrous Mineral Origin from HiRISE and CTX

Datasets for each crater were integrated in ArcGIS, with both CRISM and HiRISE data georeferenced to map-projected CTX images as a base. We mapped only confirmed hydrous mineral detections in shapefiles and did not rely solely on parameter maps because of the potential for false positives and negatives. The mineralogy shapefiles were then overlain on HiRISE imagery to determine the corresponding geomorphologic units that host the hydrous minerals. Units were distinguished based on their texture, tone, false-color attributes, and stratigraphic relation relative to other central peak units. We summarize the possible geologic settings of central peak minerals in

Figure 3 and describe our classification criteria and rationale here. These categories are meant to standardize hydrous mineral detections across all central peaks in an attempt to place them in an objective geologic context that can be used to interpret potential origins. Examples of different minerals in these different geologic settings are discussed below and illustrated in **Section 5**.

Central peak units can first be broadly categorized based on their stratigraphic position. 'Uplifted' units consist of bedrock that is locally the stratigraphically lowest unit observed at the central peak. In the event that the bedrock unit is the only distinguishable geomorphologic unit at the central peak, we still consider it to be the lowest stratigraphic unit. These uplifted units may represent material uplifted from a depth equivalent to approximately 10% of the crater diameter (D) [Ivanov et al., 1982]. In this work we use the empirically-derived stratigraphic uplift (SU) equation $SU = 0.086D^{1.03}$ from Pilkington and Grieve [1996], which has previously been used to estimate the original depth of uplifted central peak material on Mars [Caudill et al., 2012; Quantin et al., 2012]. Uplifted bedrock can be further classified as well-stratified, poorly-stratified, or massive, with variability within each of these groups. These materials can be additionally classified as 'hydrous' if CRISM spectra indicate the presence of hydrous minerals or 'anhydrous' if they lack hydrous minerals and/or host only anhydrous minerals (e.g., pyroxene, olivine). Although anhydrous phases are present at central peaks (white symbols in **Figure 2**) [Skok et al., 2012; Pan et al., 2015], they are not pursued further in this work.

In the taxonomy of **Figure 3**, 'not uplifted' units consist of all other materials that are not locally the lowest stratigraphic unit and thus are not definitively uplifted from

depth. This includes both lithified, coherent geologic units and unconsolidated deposits, where the former may be observed to onlap uplifted bedrock units. Non-uplifted units are also categorized as 'hydrous' or 'anhydrous,' with the latter not considered further in this study. We then distinguish hydrous, non-uplifted units as 'alluvial/fluvial' and 'non-fluvial' depending on their respective association or lack of association with alluvial landforms or fluvial features. Examples of alluvial or fluvial settings include alluvial fans, potential deltaic deposits, and fluvially incised channels. The non-fluvial class of non-uplifted hydrous units consists of the following seven settings: mass wasting or erosional deposits, exposures within small craters at the central peak, putative impact melt, eolian deposits, periglacial materials, other unconsolidated sedimentary deposits, and ejecta from craters external to the central peak region. 'Mass wasting or erosional' units are those that are not part of a coherent, lithified geologic unit. However, these deposits may occur as downslope streaks that can be traced back to an erosional source that is often uplifted, poorly-stratified bedrock. Therefore, these occurrences may represent hydrous minerals eroding out of uplifted bedrock. Hydrous minerals can also be associated with the walls or ejecta of small craters at the central peak, with the implication that the smaller impacts have likely exposed uplifted central peak material. Although we can objectively distinguish mass wasting deposits and small crater exposures as separate settings, both may indirectly indicate hydrous minerals in uplifted material because they can often be traced back to uplifted bedrock **(Figure 3)**.

'Impact melt' describes possibly impact-related products that occur as a lithified, brecciated [Cannon and Mustard, 2015], pitted [Tornabene et al., 2012] and/or draping unit that may also be fractured [Marzo et al., 2010]. 'Eolian' settings are characterized as

unconsolidated deposits containing wind-generated bedforms such as dunes. 'Periglacial' deposits occur as material that mantles the pre-existing surface and that is commonly associated with periglacial flow features [e.g., Squyres and Carr, 1986; Milliken et al., 2003; Baker et al., 2010]. 'Other unconsolidated deposits' encompass unlithified sedimentary materials that do not fall under 'mass wasting or erosion' or 'eolian.' Finally, 'ejecta from external craters' refers to ejecta deposits from impacts into the rim or outside of the crater that is being studied.

Hydrous minerals at each central peak are classified according to this scheme such that they are associated with at least one of the described geologic settings. Hydrous minerals that are observed in multiple contexts (e.g., uplifted bedrock and impact melt) are categorized under both settings. The methods described above were applied to all central peak regions, but further steps were taken if hydrous minerals were detected at the central peak. To place the central peak minerals in full context and take advantage of all available data at each crater, we extended our CRISM and HiRISE analysis to the entire crater, encompassing the floor, walls, rim, and sometimes ejecta. Such observations can provide further evidence to support, for example, interpretations of fluvial or excavated settings if minerals of interest are found in sedimentary deposits along the crater walls or in excavated ejecta deposits, respectively. In the absence of hydrous minerals at the central peak, only data covering the central peak region is studied.

3.5 Constraining Hydrous Mineral Formation Ages

Crater counts were performed for craters hosting central peak hydrous minerals in order to constrain the potential emplacement/formation age of these minerals. Although

there are uncertainties associated with deriving absolute ages from crater counts, this method provides a more quantitative value than metrics based on crater degradation state or superposition of target units. Crater counts were conducted on the crater's visible continuous ejecta blanket in CTX imagery. In the case of degraded craters without discernable ejecta, the counting area was defined as the region within 0.5 crater radii of the crater rim, which is a conservative estimate of the continuous ejecta [Melosh, 1989]. Craters that are >0.5 km in diameter and that superpose the ejecta blanket were counted using the CraterTools tool in ArcGIS [Kneissel et al., 2011]. We also counted craters whose centers lie on, or were very close to, the boundary of the counting area. Very young impact craters have fewer and smaller craters that are <0.5 km on their ejecta; in these situations craters were counted in order of decreasing diameter such that the total count of craters was approximately 20 to 50 to ensure a representative count of the superposing craters. In general, ages are primarily based on crater populations counted in areas of 100 km^2 to upwards of 90,000 km^2. The CraterStats2 program [Michael and Neukum, 2010] was then used to plot the cumulative size/frequency distribution and fit isochrons to the data using the Ivanov [2001] production function and the Hartmann and Neukum [2001] chronology model. We take the absolute age of the host crater to be the oldest age from the isochron fits, although we require that the isochron fits at least two data points so that the age is not entirely derived from, for example, a single anonymously large superposing crater. The derived age therefore constrains the youngest formation age of uplifted minerals, the oldest formation age of authigenic minerals, and the oldest depositional age for detrital minerals.

Although we standardize our crater counting methods for our central peak database, there are still inherent uncertainties in these age estimates. We are careful to remove obvious secondary and pre-existing craters from the counts but are otherwise conservative towards older ages in that we include ambiguous cases. To illustrate the possible errors associated with the crater counts we present an ordering of age-dated craters with their respective error bars **(Figure 4)**. However, there is no clear way to account for the rate or number of craters that have been removed via denudation. In this context the age estimates from crater counts may represent minimum values, but we attempt to reduce these effects by focusing on the population of larger superposing craters that takes longer to erase by erosional processes.

Complications with dating very old craters arise from poorly defined ejecta deposits that make it difficult to discern between craters that were pre-existing and those that superpose the host crater's ejecta. Younger craters are also difficult to age-date due to fewer and smaller craters on their ejecta, which can be more easily erased by erosion or confounded by secondaries [McEwen et al., 2005]. These young ages can vary greatly and are very responsive to the inclusion or exclusion of even a single crater in the crater counts. We therefore caution against taking very young crater count ages at face value. However, absolute ages of young craters need not be highly accurate for the purposes of our work, and we generally consider a crater to be 'young' if it has an age <2.5 Ga (i.e., Amazonian). As an alternative and independent method of assessing relative age we also assign qualitative values based on the degradation state of the crater, following the methods outlined in Mangold et al. [2012a]. Their procedure assesses the presence or absence of ejecta and fluvial landforms to place a target crater on a roughly Noachian-

Hesperian-Amazonian timeline. Results of our application of this method to the craters in this study largely corroborate our crater count results, thus we do not discuss this method further in this work. We stress that although these methods have large uncertainties, the resulting ages provide a useful metric for assessing general trends in mineralogy through geologic time at a coarse resolution. This is ultimately necessary to evaluate whether Mars may have experienced widespread or global changes in climate that were manifested as changes in the predominant mineral assemblages (e.g., Bibring et al., 2006).

3.6 Observational Biases and Caveats

3.6.1 CRISM Limitations

CRISM provides the highest spatial resolution hyperspectral data available to study martian surface compositions, but there are still limitations on how we interpret hydrous mineral detections. Minerals that are apparent in CRISM spectra only indicate mineralogy from the upper few hundreds of micrometers of the observable surface. As a result, hydrous minerals of interest could easily be masked by dust or other anhydrous phases. A lack of detected hydrous minerals therefore does not preclude their presence, either beneath surface dust or in mixtures with more spectrally dominant phases. Low signal-to-noise can further conceal absorptions of hydrous minerals, and this can be exacerbated if the exposures are small (e.g., tens of CRISM pixels). The 18 m/pixel spatial resolution of CRISM is also much coarser than the HiRISE spatial scale, which can make it difficult to correlate small scale morphologic features to mineralogical signatures, and vice versa. These resolution-limited caveats are particularly relevant when

interpreting possible emplacement mechanisms from geologic context. In summary, the distribution of hydrous minerals derived from CRISM data that are presented here should be taken as a *minimum*, and it is likely that hydrous minerals are much more common and diverse on Mars than what is discernable from the optical surface and VIS-NIR reflectance spectra alone.

3.6.2 Coverage Biases

The CRISM database is biased with regards to the density of observations in various regions, and these biases also affect our database of crater central peaks. Regions such as Arabia Terra and the Hellas basin tend to have fewer CRISM targets due to the respective high dust cover and thicker atmosphere that can dominate spectra and thus mask surface mineralogy. Conversely, regions with good exposure and impressive mineralogical diversity, such as Nili Fossae, Mawrth Vallis, and Terra Tyrrhena, are relatively overrepresented in the CRISM database due to their high scientific interest and excellent bedrock exposures.

In addition to geographic location, preservation state is also a strong influence on the targeted crater database. Many CRISM observations correspond to relatively 'younger' craters/exposures that are less likely to be obscured by dust and other mantling deposits, thus allowing VIS-NIR spectroscopy to probe surface mineralogy. Older, larger craters are more likely to be degraded by subsequent impacts and tend to be heavily eroded or infilled to the point where their central peaks are no longer identifiable. In contrast, younger and implicitly smaller craters tend to be better preserved and often exhibit prominent central peaks. CRISM observations are therefore more likely to target

smaller craters, which can be observed in our overall distribution of crater sizes **(Figure 5A)**. This bias also carries over to the distribution of crater ages, resulting in a survey of a proportionally higher number of relatively young craters despite the fact that impact rates decrease over time **(Figure 5B)**. The observation density within individual craters is also influenced by location and size. Craters in regions that are known to be mineralogically rich are more likely to have complete CRISM coverage of their central peaks, as are smaller craters that require fewer images for complete coverage. By contrast, larger craters may only have partial coverage of their central peaks. Thus it is important to note that a lack of detection of hydrous minerals at an incompletely covered central peak does not preclude their existence. We do not adjust or subsample our database to account for these biases, but instead include all central peaks with both CRISM and HIRISE coverage in our survey so as to prevent further bias.

4. Results: Central Peak Region Mineralogy

4.1 Overview of Hydrous Mineral Identifications

Our survey comprises 633 central peak craters and spans a total of 1439 analyzed CRISM images. A complete list of the craters and CRISM images studied is available in **Appendix B**. In this work, named craters are referred to by their IAU name and unnamed craters are referred to by the observation ID of the first chronological CRISM image that covers the central peak region; in the case of overlapping CRISM observations our naming scheme gives precedence to FRT, FRS, HRL, and then HRS observations. As an example, an unnamed crater whose first CRISM observation was image HRL0000B5F5 would be given the designation ‘crater B5F5’. We only report minerals detected within

the central peak region (i.e. the inner 50% of the crater diameter). Of the 633 central peaks surveyed, 265 (42%) host at least one type of hydrous mineral, while 368 (58%) show no evidence of hydrous minerals in existing CRISM data, be it due to dust cover **(Section 3.6.1)**, poor data acquisition conditions, or a true absence of hydrous minerals. Of the 265 'hydrous' central peaks, 63.4% can be classified within a single hydrous mineralogy group whereas 36.6% host mineral assemblages that fall within at least two of the hydrous mineral groups **(Table 1)**.

Our results indicate that crater central peaks display much of the mineralogical diversity that is observed across the surface of Mars as a whole [Murchie et al., 2009; Ehlmann et al., 2011b; Carter et al., 2013]. We find that Fe/Mg smectites are the most commonly detected hydrous mineral group, occurring in 81.9% of all hydrous central peak regions. They are followed by chlorite (26.8%), hydrated silica (22.6%), unidentified hydrous phases (6.8%), zeolite (4.5%), sulfate (3.0%), and Al-phyllosilicate (1.1%). Although the surveyed central peaks collectively show great mineralogical diversity, 98% of hydrous central peaks can be characterized by some permutation of the three largest hydrous mineral groups: Fe/Mg smectite (including mixed-layer chlorite/smectite), chlorite, and hydrated silica **(Figure 6)**. Only 2% of central peak regions with observable hydrous minerals appear to lack these minerals in CRISM data, and they instead exhibit spectral evidence for zeolites, sulfates, Al-phyllosilicates, or unidentified hydrous phases.

4.2 Fe/Mg Smectite

Fe/Mg smectite and/or mixed-layer chlorite/smectite occurs in 81.9% of all hydrous central peaks and is by far the most prevalent hydrous mineral identified in our survey, an observation that is consistent with previous global studies of hydrous minerals that evaluated crater and non-crater settings [Bibring et al., 2006; Mustard et al., 2008; Ehlmann et al., 2009; 2011; Murchie et al., 2009; Carter et al., 2013]. Hydrous minerals in general tend to exhibit vibrational absorptions at 1.4 μm, due to OH and H_2O overtones, and at 1.9 μm, due to a combined H_2O bend plus stretch vibration. The presence of these hydration features can reinforce or refine hydrous mineral detections, but they are shared by multiple hydrous minerals and thus are not always diagnostic of a specific mineral phase. Fe/Mg smectites can be identified by a diagnostic absorption at 2.3 μm due to Fe/Mg-OH vibrations. The exact band center of this absorption shifts with varying proportions of Fe and Mg, with Fe-rich compositions at shorter wavelengths (e.g., nontronite at 2.28-2.29 μm) and Mg-rich compositions at longer wavelengths (e.g., saponite at 2.31-2.32 μm) [Bishop et al., 2002]. Additional but weaker Fe/Mg-OH absorptions also exist in smectite clays at 2.4 and 2.5 μm and are observed in many CRISM ratio spectra.

Central peak Fe/Mg smectites show variability in their absorption band centers and shapes, possibly reflecting variations in their composition and structure (e.g., composition of octahedral cations or degree of interstratification with chlorite) [Michalski et al., 2015]. The majority of Fe/Mg smectites tend to have absorptions centered at 2.3-2.31 μm, but the full range of compositions spans from Fe-rich smectites with absorption centers as short as ~2.28 μm to Mg-rich smectites with center wavelengths as long as

2.32 μm **(Figure 7)**. Few examples show the sharp and narrow 2.3 μm absorption characteristic of 'pure' smectite. Instead, many Fe/Mg smectites show a broader spectral shape that may be more consistent with mixtures of various smectite species or the presence of mixed-layer chlorite/smectite (e.g., C554 and 10622 in **Figure 7A**), similar to results by Milliken et al. [2010; 2011]. Several Fe/Mg smectites also show additional but weaker absorptions at 2.2 and 2.25 μm, likely due to the presence of Al in octahedral coordination (i.e. they are consistent with Al-OH vibrations). Alternatively, detections that do not exhibit a defined absorption at 2.3 μm but rather a drop in reflectance and a weaker and broader absorption at 2.25 μm could indicate a poorly crystalline clay or a largely dehydroxylated clay (e.g., Soffen crater in **Figure 7A**).

Serpentine and carbonate minerals also exhibit absorptions near ~2.3 μm, but previously unrecognized detections of these minerals have not been identified with absolute certainty in this study. Serpentines can appear spectrally similar to Mg-rich smectites, as both can be characterized by Fe/Mg-OH absorptions at 2.32 and 2.5 μm in addition to the requisite 1.4 and 1.9 μm features. Previous identifications of serpentine from CRISM data have thus relied on a unique absorption at 2.1-2.12 μm as well as a very narrow 1.4 μm OH absorption [e.g., Ehlmann et al., 2010; Quantin et al., 2012]. Several central peaks exhibit spectra that may be consistent with serpentine (e.g., AAA8 in **Figure 7A**), but they should be interpreted with caution due to the low signal-to-noise in the CRISM spectra and the proximity of the 2.1 μm absorption to residual atmospheric absorptions [Murchie et al., 2007]. In addition, the strength of the H_2O feature at ~1.9 μm and the width of the weak ~1.4 μm feature suggests such potential serpentine occurrences would need to be mixed with another H_2O-bearing phase.

Though not clay minerals, carbonates can have spectral similarities to mixtures of Fe/Mg clays (e.g., both can exhibit absorptions near ~2.3 μm) and we include the possibility that they may be present at some central peaks. Carbonates are best identified by paired absorptions at 2.3 and 2.5 μm that co-vary in strength and that match the width/shape of laboratory examples [Ehlmann et al., 2008b]. From these criteria we confirm in our study the previous detection of carbonates within well-stratified uplifted bedrock at Leighton crater [Michalski and Niles, 2010]. Although we identify possible carbonates at several other craters, carbonates can be difficult to uniquely identify if they are mixed with clay minerals because of overlapping absorptions in the 2.3-2.5 μm wavelength region. Several of our Fe/Mg smectite detections have absorptions at 2.5 μm **(Figure 7A)**, but they are not clearly paralleled by the shape of the 2.3 μm absorption, and the presence of a ~2.5 μm alone is not sufficient criteria to identify carbonate. However, a carbonate component cannot be ruled out in these cases and it is possible that the typical spectral attributes of carbonate are simply masked by the spectral dominance of clays at these wavelengths.

4.3 Chlorite

Chlorite makes up the second largest group of hydrous minerals in crater central peak regions and has a detection frequency of 26.8% relative to all hydrous central peaks. Chlorite spectra are characterized by a broad and complex absorption near ~2.32 - 2.35 μm, the position of which varies with composition. Chlorite spectra are also typified by a weak or absent 1.9 μm absorption and a narrower ~1.4 μm absorption when compared to smectitic clays. The ~2.35 μm absorption is due to the stretch and bend of Fe/Mg-OH and

is often accompanied by a shoulder at 2.25 μm due to Al-OH vibrations. The 2.35 μm feature can be centered at longer wavelengths with increasing Mg content [King and Clark, 1989], although the complexity of Al-Fe-Mg substitutions in the octahedral sites make it difficult to conclusively derive composition from this absorption.

Central peak chlorites tend to have absorptions centered at 2.34-2.35 μm, although they can occur at wavelengths as short as 2.32 μm or as long as 2.36 μm **(Figure 8)**. Several detections appear to be relatively Al-rich or contain a separate Al-bearing clay, as indicated by a sharp absorption at 2.2 μm (e.g., 4B38 in **Figure 8A**) rather than the sloping shoulder at 2.25 μm that is observed for most chlorites. This sharp 2.2 μm feature could be due to a physical mixture of chlorite with an Al-phyllosilicate (e.g., montmorillonite, illite, kaolinite) rather than Al substitution in the chlorite structure, although there are no single pixels whose spectra exhibit only the 2.2 μm absorption in this example. This does not preclude the possibility that these spectra reflect physical mixtures of chlorite and Al-phyllosilicate, but these minerals would need to be mixed below the 18 meter per pixel resolution of CRISM. The majority of chlorite detections exhibit a weak or absent 1.9 μm absorption (e.g., 8528 in **Figure 8A**), consistent with these deposits having less H_2O than the Fe/Mg smectite examples discussed above. As with the Fe/Mg smectites, several chlorite spectra exhibit an absorption at ~2.5 μm (e.g., 67B5 in **Figure 8A**) that suggests another phase is present. Possibilities include carbonate, analcime, or Ca-sulfates, spectra of which can exhibit strong absorptions at this wavelength.

Pumpellyite and prehnite are spectrally very similar to chlorite, sharing the complex ~2.35 μm absorption as well as a weak/absent 1.9 μm absorption. Prehnite has

been previously distinguished in CRISM data by a characteristic absorption at 1.48 μm rather than 1.4 μm (e.g., 17EAA in **Figure 8A**) [Ehlmann et al., 2009], whereas pumpellyite spectra are more ambiguous. Based on this criteria, we identify possible prehnite at 11 central peaks, including previous detections at Toro [Ehlmann et al., 2009; Marzo et al., 2010], Horowitz [Pan et al., 2015], unnamed crater 147E9 [Loizeau et al., 2012], Micoud, and unnamed crater BF46 [Carter et al., 2010]. An additional four craters exhibit prehnite-like spectra only in their walls or ejecta and not at the central peak. Curiously, we detect potential prehnites only in central peaks in the vicinity of Isidis Basin and the Syrtis Major/Nili Fossae region. However, we caution that our prehnite detections are likely an underestimation of the true prevalence of prehnite at central peaks. Prehnite is characterized by a distinctive 1.48 μm absorption, but features in the 1.4 μm region are generally weaker than those observed at longer wavelengths (e.g., 1.9, 2.2, 2.3 μm). This is a particularly significant issue for spectra that are averaged over large ROIs (as we have done here), as more prevalent minerals can mask the 1.48 μm feature if it is present in only a few pixels. However, this suggests that even if prehnite were present it is not a dominant phase given its absence in the larger spectral averages. Conversely, the spectral presence of prehnite at the aforementioned 11 central peaks indicates that it may be a spectrally dominant component within those craters in the Isidis region.

4.4 Hydrated Silica

The third largest hydrous mineral group consists of hydrated silica, which is found in 22.6% of hydrous central peaks. Here we use the term ‘hydrated silica’ to denote

the presence of Si-OH absorptions that may or may not be associated with distinct H_2O absorptions. These features may occur in reflectance spectra of opaline silica (opal-A, -CT, or –C), chalcedony (due to silanol and H_2O that can be trapped between fibers), and hydrated glass (volcanic or impact generated). Hydrated silica spectra are identified by the presence of a broad absorption with a center between 2.21 – 2.26 μm that is the result of overlapping Si-OH vibrations [Anderson and Wickersheim, 1964; Stolper, 1982] **(Figure 9)**. Although NIR spectra of Al-phyllosilicates also bear a ~2.2 μm absorption, in spectra of hydrated silica this absorption is typically broader and more asymmetric. Detailed examination of the reflectance minimum (absorption maximum) and symmetry of the ~2.2 um feature, in addition to the band position of the ~1.4 μm feature and the strength of the ~1.9 μm feature, can be used to distinguish between opaline silica and hydrated glass [Milliken et al., 2008; Rice et al., 2013].

The symmetry of the primary Si-OH feature at ~2.2 μm, the strength of the ~1.9 μm H_2O absorption, and the position of the OH/H_2O overtones at ~1.4 μm can all be used to assess the degree of hydration of opaline silica. CRISM spectra of opaline silica with less H_2O are expected to exhibit a rather asymmetric absorption near ~2.2 μm (spanning the ~2.19-2.35 μm range but with a reflectance minimum near ~2.21 μm), a weaker or absent 1.9 μm H_2O feature, and an Si-OH overtone closer to ~1.38-1.39 μm, as described in Milliken et al. [2008]. Recent discussions of NIR spectral features associated with hydrated silica are also presented in Rice et al. [2013] and Smith et al. [2013]. We note these spectral variations in hydrated and dehydrated silica throughout our survey, though for our category of 'hydrated silica' we include all varieties.

Based on these criteria, the majority of central peak hydrated silica detections appear to contain appreciable amounts of H_2O (e.g., 3A2B and 51EE in **Figure 9**). However, several craters host hydrated silica that is relatively H_2O-poor in close proximity to more highly hydrated silica. The most striking example is at Elorza crater, where 'hydrated' and 'dehydrated' silica are found within 4 km of each other within the same CRISM image **(Figure 10)**. The proximity of these two detections in the same observation suggests differences in hydration state cannot be fully explained by differences in atmospheric conditions (e.g., relative humidity). These two examples may instead reflect different formation environments or diagenetic processes [Rice et al., 2013], such as different degrees of maturation of opaline silica. We find proportionally more hydrated silica detections at central peaks relative to the general crater population presented by Ehlmann et al. [2011] and Carter et al. [2013] and explore possible explanations for this discrepancy in **Section 7**.

4.5 Zeolites and Sulfates

Zeolites and sulfates are relatively rare occurrences at central peaks at the CRISM spatial scale, being identified in only 4.5% and 3.0% of central peaks, respectively. Reflectance spectra of many zeolites and sulfates can be difficult to identify and distinguish from one another due to similarities in the 1.4 and 1.9 μm H_2O absorptions that dominate their reflectance spectra. On Mars, analcime has been the most commonly detected zeolite due to a somewhat distinctive broad absorption centered at ~2.5 μm and a weaker absorption at ~1.8 μm [Cloutis et al., 2002; Ehlmann et al., 2009] (e.g., 51EE in **Figure 11A**). Spectra of some central peak zeolites also show an additional absorption at

2.3 μm, indicating they may be mixed with Fe/Mg clays (e.g., 2740D in **Figure 11A**). Identification of other zeolite species (e.g., stilbite, clinoptilolite, chabazite, mordenite) is complicated by the lack of diagnostic absorptions at VIS-NIR wavelengths, as well as residual atmospheric effects at wavelengths longer than 2.5 μm [Murchie et al., 2007] that can further obscure already subtle absorptions in this wavelength region. Because of this ambiguity, in this work we only classify potential analcime occurrences as zeolites, and spectra that only exhibit 1.4 and 1.9 μm absorptions are instead categorized as unidentified hydrous phases **(Section 4.7)**. Thus, the detections presented here are likely an underestimation of the true prevalence of zeolites in martian central peak regions.

Reflectance spectra of many sulfates also exhibit non-unique H_2O absorptions at ~1.4 and ~1.9 μm, similar to zeolites. However, in sulfates the reflectance minimum of the ~1.9 μm absorption is often shifted to longer wavelengths (e.g., 1.93-1.95 μm) [Cloutis et al., 2006]. Many polyhydrated sulfate spectra also have an additional subtle absorption at 2.4 μm after a reflectance decrease beginning at 2.25 μm, although this is also a trait of some zeolites [Cloutis et al., 2002; Cloutis et al., 2006]. Certain sulfates such as jarosite, alunite, and gypsum have very diagnostic reflectance spectra and absorptions [Carter et al., 2013], but none of these minerals were definitively identified in central peak regions in this study. Here we identify sulfates by a 1.93-1.95 μm absorption in addition to a strong decrease in reflectance starting at ~2.25-2.3μm and, in some cases, a subtle absorption at ~2.4 μm (e.g., 147E9 in **Figure 11A**). As with zeolites, sulfates are likely under-classified in this survey and ambiguous detections are instead categorized as unidentified hydrous phases.

4.6 Al-Phyllosilicates

Al-phyllosilicates were rarely identified in central peak regions in our study and, to date, have been detected in only three craters. These include an unnamed crater (B66C; montmorillonite or illite), Leighton crater (kaolinite) [Michalski and Niles, 2010], and Stokes crater (kaolinite) [Carter et al., 2010]. Though Al-OH absorptions can occur at similar wavelengths as Si-OH absorptions, it is possible to distinguish these clays from hydrated silica as described by Milliken et al. [2008] and as discussed in **Sections 4.4 and 7**. Specifically, spectra of Al-phyllosilicates such as montmorillonite and illite tend to have a narrower 2.2 μm absorption than is observed in hydrated silica **(Figure 12B)**. Spectra of illite exhibit an additional absorption at 2.35 μm and kaolin group minerals are characterized by a very narrow and asymmetric 'doublet' feature at ~2.2 μm. In the present study we do not attempt to distinguish between kaolinite and halloysite because both exhibit similar absorptions in the ~1.4 and ~2.2 μm wavelength regions. This is particularly true for halloysite that has dehydrated, an irreversible process that takes place at low relative humidity values as are known to occur on Mars over the course of diurnal and/or seasonal cycles.

4.7 Unidentified Hydrous Phases

As previously described, deposits of hydrous minerals whose CRISM spectra bear only 1.4 and 1.9 μm absorptions in the absence of more diagnostic features are categorized as unidentified hydrous phases. These phases could include zeolites, sulfates or other hydrated salts. The absence of other diagnostic absorptions may be due in part to low signal-to-noise and/or incomplete atmospheric removal. Poorly crystalline clays may

also fall into this category, as their spectra may show a weak 1.9 μm absorption but not a clear 2.3 μm absorption. These unidentified phases are detected at 18 central peaks and are the sole hydrous mineral at only three craters.

5. Results: Geologic Context of Hydrous Minerals

In this section we present the results of detailed CRISM-to-HiRISE analyses to assess the various geologic contexts in which hydrous minerals are found. In general, we do not observe any obvious regional or global trends in the spatial distribution of hydrous minerals associated with central peak regions **(Figure 13)**, regardless of specific geologic context. Similarly, there does not appear to be any clear relationship between hydrous mineral occurrence and the type of central structure or geologic unit [Tanaka et al., 2014]. The only exception is the occurrence of hydrated silica in uplifted bedrock, which is only observed in the southern highlands and is absent from the northern lowlands **(Section 8.1.1)**. The lack of other spatial trends is only assessed qualitatively as small populations inhibit meaningful statistical tests and the database of CRISM targeted images is spatially biased **(Section 3.6.2)**.

5.1 Fe/Mg Smectite

Fe/Mg smectites are detected in 217 central peaks distributed over a wide geographic range **(Figure 13A)**. The most prevalent hydrous mineral group, Fe/Mg smectites are the only group found in all of the geologic settings used in our classification scheme **(Figure 3)**. A single central peak can host Fe/Mg smectites in multiple settings (e.g., in uplifted bedrock, impact melt, alluvial/fluvial deposits), thus we discuss each

geologic setting independently. **Figures 14 and 15** present archetypal examples of each geologic setting where Fe/Mg smectites have been detected.

5.1.1 Fe/Mg Smectite in Uplifted Bedrock

Approximately 61% of Fe/Mg smectite and/or mixed-layer C/S in central peak regions can be linked to uplifted bedrock **(Table 2)**. Though this is a majority, it also means that a significant fraction of clays in central peak regions are *not* clearly indicative of deeper crustal composition. The 'uplifted bedrock' category encompasses examples where exposed rock units have clearly been uplifted as well as settings that are inferred to indicate uplifted material (**Figure 3**, orange boxes). Examples of directly uplifted materials are recognized at 125 out of 217 central peak regions with Fe/Mg smectite. In our study these bedrock units are locally the lowest stratigraphic unit at the central peak and may be overlain by post-impact units such as draping impact melt **(Figures 14A and 15C)**. If the bedrock unit is the only geomorphologic unit and no other clear units exist locally **(Figure 14B)**, then we still consider the bedrock to be the lowest stratigraphic unit at the central peak. We infer these bedrock units to be direct evidence for material uplifted from depth, which is a slightly different approach than previous studies of clay-bearing central peaks [e.g., Caudill et al., 2012; Quantin et al., 2012] **(Figure 14A-D)**. Stratification of uplifted bedrock is highly variable and can range from massive to well-stratified both between and within central peaks. Massive uplifted bedrock that tends to be light-toned and heavily fractured **(Figure 14A)** has previously been interpreted as ancient Noachian material that has lost its original stratification due to impact bombardment [Caudill et al., 2012] or diagenetic processes. Poorly-stratified uplifted

bedrock appears relatively dark-toned, friable, and may erode along planes or layers over short length scales **(Figure 14B)**. Well-stratified uplifted bedrock exhibits clearly defined bedding and could represent volcanic units, sedimentary strata, or interbedding of the two. These layers can be either light- or dark-toned in CTX and HiRISE images **(Figure 14C-D)**, and in some cases both light and dark-toned strata are interbedded. Of the central peaks hosting Fe/Mg smectite in uplifted bedrock, 62 (49.6%) bear smectite in massive bedrock, 70 (56%) in poorly-stratified bedrock, and 12 (9.6%) in well-stratified bedrock **(Table 3)**.

An additional seven central peaks do not have direct evidence for Fe/Mg smectite in uplifted bedrock but instead host Fe/Mg smectite in units that indirectly indicate uplifted material as a source region **(Table 3)**. These include mass wasting deposits and ejecta from local small impacts. Mass wasting deposits are often associated with erosion of poorly-stratified uplifted bedrock, with Fe/Mg smectite observed in the talus rather than the bedrock itself **(Figure 14E)**. This may be due to low signal-to-noise in the CRISM data and/or a relative decrease in volume scattering for the poorly-stratified bedrock. Numerous laboratory studies have documented that particulate materials exhibit stronger absorption features in reflectance spectra than solid rocks due to enhanced volume scattering. Due to this effect, Fe/Mg smectites may be more readily observable in the particulate talus than the intact bedrock from which it was sourced. Other indirect evidence for uplifted Fe/Mg smectite occurs when smectite is observed in the wall, rim, or ejecta of a small crater that impacted the central peak **(Figure 14F)**. These craters are at most only several kilometers in diameter and are likely too small to independently develop hydrothermal systems to form the observed clays [Rathbun and Squyres, 2002;

Abramov and Kring, 2005; Osinski et al., 2013]. Therefore, these clay detections likely represent material that has been excavated from the underlying bedrock in the central peak.

In this work we interpret Fe/Mg smectites in uplifted bedrock to represent pre-impact materials uplifted from depth, but we caution that an authigenic origin is also possible within these bedrock units. The distinction between pre-impact uplifted clays and post-impact authigenic clays carries very different implications for the timeline of martian clay formation **(Section 8.3)**. The Holden crater impact event illustrates the complexity involved with such observations, as uplifted bedrock units outside of Holden are mafic and apparently unaltered but are injected by meter-scale, Fe/Mg smectite-bearing melt veins [Tornabene et al., 2009]. Hydrothermal processes are also capable of forming alteration products within uplifted materials, where intense fracturing and interaction with impact melt can form mineralized veins and/or alter primary igneous minerals [Schwenzer and Kring, 2009; Osinski et al., 2013]. Although we observe Fe/Mg smectites in many uplifted bedrock units that are heavily fractured, we did not observe any clear examples of Fe/Mg smectites that were isolated to fractures and veins rather than the bulk central peak bedrock. This may simply represent a limitation of the spatial resolution of CRISM, which at 18 meters per pixel would be too coarse to resolve the mineralogy of meter or submeter-scale features such as fractures and veins. We therefore cannot rule out authigenic clay formation within uplifted bedrock, but assuming the simplest scenario we consider Fe/Mg smectites in uplifted bedrock units to also be uplifted.

High temperatures and peak shock pressures induced by impacts are also capable of dehydroxylating smectites and altering their NIR spectral features [Fairen et al., 2010; Che and Glotch, 2012; Kraus et al., 2013; Friedlander et al., 2015], which would suggest that the lack of detected clays in uplifted material does not necessarily mean such minerals were never present. The likelihood of dehydroxylation increases with peak heating and shock pressure from the impact, but it is worth noting that smectites are still observed in uplifted material at craters >100 km in diameter. On the other hand, it is possible that the observed smectite-bearing central peak material was shielded from the highest impact conditions, allowing for the preservation of clays. Impact shock effects can also be chaotic and not uniformly distributed, making it difficult to predict if a section of bedrock was in fact raised to dehydroxylation temperatures. Although shock effects are dependent on many factors (e.g., target rock type, impact angle, impact velocity), it is still interesting that uplifted clays can be present in one central peak and absent in another for a similar size crater in the same region.

5.1.2 Detrital Fe/Mg Smectite in Alluvial/Fluvial Systems

Eleven craters, or 5.1% of Fe/Mg smectite-bearing central peak regions, host fluvial systems associated with the clay detections. The walls of these craters are incised by fluvial channels that commonly terminate in alluvial fan deposits that can extend to the central peak region **(Figure 15E)**. Surfaces of the fans themselves are often spectrally bland (with the exception of Runaga in **Figure 15E**), and Fe/Mg smectites typically occur at the toes or distal ends of the fans where finer-grained, clay-sized sediment is expected to be concentrated due to deceleration of fluids. Despite extensive fluvial incision in

many of these craters, very few craters appear to be clearly integrated with more regional valley networks, and in most cases the channels are not traceable past the crater rim. In addition, there is no clear spatial distribution of craters in this category that would indicate genetic links to more regional fluvial transport systems.

As was the case for the uplifted bedrock examples, it is difficult to use current orbital data to distinguish between detrital and authigenic origins for smectites in alluvial/fluvial deposits. Detrital clays that have been fluvially transported to the central peak would represent sediment sourced from the crater wall or surrounding watershed and therefore do not necessarily provide information about deep crustal compositions. On the other hand, authigenic smectites that formed within the fluvial systems and/or any associated lacustrine systems could record local environmental conditions. Specifically, the presence of authigenic clays would indicate local conditions were conducive to clay formation after the impact event, the age of which can be constrained by crater counting. However, distinguishing between detrital and authigenic origins requires much higher resolution, likely rover-scale, data on chemistry, mineralogy, and geologic context [e.g., Vaniman et al., 2014]. Though we cannot entirely discount an authigenic origin for this group of central peak clays we adopt a simplistic ‘guilt by association’ approach and assume that clays in fluvial deposits represent detrital sediments. A detailed source-to-sink analysis of these clay occurrences would provide further constraints [e.g., Ehlmann et al., 2008a; Milliken and Bish, 2010; Goudge et al., 2015] but is beyond the scope of this study.

5.1.3 Authigenic Fe/Mg Smectite in Impact Melt

Nearly 25% (54 craters) of Fe/Mg smectite occurrences are associated with deposits that may be interpreted as impact melt. Of these, 32 central peaks host additional smectites in uplifted material, whereas 22 central peaks host smectites exclusively in impact melt. Potential impact melt units are lithified, commonly dark-toned in HiRISE images, and lack evidence for fluvial emplacement (otherwise these clays would be categorized as possibly detrital). They are characterized by some combination of brecciation **(Figure 15A)**, pitting [Tornabene et al., 2012] **(Figure 15B)**, draping morphology **(Figure 15C)**, and/or fracturing [Marzo et al., 2010] within a draping/onlapping unit **(Figure 15D)**. Many potential impact melt units exhibit several of these characteristics.

Fe/Mg smectites in these units may be authigenic and indicate volatile-rich melt products or impact-induced aqueous alteration. A caveat to this interpretation is that the clays may simply represent pre-impact clay-bearing lithologies that mixed into the melt and retained their spectral signature. This is particularly relevant for central peaks where smectites are observed in both uplifted bedrock and impact melt deposits; some examples of the latter are brecciated and could contain clay-rich clasts. However, these clasts are difficult to resolve in CRISM data and it is uncertain whether it is the clasts and/or the melt matrix hosting the clay signatures. The most convincing examples of authigenic clay formation are therefore the smectite-bearing impact melt units that drape over unaltered uplifted bedrock **(Figure 15C)**. As a group, we consider clays in impact melt deposits to have a high potential to be authigenic in origin, particularly because clay minerals typically dehydroxylate at temperatures upwards of 500-850°C [Milliken and Mustard,

2005; 2007; Che et al., 2011] and impact melts can reach substantially higher temperatures. Again, however, we note that impact effects can be quite heterogeneous and may not affect all components of the melt uniformly.

5.1.4 Fe/Mg Smectite in Periglacial Deposits

Fe/Mg smectites are found in potential periglacial deposits at 29 central peaks, split between nine that occur alongside uplifted Fe/Mg smectites and 20 that solely occur in the central peak region. These occurrences are found only in mid-latitude craters where it is well recognized that ice-related processes have been important over the past several billions of years [e.g., Squyres and Carr, 1986; Mustard et al., 2001; Head et al., 2003]. Periglacial deposits are inferred by their relatively smooth and draping morphology, and sometimes by the presence of lobate flow features or gullies **(Figure 15F)**. The origin of smectite in these deposits is difficult to determine and could be related to uplifted, detrital, or authigenic materials. These materials may represent pre-existing uplifted material that has been locally reworked by periglacial activity or they may be authigenically formed at low temperature [e.g., Velde and Meunier, 2008] by thin films of water interacting with fine sediment. Smectites are also observed in lobate deposits at the terminus of gullies that incise crater walls and peaks **(Figure 15F)**, suggesting they may be transported and concentrated by localized fluid flow.

5.1.5 Fe/Mg Smectite of Unknown Origins

Fe/Mg smectites whose origin we do not attempt to classify are identified in eolian deposits, 'other unconsolidated' deposits, and in ejecta from superposing craters. These settings do not convey any easily interpretable information about the origin or formation environment of the clays. Both eolian and 'other' deposits consist primarily of what are likely to be unconsolidated sediments, the distinguishing factor being that eolian deposits are associated with dunes and other eolian bedforms **(Figure 15G)**. However, even in these cases it is not clear if the dunes or ripples are actively migrating or if they are instead partially lithified. 'Other' sedimentary deposits also tend to appear unconsolidated (e.g., **Figure 15H**), but in some instances these units exhibit steep and well-defined edges, retain craters, and may be partially lithified (e.g., **Figure 16D**). Fe/Mg smectites in these settings often occur alongside clays in more well-defined geologic contexts, typically uplifted bedrock and potential impact melt.

At eight craters we observe Fe/Mg smectite in ejecta deposits from other large craters that superpose the primary crater of interest. In our survey, these ejecta deposits always originate from craters that impacted onto the rim of the host crater with ejecta patterns that reach the central peak region **(Figure 15I)**. The smectites in these ejecta deposits likely do not represent deep crustal lithologies (as uplifted smectites do), but instead could represent shallower crustal material or authigenic impact-induced alteration within the ejecta [Osinski et al., 2013].

5.2 Geologic Contexts of Chlorite

Chlorite is the second most prevalent hydrous mineral and was detected in 71 central peaks, representing 26.8% of hydrous central peaks **(Figure 13B, Table 2)**. Occurrences of chlorite share many similarities with Fe/Mg smectite in terms of their geologic settings **(Figures 14-15)**, but the smaller chlorite population is a caveat that must be considered when interpreting the implications of the presence or absence of chlorite. The majority (69%) of chlorite detections at central peaks are found in uplifted materials, which again can be categorized as uplifted bedrock or inferred to represent uplifted bedrock (44 and 6 craters, respectively). The former are identified in massive, poorly-stratified, and well-stratified bedrock. Examples of chlorite that may be indirectly associated with uplifted bedrock most commonly occur as mass wasting deposits **(Table 3)**. As with Fe/Mg smectites, it is possible that chlorite in uplifted bedrock could have formed authigenically (possibly hydrothermally) within fractures below CRISM resolution or through near-surface weathering. Unlike Fe/Mg smectites, we did not identify any craters where chlorite was clearly associated with larger alluvial/fluvial transport systems in the central peak region **(Table 2)**. This may simply represent a statistical bias given the smaller sample size of the 71 chlorite-bearing central peaks, but it is also possible that chlorite is simply not common in these settings within central peak regions.

We identified seven occurrences of chlorite as being associated with potential impact melt deposits. In contrast to the Fe/Mg smectite population, in all cases they were found alongside chlorite in uplifted bedrock. This observation is consistent with melt entrainment of chlorite-bearing clasts of pre-impact material, although this is difficult to

unequivocally demonstrate with current orbital data. Authigenic chlorite in these deposits could indicate a relatively higher-temperature hydrothermal system within the crater [Kirsimäe et al., 2002], although chlorites are also known to form in soils and other low-temperature non-hydrothermal environments [Velde and Meunier, 2008]. Detection of pumpellyite or prehnite would strengthen the hydrothermal case, as these are more diagnostic of higher-temperature systems [Bishop, 1972], but most of our potential prehnite detections **(Figure 8)** are not identified in impact melt or even uplifted fractured bedrock. Therefore, the presence of chlorite in these craters and environments is consistent with hydrothermal alteration but there are other equally plausible origins, as discussed below.

Chlorite is also present in contexts with more ambiguous origins. Thirteen mid-latitude craters exhibit chlorite spectral signatures in periglacial deposits, which again could represent detrital materials or authigenic formation at low temperatures [e.g., Velde and Meunier, 2008]. Chlorite in the 'unconsolidated deposits' category is found at three central peaks in association with eolian features and at ten central peaks without. Lastly, seven craters have central peak region chlorite that is associated with ejecta from superposing craters.

5.3 Geologic Contexts of Hydrated Silica

Hydrated silica is the third major hydrous mineral group (22.6% of hydrous central peak regions) after Fe/Mg smectite and chlorite and is the last of our mineral groups that is found in a wide range of our defined geologic contexts **(Figure 13C)**. Of the possible settings, hydrated silica is absent only in alluvial/fluvial settings and in ejecta

deposits from superposing craters exterior to the central peak region **(Table 3)**. As with chlorite, the population of hydrated silica is relatively small and this must be kept in mind when interpreting the implications of its presence or absence.

5.3.1 Hydrated Silica in Uplifted Bedrock

Examples of hydrated silica associated with uplifted bedrock are found at 17 southern highlands central peaks, either in directly uplifted bedrock (14 cases) or settings inferred to be uplifted (3 cases). For the former, it is only observed in uplifted massive **(Figure 16A)** or poorly-stratified bedrock **(Figure 16B)** and has yet to be identified in uplifted well-stratified bedrock. Additional contexts that are inferred to be uplifted are split between two instances of hydrated silica in mass wasting deposits and one instance associated with the ejecta of a small impact at a central peak **(Table 3)**.

5.3.2 Authigenic Hydrated Silica in Impact Melt

Impact melt deposits bearing hydrated silica (15 craters) are distinct from those hosting Fe/Mg smectite and chlorite. In contrast to the dark-toned, brecciated, or pitted features typical of most clay-bearing impact melts, those associated with hydrated silica are light-toned, fractured, and in some instances exhibit morphologies suggestive of flow **(Figure 16C)**. We still interpret the latter to be impact melt due to their superposition over other units and the lack of obvious fluvial features. The characteristic morphologic differences between hydrated silica and smectite-bearing impact melt deposits may be related to their different compositions. Unlike clay-bearing melts, hydrated-silica bearing melts are never identified alongside uplifted equivalents. Therefore, we interpret the

hydrated silica in these settings to be likely authigenic in origin, formed either during generation and emplacement of a volatile-rich melt or as a later weathering/diagenetic product.

5.3.3 Hydrated Silica in Unconsolidated Deposits

The most significant distinction between hydrated silica and clay occurrences is that the largest group of hydrated silica detections is classified as 'unconsolidated deposits' rather than in uplifted material **(Table 2)**. In nearly half of hydrated silica-bearing craters, these deposits are the only source of the spectral signature, leaving the origins of almost half of central peak hydrated silica unknown. Although these deposits often appear to be poorly lithified, in some locations they occur as coherent units that superpose or onlap the central peak, have steep edges, retain craters, and thus may be at least partially lithified **(Figure 16D)**.

5.4 Geologic Contexts of Al-Phyllosilicates

We have identified Al-phyllosilicates for only three central peak regions, but each occurrence represents a distinct mineralogical and geological setting. At Stokes crater we identify kaolinite in likely periglacial material [Carter et al., 2010], kaolinite in uplifted well-stratified bedrock at Leighton carter [Michalski and Niles, 2010], and montmorillonite or illite in an unnamed crater (B66C) in uplifted poorly-stratified bedrock.

Geologic processes could explain the relative lack of Al-phyllosilicates at central peak regions relative to what was observed for entire crater systems by Carter et al.

[2013]. Al-phyllosilicates have been identified in Columbus crater and several other craters in the Terra Sirenum region and hypothesized to have formed from groundwater interaction [Wray et al., 2011]. This process may not affect topographically higher portions of the central peak region as much as other regions [Rathbun and Squyres, 2002], such as the crater floor where Al-phyllosilicates were detected at Columbus crater. When considered on a global scale, Al-phyllosilicates are also almost always observed stratigraphically above Fe/Mg smectites in a scenario suggestive of leaching by enhanced chemical weathering [Carter et al., 2013]. However, we have not identified any such sequences in our study of crater central peak regions.

5.5 Geologic Contexts of Zeolites and Sulfates

Most of the twelve zeolite detections occur in the Terra Tyrrhena and Nili Fossae regions **(Figure 13D)**. These potential zeolite detections are always observed in 'other' sedimentary deposits that represent unconsolidated materials not corresponding to well-bounded geologic units. Curiously, some of these deposits appear relatively light-toned and exhibit morphologies suggestive of downslope transport or slumping from a clear source region, possibly uplifted bedrock **(Figure 17)**. If these zeolites have eroded from uplifted material, then it is intriguing that no cohesive, well-lithified, zeolite-bearing bedrock has been observed in any of our central peak regions. An authigenic origin in these craters is also possible [e.g., Carter et al., 2013], though for these unconsolidated deposits it would suggest the bedrock is being altered in situ at a very local scale, as adjacent mass wasting deposits do not exhibit spectral signatures of zeolite. In contrast, sulfates were detected at eight central peaks **(Figure 13D)** and are found in 'other

sedimentary deposits' as well as uplifted (massive or poorly-stratified) bedrock. Half of these detections occur alongside Fe/Mg smectite and chlorite. It is also worth noting that most of these candidate sulfate deposits occur in regions where sulfates have been previously detected on a more regional scale [Ehlmann and Edwards, 2014].

6. Results: Ages of Host Craters

Clay minerals and hydrated silica, by far the dominant hydrous minerals in central peak regions, can form under a wide range of pressure, temperature, pH, and geochemical conditions, making it difficult to uniquely infer these conditions solely from their presence. These minerals can occur as detrital components, primary precipitates, or as products of in situ alteration/diagenesis, and thus may be older, equivalent, or younger than the rocks in which they reside. These complications notwithstanding, we attempt to loosely constrain the formation ages of clay mineral occurrences by integrating their geologic context with age estimates of their host crater.

Craters with examples of clays uplifted from depth span the entire range of ages in our survey, with the distribution peaking near ~3.6-3.7 Ga and the oldest craters at approximately 3.9 Ga **(Figure 18)**. The ages of these host craters constrain the youngest ages of the uplifted minerals, which were present within the crust prior to the impact and uplift event. Craters that bear likely detrital Fe/Mg smectites at their central peaks (e.g., clays associated with alluvial/fluvial systems) have age estimates that range from 3.4-3.9 Ga, with the exception of one crater with an age of 3.1 Ga **(Figure 18)**. Therefore, the deposits that host these clays must be no older than these ages, as the transport systems

post-date the impact events. However, the clays themselves may be significantly older if they are in fact detrital.

The distribution of clay-bearing deposits that may have an authigenic origin (e.g., clays in impact melt) seemingly occurs without any spatial preference and only a weak temporal preference **(Figure 18)**. Craters that host these examples have age estimates from <1 to ~3.9 Ga, which constrain the oldest formation ages of authigenic clays. Although the distribution of these values has a clear peak at ages >3 Ga, it is not possible to determine if this is statistically significant given the overall paucity of craters with younger ages in this category. However, the observed age range still holds even if we discard craters that host clays in both impact melt and uplifted bedrock, as it could be argued that clays in the former are simply recycled components of the latter **(Section 5.1.3)**. Therefore, even if the observed peak at >3 Ga is not due to sampling bias, it is likely that the distribution of impact melt clays has a long tail towards younger ages.

7. Results: Comparison with Previous Global Studies

Results from our study of central peak regions compare favorably with previous assessments of global central peak mineralogy by Pan et al. [2015] and global surface mineralogy by Ehlmann et al. [2011] and Carter et al. [2013]. Pan et al. [2015] conducted a global survey of central peaks using thermal infrared data from the Mars Odyssey Thermal Emission Imaging System and identified 26 central peaks that exhibited locally distinct spectral signatures, 21 of which are also surveyed in our work **(Appendix B)**. The 26 central peaks were further characterized with CRISM data, which identified clays within three Tyrrhena Terra craters and prehnite within Horowitz crater. We confirm

these four detections and additionally find Fe/Mg smectite, chlorite, and/or hydrated silica at 14 other central peaks, which were characterized as mafic and not hydrous by Pan et al. [2015].

Although Ehlmann et al. [2011] did not focus specifically on central peak mineralogy, they found Fe/Mg smectites and chlorites to be the most commonly detected minerals in 'crustal' settings (including crater environments). They also noted that chlorite and other phases such as prehnite, analcime, and illite/muscovite were not detected in 'sedimentary' settings, a designation that is similar to our 'detrital' contexts (e.g., alluvial/fluvial settings). We similarly have yet to observe chlorite and these other phases in these deposits. Finally, the global survey of Ehlmann et al. [2011] found limited instances of Al-clays in crater environments, instead assigning most Al-clays to the category of 'in stratigraphy', and in many instances these were found to overlie Fe/Mg clays. Our results support this observation, as we observe Al-clays in only three central peak regions. Therefore, our results are consistent with this more global study in that we find Fe/Mg clays (smectite, mixed-layer chlorite/smectite, and/or chlorite) in central peak regions to be vastly more common than occurrences of Al-clays.

We also compared our results to a global survey of hydrous minerals conducted by Carter et al. [2013], which also relied on a uniform and systematic gathering of observations from CRISM data (though using an automated detection method). That work also discussed a population of crater-related hydrous minerals, allowing us to compare central peak mineral assemblages identified in this study with those found within entire crater systems. Mineralogical differences between crater populations and other geologic contexts are discussed in detail by Carter et al. [2013], but here we

compare only their population of hydrous minerals that occur in crater environments with our central peak population. Our results are similar in the sense that the two largest hydrous mineral groups are Fe/Mg smectites (including mixed-layer chlorite/smectite) and chlorite, but the relative detection frequencies between Al-clays and hydrated silica at central peaks appear distinct from the results of Carter et al. [2013] **(Table 4, Figure 19)**.

These disparities are not readily quantifiable using statistical tests due to differences in data selection methods between Carter et al. [2013] and our study. For example, their global and crater survey utilized a select subset of the available CRISM database, with the exception of certain regions (e.g., all northern plains craters >10 km). Our study focused on all available CRISM data within central peak regions that also had HiRISE coverage, including data released after the publication of Carter et al. [2013]. Carter et al. [2013] also present their hydrous mineral detections in terms of number of exposures, which can be greater than one for a given crater. By contrast, we consider each hydrous mineral-bearing central peak as a single data point (though a given central peak can have multiple minerals and thus appear in more than one of our categories of mineral type). Thus it is important to keep in mind that these crater and central peak databases have fundamental differences in terms of the datasets used, the selected data, and the representation of results, which precludes a meaningful statistical comparison of the two. Although we are not able to perform statistical tests between the results of Carter et al. [2013] and our study, it is still useful to compare these studies to assess if and how the mineralogy of central peak regions may differ from crater settings as a whole.

The largest difference between the global crater population results of Carter et al. [2013] and our crater central peak results lies in the Al-phyllosilicate and hydrated silica detections **(Figure 19)**. Al-phyllosilicates were previously considered to be largely subordinate to other types of hydrous minerals on Mars [Mustard et al., 2008; Ehlmann et al., 2011b], but recent work by Carter et al. [2013] has suggested these minerals are as prevalent as the chlorite/prehnite group on the global and crater-wide scale. However, in our central peak region study Al-phyllosilicates are a minor contribution to the overall population of hydrous minerals, and we identify them in only three central peak regions. Although Carter et al.'s [2013] crater population (659 hydrous mineral detections) is nearly two and a half times larger than our hydrous central peak population (265 craters), we find almost the same number of hydrated silica occurrences **(Figure 19)**. This results in an apparently larger proportion of hydrated silica at central peak regions than in general crater environments, which may be due to differences in methodology or real phenomena such as emplacement or alteration mechanisms that favor the occurrence of hydrated silica in central peak regions.

We may find proportionally more hydrated silica at central peaks because many of these detections are in small exposures (e.g., tens of pixels) that may not be easily identified by automated methods. These small exposures were often not highlighted in the spectral parameter maps and were instead found in our study by manually exploring the false color CRISM images. An additional complication is that spectra of hydrated silica and Al-phyllosilicates are both characterized by an absorption with a reflectance minimum near ~2.2 μm, and it is the full width and symmetry of the absorption that is more diagnostic. This is a plausible explanation for the apparent tradeoff between

hydrated silica and Al-phyllosilicate detections in craters versus central peak regions, as we find hydrated silica to be proportionally more prevalent than Al-phyllosilicates at central peaks. An example of this is at Stokes crater, which had previously been characterized as having both kaolinite and montmorillonite at the central peak [Carter et al., 2010] but is classified as having kaolinite and hydrated silica in this survey **(Figure 12A)** based on the width and asymmetry of the ~2.2 μm absorption. Although the hydrated silica spectrum at Stokes **(Figure 12A)** has a 2.2 μm feature that is somewhat narrower than the laboratory example **(Figure 12B)**, the width is still greater than is observed for montmorillonite or illite, and the asymmetry of the 2.2 μm band in the CRISM spectrum is more consistent with an H_2O-poor hydrated silica. Additional study is warranted to determine the extent to which the denominator (background) spectrum affects the ratio spectra for these examples. Regardless, current results suggest that hydrated silica may be more common in central peak regions when compared to entire crater systems, and physical processes that may explain this observation are discussed in **Section 8.1.1**.

8. Discussion

Our study of central peak hydrous minerals provides a global dataset that can be used to infer mineralogical trends and variations with location, age, and other crater features. To investigate whether significant mineralogical differences exist between sub-populations of central peaks we used the Mann-Whitney U Test, the Chi-square test of independence, and Fisher's exact test. These tests were selected for their assumptions of non-normally distributed populations and their applicability to small sample sizes when

appropriate. We direct the reader to the relevant figures in each section for the data used in these statistical tests. In this section we choose to bin our data in intervals of 10 km diameter and 1 km uplift depth and label the bins based on the lower limit. For example, the '10 km' bin in **Figure 20** would include crater diameters in the range 10-20 km. The choice of bin size did not significantly influence our results, but we found these values sufficiently balanced bin population without sacrificing the resolution of the resulting distributions.

8.1 Depth of Hydrous Minerals in the Martian Crust

Previous studies have heralded the widespread occurrence of clay minerals in ancient terrains as compelling evidence for past habitable environments on Mars, but the exact age, formation mechanism, and origin of these minerals has been difficult to constrain from orbital data alone. One hypothesis is that clay minerals formed at the surface or near-surface during the Noachian in a warmer and wetter climate, and in some regions these were subsequently buried by younger deposits [e.g., Bibring et al., 2006; Carter et al., 2015]. In this scenario, clays found in post-Noachian impact craters represent excavation of pre-existing clay-bearing rocks [e.g., Mustard et al., 2008; Carter et al., 2010; Quantin et al., 2012]. An alternative view is that many of the clays may have formed in the deep, warmer subsurface on a planet that has otherwise been dominated by a cold and arid climate for the majority of its history [Ehlmann et al., 2011b]. Impact events also provide a mechanism to bring deep-seated clays to the near-surface in this scenario, thus in both cases crater central peaks are primarily viewed as hosting older, excavated hydrous minerals. However, on Earth it is widely recognized that clay minerals

can also form in impact crater contexts and the same is likely true of Mars [Osinski et al., 2013]. Thus these scenarios are best viewed as endmembers, and attempting to distinguish between them using only orbital data has practical limitations. Despite these constraints, the results of the present study can still provide insight into the relationship between crustal composition at depth and hydrous minerals detected in crater environments.

8.1.1 Hydrated Silica in the Crust and in Putative Impact Melt

Though slightly more than 25% of hydrated silica-bearing central peak regions contain examples in uplifted bedrock, consistent with exhumation of deep crustal materials, there are significantly more examples of hydrated silica in other geologic contexts **(Table 2)**. More than half of hydrated silica detections occur in 'eolian' or 'unconsolidated' deposits and indicate a global occurrence of hydrated silica in mobile, non-bedrock materials. These deposits were previously observed by Ehlmann et al. [2009] in the Nili Fossae region and interpreted as eolian lag. In addition, we find that the frequency of hydrated silica occurrences increases with crater size **(Figure 20)**. Compared with the frequency distribution of all hydrous minerals as a function of crater diameter, the distribution of hydrated silica with crater diameter is statistically distinct at the 99% confidence level from a Mann-Whitney-U test. This suggests some hydrated silica deposits may be diagenetic or related to the impact process itself, which is further supported by our observations of hydrated silica in numerous putative impact melt deposits. One possible mechanism is impact-induced shocking of clays, which scales with impact magnitude and can form hydrated silica under certain conditions [Friedlander

et al., 2015]. This is supported by a relative decrease in central peaks that host only clays as hydrated silica occurrences increase **(Figure 20B)**, though we note that larger crater diameters suffer from small sample sizes. However, the fraction of target material that experiences the peak shock pressures necessary for this transformation is relatively small and may not explain our observations for central peak regions.

Alternatively, some of these deposits may represent primary or recycled components of hydrous impact melts, particularly for those occurrences cataloged as potential impact melt deposits since melt production scales with crater size [Cintala and Grieve, 1998]. Given the widespread occurrence of hydrous minerals in the martian crust it is not unexpected that volatiles could be incorporated into some impact-generated melts, as was inferred in a previous case study of Ritchey crater [Sun and Milliken, 2014]. This is also suggested from recent work by Cannon and Mustard [2015], which identified glass-rich, sometimes hydrated, impactites with geomorphologic characteristics similar to those observed in our study. However, further study of the spectral properties of hydrated impact melt products and how they vary as a function of hydration state is needed to rigorously assess this hypothesis.

At first glance our results suggest central peaks in the southern highlands may be relatively enriched in hydrated silica compared to counterparts in the northern lowlands **(Figure 21)**. Although small and disparate sample sizes are an issue, we used Fisher's exact test to quantitatively assess if there is a statistical difference between the two central peak populations. We determine that at the 90% confidence level, there is a statistically significant difference between the frequency of hydrated silica occurrences in northern and southern central peak regions. This may be attributed to the fact that all 17

instances of definitively uplifted hydrated silica are found in the southern highlands, suggesting more frequent occurrence of hydrated silica within the southern highland crust.

To summarize, although we find convincing evidence for hydrated silica uplifted from depth in a number of craters, we find equally if not more compelling evidence for post-impact hydrated silica associated with impact melt and/or diagenetic processes. The latter may occur as primary precipitates, including pore-filling cements, in which case the hydrated silica would provide constraints on local aqueous geochemistry during the time of its formation. Unconsolidated and mobile hydrated silica-rich deposits may also be concentrated by physical weathering of altered central peak material [Ehlmann et al., 2009; Smith et al., 2013]. As discussed in detail by McLennan [2003], such occurrences of sedimentary silica are likely to be common even on a basaltic planet like Mars. Recent studies by Rice et al. [2013] and Smith et al. [2013] have examined a variety of hydrated silica deposits on Mars, but further study of these central peak hydrated silica deposits, the spectral properties of hydrated silica under Mars-like conditions, and experimental work on the effects of impacts into hydrous minerals are warranted to help constrain their origins.

8.1.2 Depth of Clays in the Crust

From our global study we find that ~61% and ~69% of central peak regions with Fe/Mg smectite or chlorite, respectively, contain evidence for clays uplifted from depths of at least 7 km and up to 17 km **(Figure 22)**. However, these and other craters contain numerous additional examples of clay minerals that are *not* clearly associated with

uplifted bedrock or erosion of uplifted bedrock. These results demonstrate the importance of assessing the local geologic context of hydrous minerals that are detected in central peak regions. As with hydrated silica deposits, clays found in central peak regions are not necessarily indicative of deeper crustal compositions. Stratigraphic relationships dictate that 31-39% of clay-bearing central peaks lack uplifted clays, and instead the clays only reside in deposits that are equivalent or younger in age than the impact event that formed the host crater.

Clays in non-uplifted contexts (e.g., alluvial/fluvial settings, eolian deposits, etc.) may be recycled components of pre-existing crust. However, such origins cannot be unequivocally proven nor disproven using orbital data alone, and it is also plausible that these phases are authigenic. Either interpretation is inherently speculative even with high-resolution mineralogy and morphology provided by the CRISM and HiRISE instruments. A detrital origin may be favored if similar minerals are found in sediment provenance regions [Ehlmann et al., 2008a; Milliken and Bish, 2010; Goudge et al., 2015], but even in these cases the clays and associated minerals likely represent a shallower portion of the crust than is typically sampled by uplifted materials in crater central peaks.

The statistics of uplifted clays is also difficult to quantify at larger crater diameters due to the small sample sizes. This is particularly true for uplift depths greater >11 km, above which there is usually only one crater in each 1 km depth bin **(Figure 22B)**. Thus, it is possible there are clays at greater depths, but if so they are at central peaks currently lacking CRISM and HiRISE coverage or they occur in geologic units that are not recognized as uplifted crustal materials in our classification scheme **(Figure 3)**. Conversely, clays in uplifted material could instead represent authigenic products from

local chemical weathering of previously unaltered lithologies. In this case the maximum depth of clays in the crust could be significantly shallower than is depicted in **Figure 22**. However, we note that in many cases the clays detected in uplifted bedrock are directly adjacent to units that lack clays, suggesting post-impact near-surface weathering is an unlikely origin, or was at least very heterogeneous in these locations.

The spatial distribution of clay detections within the largest craters is also variable, and several of these large craters have relatively small and/or patchy exposures of clay at their central peak **(Figure 23).** This could be due to a paucity of clays at those crustal depths, heterogeneous mixing of strata with different compositions, or incomplete CRISM coverage over the central peak region, as discussed in **Section 3.6.2**. In contrast, smaller craters tend to have larger and more continuous expanses of uplifted clays and provide a more robust indication of how clay minerals vary within the upper ~10 km of the crust. The data point for the 17 km uplift depth, for example, is ambiguous as it occurs in the peak ring structure of the ~173 km diameter Baldet crater. The process of peak ring formation is not entirely understood, and it is possible that the uplift equation from Pilkington and Grieve [1996] may not be appropriate for the uplifted chlorite-bearing material within the ring structure at Baldet. We also note that although Baldet may host the deepest uplifted clays it is not the largest crater with clays in the central peak region. Lyot, a 216 km diameter crater in the northern hemisphere, contains chlorite and a small instance of Fe/Mg smectite in the central peak and ring structure. However, these clays occur in deposits of ambiguous (possibly periglacial) origin, and the clays may or may not be sourced from depth.

These complications aside, and taken at face value, the clays found in uplifted bedrock provide the most direct insight into the presence and vertical distribution of these minerals within the deeper martian crust. Based on our results and the relationships described above, we find the maximum possible depth of uplifted clays to be ~17 km **(Figure 22B)**, despite our survey including craters that likely uplifted material from greater depths **(Figure 22A)**. This suggests that clays are either not common or not present beneath a depth of 17 km or that, if present, they have been modified such that their diagnostic spectral properties have not been preserved. As an example, sufficiently high temperatures or pressures such as those induced by large impact events could dehydroxylate clays and render them undetectable at VIS-NIR wavelengths [Fairen et al., 2010; Che and Glotch, 2012; Kraus et al., 2013]. If the chlorite uplifted from 17 km does indeed approximate a depth limit of clays in the martian crust, then they could be buried remnants of the earliest period of near-surface clay-forming conditions or indicate a crustal boundary in conditions favorable to subsurface clay formation.

8.2 Changes in Clay Mineralogy with Depth

Within the population of uplifted clays we observe a trend in the relative proportions of chlorite-bearing central peaks with uplift depth (**Figure 24**). We focus on uplift depths ranging from 0 to 7 km due to the scarcity of craters uplifting from greater depths and associated uncertainties. The frequency of uplifted bedrock with spectral signatures of chlorite increases with uplift depth relative to central peaks that only uplift Fe/Mg smectite (**Figure 24B,C**). This assessment is significant at the 99% confidence level as determined by the Mann-Whitney-U test.

Our central peak results are consistent with observations of increasing chlorite with depth by Carter et al. [2013], which determined that ejecta from smaller craters (<5 km) frequently excavated Fe/Mg smectite whereas larger craters (>5-20 km) excavate chlorite. Our work supports this chloritization trend when considering specifically Fe/Mg smectite and chlorite that is uplifted from depth, and not clays that may reside in post-impact deposits. These results also provide a higher-resolution view of mineralogy with depth and allow for a more precise identification of the depths at which chloritization may occur. The transition of smectite-to-chlorite with depth is a common phenomenon on Earth during burial diagenesis [e.g., Chang et al., 1986; Inoue et al, 1991; Środoń, 1999, and references therein]. Importantly, this process requires fluids for cation exchange, and the rate is dependent on the integration of time and temperature. Our results indicate that at depths greater than 4 km, chlorite-bearing material appears to dominate over non-chlorite-bearing material, a trend that is apparent in both the raw frequency **(Figure 24B)** and percentage **(Figure 24C)** of central peak regions with uplifted clays.

Evidence for increasing chloritization with depth is more difficult to interpret at uplift depths greater than 7 km. Though Baldet crater may host chlorite uplifted from 17 km, four craters spanning uplift depths from 8 to 12 km host Fe/Mg smectites rather than chlorites. These are Oudemans (119 km diameter), Milankovic (111 km), Li Fan (102 km), and Saheki (84 km). However, various factors weaken the case for the clays at these craters being uplifted. The majority of hydrous mineral exposures at Oudemans are unidentified phases whose spectra exhibit only weak evidence for a 1.9 μm H_2O absorption (previously reported in a crater survey by Quantin et al. [2012]). We find only one instance where the spectrum of potential uplifted material has a slight absorption at

2.3 µm, although low signal-to-noise complicate the validity of this feature **(Figure 23A)**. This potential clay exposure is also rather small (i.e. tens of CRISM pixels), despite numerous larger outcrops of uplifted bedrock in this central peak region and extensive CRISM coverage. Both Milankovic **(Figure 23B)** and Li Fan **(Figure 23C)** bear more convincing spectral evidence for Fe/Mg smectites, but the clays occur in both uplifted and periglacial materials in these craters. This raises the possibility of spectral 'contamination' of uplifted bedrock, where the Fe/Mg smectites may be of authigenic origin, possibly associated with periglacial processes, and are simply deposited on or formed within what appears to be uplifted material.

Finally, the central peak of Saheki crater contains mostly hydrated silica with only very small exposures (e.g., tens of CRISM pixels) of Fe/Mg smectite. Although these smectite detections lie within the central peak region, they are only present at the base of the central peak and are not clearly hosted in the peak structure itself **(Figure 23D)**. In our classification scheme these clays are in units that we interpret to be uplifted, but Saheki crater also hosts extensive fan deposits that extend from the crater wall to the base of the central peak. Given the topographic position of these clay detections and their proximity to the fan deposits we cannot rule out the possibility that they are detrital. Therefore, current evidence for uplifted Fe/Mg smectite in craters with uplift depths >7 km is rather weak, and the paucity of craters at these associated diameters makes interpretation of crustal mineralogy at these depths ambiguous. However, the trend of a relative increase in chlorite with depth is clear for smaller craters (uplift depth ≤7 km) that have significantly larger sample sizes in our database **(Figure 24)**, and Baldet may be excavating chlorite from as deep as ~17 km.

The gradual decline of Fe/Mg smectite and relative increase in chlorite with depth in the upper ~7 km is suggestive of the conversion of smectite, to mixed-layer chlorite/smectite, to chlorite within the crust, a process that has also been suggested to occur on Mars based on analysis of clays in non-crater environments [e.g., Milliken et al., 2010; 2011]. One possibility is that clays in uplifted bedrock were initially formed at or near the surface as smectites (e.g., Fe/Mg-rich clays such as saponite or nontronite) and subsequently buried and exposed to progressively higher temperatures, thus promoting conversion to chlorite. If true, then these uplifted clays may provide some metric for estimating long-term burial rates in the first 1-2 billion years of martian history. Another possibility is that the ancient environment promoted chloritization at the surface, as can happen in terrestrial soils, these materials were deeply buried, and later surface conditions promoted smectite formation and/or prohibited low-temperature chloritization. Alternatively, if these clays were originally formed at depth [e.g., Ehlmann et al., 2011b], the observed transition from smectite to chlorite may simply reflect changes in clay mineral formation as a function of the geothermal gradient. Although the transition from smectite-dominated to chlorite-dominated crust may not be diagnostic of either surface [Bibring et al., 2006] or subsurface [Ehlmann et al., 2011b] clay formation, other diagnostic higher temperature phases such as pumpellyite, prehnite, amphibole, etc. are conspicuously absent from central peaks on a global scale (though we note that our prehnite detections are likely an underestimation of their prevalence, see **Section 4.3**). This suggests temperatures in excess of 200°C in the presence of crustal fluids may not have been common or spatially extensive in the upper portions of the martian crust. Regardless of whether the surface or subsurface formation process is dominant, an

important outcome of our results is that there is strong evidence for crustal fluid circulation in at least the upper ~7 km, and possibly as deep as 10-17 km. As discussed above, we find no clear evidence for the presence of hydrous minerals in the crust at depths >17 km.

The proportion of chlorite appears to increase relative to smectite starting at a depth of ~2-3 km and chloritization, from a near-infrared spectral point of view, is largely complete by a depth of ~7 km (**Figure 24**). Therefore, smectite does not appear to have been stable or favored on Mars at depths greater than ~7 km over geological timescales. However, the apparent persistence of smectite or mixed-layer chlorite/smectite at shallower depths (~2-6 km) indicates these regions of the crust did not have the appropriate combination of temperature and fluid availability over the necessary timescales to allow for complete chloritization. Chloritization can take place over a wide range of temperatures, including ambient conditions in soils on Earth, thus incomplete chloritization on Mars may be more indicative of decreasing water availability through time than of changes in the geothermal gradient. Tosca and Knoll [2009] discussed the importance of apparent long-term smectite stability on Mars in the context of water availability in the near-surface. However, our results now provide evidence for maturation of clay minerals via diagenesis in the martian crust, though it appears even these processes may have been water-limited over the timescales necessary for chloritization to complete at temperatures corresponding to depths <7 km. Importantly, in the case of uplifted clays the age of the host crater places a minimum age on the time of clay formation itself, which provides insight into water-rock interaction through time on Mars.

The degree of chloritization with depth need not be uniform across the globe, but the general trend would predict that shallower materials exposed in crater walls should commonly consist of Fe/Mg smectite, whereas deeper uplifted materials at central peaks should be more chloritic [Milliken et al., 2010; 2011; Ehlmann et al., 2011a]. However, we note that five craters in our survey exhibit the opposite trend and instead exhibit Fe/Mg smectite at their central peaks and excavate chlorite in their walls. These near-surface examples of chlorite could represent deposits of recycled crustal materials (including buried ejecta deposits that excavated material from greater depths), near-surface low-temperature chlorite formation, or local enhancements in the geothermal gradient. A more refined view of the degree of chloritization with depth, and thus the extent and duration of water-rock interaction in the crust, could be gained by detailed spectral discrimination between smectite and mixed-layer chlorite/smectite [e.g., Milliken et al., 2011], which will be the focus of future work.

8.3 Timeline of Clay Formation on Mars

The ages of craters bearing detrital Fe/Mg smectites span 3.4-3.9 Ga **(Figure 18)**, which is near the Noachian-Hesperian time stratigraphic boundary and is largely consistent with the final period of valley network formation as recorded in the modern surface topography [Fassett and Head, 2010]. However, the majority of channels in these craters are not visibly integrated with these more regional networks, and we cannot rule out that they are younger as our only age constraint is that they formed after the host crater. Yet it is notable that craters with younger ages in our survey do not exhibit strong evidence for fluvial incision or likely detrital clays; thus our results are largely consistent

with previous studies that indicate surface water and fluvial transport of sediment were much more limited after the Early Hesperian epoch. By extension, the role of fluvial recycling of sediment, including clays, decreased relative to eolian and impact processes after the first ~1 Gyr of martian history.

The distribution of possibly authigenic impact melt clays has little temporal dependence **(Figure 18)**, which suggests these examples of clay minerals may be more indicative of local, intra-crater conditions rather than global climatic conditions. If true, then the likelihood of clays forming by any given impact event (of a similar magnitude) may not have varied much through time. Instead, the decline in the absolute number of impact melt clay occurrences over time may simply reflect changes in the cratering rate. Thirty-two of the craters in the 'authigenic' clay population are approximately Hesperian in age (2.7-3.6 Ga) and ten craters yield Amazonian ages (<2.7 Ga). When considering only craters that host clays exclusively in impact melt units (and not uplifted bedrock) there is still a substantial population of thirteen Hesperian craters and four Amazonian craters. A key point is that clay formation requires water, thus if some of these clays are indeed authigenic then they provide strong evidence for the presence of water at the time of crater formation or after. Despite the large uncertainties for some of these ages, it is likely that water continued to play an important role in clay mineral formation on Mars well after the Noachian period, whether that water originated from hydrous minerals or ice in the impactors or target rocks.

Craters uplifting clays from depth span the entire range of ages in our survey, although most are concentrated during the Noachian and Early Hesperian **(Figure 18)**. The oldest craters uplifting clays date to approximately 3.9 Ga, indicating that clay

formation must have started very early in Mars' history, either at the surface or in the subsurface. If these early clays formed at or near the surface then they may have formed significantly earlier than 3.9 Ga, particularly if burial rates were slow. However, even this old age provides an amount of time in early martian history that is roughly equivalent to the Phanerozoic, during which significant geological changes can take place. It should be noted that crater age estimates for uplifted clays are minimum values in terms of clay formation, as they could have formed at any point prior to the impact event. If subsurface clay formation is considered, then they could even be roughly equivalent in age to the host crater. In other words, although uplifted clays in young craters may have originally formed in the Noachian (as has been interpreted in previous studies), it is equally plausible that they formed in more recent times. Craters with ages <2 Ga, for example, may have uplifted clays that formed within that same time interval. Such considerations greatly extend the possible timeline of clay formation and water-rock interaction on Mars, possibly into the Amazonian, and highlight the need for higher resolution observations to place these clays in a detailed geologic context. However, given our results and previous extensive observations of an arid and cold surface environment for the past several billion years, it is still likely that non-impact clay-forming conditions were largely restricted to the subsurface during the Amazonian. In our analysis we have found that the majority of craters with uplifted clays tend to be Early Hesperian or older in age, indicating that this time period may indeed have been the dominant one for clay formation on a more global scale, in agreement with existing paradigms [e.g., Bibring et al., 2006].

9. Conclusion

We have conducted a study of hydrous minerals in martian central peak regions in order to assess which occurrences are indicative of deeper crustal compositions and to constrain the extent and timing of clay mineral formation. Of the 633 central peak regions that were examined, 265 exhibit evidence for hydrous minerals in existing CRISM VIS-NIR reflectance data. Our results largely affirm current paradigms of Mars' aqueous history in terms of mineralogical evolution, but we also find that many hydrous minerals in central peak regions are not clearly associated with uplifted bedrock. This highlights the importance of placing hydrous mineral detections in their proper geologic context when attempting to use the mineralogy of central peak regions as indicators of crustal composition. Key findings from our study are as follows.

1. Previous mineralogical surveys detected abundant outcrops of Fe/Mg smectite, chlorite, and hydrated silica in abundance on regional and global scales [e.g., Bibring et al., 2006; Mustard et al., 2008; Ehlmann et al., 2009; Murchie et al., 2010; Carter et al., 2013]. We observe similar trends in our survey of crater central peak regions, and these three mineral groups comprise 98% of our hydrous mineral detections.
2. We find proportionally more hydrated silica and fewer Al-clay occurrences in central peak regions relative to what was observed for entire crater systems [e.g., Carter et al., 2013]. This suggests hydrated silica may be preferentially formed in these portions of martian craters, or the discrepancies may be attributed to different methodologies between Carter et al. [2013] and our study. In addition, hydrated silica occurrences increase with crater diameter, coinciding with a

relative decrease in central peaks that host only clays. Furthermore, 71.7% of hydrated silica detections are found in non-uplifted contexts, including potential impact melt and unconsolidated deposits. These observations suggest that hydrated silica may be a common impact product on Mars, possibly formed by impact melting of volatile-rich crustal materials or concentration by physical weathering of altered central peak material.

3. Although the majority of clays (60.8% of Fe/Mg smectite and mixed-layer clays and 69% of chlorite) observed in central peak regions likely represent uplifted crustal material, a significant fraction are *not* obviously related to deeper crustal compositions. In addition, nearly 25% of central peak clay detections occur in potential impact melts units, which is suggestive of impact-induced authigenic clay formation. These observations confirm the importance of correlating mineralogical data with stratigraphic relationships from high-resolution imagery, particularly when attempting to discern deep crustal composition from crater central peak mineralogy.
4. Clay minerals appear to be common in the martian crust at depths $\leq$7 km, particularly in the southern highlands, and we find evidence for clays (chlorite) uplifted from depths up to 17 km. This suggests very deep burial of clays if they were originally formed in near-surface environments or very deep-seated clay formation, where the latter would imply the presence of crustal fluids at these depths. If these clays were originally formed at the surface or near-surface, then their presence at depth can provide constraints on long-term burial rates during the Noachian and Hesperian.

5. We observe a trend of increasing chlorite frequency relative to smectite frequency with increasing uplift depth, which is consistent with progressive chloritization within the crust. Our results build on the earlier findings of Carter et al. [2013], which found evidence for increasing chlorite frequency with depth based on crater ejecta. This may indicate widespread burial diagenesis on Mars or reflect changes in clay formation conditions with depth (e.g., temperature and/or fluid composition). In either case, this observation indicates the widespread presence of fluids within the upper ~7 km of the martian crust and that spectrally dominant clay mineral assemblages vary with depth. However, there is also evidence that chloritization is not complete even at depths of 2-6 km, suggesting water may have been limited over the necessary timescales for this process to complete at the temperatures associated with these depths.
6. Finally, we find that uplifted and potentially authigenic clays span almost the entirety of Mars' history, with most examples occurring in Noachian and Early Hesperian craters but additional examples occurring in Amazonian craters. Potential authigenic clays in impact melt deposits are identified in a number of Amazonian-aged craters, indicating that conditions conducive to clay formation may have been locally present well after the Noachian. Craters that host uplifted clays are predominantly Early Hesperian or older, with the oldest dating to 3.9 Ga. These observations support the Noachian and Early Hesperian as being the predominant time of widespread clay formation on Mars, whether at the surface or in the subsurface, but they also highlight the important role of local aqueous environments in more recent martian history. Given the diversity in mineralogy

and geologic setting for hydrous minerals in central peaks, and the prospect that such minerals can record important information about aqueous and/or atmospheric conditions, these are compelling regions for study by future surface missions.

Acknowledgements

We are especially grateful to Joe Michalski, Deanne Rogers, and Bethany Ehlmann for thorough and constructive reviews that helped improve this manuscript. We also thank Woodward Fischer, Jack Mustard, Brandon Johnson, and Jim Head for their thoughtful comments, Thomas Kneissl for assistance with CraterTools, the NASA Reflectance Experiment LABoratory (RELAB) at Brown University for making available some of the spectra used in this work, and the MRO science teams for producing high-resolution datasets. The CRISM data used in this paper are available at NASA's Planetary Data System Geoscience Node (http://pds-geosciences.wustl.edu/missions/mro/crism.htm). HiRISE images were obtained from the HiRISE team website (https://hirise.lpl.arizona.edu/) and CTX images from Arizona State University's online viewer (http://viewer.mars.asu.edu/viewer/ctx). This work was supported by the NASA Mars Data Analysis Program, grant NNX12A063G.

References

Abramov, O., and D. A. Kring (2005), Impact-induced hydrothermal activity on early Mars, *Journal of Geophysical Research: Planets*, *110*, E12S09, doi:10.1029/2005JE002453.

Allen, C. C., J. L. Gooding, and K. Keil (1982), Hydrothermally altered impact melt rock and breccia: Contributions to the soil of Mars, *Journal of Geophysical Research: Solid Earth*, *87*(B12), 10083–10101, doi:10.1029/JB087iB12p10083.

Anderson, J. H., and K. A. Wickersheim (1964), Near infrared characterization of water and hydroxyl groups on silica surfaces, *Surface Science*, *2*, 252–260, doi:10.1016/0039-6028(64)90064-0.

Ansan, V. et al. (2011), Stratigraphy, mineralogy, and origin of layered deposits inside Terby crater, Mars, *Icarus*, *211*(1), 273–304, doi:10.1016/j.icarus.2010.09.011.

Arvidson, R. E. et al. (2014), Ancient Aqueous Environments at Endeavour Crater, Mars, *Science*, *343*(6169), 1248097, doi:10.1126/science.1248097.

Baker, D. M. H., J. W. Head, and D. R. Marchant (2010), Flow patterns of lobate debris aprons and lineated valley fill north of Ismeniae Fossae, Mars: Evidence for extensive mid-latitude glaciation in the Late Amazonian, *Icarus*, *207*(1), 186–209, doi:10.1016/j.icarus.2009.11.017.

Barlow, N. G., and T. L. Bradley (1990), Martian impact craters: Correlations of ejecta and interior morphologies with diameter, latitude, and terrain, *Icarus*, *87*(1), 156–179, doi:10.1016/0019-1035(90)90026-6.

Barlow, N. G., J. M. Boyce, F. M. Costard, R. A. Craddock, J. B. Garvin, S. E. H. Sakimoto, R. O. Kuzmin, D. J. Roddy, and L. A. Soderblom (2000), Standardizing

the nomenclature of Martian impact crater ejecta morphologies, *J. Geophys. Res.*, *105*(E11), 26733–26738, doi:10.1029/2000JE001258.

Bibring, J.-P. et al. (2006), Global Mineralogical and Aqueous Mars History Derived from OMEGA/Mars Express Data, *Science*, *312*(5772), 400–404, doi:10.1126/science.1122659.

Bishop, D. G. (1972), Progressive Metamorphism from Prehnite-Pumpellyite to Greenschist Facies in the Dansey Pass Area, Otago, New Zealand, *Geological Society of America Bulletin*, *83*(11), 3177–3198, doi:10.1130/0016-7606(1972)83[3177:PMFPTG]2.0.CO;2.

Bishop, J., J. Madejová, P. Komadel, and H. Fröschl (2002), The influence of structural Fe, Al and Mg on the infrared OH bands in spectra of dioctahedral smectites, *Clay Minerals*, *37*(4), 607–616, doi:10.1180/0009855023740063.

Bishop, J. L. et al. (2008), Phyllosilicate Diversity and Past Aqueous Activity Revealed at Mawrth Vallis, Mars, *Science*, *321*(5890), 830–833, doi:10.1126/science.1159699.

Bristow, T. F., and R. E. Milliken (2011), Terrestrial Perspective on Authigenic Clay Mineral Production in Ancient Martian Lakes, *Clays and Clay Minerals*, *59*(4), 339–358, doi:10.1346/CCMN.2011.0590401.

Bristow, T. F. et al. (2015), The origin and implications of clay minerals from Yellowknife Bay, Gale crater, Mars, *American Mineralogist*, *100*(4), 824–836, doi:10.2138/am-2015-5077CCBYNCND.

Cannon, K. M., and J. F. Mustard (2015), Preserved glass-rich impactites on Mars, *Geology*, *43*(7), 635–638, doi:10.1130/G36953.1.

Carr, M.H. (1996), *Water on Mars*, Oxford University Press, New York.

Carter, J., F. Poulet, J.-P. Bibring, and S. Murchie (2010), Detection of Hydrated Silicates in Crustal Outcrops in the Northern Plains of Mars, *Science*, *328*(5986), 1682–1686, doi:10.1126/science.1189013.

Carter, J., F. Poulet, J.-P. Bibring, N. Mangold, and S. Murchie (2013), Hydrous minerals on Mars as seen by the CRISM and OMEGA imaging spectrometers: Updated global view, *J. Geophys. Res. Planets*, *118*(4), 831–858, doi:10.1029/2012JE004145.

Carter, J., D. Loizeau, N. Mangold, F. Poulet, and J.-P. Bibring (2015), Widespread surface weathering on early Mars: A case for a warmer and wetter climate, *Icarus*, *248*, 373–382, doi:10.1016/j.icarus.2014.11.011.

Caudill, C. M., L. L. Tornabene, A. S. McEwen, S. Byrne, L. Ojha, and S. Mattson (2012), Layered MegaBlocks in the central uplifts of impact craters, *Icarus*, *221*(2), 710–720, doi:10.1016/j.icarus.2012.08.033.

Chang, H. K., F. T. MacKenzie, and J. Schoonmaker (1986), Comparisons between the diagenesis of dioctahedral and trioctahedral smectite, Brazilian offshore basins, *Clays and Clay Minerals*, *34*(4), 407–423.

Che, C., T. D. Glotch, D. L. Bish, J. R. Michalski, and W. Xu (2011), Spectroscopic study of the dehydration and/or dehydroxylation of phyllosilicate and zeolite minerals, J. Geophys. Res., 116, E05007, doi:10.1029/2010JE003740.

Cintala, M. J., and R. a. F. Grieve (1998), Scaling impact melting and crater dimensions: Implications for the lunar cratering record, *Meteoritics & Planetary Science*, *33*(4), 889–912, doi:10.1111/j.1945-5100.1998.tb01695.x.

Cloutis, E. A., P. M. Asher, and S. A. Mertzman (2002), Spectral reflectance properties of zeolites and remote sensing implications, *J.-Geophys.-Res.*, *107*(E9), 5067, doi:10.1029/2000JE001467.

Cloutis, E. A. et al. (2006), Detection and discrimination of sulfate minerals using reflectance spectroscopy, *Icarus*, *184*(1), 121–157, doi:10.1016/j.icarus.2006.04.003.

Crater analysis techniques working group (1979), Standard techniques for presentation and analysis of crater size-frequency data, *Icarus*, *37*(2), 467–474, doi:10.1016/0019-1035(79)90009-5.

Ehlmann, B. L., and C. S. Edwards (2014), Mineralogy of the Martian Surface, *Annual Review of Earth and Planetary Sciences*, *42*(1), 291–315, doi:10.1146/annurev-earth-060313-055024.

Ehlmann, B. L., J. F. Mustard, C. I. Fassett, S. C. Schon, J. W. Head Iii, D. J. Des Marais, J. A. Grant, and S. L. Murchie (2008a), Clay minerals in delta deposits and organic preservation potential on Mars, *Nature Geosci*, *1*(6), 355–358, doi:10.1038/ngeo207.

Ehlmann, B. L. et al. (2008b), Orbital Identification of Carbonate-Bearing Rocks on Mars, *Science*, *322*(5909), 1828–1832, doi:10.1126/science.1164759.

Ehlmann, B. L. et al. (2009), Identification of hydrated silicate minerals on Mars using MRO-CRISM: Geologic context near Nili Fossae and implications for aqueous alteration, *Journal of Geophysical Research: Planets*, *114*, E00D08, doi:10.1029/2009JE003339.

Ehlmann, B. L., J. F. Mustard, and S. L. Murchie (2010), Geologic setting of serpentine deposits on Mars, *Geophysical Research Letters*, *37*, L06201, doi:10.1029/2010GL042596.

Ehlmann, B. L., J. F. Mustard, R. N. Clark, G. A. Swayze, and S. L. Murchie (2011a), Evidence for Low-Grade Metamorphism, Hydrothermal Alteration, and Diagenesis on Mars from Phyllosilicate Mineral Assemblages, *Clays and Clay Minerals*, *59*(4), 359–377, doi:10.1346/CCMN.2011.0590402.

Ehlmann, B. L., J. F. Mustard, S. L. Murchie, J.-P. Bibring, A. Meunier, A. A. Fraeman, and Y. Langevin (2011b), Subsurface water and clay mineral formation during the early history of Mars, *Nature*, *479*(7371), 53–60, doi:10.1038/nature10582.

Fairén, A. G. et al. (2010), Noachian and more recent phyllosilicates in impact craters on Mars, *PNAS*, *107*(27), 12095–12100, doi:10.1073/pnas.1002889107.

Farmer, J.D. (1996), Hydrothermal processes on Mars: An assessment of present evidence, in *Evolution of Hydrothermal Ecosystems on Earth (and Mars?)*, pp. 273–299, John Wiley and Sons.

Fassett, C. I., and J. W. Head III (2008), The timing of martian valley network activity: Constraints from buffered crater counting, *Icarus*, *195*(1), 61–89, doi:10.1016/j.icarus.2007.12.009.

Friedlander, L. R., T. D. Glotch, D. L. Bish, M. D. Dyar, T. G. Sharp, E. C. Sklute, and J. R. Michalski (2015), Structural and spectroscopic changes to natural nontronite induced by experimental impacts between 10 and 40 GPa, *J. Geophys. Res. Planets*, *120*(5), 2014JE004638, doi:10.1002/2014JE004638.

Goudge, T. A., J. F. Mustard, J. W. Head, C. I. Fassett, and S. M. Wiseman (2015), Assessing the mineralogy of the watershed and fan deposits of the Jezero crater paleolake system, Mars, *J. Geophys. Res. Planets*, *120*(4), 2014JE004782, doi:10.1002/2014JE004782.

Grant, J. A., R. P. Irwin, J. P. Grotzinger, R. E. Milliken, L. L. Tornabene, A. S. McEwen, C. M. Weitz, S. W. Squyres, T. D. Glotch, and B. J. Thomson (2008), HiRISE imaging of impact megabreccia and sub-meter aqueous strata in Holden Crater, Mars, *Geology*, *36*(3), 195–198, doi:10.1130/G24340A.1.

Grieve, R. A. F., and M. Pilkington (1996), The signature of terrestrial impacts, *AGSO J Austral Geol Geophys*, *16*, 399–420.

Grotzinger, J. P., and R. E. Milliken (Eds.) (2012), *Sedimentary Geology of Mars*, SEPM (Society for Sedimentary Geology).

Grotzinger, J. P. et al. (2014), A Habitable Fluvio-Lacustrine Environment at Yellowknife Bay, Gale Crater, Mars, *Science*, *343*(6169), 1242777, doi:10.1126/science.1242777.

Hartmann, W. K., and G. Neukum (2001), Cratering Chronology and the Evolution of Mars, *Space Science Reviews*, *96*, 165–194.

Head, J. W., J. F. Mustard, M. A. Kreslavsky, R. E. Milliken, and D. R. Marchant (2003), Recent ice ages on Mars, *Nature*, *426*(6968), 797–802, doi:10.1038/nature02114.

Inoue, A., M. Utada, and K. Wakita (1992), Smectite-to-illite conversion in natural hydrothermal systems, *Applied Clay Science*, *7*(1-3), 131–145, doi:10.1016/0169-1317(92)90035-L.

Ivanov, B.A., and et al. (1982), Formation of the central uplift in mete- oritic craters, *Meteoritika*, *40*, 60–81.

Kirsimäe, K., S. Suuroja, J. Kirs, A. Kärki, M. Polikarpus, V. Puura, and K. Suuroja (2002), Hornblende alteration and fluid inclusions in Kärdla impact crater, Estonia:

Evidence for impact-induced hydrothermal activity, *Meteoritics & Planetary Science*, *37*(3), 449–457, doi:10.1111/j.1945-5100.2002.tb00827.x.

Kneissl, T., S. van Gasselt, and G. Neukum (2011), Map-projection-independent crater size-frequency determination in GIS environments—New software tool for ArcGIS, *Planetary and Space Science*, *59*(11–12), 1243–1254, doi:10.1016/j.pss.2010.03.015.

Kraus, R. G., S. T. Stewart, M. G. Newman, R. E. Milliken, and N. J. Tosca (2013), Uncertainties in the shock devolatilization of hydrated minerals: A nontronite case study, *J. Geophys. Res. Planets*, *118*(10), 2137–2145, doi:10.1002/jgre.20147.

Loizeau, D. et al. (2007), Phyllosilicates in the Mawrth Vallis region of Mars, *Journal of Geophysical Research: Planets*, *112*, E08S08, doi:10.1029/2006JE002877.

Loizeau, D., J. Carter, S. Bouley, N. Mangold, F. Poulet, J.-P. Bibring, F. Costard, Y. Langevin, B. Gondet, and S. L. Murchie (2012), Characterization of hydrated silicate-bearing outcrops in Tyrrhena Terra, Mars: Implications to the alteration history of Mars, *Icarus*, *219*(1), 476–497, doi:10.1016/j.icarus.2012.03.017.

Malin, M. C. et al. (2007), Context Camera Investigation on board the Mars Reconnaissance Orbiter, *Journal of Geophysical Research: Planets*, *112*, E05S04, doi:10.1029/2006JE002808.

Mangold, N., S. Adeli, S. Conway, V. Ansan, and B. Langlais (2012a), A chronology of early Mars climatic evolution from impact crater degradation, *Journal of Geophysical Research: Planets*, *117*(E4), n/a–n/a, doi:10.1029/2011JE004005.

Mangold, N., J. Carter, F. Poulet, E. Dehouck, V. Ansan, and D. Loizeau (2012b), Late Hesperian aqueous alteration at Majuro crater, Mars, *Planetary and Space Science*, *72*(1), 18–30, doi:10.1016/j.pss.2012.03.014.

Marzo, G. A., A. F. Davila, L. L. Tornabene, J. M. Dohm, A. G. Fairén, C. Gross, T. Kneissl, J. L. Bishop, T. L. Roush, and C. P. McKay (2010), Evidence for Hesperian impact-induced hydrothermalism on Mars, *Icarus*, *208*(2), 667–683, doi:10.1016/j.icarus.2010.03.013.

McEwen, A. S., B. S. Preblich, E. P. Turtle, N. A. Artemieva, M. P. Golombek, M. Hurst, R. L. Kirk, D. M. Burr, and P. R. Christensen (2005), The rayed crater Zunil and interpretations of small impact craters on Mars, *Icarus*, *176*(2), 351–381, doi:10.1016/j.icarus.2005.02.009.

McEwen, A. S. et al. (2007), Mars Reconnaissance Orbiter's High Resolution Imaging Science Experiment (HiRISE), *Journal of Geophysical Research: Planets*, *112*, E05S02, doi:10.1029/2005JE002605.

McGuire, P. C. et al. (2009), An improvement to the volcano-scan algorithm for atmospheric correction of CRISM and OMEGA spectral data, *Planetary and Space Science*, *57*(7), 809–815, doi:10.1016/j.pss.2009.03.007.

McLennan, S. M. (2003), Sedimentary silica on Mars, *Geology*, *31*(4), 315–318, doi:10.1130/0091-7613(2003)031<0315:SSOM>2.0.CO;2.

Melosh, H.J. (1989), *Impact Cratering: A Geologic Process*, Oxford University Press, New York.

Michael, G. G., and G. Neukum (2010), Planetary surface dating from crater size–frequency distribution measurements: Partial resurfacing events and statistical age uncertainty, *Earth and Planetary Science Letters*, *294*(3–4), 223–229, doi:10.1016/j.epsl.2009.12.041.

Michalski, J. R., and P. B. Niles (2010), Deep crustal carbonate rocks exposed by meteor impact on Mars, *Nature Geosci*, *3*(11), 751–755, doi:10.1038/ngeo971.

Michalski, J. R., J. Cuadros, J. L. Bishop, M. Darby Dyar, V. Dekov, and S. Fiore (2015), Constraints on the crystal-chemistry of Fe/Mg-rich smectitic clays on Mars and links to global alteration trends, *Earth and Planetary Science Letters*, *427*, 215–225, doi:10.1016/j.epsl.2015.06.020.

Milliken, R. E., and D. L. Bish (2010), Sources and sinks of clay minerals on Mars, *Philosophical Magazine*, *90*(17-18), 2293–2308, doi:10.1080/14786430903575132.

Milliken, R. E., and J. F. Mustard (2005), Quantifying absolute water content of minerals using near-infrared reflectance spectroscopy, *Journal of Geophysical Research: Planets*, *110*(E12), n/a–n/a, doi:10.1029/2005JE002534.

Milliken, R. E., and J. F. Mustard (2007), Estimating the water content of hydrated minerals using reflectance spectroscopy: II. Effects of particle size, *Icarus*, *189*(2), 574–588, doi:10.1016/j.icarus.2006.12.028.

Milliken, R. E., J. F. Mustard, and D. L. Goldsby (2003), Viscous flow features on the surface of Mars: Observations from high-resolution Mars Orbiter Camera (MOC) images, *J. Geophys. Res.*, *108*(E6), 5057, doi:10.1029/2002JE002005.

Milliken, R. E., D. L. Bish, and T. Bristow (2010), The case for mixed-layered clays on Mars, *Lunar Planet. Sci. XLI*, Abstract 2030.

Milliken, R. E., T. Bristow, and D. L. Bish (2011), Diagenesis of clay minerals on Mars and implications for the Mars Science Laboratory Rover, *Lunar Planet. Sci. XLII*, Abstract 2230.

Milliken, R. E., R. C. Ewing, W. W. Fischer, and J. Hurowitz (2014), Wind-blown sandstones cemented by sulfate and clay minerals in Gale Crater, Mars, *Geophys. Res. Lett.*, *41*(4), 2013GL059097, doi:10.1002/2013GL059097.

Murchie, S. et al. (2007), Compact Reconnaissance Imaging Spectrometer for Mars (CRISM) on Mars Reconnaissance Orbiter (MRO), *Journal of Geophysical Research: Planets*, *112*, E05S03, doi:10.1029/2006JE002682.

Murchie, S. L. et al. (2009), Compact Reconnaissance Imaging Spectrometer for Mars investigation and data set from the Mars Reconnaissance Orbiter's primary science phase, *Journal of Geophysical Research: Planets*, *114*, E00D07, doi:10.1029/2009JE003344.

Mustard, J. F., C. D. Cooper, and M. K. Rifkin (2001), Evidence for recent climate change on Mars from the identification of youthful near-surface ground ice, *Nature*, *412*(6845), 411–414, doi:10.1038/35086515.

Mustard, J. F. et al. (2008), Hydrated silicate minerals on Mars observed by the Mars Reconnaissance Orbiter CRISM instrument, *Nature*, *454*(7202), 305–309, doi:10.1038/nature07097.

Newsom, H. E. (1980), Hydrothermal alteration of impact melt sheets with implications for Mars, *Icarus*, *44*(1), 207–216, doi:10.1016/0019-1035(80)90066-4.

Pan, C., A. D. Rogers, and J. R. Michalski (2015), Thermal and near-infrared analyses of central peaks of Martian impact craters: Evidence for a heterogeneous Martian crust: Martian crater central peak compositions, *Journal of Geophysical Research: Planets*, *120*(4), 662–688, doi:10.1002/2014JE004676.

Parente, M. (2008), A new approach to denoising CRISM images, *Lunar Planet. Sci., XXXIX*, Abstract 2528.

Pelkey, S. M. et al. (2007), CRISM multispectral summary products: Parameterizing mineral diversity on Mars from reflectance, *Journal of Geophysical Research: Planets*, *112*, E08S14, doi:10.1029/2006JE002831.

Quantin, C., J. Flahaut, H. Clenet, P. Allemand, and P. Thomas (2012), Composition and structures of the subsurface in the vicinity of Valles Marineris as revealed by central uplifts of impact craters, *Icarus*, *221*(1), 436–452, doi:10.1016/j.icarus.2012.07.031.

Rathbun, J. A., and S. W. Squyres (2002), Hydrothermal Systems Associated with Martian Impact Craters, *Icarus*, *157*(2), 362–372, doi:10.1006/icar.2002.6838.

Rice, M. S., E. A. Cloutis, J. F. Bell III, D. L. Bish, B. H. Horgan, S. A. Mertzman, M. A. Craig, R. W. Renaut, B. Gautason, and B. Mountain (2013), Reflectance spectra diversity of silica-rich materials: Sensitivity to environment and implications for detections on Mars, *Icarus*, *223*(1), 499–533, doi:10.1016/j.icarus.2012.09.021.

Robbins, S. J., and B. M. Hynek (2012), A new global database of Mars impact craters ≥1 km: 1. Database creation, properties, and parameters, *Journal of Geophysical Research: Planets*, *117*(E5), n/a–n/a, doi:10.1029/2011JE003966.

Schwenzer, S. P., and D. A. Kring (2009), Impact-generated hydrothermal systems capable of forming phyllosilicates on Noachian Mars, *Geology*, *37*(12), 1091–1094, doi:10.1130/G30340A.1.

Schwenzer, S. P., and D. A. Kring (2013), Alteration minerals in impact-generated hydrothermal systems – Exploring host rock variability, *Icarus*, *226*(1), 487–496, doi:10.1016/j.icarus.2013.06.003.

Skok, J. R., J. F. Mustard, L. L. Tornabene, C. Pan, D. Rogers, and S. L. Murchie (2012), A spectroscopic analysis of Martian crater central peaks: Formation of the ancient crust, *J. Geophys. Res.*, *117*(E11), E00J18, doi:10.1029/2012JE004148.

Smith, M. R., J. L. Bandfield, E. A. Cloutis, and M. S. Rice (2013), Hydrated silica on Mars: Combined analysis with near-infrared and thermal-infrared spectroscopy, *Icarus*, *223*(2), 633–648, doi:10.1016/j.icarus.2013.01.024.

Squyres, S. W., and M. H. Carr (1986), Geomorphic Evidence for the Distribution of Ground Ice on Mars, *Science*, *231*(4735), 249–252.

Środoń, J. (1999), Nature of Mixed-Layer Clays and Mechanisms of Their Formation and Alteration, *Annual Review of Earth and Planetary Sciences*, *27*(1), 19–53, doi:10.1146/annurev.earth.27.1.19.

Stolper, E. (1982), Water in silicate glasses: An infrared spectroscopic study, *Contr. Mineral. and Petrol.*, *81*(1), 1–17, doi:10.1007/BF00371154.

Sun, V. Z., and R. E. Milliken (2014), The geology and mineralogy of Ritchey crater, Mars: Evidence for post-Noachian clay formation, *J. Geophys. Res. Planets*, *119*(4), 2013JE004602, doi:10.1002/2013JE004602.

Tanaka, K. L., S. J. Robbins, C. M. Fortezzo, J. A. Skinner Jr., and T. M. Hare (2014), The digital global geologic map of Mars: Chronostratigraphic ages, topographic and crater morphologic characteristics, and updated resurfacing history, *Planetary and Space Science*, *95*, 11–24, doi:10.1016/j.pss.2013.03.006.

Tornabene, L. L. (2009), Parautochthonous Megabreccias and Possible Evidence of Impact-Induced Hydrothermal Alteration in Holden Crater, Mars., *Lunar Planet. Sci. XL*, Abstract 1766.

Tornabene, L. L., G. R. Osinski, A. S. McEwen, J. M. Boyce, V. J. Bray, C. M. Caudill, J. A. Grant, C. W. Hamilton, S. Mattson, and P. J. Mouginis-Mark (2012), Widespread crater-related pitted materials on Mars: Further evidence for the role of target volatiles during the impact process, *Icarus*, *220*(2), 348–368, doi:10.1016/j.icarus.2012.05.022.

Vaniman, D. T. et al. (2014), Mineralogy of a Mudstone at Yellowknife Bay, Gale Crater, Mars, *Science*, *343*(6169), 1243480, doi:10.1126/science.1243480.

Velde, B., and A. Meunier (2008), *The Origin of Clay Minerals in Soils and Weathered Rocks*, Springer Berlin Heidelberg, Berlin, Heidelberg.

Viviano-Beck, C. E. et al. (2014), Revised CRISM spectral parameters and summary products based on the currently detected mineral diversity on Mars, *J. Geophys. Res. Planets*, *119*(6), 2014JE004627, doi:10.1002/2014JE004627.

Wray, J. J., B. L. Ehlmann, S. W. Squyres, J. F. Mustard, and R. L. Kirk (2008), Compositional stratigraphy of clay-bearing layered deposits at Mawrth Vallis, Mars, *Geophys. Res. Lett.*, *35*(12), L12202, doi:10.1029/2008GL034385.

Wray, J. J. et al. (2011), Columbus crater and other possible groundwater-fed paleolakes of Terra Sirenum, Mars, *Journal of Geophysical Research: Planets*, *116*, E01001, doi:10.1029/2010JE003694.

Tables

Table 1. Categories of hydrous minerals and their prevalence at 265 central peaks with spectral evidence for hydrous phases. An individual crater that hosts multiple hydrous minerals appears in more than one hydrous mineral category. The category of Fe/Mg smectite includes possible mixed-layer chlorite/smectite.

Hydrous Mineral	Number of Craters	Percent of All Hydrous Craters
Fe/Mg smectite	217	81.9
Chlorite	71	26.8
Hydrated/opaline silica	60	22.6
Unidentified hydrous phase	18	6.8
Zeolite	12	4.5
Sulfate	8	3.0
Al phyllosilicate	3	1.1

Table 2. Summary of the occurrence frequency for geologic contexts of Fe/Mg smectite, chlorite, and hydrated silica in central peak regions. Note that the percentages in each column are relative to the total number of central peaks hosting that specific mineral, thus they do not sum to 100% as an individual central peak can host hydrous mineral occurrences in multiple settings. A more detailed breakdown of the distribution of uplifted contexts is shown in **Table 3**.

Geologic Context	Fe/Mg Smectite-Bearing	Chlorite-Bearing	Hydrated Silica-Bearing
All Uplifted Contexts	132 (60.8%)	49 (69%)	17 (28.3%)
Uplifted Bedrock	125 (57.6%)	44 (62%)	14 (23.3%)
Inferred Uplifted	19 (8.8%)	13 (18.3%)	3 (5%)
Alluvial/Fluvial	11 (5.1%)	0 (0%)	0 (0%)
Impact Melt	54 (24.9%)	7 (9.9%)	15 (25%)
Periglacial	29 (13.4%)	13 (18.3%)	5 (8.3%)
Eolian	9 (4.1%)	3 (4.2%)	9 (15%)
Other Unconsolidated Deposits	44 (20.3%)	10 (14.1%)	23 (38.3%)
Ejecta from External Craters	8 (3.7%)	7 (9.9%)	0 (0%)
Total Central Peaks	**217**	**71**	**60**

Table 3. Occurrence frequency for detailed contexts of uplifted examples of Fe/Mg smectite, chlorite, and hydrated silica at central peaks. Percentages are relative to the total number of uplifted contexts and sum to 100% at successively higher levels.

Uplifted Context	Fe/Mg Smectite-Bearing	Chlorite-Bearing	Hydrated Silica-Bearing
Uplifted Bedrock	**113 (85.6%)**	**36 (73.5%)**	**14 (82.4%)**
Massive	43 (32.6%)	13 (26.5%)	8 (47.1%)
Well-Stratified	9 (6.8%)	2 (4.1%)	0 (0%)
Poorly-Stratified	42 (31.8%)	17 (34.7%)	6 (35.3%)
Massive and Poorly-Stratified	17 (12.9%)	3 (6.1%)	0 (0%)
Well-Stratified and Poorly-Stratified	2 (1.5%)	1 (2%)	0 (0%)
Inferred Uplifted	**7 (5.3%)**	**5 (10.2%)**	**3 (17.6%)**
Mass Wasting/Erosion	6 (4.5%)	5 (10.2%)	2 (11.8%)
Small Craters at Central Peak	0 (0%)	0 (0%)	1 (5.9%)
Mass Wasting/Erosion and Small Crater	1 (0.8%)	0 (0%)	0 (0%)
Both Uplifted Bedrock and Inferred Uplifted	**12 (9.1%)**	**8 (16.3%)**	**0 (0%)**
Massive and Mass Wasting	1 (0.8%)	1 (2%)	0 (0%)
Massive and Small Crater	1 (0.8%)	0 (0%)	0 (0%)
Layered and Mass Wasting	0 (0%)	0 (0%)	0 (0%)
Layered and Small Crater	1 (0.8%)	0 (0%)	0 (0%)
Friable and Mass Wasting	7 (5.3%)	4 (8.2%)	0 (0%)
Friable and Small Crater	2 (1.5%)	3 (6.1%)	0 (0%)
All Uplifted Contexts	**132**	**49**	**17**

Table 4. Hydrous mineral frequencies from *Carter et al.'s* [2013] global and crater survey and our central peak survey. Numbers for *Carter et al.*'s [2013] global detections are taken directly from Figure 9 of their paper, whereas the numbers of crater-related detections are estimated from their Figure 16. Note that the absolute numbers are not comparable across the two studies, as *Carter et al.* [2013] present detection frequencies whereas we present crater frequencies.

Hydrous Mineral Group	**Carter et al. [2013] # Detections Globally**	**Carter et al. [2013] # Detections in Craters**	**This Study (Central Peaks) # Craters**
Fe/Mg smectite	1054	554	217
Chlorite	268	211	71
Al phyllosilicates	362	145	3
Hydrated silica	153	59	60
Zeolites and sulfates	152	79	20
Total	1989	1048	371

Figures

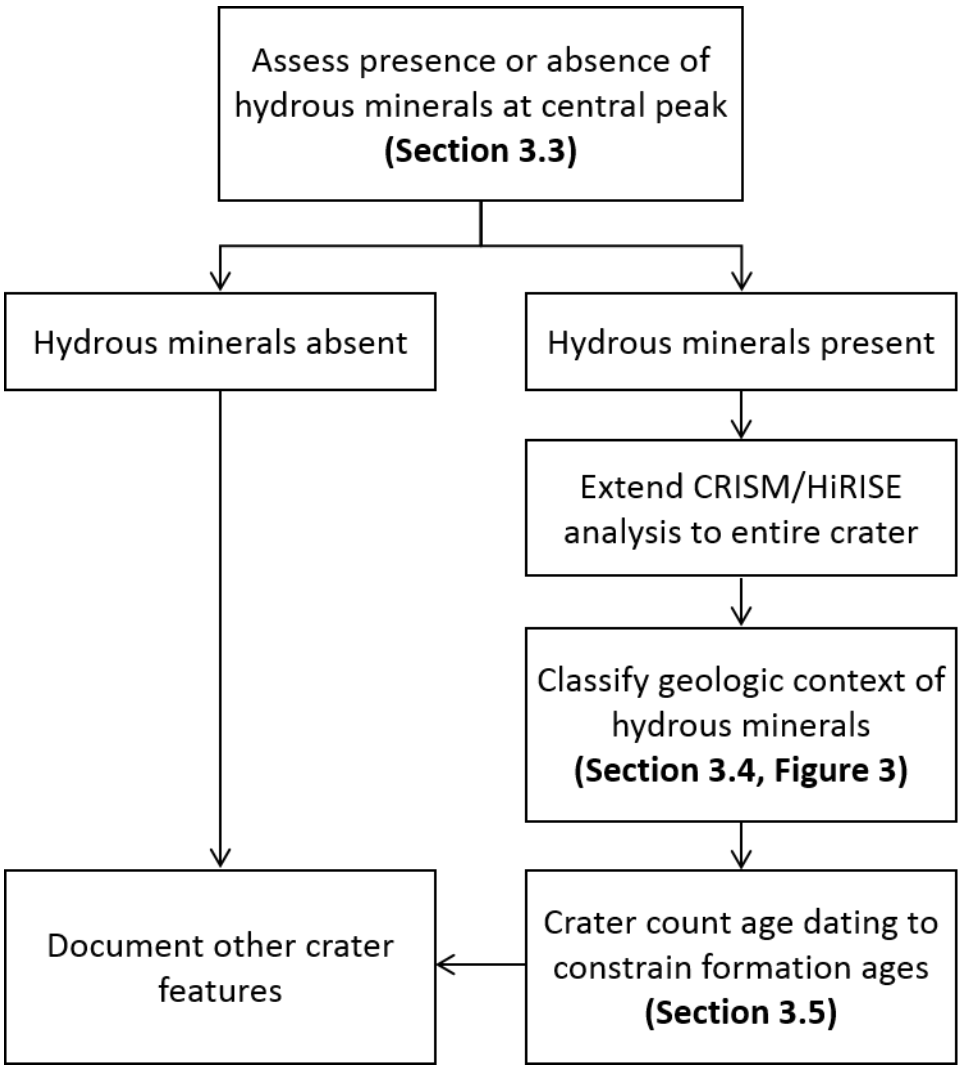

Figure 1. Flow chart illustrating the methodology used for analyzing the craters studied in this work.

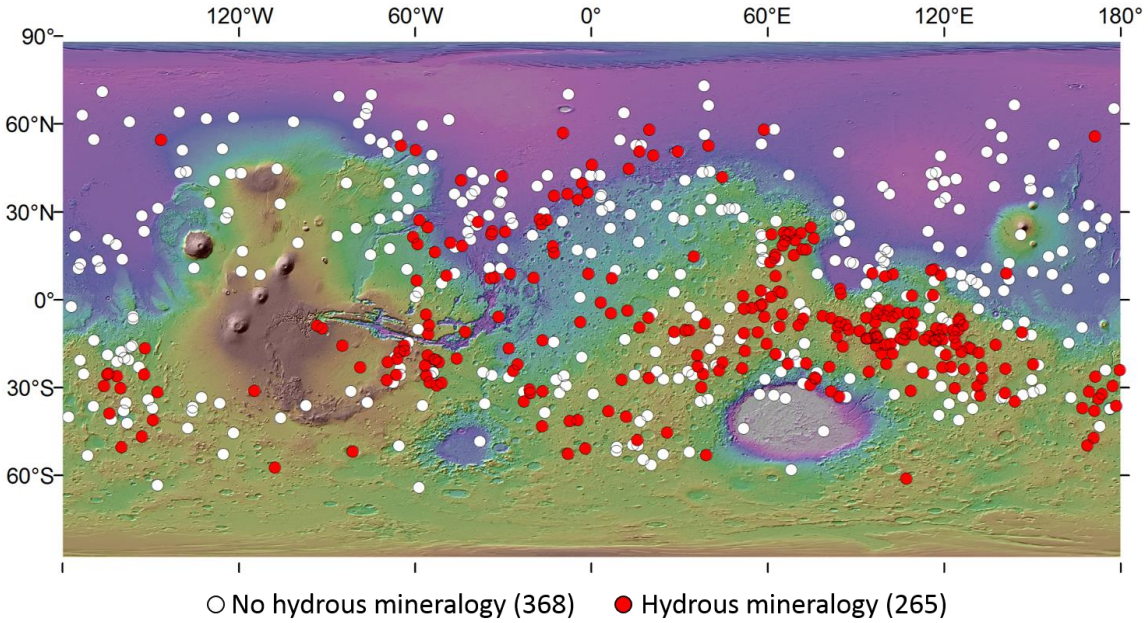

Figure 2. Global map of Mars (MOLA topography) showing the locations of the 633 central peaks that met our criteria for necessary HiRISE and CRISM coverage.

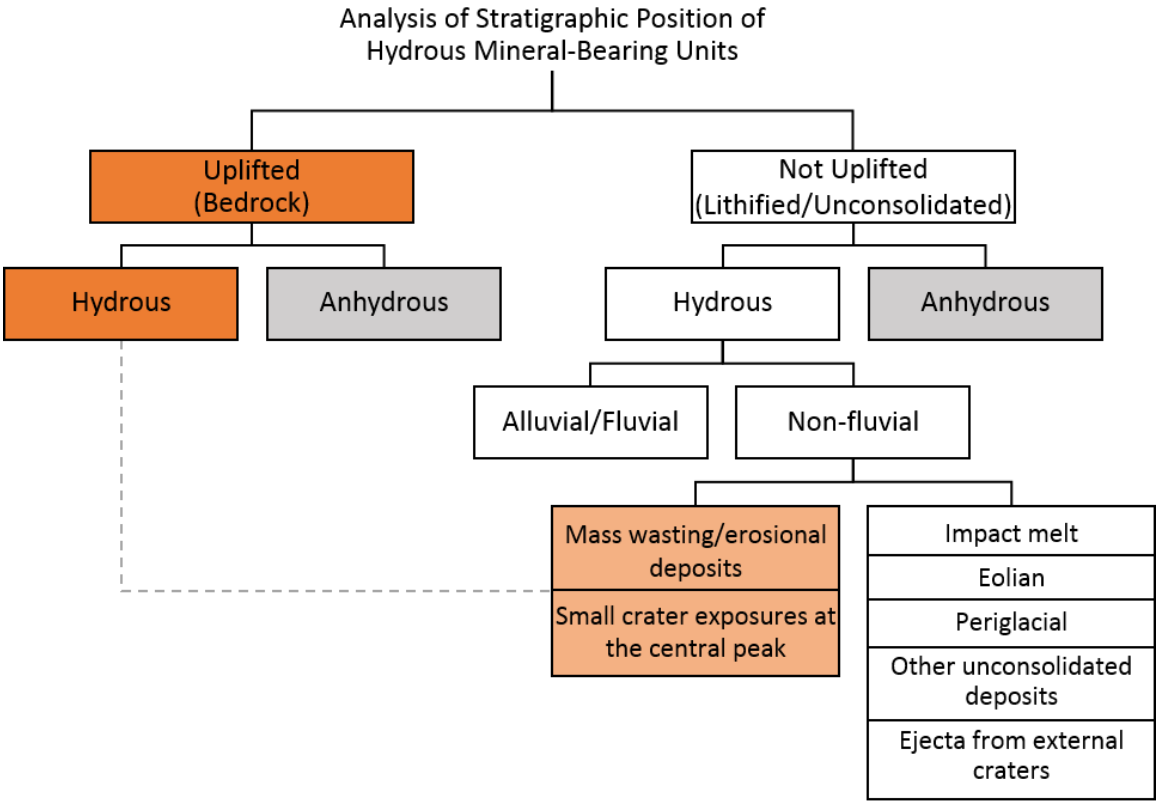

Figure 3. Schematic of the classification scheme for the geologic settings of central peak clays and other hydrous minerals. Grey (anhydrous) boxes represent central peak regions with no clear evidence in CRISM data for hydrous minerals; these craters were not studied further as part of this work. Directly uplifted bedrock is indicated in orange, and settings that can be indirectly linked to uplifted materials are indicated in light orange and by the dotted grey line (i.e. mass wasting/erosional deposits and small crater exposures at the central peak). See the text for a description of the characteristics that define each category (**Section 3.4**).

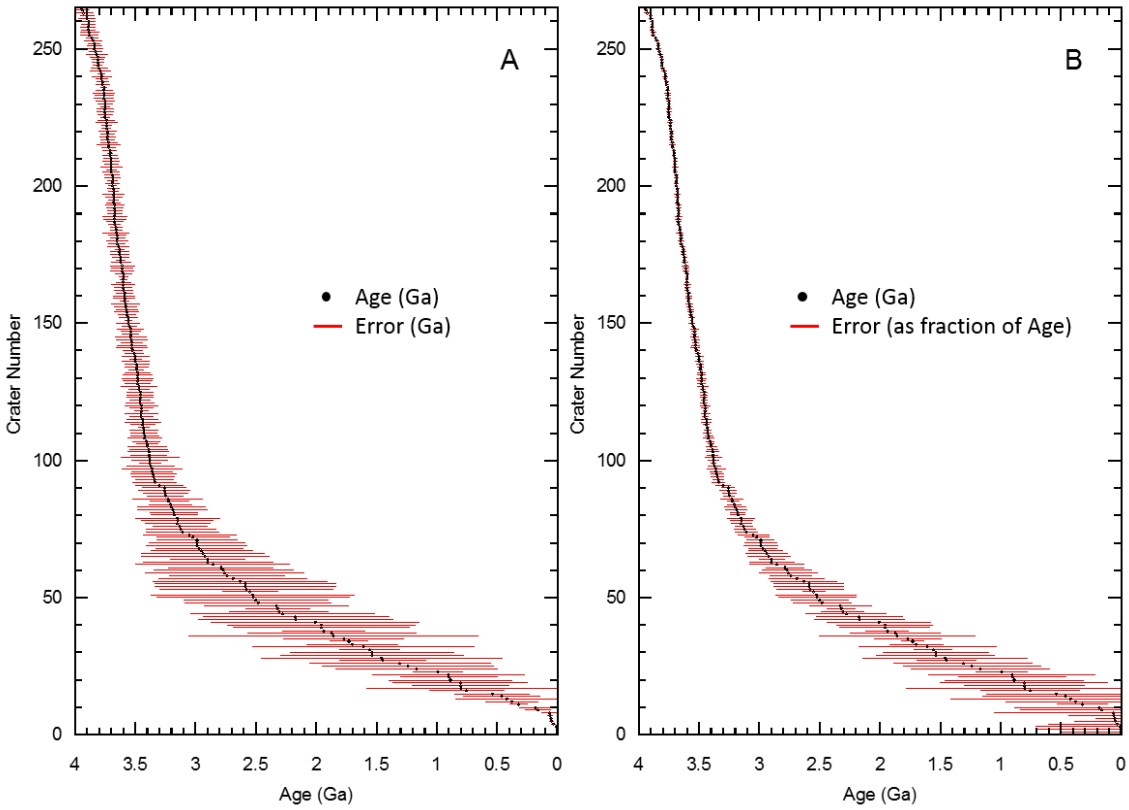

Figure 4. A) Crater count-derived ages and associated error bars [defined in Michael and Neukum, 2010] for each crater with hydrous minerals in the central peak region. We use the error towards older ages and mirror it on either side of each crater count age. We discard the younger error because our counts of small craters <0.5 km are incomplete, resulting in larger younger errors. The degree of crater count completeness below 0.5 km diameter varies for each host crater, thus younger errors are not comparable across our database. **B)** Crater count-derived ages and error bars calculated as a fraction of the associated age. This representation emphasizes the larger errors associated with younger craters. Crater names, with their corresponding number in this figure, are provided in the **Appendix B.**

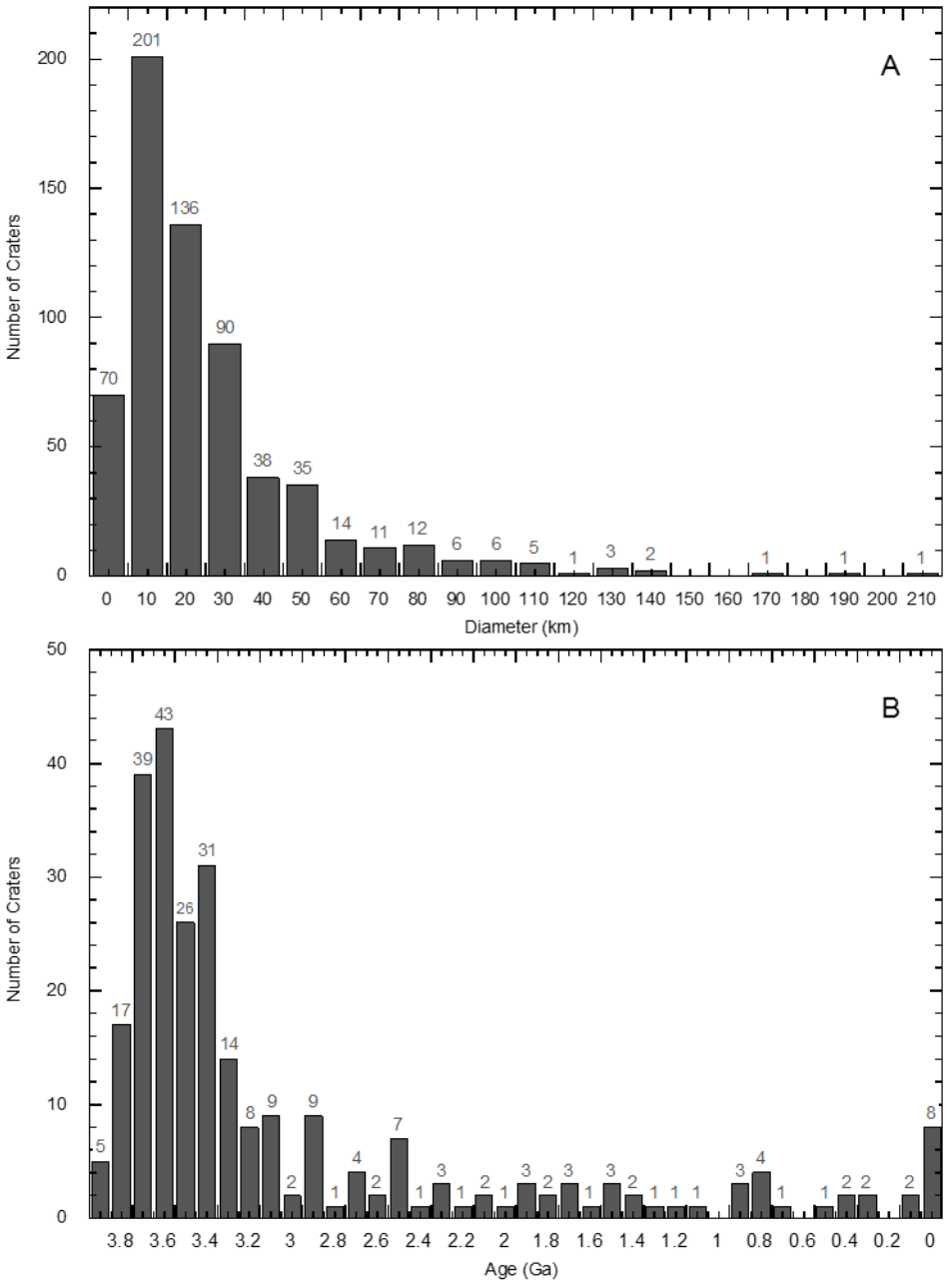

Figure 5. A) Size distribution of the 633 craters studied in this survey, showing a bias towards craters less than 30-50 km in diameter. **B)** Distribution of ages for the 265 craters with hydrous central peaks for which we have derived crater-count ages. Although most craters date to Noachian or Hesperian periods (~3.1 Ga or older), a number of craters in this study yield younger Amazonian ages (< 3.1 Ga).

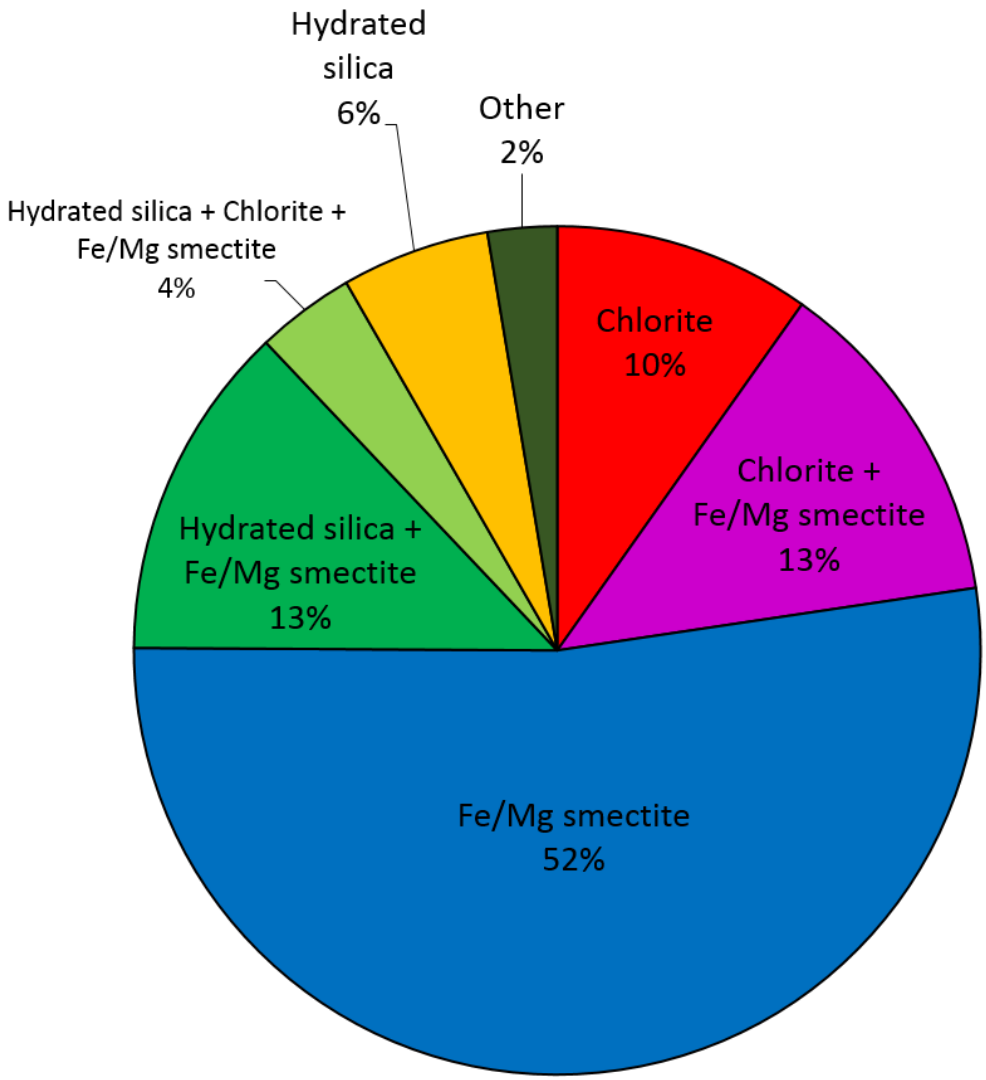

Figure 6. Occurrence of hydrous minerals as a percentage of central peak regions with hydrous minerals. Fe/Mg smectite, chlorite, and hydrated silica are the three most prevalent types of hydrous minerals and are found in 98% of the 265 central peak regions with hydrous minerals. Only 2% of central peak regions host other hydrous minerals (zeolites, sulfates, Al phyllosilicates, and unidentified hydrous phases) in the apparent absence of Fe/Mg smectite, chlorite, and/or hydrated silica. Each central peak falls into only one of the groups depicted in this chart.

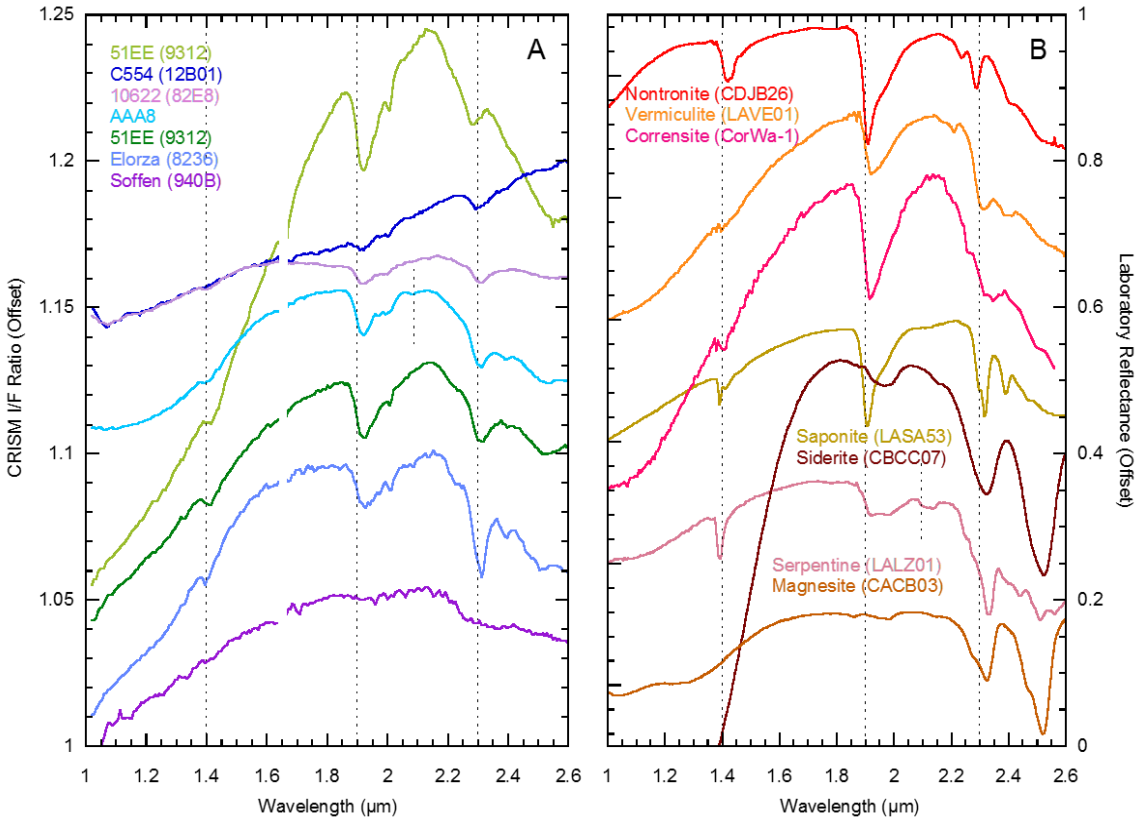

Figure 7. CRISM and laboratory reflectance spectra of select Fe/Mg clay minerals. **A)** CRISM spectra consistent with Fe/Mg smectites or mixed-layer clays. Spectra are labeled by IAU crater name when possible and/or by the targeted CRISM observation ID. **B)** Laboratory spectra of various Fe/Mg clay minerals, including smectite, serpentine, and mixed-layer clays (e.g., corrensite) as well as select carbonate minerals. Lab spectra were acquired from the CRISM and USGS spectral libraries and associated library IDs are in parentheses. Dashed lines indicate characteristic absorptions at 1.4, 1.9, and 2.3 µm, as well as a potential absorption at 2.1 µm for serpentine. Spurious features in CRISM data near ~1.65 µm are due to a filter boundary and are masked in this figure.

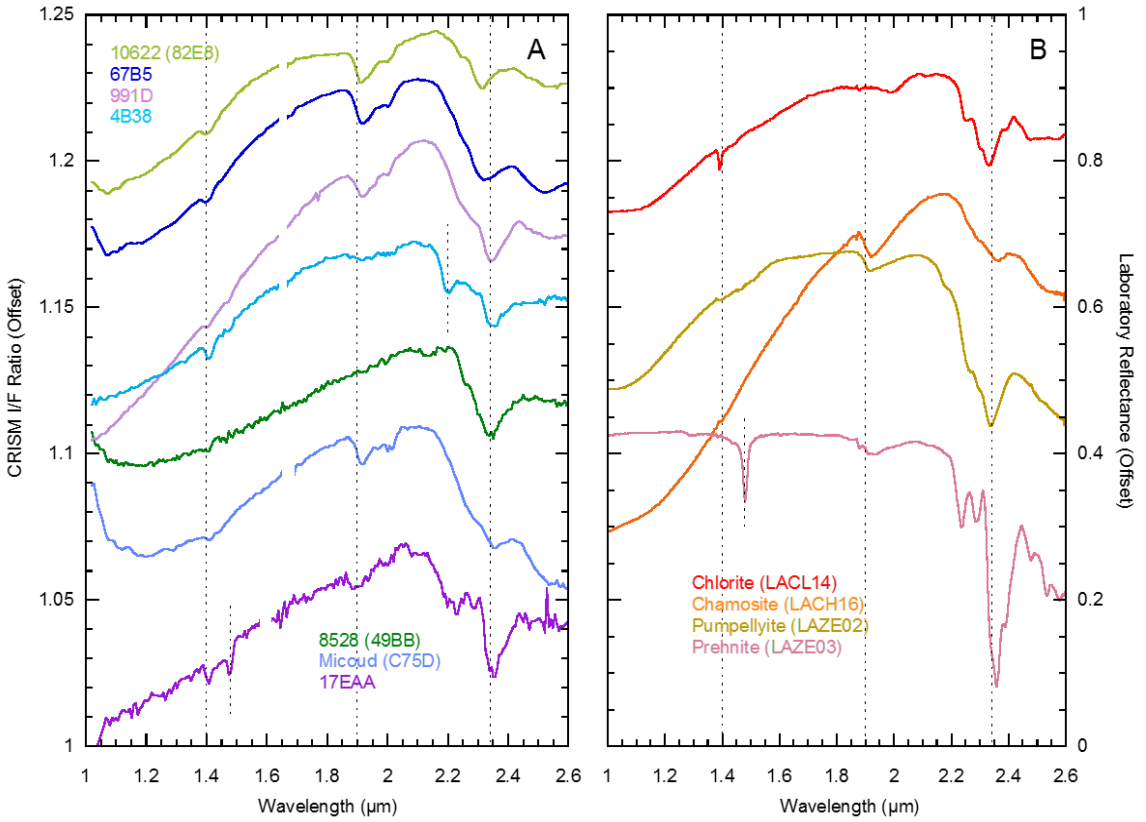

Figure 8. CRISM and laboratory reflectance spectra of select chlorite and higher-temperature minerals. **A)** CRISM spectra consistent with Fe/Mg-rich chlorite. Spectra are labeled by IAU crater name when possible and/or by the targeted CRISM observation ID. **B)** Laboratory spectra of select minerals with absorptions similar to those found in CRISM data presented in (**A**). Lab spectra were acquired from the CRISM spectral library and associated library IDs are in parentheses. Dashed lines indicate characteristic absorptions at 1.4, 1.9, and 2.34 µm. Shorter dashed lines indicate the 1.48 µm feature of prehnite, and a sharp Al-related absorption at 2.2 and 2.25 µm in the 4B38 CRISM spectrum. Spurious features in CRISM data near ~1.65 µm are due to a filter boundary and are masked in this figure.

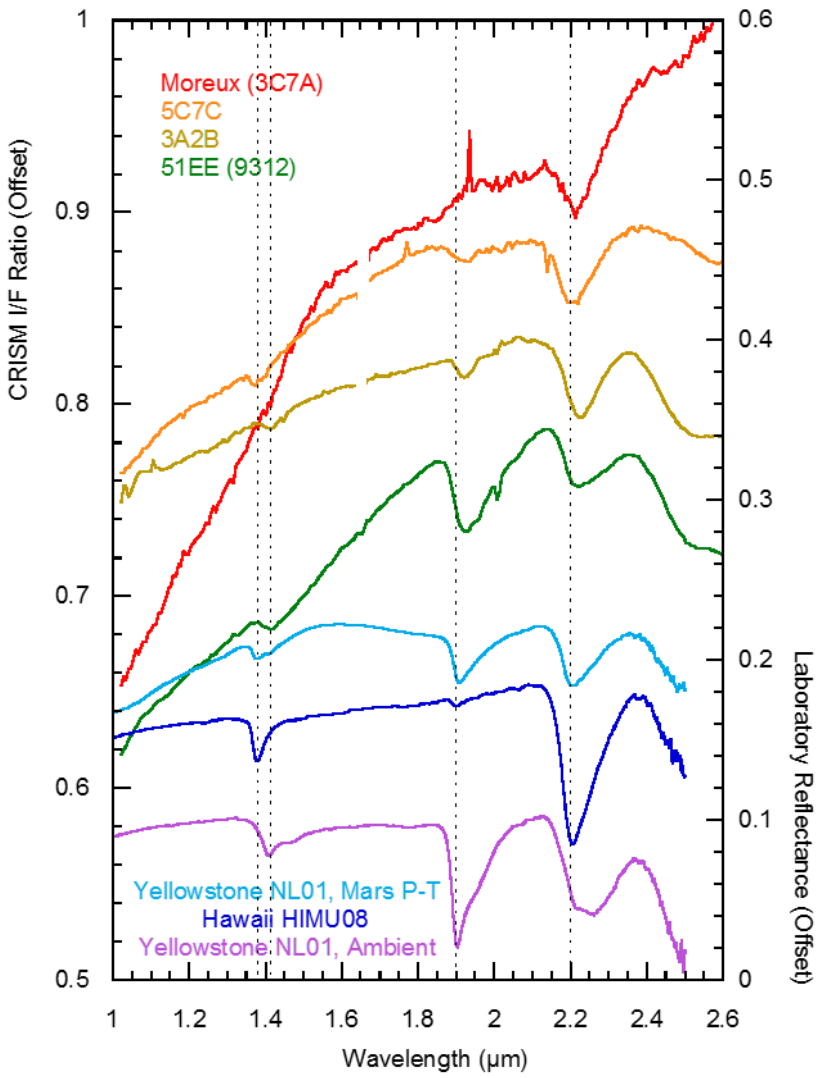

Figure 9. Examples of CRISM ratio spectra consistent with the presence of hydrated silica. Spectra are labeled by IAU crater name when possible and/or by the targeted CRISM observation ID. Laboratory spectra are presented for comparison and are for opal-bearing samples collected in Yellowstone National Park (sinter deposit collected near Nymph Lake, measured under ambient and Mars-relevant pressure and temperature) and Hawaii (altered basalt collected near Mauna Ulu). Dashed lines indicate characteristic absorptions at 1.38, 1.42, 1.9, and 2.2 μm. The Yellowstone sample contains less H_2O when measured under Mars-like conditions (light blue) compared with ambient conditions (purple) and compared with the Hawaii sample (dark blue). Note the variation in width and shape of the 1.4 μm feature due to different hydration states. Spurious features in CRISM data near ~1.65 μm are due to a filter boundary and are masked in this figure.

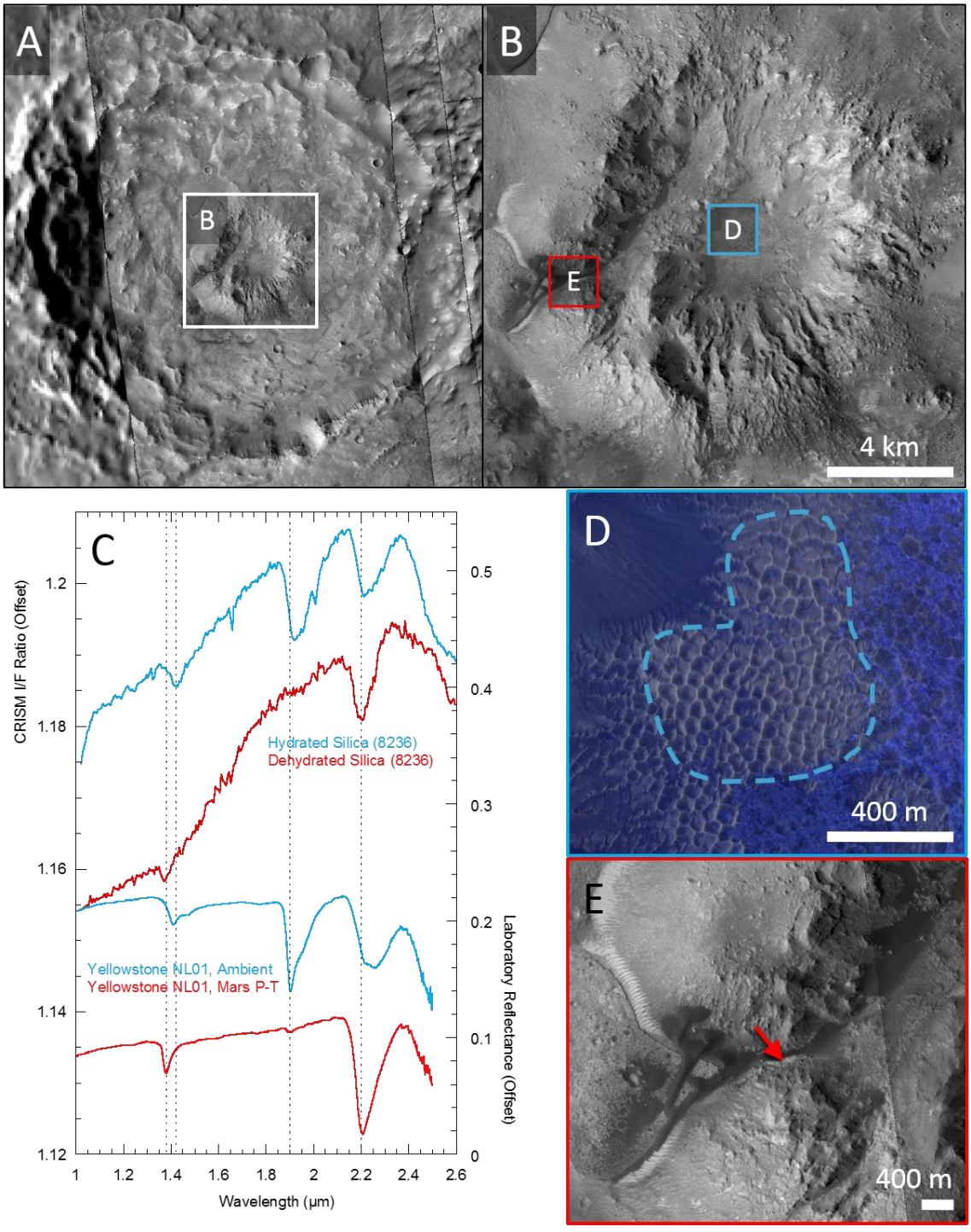

Figure 10. Examples of hydrated silica in Elorza crater (55.21°W, 8.74°S). **A)** CTX context image. **B)** Central pit of Elorza crater showing the close proximity of dehydrated (red) and hydrated (blue) silica. **C)** CRISM ratio spectra of dehydrated and hydrated silica at (FRT00008236) compared with laboratory spectra of Yellowstone sample NL01 acquired under ambient and Mars-relevant pressure and temperature conditions. This sample is dominated by opal-A. Dashed lines indicate absorptions at 1.38, 1.42, 1.9, and

2.2 μm. Note the shift in the 1.4 μm feature for both the CRISM and laboratory spectra of 'dehydrated' silica, which also has a weak to absent 1.9 μm H_2O absorption. **D)** Hydrated silica occurs in light-toned (likely dust-covered) eolian material (HiRISE image ESP_021551_1710), whereas **E)** the dehydrated silica appears to occur in bedrock (CTX image G09_021551_1712_XN_08S055W).

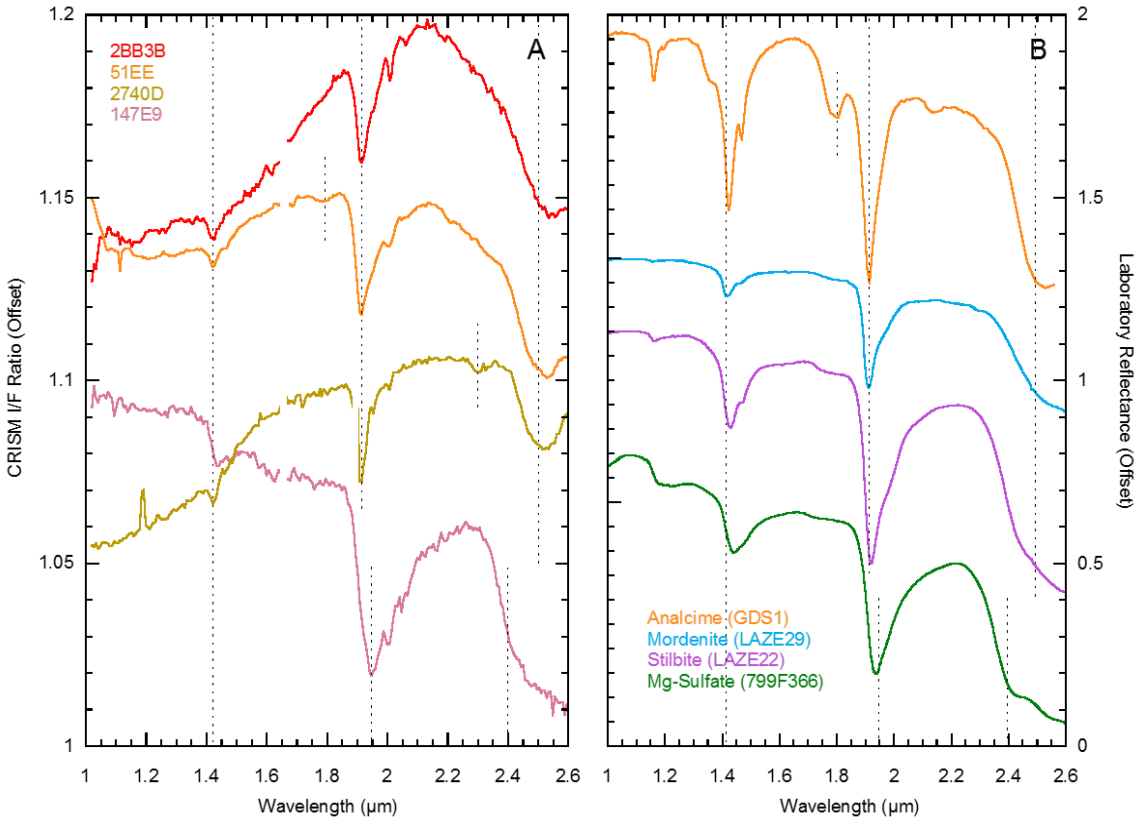

Figure 11. A) CRISM spectra consistent with zeolites or sulfates. Spectra are labeled by IAU crater name when possible and/or by the targeted CRISM observation ID. **B)** Laboratory spectra from the CRISM and USGS spectral libraries are also provided for comparison, with IDs in parentheses. Dashed lines indicate characteristic absorptions at 1.42, 1.91, and 2.5 μm for analcime, with a shorter dashed line indicating possible mixing with Fe/Mg smectite at 2.3 μm (2740D). For sulfate, dashed lines indicate absorptions at 1.42 and 1.95 μm and an inflection at 2.4 μm. Spurious features in CRISM data near ~1.65 μm are due to a filter boundary and are masked in this figure.

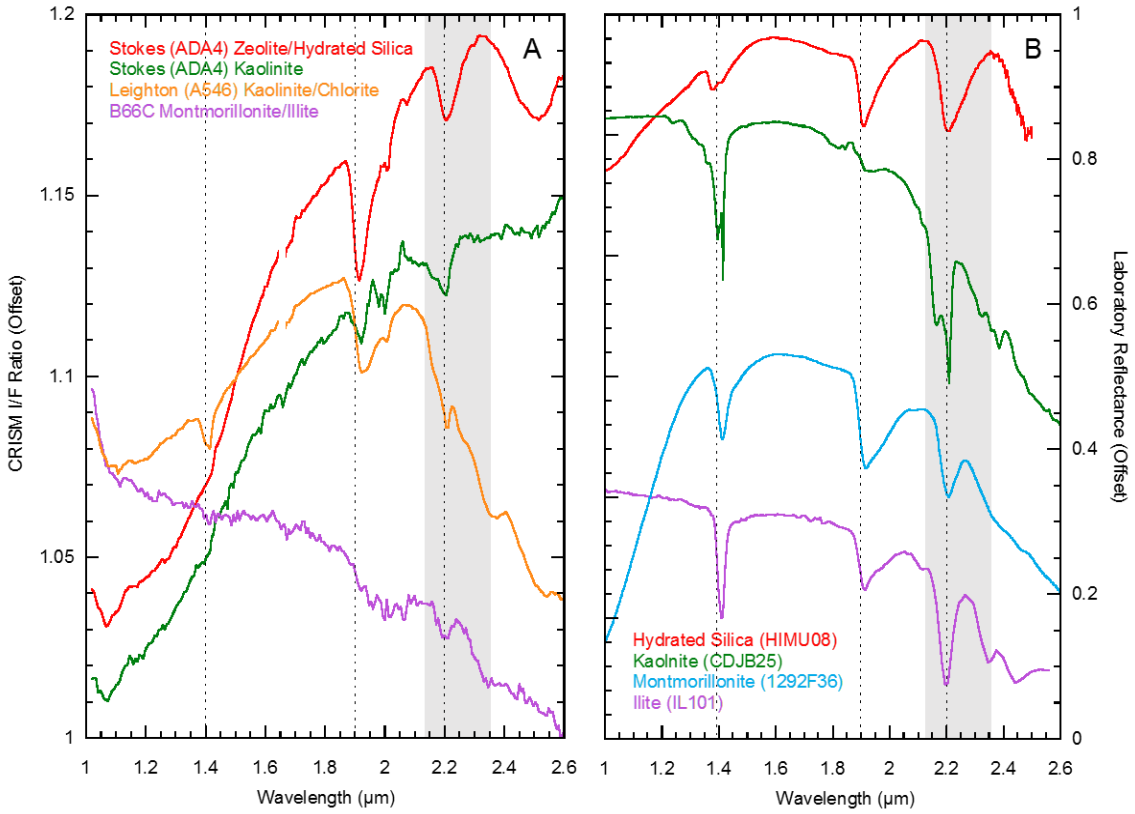

Figure 12. A) CRISM ratio spectra consistent with Al phyllosilicates and a hydrated silica spectrum for comparison. Spectra are labeled by IAU crater name when possible and/or by the targeted CRISM observation ID. Note that the Stokes hydrated silica spectrum may be mixed with zeolites. **B)** Laboratory spectra of select zeolites and clay minerals from the CRISM and USGS spectral libraries, with IDs in parentheses. Dashed lines indicate characteristic absorptions at 1.4, 1.9, and 2.2 μm. Grey regions indicate the width of the 2.2 μm absorption for laboratory hydrated silica and show that it is distinctly broader than the 2.2 μm feature found in Al-phyllosilicates such as montmorillonite and illite. Spurious features in CRISM data near ~1.65 μm are due to a filter boundary and are masked in this figure.

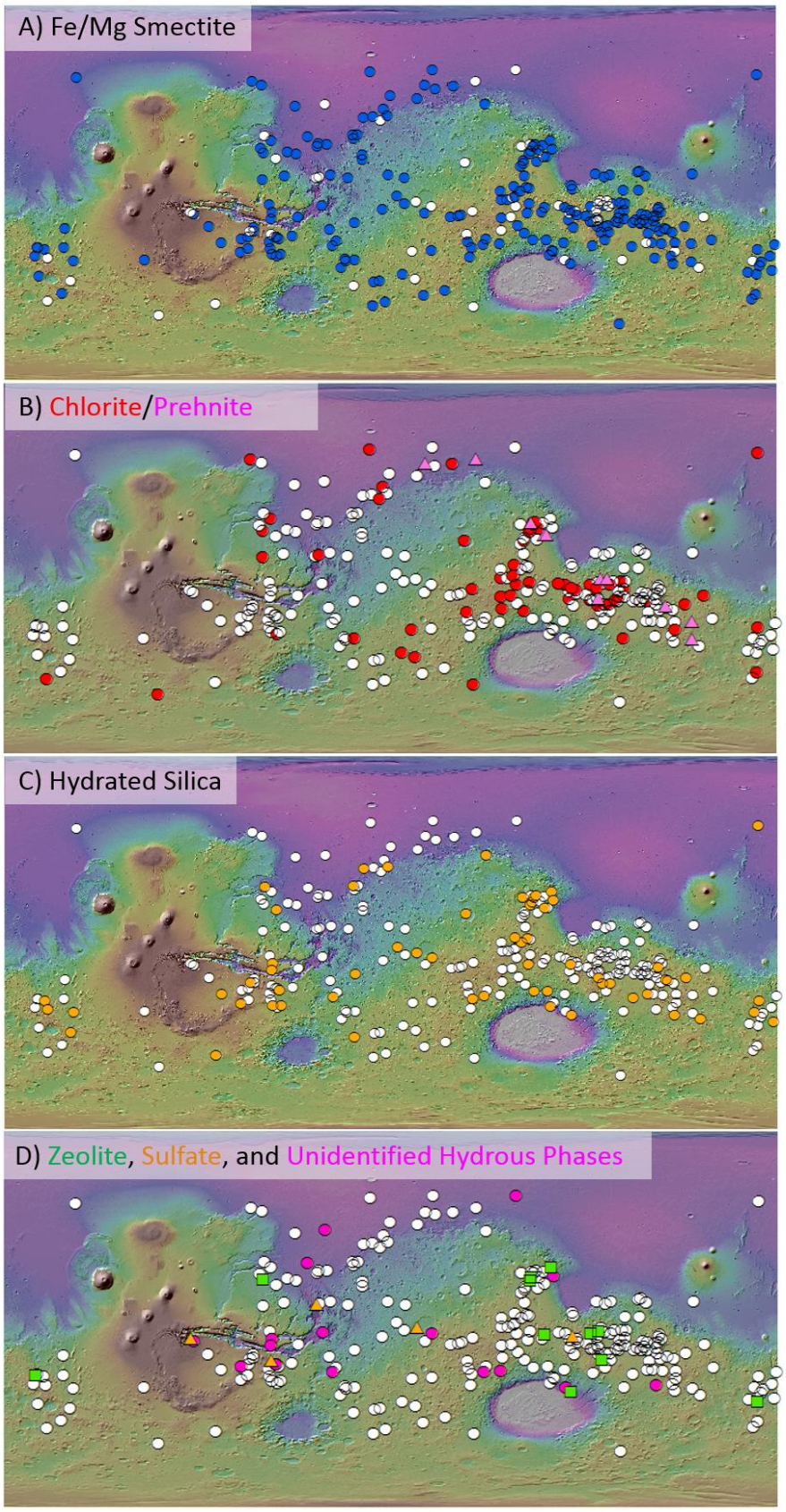
A) Fe/Mg Smectite
B) Chlorite/Prehnite
C) Hydrated Silica
D) Zeolite, Sulfate, and Unidentified Hydrous Phases

Figure 13. Global distribution of hydrous mineral groups for crater central peak regions. **A)** Fe/Mg smectite, **B)** chlorite (red) and prehnite (pink, in addition to chlorite), **C)** hydrated silica, and **D)** zeolite (green squares), sulfate (orange triangles), and unidentified hydrous phases (magenta circles) at central peaks. Colored symbols represent the presence of a specific hydrous mineral, while white symbols indicate hydrous central peaks that lack that the specified hydrous mineral group.

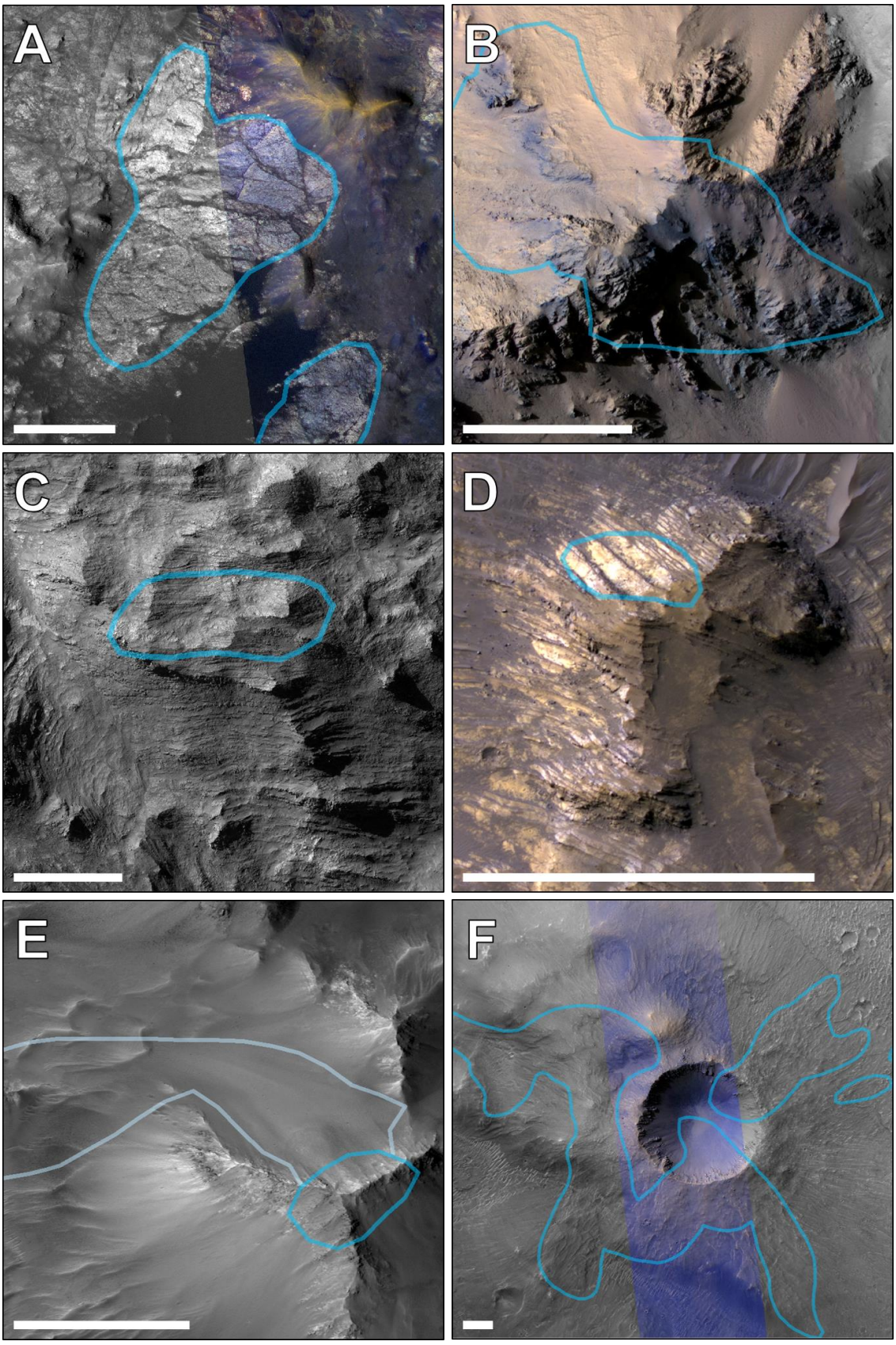
A
B
C
D
E
F

Figure 14. Archetypal examples of Fe/Mg smectites in uplifted bedrock: **A)** massive at crater 10763 (123.12°E, 10.56°S; ESP_012367_1695), **B)** poorly-stratified at Santa Fe (47.93°W, 19.26°N; PSP_009749_1995), **C)** dark-toned well-stratified at Mazamba (69.68°W, 27.53°S; ESP_033538_1520), and **D)** light-toned well-stratified at crater 16D57 (78.64°W, 23.15°S; ESP_016805_1565). Units inferred to represent uplifted material are **E)** mass wasting deposits at crater 12428 (147.66°W, 31.72°S; ESP_013155_1480) and **F)** in exposures from small craters that impact the central peak at crater 16A9E (56.32°W, 5.21°S; ESP_016725_1745). Scale bars indicate 300 m. Blue outlines highlight Fe/Mg smectite detections from CRISM data, and lighter blue outlines indicate weaker Fe/Mg smectite absorptions.

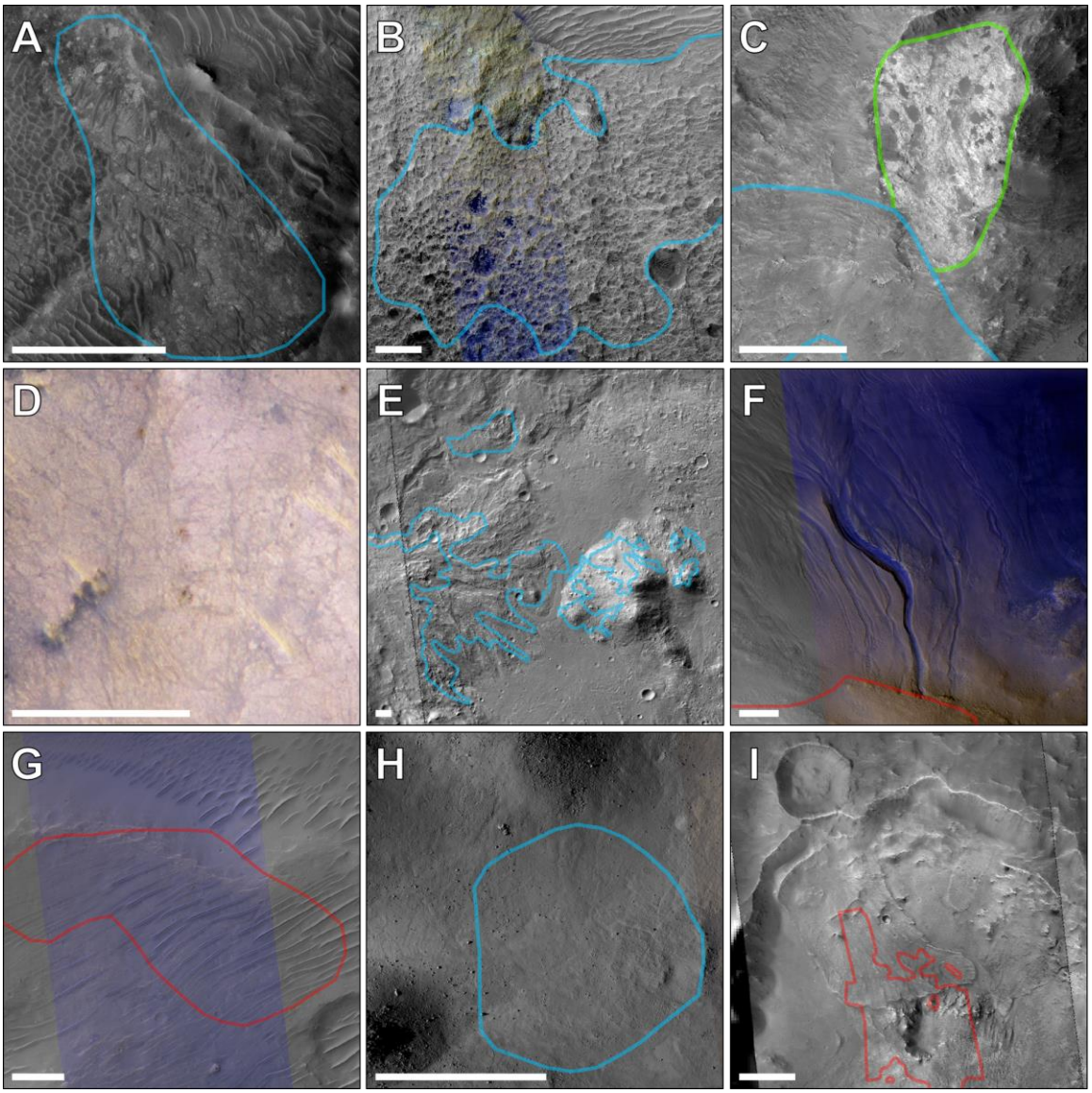

Figure 15. Archetypal examples of non-uplifted geologic settings where Fe/Mg smectites and chlorites are detected. Scale bars indicate 300 m unless stated otherwise for D, E, and I. Blue outlines highlight Fe/Mg smectite detections and red outlines highlight the presence of chlorite. Examples of Fe/Mg smectite-bearing impact melt show **A)** brecciation at crater 141DA (51.6°E, 1.2°N; ESP_014176_1810), **B)** pitting at Rayadurg (102.44°E, 18.45°S; PSP_006619_1615), **C)** draping morphology at crater C554 (62.64°E, 18.7°S; ESP_021639_1610), where green represents pyroxene-rich uplifted bedrock, and **D)** fractured, coherent units that drape and onlap bedrock at crater 27496 (64.83°E, 2.28°N; ESP_027586_1825); scale bar indicates 100 m. **E)** Example of an alluvial/fluvial setting at Runaga (102.44°E, 26.64°S; G21_026267_1534_XN_26S284W); scale bar indicates 1 km. **F)** Likely periglacial deposits at crater BF46 (95.74°E, 8.86°N; PSP_010260_2325). **G)** Unconsolidated deposits associated with eolian features at crater 1FC1F (96.59°E, 7.83°S; ESP_017260_1720), and **H)** in 'other sedimentary' deposits at crater 37AE (74.71°E,

24.65°N; PSP_001886_2050) that are not readily classified as any other geologic context. **I)** Ejecta and associated slump material due to a younger impact onto the rim of crater 67B5 (78.71°E, 5.62°S; P09_004365_1741_XI_05S281W); scale bar indicates 5 km.

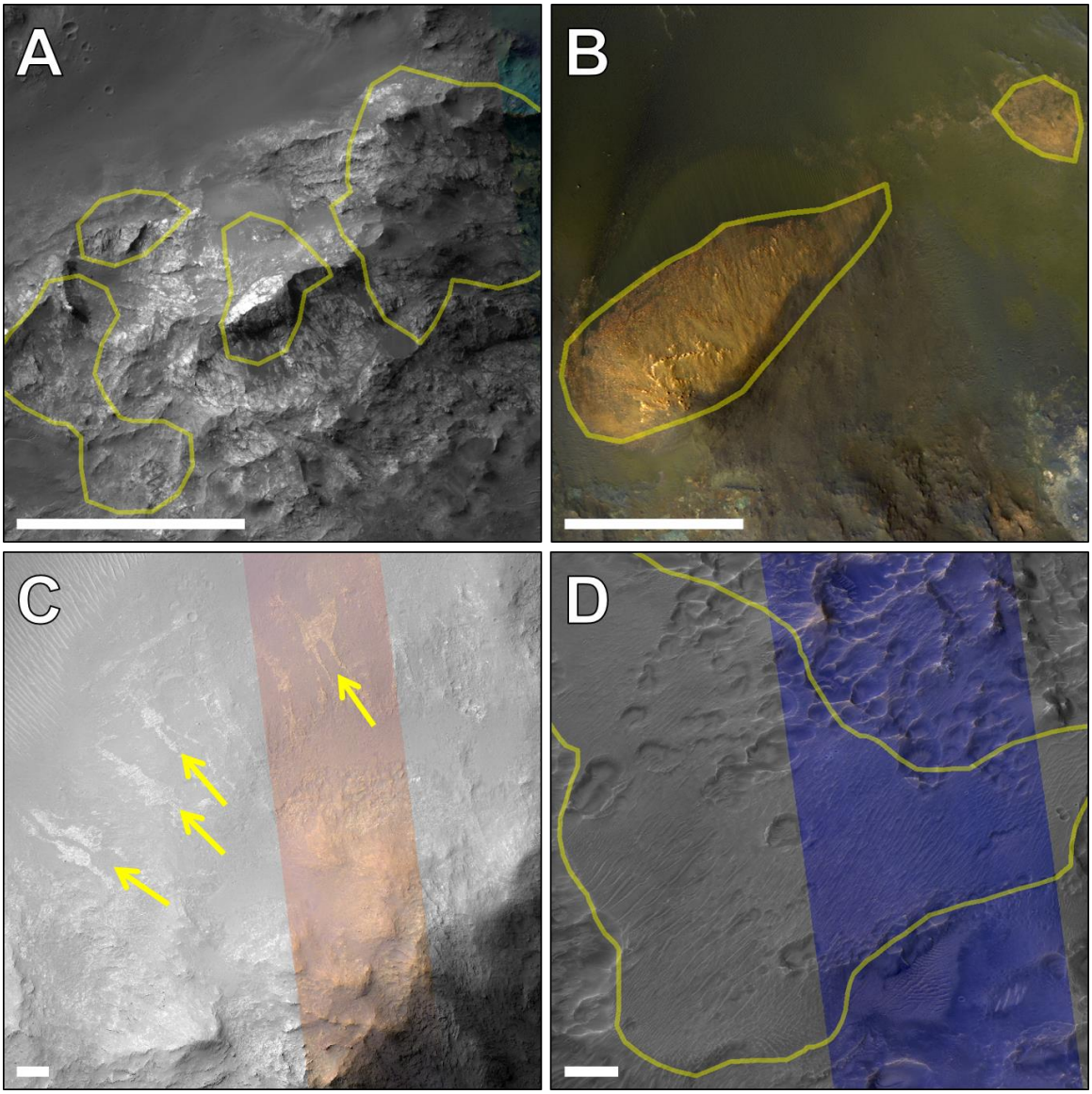

Figure 16. Examples of geologic settings unique to hydrated silica. Scale bars indicate 300 m. Yellow outlines highlight hydrated silica detections from CRISM data. **A)** Uplifted massive bedrock at Alga (26.67°W, 24.34°S; PSP_007573_1555). **B)** Uplifted poorly-stratified bedrock at crater 129FA (129.06°E, 16.9°S; ESP_013092_1630). **C)** Yellow arrows point to light-toned, fractured deposits that may be related to impact melt and that exhibit a flow-like morphology at crater 198FB (16.61°W, 13.98°S; PSP_007744_1660); the direction of the arrows indicate inferred downslope flow. **D)** Partially lithified deposits and superposing eolian deposits in the central peak region of crater 12428 (147.66°W, 31.72°S; ESP_013155_1480).

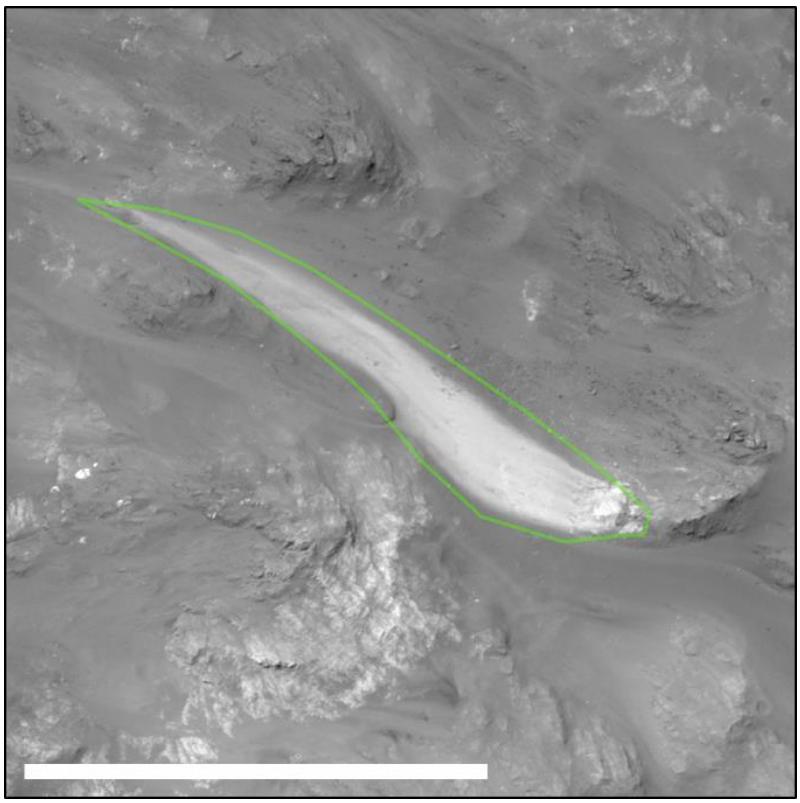

Figure 17. Example of a zeolite detection, outlined in green, at crater 9E58 (98.73°E, 18.49°S; ESP_015981_1615). Zeolite is typically found in association with light-toned unconsolidated deposits, some of which exhibit a morphology suggestive of mass wasting. Scale bars indicate 300 m.

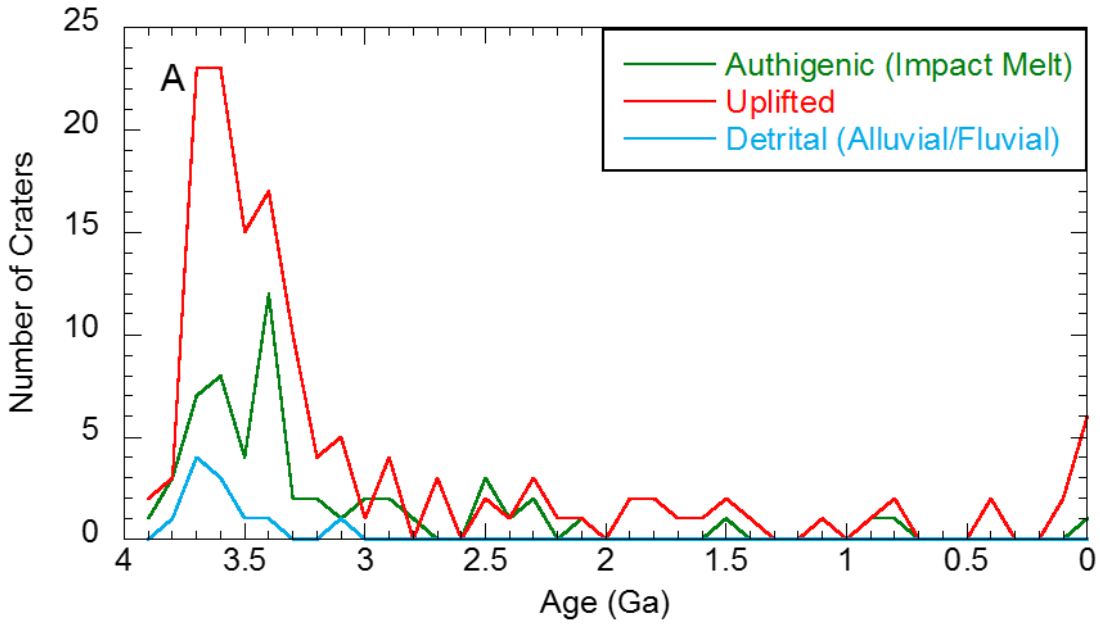

Figure 18. Distribution of clay occurrences in martian central peak regions as a function of age and as grouped by inferred origin.

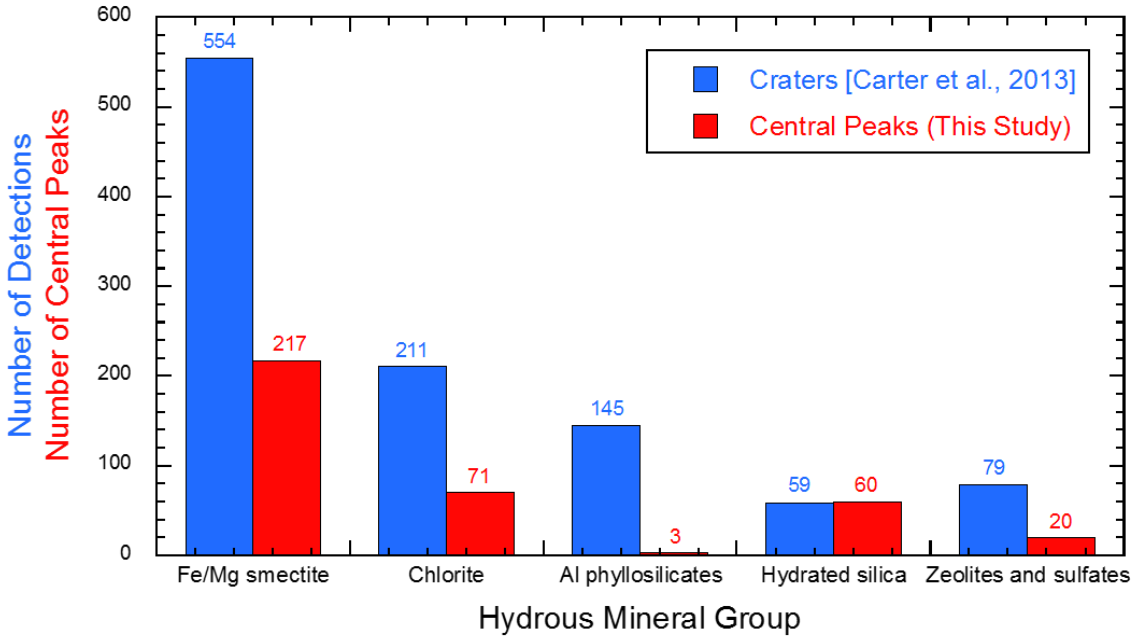

Figure 19. Histogram comparing the hydrous mineral distribution of Carter et al.'s [2013] crater survey with our central peak survey. Numbers for Carter et al.'s [2013] crater-related detections are estimated from Figure 16 of their paper. Note that the absolute numbers are not comparable across the two studies due to different measurement units, but the relative differences between mineral groups within each study can be

further assessed. Note the paucity of Al-phyllosilicate detections and relative increase in hydrated silica detections in central peak regions relative to crater settings as a whole. This is attributable to either geologic processes preferentially affecting central peaks or differences in methodologies between the two studies **(Section 7)**.

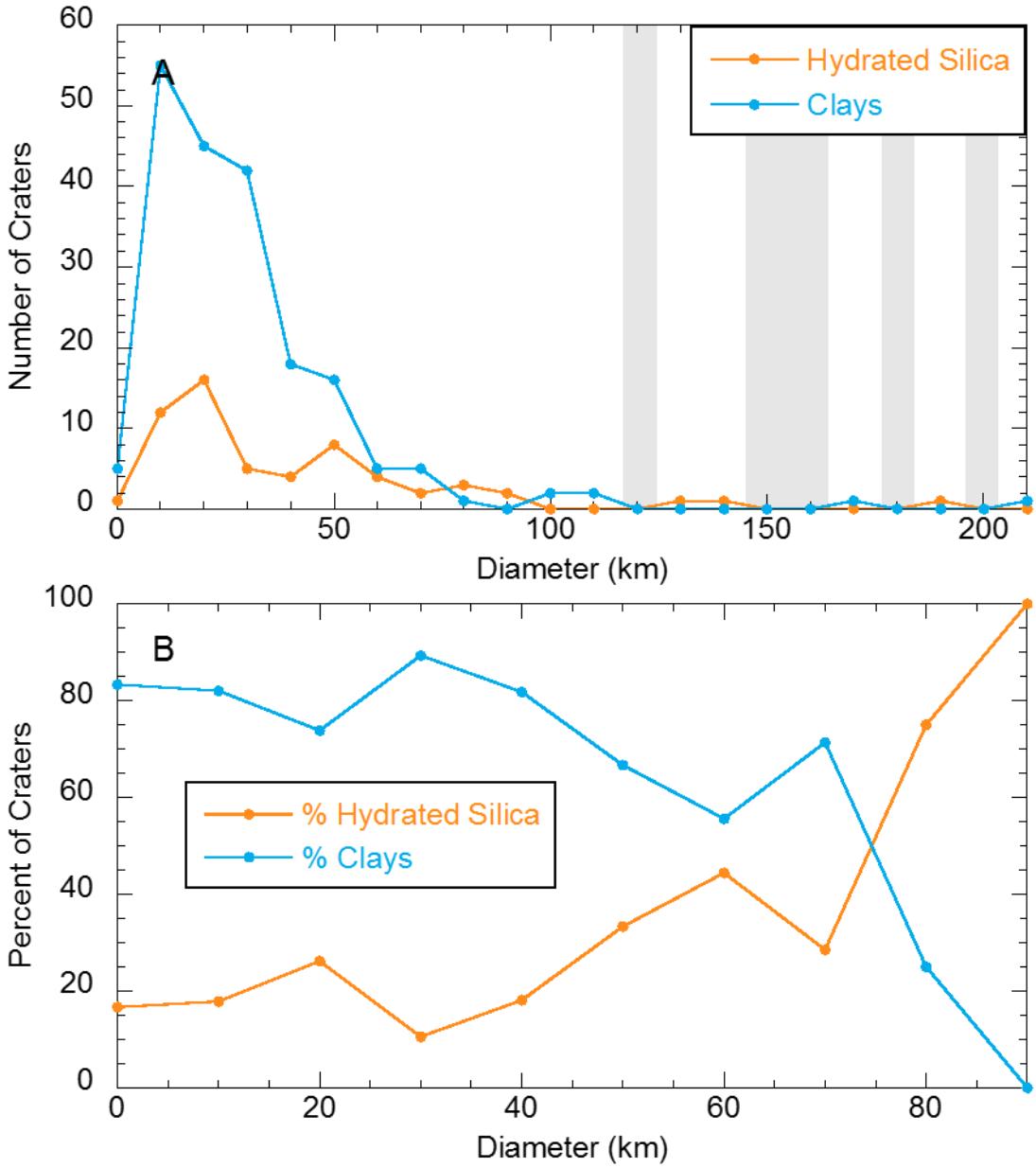

Figure 20. A) Distribution of central peak regions with occurrences of hydrated silica (orange) as a function of crater diameter, with the clay-bearing (blue) population of central peaks for comparison. Grey regions indicate where there are no craters in our survey. Note the occurrence of hydrated silica at larger craters >100 km. **B)** Distribution plotted as a percent of the total population of central peak regions with hydrated silica and clays. Note the increasing occurrence of hydrated silica at larger diameters relative to clay occurrences. Only craters <90 km in diameter are depicted here for clarity.

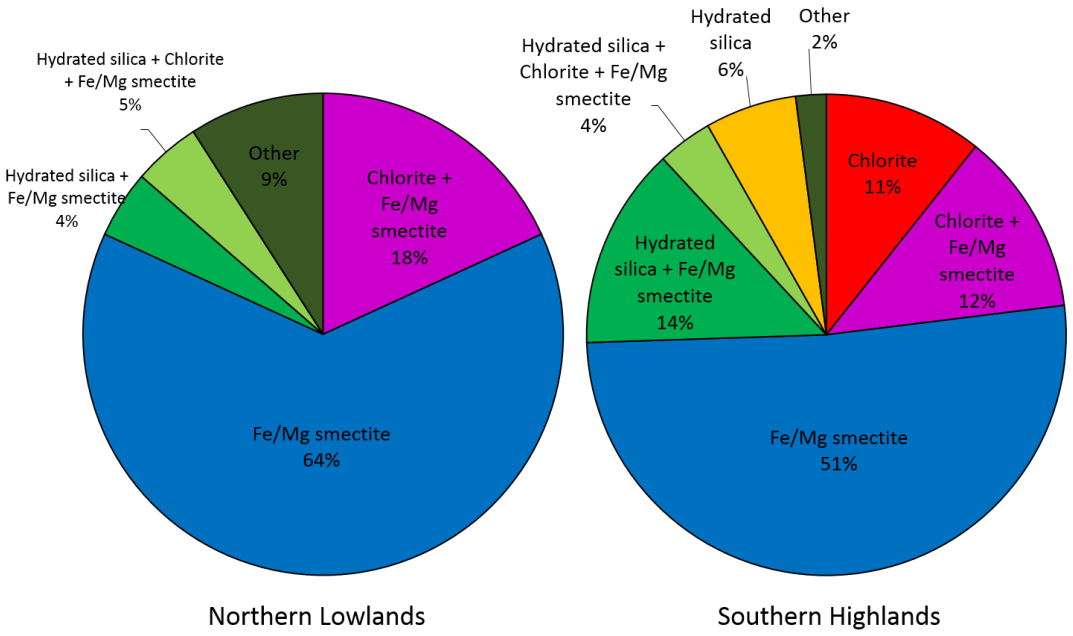

Figure 21. Hydrous mineral distributions for central peak regions in the northern lowlands versus those in the southern highlands.

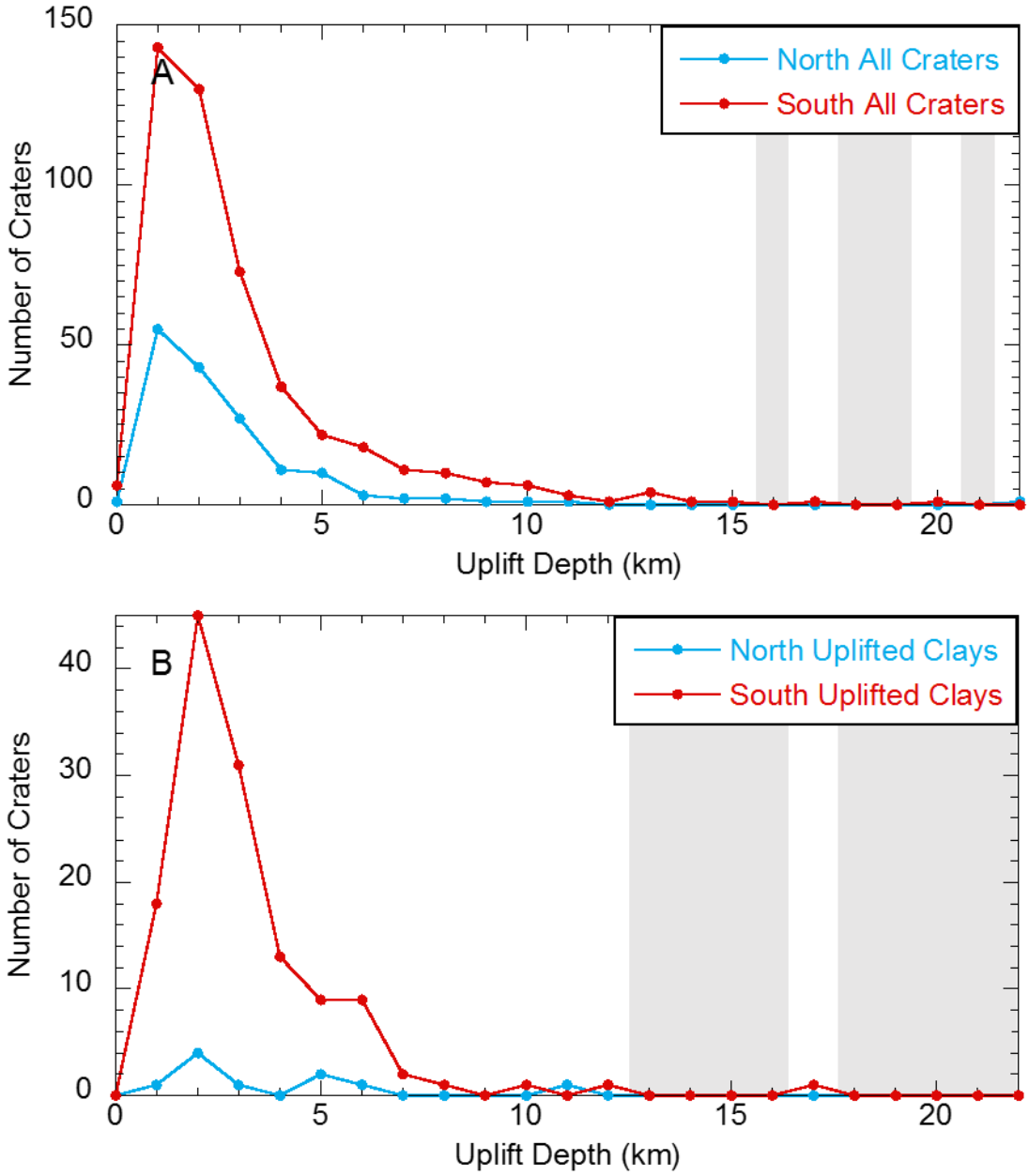

Figure 22. A) Distribution of inferred uplift depths for all craters in our survey, depicted separately as northern lowlands (blue) and southern highlands (red) craters. **B)** Distribution of uplift depth for all craters uplifting clay-bearing rocks, depicted separately as northern lowlands (blue) and southern highlands (red) craters. Greyed regions indicate where there are no craters in our study that sample those depths.

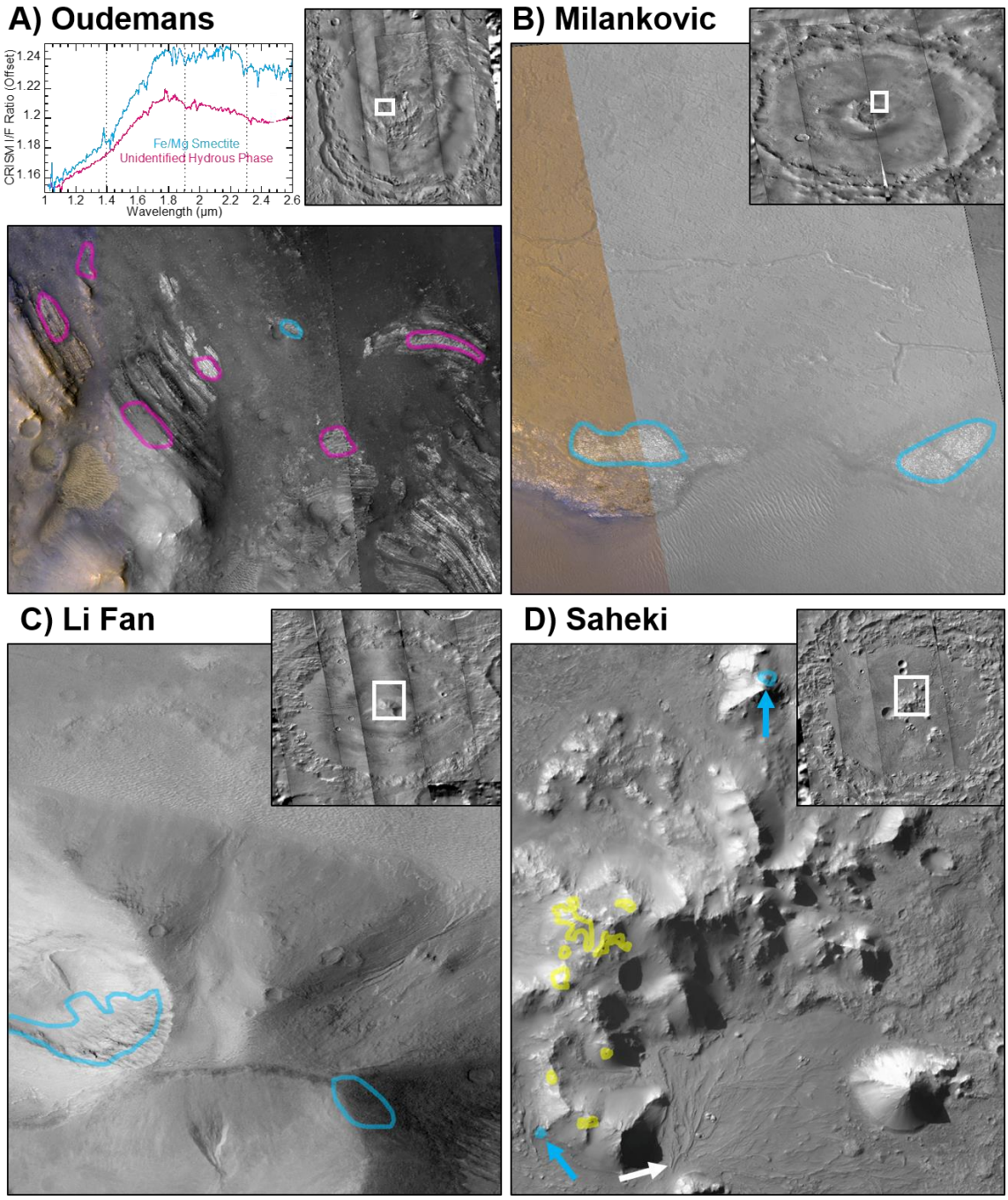

Figure 23. Examples of large craters with clay in central peak regions. **A)** 119 km Oudemans crater (91.77°W, 9.9°S; ESP_011676_1700). The only instance of Fe/Mg smectite (blue) is located in uplifted bedrock on the scale of tens of CRISM pixels, whereas the majority of uplifted units consist of an unidentified hydrous phase (magenta). The 2.3 µm absorption is more ambiguous than for other central peak detections due to the low signal-to-noise of these CRISM data. **B)** 111 km Milankovic crater (146.57°W, 54.49°N; PSP_009225_2350). Fe/Mg smectite (blue) is found in uplifted bedrock but is also detected in periglacial mantling elsewhere at the central peak. **C)** 102 km Li Fan

crater (153.04°W, 46.87°S; P08_004321_1317_XI_48S152W). Fe/Mg smectite (blue) is found in uplifted bedrock exposed by a smaller impact, but clays are also present in periglacial mantling materials. **D)** 84 km Saheki crater (73.18°E, 21.82°S; D01_027665_1591_XN_20S287W). The central peak structure largely consists of hydrated silica (yellow), and the only Fe/Mg smectite detections (blue) are spatially small and are found at the base of the central peak, where they may have been emplaced by the numerous fan deposits (e.g., white arrow) that cover the crater floor.

A

Uplift Depth (km)	Craters Uplifting Only Fe/Mg Smectite	Craters Uplifting Chlorite
0	0	0
1	15	4
2	40	6
3	23	8
4	7	5
5	3	8
6	3	5
7	0	2
8	1	0
9	0	0
10	1	0
11	1	0
12	1	0
13	0	0
14	0	0
15	0	0
16	0	0
17	0	1

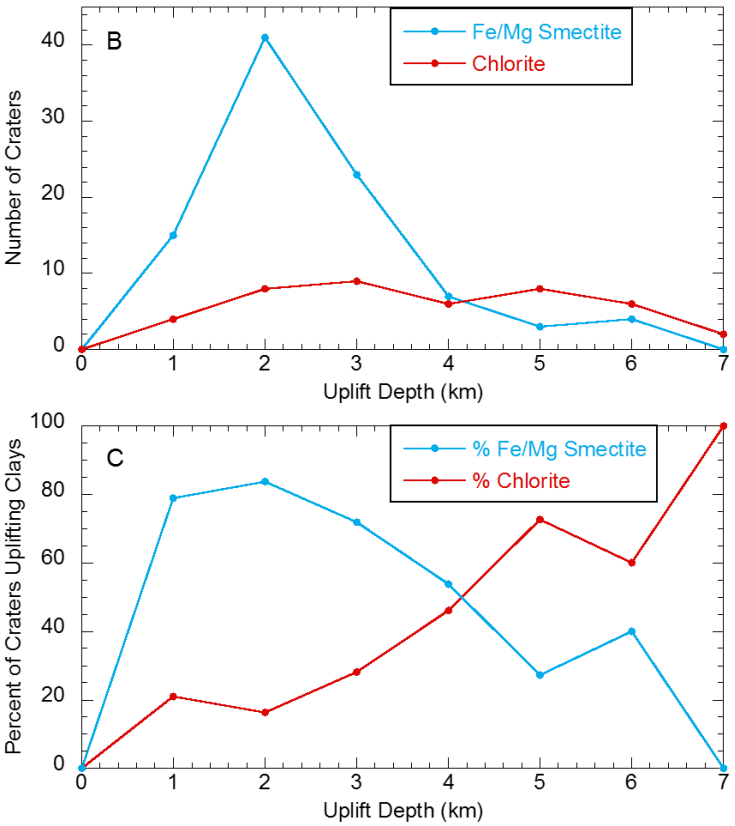

Figure 24. A) Table listing uplift depths, the number of craters that uplift only Fe/Mg smectite, and the number of craters that uplift chlorite. **B)** Distribution of craters as a function of uplift depth, with those that uplift chlorite (red) and craters that only uplift Fe/Mg smectite (blue). **C)** Distribution of craters as in B), but represented as percentages of the total population of craters uplifting clays (Fe/Mg smectite and chlorite). The plots in B) and C) only present data from craters uplifting up to 7 km depth in Table A), as these craters have conclusive evidence of uplifting clays. Observations from larger craters that uplift from deeper than 7 km depth are more ambiguous and may not necessarily indicate uplifted clays (see **Section 8.2** and **Figure 22** for more details on this point).

CHAPTER 3:

Mineralogy and Chemistry of Opal-Rich Samples from Mars Analog Sites and Implications for Rover Observations

Vivian Z. Sun[1],

Ralph E. Milliken[1], Kevin M. Robertson[1], Steve W. Ruff[2], Jack D. Farmer[2]

[1] Department of Earth, Environmental, and Planetary Sciences, Brown University, Providence, RI 02912, USA

[2] School of Earth and Space Exploration, Arizona State University, Tempe, AZ 85287, USA

To be submitted:

Summer 2017

Abstract

Determination of opaline silica's formation environments on Mars have largely relied on chemistry and accessory mineralogy. For example, acidic accessory minerals like jarosite and high Ti concentrations have been used to infer acid-sulfate leaching or other acidic processes at Gusev crater and Gale crater. However, at times these indicators may be inconsistent with other morphologic and geologic observations, requiring further determination of whether bulk chemical and mineralogic measurements alone can be representative of formation conditions. In this work we conduct a study of 135 opal-rich samples from fumarolic and hot spring environments in Hawaii, Yellowstone National Park, and New Zealand to determine if their bulk chemistry and mineralogy are uniquely diagnostic of their formation environment. Our results are generally consistent with previous literature in that acid-leached basalts from fumarolic environments contain acidic accessory mineral assemblages. However, Ti content does not appear to be uniquely diagnostic of acidic conditions, as many unaltered and altered, opal-rich basalts are observed to have overlapping Ti values. Interpretations are also complicated by inherently high Ti in Hawaiian basalts, and by relatively high Ti values in some sinter samples of up to 0.5 wt%. In conjunction with a previous report of 0.9 wt% TiO_2 in Icelandic sinter samples, this suggests that some of the high Ti levels reported by martian rovers are not necessarily indicative of acid-leached basalt. These results therefore suggest that chemical data must be interpreted in the context of other mineralogic, microtextural, and geologic observations.

1. Introduction

Opaline (hydrated) silica has been detected on Mars at all available scales of observation, including orbital spectroscopic data in the visible-near-infrared [e.g., Milliken et al., 2008; Skok et al., 2010; Smith and Bandfield, 2012; Sun and Milliken, 2015] and thermal infrared wavelengths [Bandfield, 2008], *in situ* observations by the Spirit [Squyres et al., 2008; Ruff et al., 2011] and Curiosity [Morris et al., 2016; Rampe et al., 2017] rovers, and high-resolution laboratory analyses of the Nakhla meteorite [Lee et al., 2015]. The widespread occurrence of this phase in a variety of geologic settings of disparate ages is further evidence of Mars' diverse aqueous history. It is well-understood that the progressive interaction of amorphous opal-A with water can allow it to convert into increasingly crystalline forms such as opal-CT, opal-C, and microcrystalline quartz [e.g., Siever, 1962; Williams and Crerar, 1985; Tosca and Knoll, 2009]. Examination of opal-rich materials therefore offers a metric to assess the degree of water-rock interaction for a given deposit. It is also known from the terrestrial rock record that silica phases are excellent preservers of microfossils and organic material, thus opal-bearing deposits on Mars may be of high astrobiological interest [e.g., Cady and Farmer, 1996; Konhauser et al., 2003; Ruff and Farmer, 2016] in addition to providing information about water availability through time [Tosca and Knoll, 2009; Smith et al., 2013].

Opal and other silica-rich phases are expected to be common products of silicate weathering, even on planetary bodies with basaltic crusts such as Mars [McLennan, 2003]. However, opaline silica can form under a wide range of geochemical conditions, and inferring its formation environment is often based on petrographic, textural, and chemical attributes as well as identification of accessory minerals. Occurrence with

minerals such as kaolinite, Fe-sulfates (e.g., jarosite), and Al-sulfate (e.g., alunite) can be indicative of acidic environments on Earth [e.g., Rodgers et al., 2002; Jones and Renaut, 2003] as well as on Mars [e.g., Milliken et al., 2008; Weitz et al., 2011; Wray et al., 2011; Ehlmann et al., 2016]. The chemistry of opal-rich materials is also relevant to investigations by the Spirit and Curiosity rovers, as the mobility of elements such as Ti, Zn, Ni, Mn, and Al relative to Si may be indicative of pH, redox, and other aqueous conditions [e.g., Jutras et al., 2009; Degryse et al., 2009; Galvez et al., 2012]. In particular, high Ti concentrations have been invoked to suggest acid-sulfate leaching at Gusev crater [Morris et al., 2008; Squyres et al., 2008] and leaching or deposition of mudstones under acidic conditions at Gale crater [Morris et al., 2016; Rampe et al., 2017].

Acidic and oxidative conditions are generally not favorable to preservation of biosignatures [Summons et al., 2011], and environments characterized by low pH and/or low water activity pose challenges for most life [Tosca and Knoll, 2009]. Thus being able to discriminate between diagenetic, lacustrine, fumarolic, hot spring, and other origins for individual martian opal deposits is of great importance for assessing their habitability and preservation potential. However, mineralogical and chemical measurements alone may not be sufficient to determine formation conditions of opal-bearing deposits. Comparable Ti enrichments can occur in both acidic and neutral-alkaline hot spring sinters [Preston et al., 2008], and modification by later diagenetic processes can affect relative elemental abundances and/or mineralogy. In the Pahrump Hills region in Gale crater, the co-occurrence of jarosite with apatite, a phase that readily dissolves at low pH, contradicts an acidic environment unless it was precipitated later during non-acidic conditions

[Rampe et al., 2017]. Silica enrichments at Gusev crater's Home Plate have also been attributed to acid-sulfate leaching based on measurements of bulk chemistry, but observations of porosity, microtexture, and stratigraphic context may be more consistent with sinter deposition [Ruff et al., 2011]. Ideally it is best to examine spatially resolved chemical and mineralogical information in conjunction with geologic context, including macro- and micro-textural observations. Ti enrichment in silica coatings and rinds, for instance, are considered an indicator of acid-sulfate leaching [e.g., Chemtob et al., 2010]. Unfortunately, the fine-scale spatial context of such elemental and mineralogical variations are not acquired in bulk rock and rock powder measurements made by rover instruments such as the CheMin X-ray diffractometer and Alpha Particle X-ray Spectrometers (APXS). In addition, diagnostic textural information observed at thin-section scale (or smaller) is not possible with current rover technology.

These complexities associated with silica formation and the limitations of current rover instrumentation make it necessary to understand how bulk chemistry and mineralogy of opal-bearing rocks and deposits may or may not be indicative of specific formation environments. In this study we examine a variety of opal-rich samples from potential terrestrial Mars analog sites, spanning acidic fumarole environments to neutral-alkaline hot springs, to determine if their bulk chemistry and mineralogy (including opal type) yield diagnostic indicators of their formation conditions. Such studies can provide a framework in which to interpret current and future rover data and help determine if chemistry and mineralogy are sufficient to constrain likely formation environments or if additional information is required.

2. Background

2.1 Formation and Diagenesis of Opals on Earth

On Earth, inorganic amorphous silica can precipitate in neutral-to-alkaline and acidic conditions under a range of water/rock ratios due to the relatively constant solubility of silica at pH<9 [Krauskopf, 1956]. As a result, opaline silica ($SiO_2 \cdot nH_2O$) is found in a variety of aqueous settings, including soils [e.g., Tokashiki and Wada, 1975], marine environments [e.g., Kastner et al., 1977], hot spring sinters [e.g., Jones and Renaut, 2003], and residues, rinds, and coatings in fumarolic environments [e.g., Morris et al., 2000; Rodgers et al., 2002; Lynne et al., 2006; Minitti et al., 2007; Chemtob et al., 2010]. The initially precipitated form is commonly amorphous (opal-A) and noncrystalline. With subsequent interaction with water, opal-A may undergo maturation through the Ostwald ripening process, in which repeated dissolution and reprecipitation forms progressively more crystalline silica varieties such as opal-CT (formation of discrete cristobalite/tridymite), opal-C (cristobalite), and microcrystalline quartz (e.g., chalcedony) [Siever, 1962]. The later stages of diagenesis favor preferential dissolution of tridymite and reprecipitation as cristobalite during the transition from opal-CT to opal-C, and it ends with slow precipitation of microcrystalline quartz [Williams et al., 1985; Williams and Crerar, 1985].

Opal types therefore carry different implications for the degree of water-rock interactions, and distinguishing between these different types provides information about environmental conditions beyond the simple presence or absence of water at a given point in time. Opal diagenesis requires a prolonged period of aqueous conditions and can be accelerated at higher temperatures [e.g., Mizutani, 1977; Herdianita et al., 2000a], thus

a particular opal type can indicate the chemical maturity and cumulative longevity of water-rock interactions in its formation environment. An environment that yielded opal-C, for instance, was likely subject to higher temperatures or more prolonged aqueous alteration than an environment that produced only opal-A. These relationships and the tradeoffs between time and temperature observed for terrestrial opals were conceptually applied to martian opal deposits by Tosca and Knoll [2009], who proposed that aqueous conditions were likely limited in Mars' history due to the prevalence of opal-A and the lack of more geochemically mature phases such as opal-CT and opal-C.

2.2 X-Ray Diffraction (XRD) Identification of Opal Types

Phase identification via XRD relies on characteristic diffraction patterns generated by the interaction of X-rays with the crystal structure of a target material. The resulting patterns are highly sensitive to mineral unit cell configuration and long-range order, thus XRD is best suited for identification of well-crystalline materials that produce prominent, sharp peaks rather than amorphous materials that diffract to produce broad, ambiguous "humps". Despite opal's generally amorphous nature, Jones and Segnit [1971] provided the first classification of opal-A/CT/C on the basis of observed XRD patterns.

All members of the opal family display a primary XRD feature centered at a d-spacing of approximately 4.1-4.0 Å (21.68-22.22˚ 2θ for CuKα), but the breadth and shape of this feature varies for different opal types **(Figure 1)**. Due to its highly disordered and amorphous nature, opal-A is characterized by a single broad peak or hump centered at approximately 4.0 Å and spanning 2.6-5.9 Å (or 15-35˚ 2θ). XRD patterns of opal-CT exhibit four narrow features, consisting of a primary peak at 4.13-4.06 Å (21.51-

21.89˚ 2θ), less intense tridymite shoulders at 4.32 and 3.9 Å (20.56˚ and 22.80˚ 2θ), and a weaker reflection at 2.50 Å (35.92˚ 2θ). Patterns for opal-C exhibit an even sharper peak at approximately 4.06-4.04 Å (21.89-22.00˚ 2θ) with weaker features present at 3.14, 2.95, 2.21, 2.02, and 1.93 Å (28.43, 30.30, 40.83, 44.87, 47.09˚ 2θ). The latter reflects an increase in ordering and the XRD pattern for opal-C is similar to that of α-cristobalite except for slight peak broadening from tridymite stacking disorder. Similarly, diffraction patterns of microcrystalline quartz appear much the same as those of quartz, with strong peaks at 4.26 and 3.34 Å (20.85 and 26.69˚ 2θ) [Jones and Segnit, 1971; Graetsch et al., 1994; Elzea and Rice, 1996; Campbell et al., 2001].

The continuous progression of opal-A to opal-CT to opal-C is reflected in the gradation of their diffraction patterns. Within the opal-A continuum, the d-spacing of the primary 4.1 Å peak increases with crystallinity [Lynne and Campbell, 2004]. For opal-CT/C, the ~4.1 Å peak position then decreases with increasing structural order, ranging from 4.12 Å for disordered opal-CT to 4.04 Å for well-ordered opal-C or cristobalite. For opal-CT and opal-C this d-spacing shift reflects the change from stacking that is dominated by tridymite (with its strongest reflection at 4.11 Å) to stacking dominated by cristobalite (4.04 Å) [Murata and Nakata, 1974; Mizutani, 1977; Kano and Taguchi, 1981; Graetsch et al., 1994]. However, the position of the 4.1 Å peak might not be effective for distinguishing opal-CT from opal-C due to both the lack of precision afforded by most instrumental capabilities and the lack of consensus on the exact XRD peak position at which opal-CT transitions to opal-C [Elzea and Rice, 1996; Campbell et al., 2001; Wilson, 2014].

A second indicator of opal type is the width of the 4.1 Å feature, which can be parameterized using the full width at half-maximum intensity (FWHM) with more ordered materials corresponding to smaller FWHM values. These values tend to be greater than 6.0˚ 2θ for opal-A and decrease sharply for opal-CT, which ranges between 0.5-1.7˚ 2θ, and opal-C, which ranges from 0.4-0.57˚ 2θ [Graetsch et al., 1994; Elzea and Rice, 1996; Herdianita et al., 2000ab]. When multiple species are present in a sample, the FWHM values tend to be intermediate between the individual opal component values [Campbell et al., 2001]. The overall shape of the 4.1 Å band is indicative of the proportions of cristobalite and tridymite, and the relative intensity of the contributing 4.32 Å peak can be used to infer tridymite content [Greenwood, 1973]. Additional measures of the relative proportions of opal-CT versus opal-C can be obtained from other weaker reflections and are discussed in detail by Guthrie et al. [1995]. Though interpretation and quantification may be complicated when mixed with other phases, XRD patterns thus provide a means to distinguish between opal types and to assess the relative degree of crystallinity of opal-bearing samples.

2.3 Accessory Mineralogy and Chemistry of Opal-Rich Environments

Because opals can form under a wide variety of aqueous conditions, characterization of accessory minerals and chemistry can provide a better understanding of environmental variables such as pH, water/rock ratio, and redox conditions during opal formation and/or diagenesis. Common accessory minerals associated with acidic opal-rich environments include kaolinite, Fe-sulfates (e.g., jarosite), Al-sulfates (e.g., alunite), iron oxyhydroxides, pyrite, sulfur, and poorly crystalline clays. In contrast, environments

with neutral to alkaline pH may contain calcite, Mg/Si-rich clays, and chlorides [Morris et al., 2000; Rodgers et al., 2002; Jones and Renaut, 2003; Guidry and Chafetz, 2003]. These accessory minerals can in turn affect opal genesis; Mg-rich carbonates expedite the opal-A to opal-CT transformation, whereas clay minerals may have an impeding effect [Greenwood, 1973; Kastner et al., 1977; Williams and Crerar, 1985].

The aqueous history of a rock or sediment can be derived in part from the mobility or immobility of certain elements at specific pH, water/rock, and redox conditions. In general, alkali and alkaline earth elements are considerably more mobile than higher-valence elements such as Ti, Al, and Fe^{3+}, particularly at low pH [Nesbitt and Young, 1989]. Ti and Al are considered immobile at pH ranging from 2-14 and 4-10, respectively [Young and Nesbitt, 1998], and their concentrations can be used to diagnose if conditions were highly acidic [e.g., Jutras et al., 2009]. Iron solubility is redox- and pH-dependent; in an oxidizing environment, Fe^{3+} solubility increases at pH<3 but will remain or precipitate as Fe^{3+} within a narrow pH range of 3-4 [Morris et al., 2000; Minitti et al., 2007]. Other elements of interest are Zn, Ni, and Mn, which are mobile at pH<6 and, in the case of Mn, redox-dependent [Degryse et al., 2009; Rampe et al., 2017]. As an example of how elemental chemistry can be linked to formation conditions, it has been observed that silica coatings on Hawaiian basaltic rocks are enriched in Fe and Ti but poor in Al. This may be indicative of oxidizing conditions and a pH slightly above 3, which allows Al to be leached away while retaining Fe and Ti in the rock [Minitti et al., 2007; Chemtob et al., 2010; Seelos et al., 2010].

By analogy, observed depletions and enrichments of these and other elements in martian opal-bearing deposits may help pinpoint environmental conditions, and Al, Fe_{total},

Ti, Zn, Ni, and Mn are all measured and reported by APXS instruments on the Spirit, Opportunity, and Curiosity rovers [Squyres et al., 2003; Thompson et al., 2016]. Based on its relative immobility, elevated Ti concentrations measured by rovers for certain high-silica materials, for example, have served as a basis for inferring local acidic conditions on Mars. Passive Ti enrichment (~1.5 wt%) resulting from acid-sulfate leaching has been invoked for opal-A detections by the Spirit rover at Home Plate, Gusev crater and compared with present-day processes in Hawaii [Morris et al., 2008; Squyres et al., 2008]. At Gale crater, it has been suggested that lacustrine sediments with jarosite (up to 3.5 wt% in bulk rock) and high Ti (up to 1.57 wt%) may have been deposited under initially acidic conditions that later transitioned to more neutral-alkaline pH levels [Rampe et al., 2017].

However, this interpretation is non-unique and Ti enrichment alone may not be sufficient to indicate formation environment, as elaborated in Ruff et al. [2011] and Rampe et al. [2017]. Indeed, comparable levels of Ti have also been observed in acidic and neutral-alkaline hot spring sinters from Iceland and New Zealand, although acidic sinters tend to have higher Ti than alkaline counterparts [Preston et al., 2008]. Titanium solubility can also be enhanced by complexing with P and organic matter under reducing and acidic conditions [Pe-Piper et al., 2011; Galvez et al., 2012], providing further evidence that Ti abundance alone may not be diagnostic of pH during formation and/or diagenesis. Interpretations of acidic conditions for silica-bearing rocks in Gusev and Gale may also be at odds with the geologic context and morphology of these deposits. For instance, leaching processes should lead to porosity loss and overprinting of microtextures and fine-scale laminations, but these features have not been observed in the

materials at Gusev crater [Ruff et al., 2011] or Gale crater [Grotzinger et al., 2015]. A goal of this study is to characterize the chemical and mineralogical properties of opaline materials formed in hot spring and volcanic fumarole environments to evaluate the extent to which these properties yield information that is diagnostic of these settings.

3. Overview of Sampling Locations

Samples examined for this study were collected at various sites from Hawaii, Yellowstone National Park, and New Zealand. Sample locations include modern acid-sulfate fumaroles and acidic to neutral-alkaline hot springs that have been proposed as possible ancient martian environments, particularly for silica-enriched deposits observed in Gusev crater [e.g., Morris et al., 2008; Squyres et al. 2008; Ruff et al., 2011]. We highlight the mineralogy and chemistry reported at these locations and their hypothesized formation processes and refer the reader to the cited works for more extensive descriptions of the overall geologic settings of these sites.

3.1 Hawaii

Hawaii has long been favored as a Mars analog site by virtue of its basaltic composition, long history of volcanic activity, and water-rock interaction of mafic protoliths (including under acidic conditions via fumarolic or solfataric alteration) [e.g., Allen et al., 1981; Morris et al., 2000]. Amorphous or opaline silica occurring as coatings and/or rinds on basaltic rocks has been observed at a variety of locations [Minitti et al., 2007; Seelos et al., 2010; Chemtob et al., 2010]. The sampling locations that we describe here include the Ka'u Desert, Mauna Loa, Mauna Ulu, as well as the Sulphur Banks and

the Steam Vents locations within Hawaii National Park. Hand samples and reflectance spectra (to be described in a companion paper, Sun et al., 2017) were during a January 2012 field visit.

The semiarid Ka'u Desert is often studied due to its young surface (<1000 years) and acid-sulfate leaching processes enabled by sulfuric gases from the nearby Kilauea volcano [Schiffman et al., 2006]. Altered basalts at this location exhibit surficial coatings enriched in silica, Al-phases (e.g., allophane, imogolite, disordered gibbsite, halloysite) [Curtiss et al., 1985], and Fe/Ti-minerals (e.g., anatase, rutile) [Seelos et al., 2010; Chemtob et al., 2010]. Hypotheses for the formation of opaline silica range from dissolution and precipitation [Curtiss et al., 1985] to acid-sulfate leaching for samples bearing jarosite [Chemtob et al., 2010].

The adjacent Mauna Loa volcanic environment produces similar thin, grainy silica-rich (>80% SiO_2) coatings that have a substantial Al-component (7% Al_2O_3) [Farr and Adams, 1984]. Materials at Mauna Ulu also exhibit fumarolic alteration that produces silica-rich coatings elevated in Al and Fe [Chemtob and Rossman, 2014] or in Fe and Ti [Minitti et al., 2007; Chemtob et al., 2010]. These enrichments are accompanied by the depletion of more mobile elements (e.g., K, Ca, Mg, and Na) that is considered a hallmark of acidic leaching processes. Other reported secondary minerals associated with this alteration include hematite, anatase, sulfur, sulfates, and akaganeite [Mathews, 1983 BS thesis; Morris et al., 2000; Chemtob et al., 2010].

The Sulphur Banks and Steam Vents sites are situated next to the Kilauea caldera and thus subject to acid-sulfate leaching and solfataric alteration [Payne and Mau, 1946]. These processes produce a wealth of alteration products including opal, sulfur, sulfates

(e.g., gypsum), Al-phases (e.g., kaolinite, halloysite), and Fe-oxides (e.g., hematite, goethite). Samples from the Sulphur Banks tend to be volatile-rich and heavily oxidized, and leaching causes passive enrichment in Fe, Ti, and P with varying Al whereas other elements are depleted [Morris et al., 2000].

In summary, the samples collected from the Hawaii sites are expected to be reflective of acid-sulfate alteration of basaltic parent material, with the exception that some vents sampled at the Steam Vents location exhibit non-acidic pH measurements.

3.2 Yellowstone National Park

Yellowstone is home to a variety of acidic or alkaline hot spring environments that host abundant microbial life. Opals commonly form from dissolution of the rhyolitic country rock and may encase and preserve microfossils [e.g., Walter and Des Marais, 1993; Cady and Farmer, 1996; Guidry and Chafetz, 2003]. Samples examined in this study come from locations at Octopus Spring, Rabbit Creek, Nymph Lake, Sentinel Meadow, and Steep Cone that were sampled in July 2010.

Octopus Spring is an alkali-chloride hot spring with pH~8 and temperatures in the 60-90°C range. Previous studies indicate that opal-A dominates the mineralogy here (up to 82.3% Si), in addition to cristobalite and detrital quartz [Bishop et al., 2004]. However, a single sample has been documented with opal-CT, smectite, and minor amounts of ilmenite, rutile, and hematite [Kyle and Schroeder, 2007].

The Rabbit Creek location is primarily alkaline with a pH of 9-10 and temperatures ranging from 70-80°C. Opal-A has been observed extensively at these locales, along with small amounts of quartz, cristobalite, and tridymite; only one

occurrence of opal-CT/C is noted and co-occurs with kaolinite [Vitale, 2002 MS thesis]. However, some areas can reach more acidic pH (3-5) and are documented as containing opal-A, opal-CT/C, quartz, volcanic glass, kaolinite, halloysite, hematite, amorphous gibbsite, and minor ilmenite [Hanna, 2003 MS thesis].

Less mineralogical information has been reported for the remaining Yellowstone sites. Nymph Lake is an acidic hot spring environment with a temperature of approximately 25°C, and much of the acidity comes from the Nymph Creek (pH ~3) that feeds into the lake [Nordstrom et al., 2005; Ball et al., 2008]. Hot springs at Sentinel Meadow range in pH from 7-9.5 and temperatures can exceed 80°C [Meyer-Dombard et al., 2005]. Steep Cone is an alkaline hot spring co-located with Sentinel Meadow and thus has similar characteristics, with pH upwards of 7-8.6 and temperatures reaching >75°C [Inagaki et al., 2001; Ball et al., 2008]. In contrast to the Hawaiian fumarolic sites described above, the Yellowstone sites are hot spring deposits that span a wide range in pH and temperature. In addition, the surrounding country rock is typically more siliceous (e.g., rhyolite).

3.3 New Zealand

New Zealand's Taupo Volcanic Zone (TVZ) is home to several geothermal fields with numerous hot springs, geysers, and fumaroles that enable opal production and diagenesis under many different conditions. Sinters precipitate from both alkali-chloride and acid-sulfate waters and silica residue has formed at sites undergoing acidic steam condensate or fumarolic alteration. These processes have produced deposits spanning the full opal sequence from opal-A to microcrystalline quartz (including moganite, a

metastable precursor to quartz; Rodgers and Cressey, 2001). Accessory mineral assemblages are also diverse across these environments, with calcite and Mg/Si-rich clays commonly found in alkaline regions and kaolinite, poorly crystalline clays, jarosite, and alunite in acidic regions. Our samples originate from sites near the Orakei Korako geothermal field of the TVZ: Umukuri, Sinter Island, Tahunaatara, and Te Kopia. The literature on opal at these locations is rich, with extensive documentation of opal morphology and XRD data by the workers cited below.

The Umukuri sinter is a late Pleistocene deposit (27,000-200,000 years old) that extends over an area of 0.8 km^2 and is divided into southern, central, and northern sections [Campbell et al., 2001]. Opal-A is noticeably absent, with opal-CT in the upper horizons, opal-C in the middle layers, and microcrystalline quartz in the lowermost portions. The deposit has been uplifted by fault activity, which may have hindered alteration and resulted in a lack of accessory minerals (particularly compared to the other TVZ sites) [Herdianita et al. 2001a; Campbell et al., 2001; Lynne and Campbell, 2003; Campbell et al., 2015].

The Tahunaatara sinter is approximately 14,000-20,000 years old and originally covered an area of 1-2 km^2. The present-day 90-meter-long deposit has a well-exposed vertical profile dominated by opal-A and some opal-CT in the lower, older strata. Detrital plagioclase and quartz remain from incorporated fluvial, lacustrine, and volcaniclastic sediments, and kaolinite suggests some acidic steam condensate alteration in the sinter's history [Campbell et al., 2003; Rodgers et al., 2004].

Sinter Island is a ~4-meter-wide sinter deposit initially deposited from alkali-chloride waters and subsequently affected by acidic steam condensate processes. Despite

its young age of 450 years, Sinter Island contains the full opal-A to quartz sequence, produced from rapid diagenesis facilitated by acidic conditions [Lynne et al., 2007; Campbell et al., 2015].

The Te Kopia sinter is ~3,500 years old [Martin et al., 2000] and has undergone several alteration events as recorded in its diverse mineral assemblage. Detrital remnants of the ignimbrite country rock include quartz, plagioclase, pyroxene, hornblende, Fe/Ti-oxides, and rhyolitic glasses. Opal-A was initially deposited from near-neutral alkali-chloride waters, which also produced chlorite, calcite, pyrite, and illite. Present-day alteration is dominated by acid-sulfate and fumarolic processes, which have altered some opal-A to opal-CT and formed kaolinite, alunite, alunogen, hematite, and jarosite [Herdianita et al., 2000a; Rodgers et al., 2002; Lynne and Campbell, 2003; 2004]. Complex chemical changes also occur, with initial alteration mobilizing Al and depleting Na. As silica residue forms as the last and final alteration phase, Al, Fe, and K are also eventually depleted and leave behind elevated levels of residual Si [Martin et al., 1999].

4. Experimental Methods

A total of 135 samples were obtained from the Hawaii, Yellowstone, and New Zealand sites to study the mineralogical and chemical characteristics of opal-rich materials. One additional sample of pure opal-CT was also examined, provided courtesy of Dr. David Bish (Indiana University). Opal type and accessory mineralogy were determined from XRD and chemistry was measured by ICP-AES at Brown University**.** Visible-near infrared reflectance spectra of these samples were also acquired and are discussed in terms of opal-type and mineralogy in a companion paper [Sun et al., 2017].

Bulk rocks (hand samples) and chips were obtained for 43 samples from Hawaii, 16 from Yellowstone National Park, and 45 from New Zealand (in the form of small <0.5 g cores). An additional 27 Yellowstone samples were measured only as bulk powders. Chips and cores were ground by hand using a corundum mortar and pestle until all of the sample could be dry-sieved to <45 µm. Separate powders for coatings, weathering rinds, and rock interiors were prepared when feasible. Our preparation resulted in powders for 47 Hawaii samples (including separates of three chips), 43 Yellowstone samples (including the 27 pre-powdered samples), and 45 New Zealand samples. Specific sample localities are documented in **Appendix C**, and images of the samples are provided in **Appendix D**.

4.1 X-Ray Powder Diffraction (XRD)

XRD patterns of the powder samples were obtained using a Bruker D2 Phaser fitted with a Cu Kα source. Samples were loaded onto a 2.5 cm diameter PMMA polymer mount or a 1.0 cm diameter zero-background plate for less abundant samples. Each sample was first scanned from 10-50˚ 2θ at a 0.02˚ 2θ step size with a time step of 1 second per 0.02˚ 2θ. Samples loaded in the zero-background plates were scanned at a longer time step of 5 seconds per 0.02˚ 2θ to compensate for the smaller surface area. These data were used for a cursory analysis for the presence or absence of an amorphous hump in the 15˚-35˚ 2θ range and to identify other dominant crystalline phases. Samples that displayed an XRD amorphous component were measured again with longer time steps (up to ~20-30 seconds per 0.02˚ 2θ) from 10-70˚ 2θ to refine mineral identification. Crystalline phases were identified using the DIFFRAC.EVA software by comparison

with the ICDD PDF2 and ICDD PDF4 libraries. Minor inconsistencies in sample loading may result in a slight 2θ displacement between measurements.

Based on the literature described above **(Section 2.2)**, three parameters were used to distinguish between XRD patterns of opal-A, -CT, and -C: 1) The full width at half-maximum intensity (FWHM) of the 4.1 Å feature, 2) the position of the 4.1 Å peak, and 3) the intensity ratio of the 4.32 Å tridymite shoulder to the 4.1 Å cristobalite peak **(Figure 1)**. The FWHM and tridymite/cristobalite intensity ratio (for opal-CT to opal-C) should decrease with increasing opal crystallinity, except for the 4.1 Å peak position which increases with opal-A maturation but decreases from opal-CT and onwards. The raw XRD data were first background-corrected in DIFFRAC.EVA to remove the low-angle background slope that is attributed to scattering from the sample mount. For purposes of the FWHM calculation for opal-A only, the discrete peaks (e.g., of cristobalite or quartz) were removed from the background-corrected opal-A pattern to avoid overestimation of the 4.1 Å peak intensity. Calculation of the 4.1 Å peak position was applied to the background-corrected patterns for all opal samples. The tridymite/cristobalite intensity (T/C) ratio was calculated by ratioing the tridymite peak intensity to the cristobalite or opal peak intensity in the background-corrected data. The tridymite intensity was taken at a fixed 4.32 Å position due to the lack of a discrete tridymite peak in most samples and the peak intensity of the entire 4.1 Å feature was used for the cristobalite intensity. For consistency, this intensity ratio was also calculated for the opal-A samples despite the lack of discrete disordered cristobalite and tridymite.

4.2 Inductively Coupled Plasma Atomic Emission Spectroscopy (ICP-AES)

Bulk chemistry for 44 samples from the Hawaii (22), Yellowstone (11), and New Zealand (11) suites were obtained using ICP-AES for the elements Al, Ca, Cr, Fe, K, Mg, Mn, Na, Ni, P, Si, and Ti. Samples were selected to represent the opal and mineralogical diversity indicated from XRD, and this subset spans all of the individual sampling localities. Samples were first prepared using flux fusion methods outlined in Murray et al. [2000]. Approximately 40 ± 5 mg of powdered sample and 150 ± 5 mg of lithium metaborate flux were combined in graphite crucibles. The mixtures were then fused in a 1050°C oven for 10 minutes, poured into 20 mL of 10% nitric acid, shaken for 30 minutes, and passed through a 0.45 mm filter. Five blanks and 7 reference standards (plus a duplicate set) – RGM-1, NIST1646a, BIR-1, BHVO-2, NIST2711, BCR-2, DTS-2B – were also processed in this manner. All liquid solutions were further diluted to a factor of 4000 and measured on the ICP-AES. The sequence was bookended by the two sets of reference standards and a blank was placed after every 10 samples. The resulting peak intensities were then corrected for instrument drift and subtraction of the blank intensities. Intensities for the reference standards were compared to their known elemental composition, and the linear regression of that relation was used to convert intensity into elemental weight percent oxide concentrations for the unknown standards.

5. Results

This section describes the overall trends observed in the mineralogy and chemistry of our three sample suites. Mineralogical and chemical results for all of the

individual samples are presented in **Appendix C**, and individual XRD patterns are documented in **Appendix E**.

5.1 Opal Types and Accessory Mineralogy from XRD

A summary of the XRD-derived opal types and accessory minerals is presented in **Table 1** for the 136 samples examined in this study, grouped by sampling location. From left to right column on **Table 1**, we have categorized these phases as follows:

1) Opal-A/CT/C type if present, or quartz (if the only phase present)

2) Crystalline silica, (i.e. discrete peaks of quartz, cristobalite, and tridymite that superpose the broad 4.1 Å opal peak)

3) Sulfates and Al-bearing alteration minerals (e.g., kaolinite, gibbsite, gypsum, jarosite, etc.)

4) Ti- or Zn-bearing minerals (e.g., anatase, ilmenite, rutile, sphalerite)

5) Igneous minerals (olivine, pyroxene, plagioclase or orthoclase)

6) Other, typically alteration, minerals (e.g., hematite, calcite, sulfur)

Each of the Hawaii, Yellowstone, and New Zealand suites can be further divided into two subgroups on the basis of common mineralogic characteristics. We attribute any amorphous humps to opal-A and do not distinguish opal-A from other XRD-amorphous materials such as glass, which exhibit only slightly different patterns due to composition. We therefore cannot preclude the presence of glass instead of opal-A, particularly for Hawaii samples that may retain volcanic glass.

5.1.1 Hawaii Suite

Samples from the Hawaii sites exhibit the most complex mineralogy out of the three sample suites. The majority of amorphous phases in the Hawaii suite are consistent with opal-A (or glass), but importantly almost half of these samples lack a discernable amorphous or opaline component. Interpretation of XRD patterns for some samples is complicated by the abundance of igneous minerals such as olivine, pyroxene, and plagioclase, that exhibit many diffraction peaks that can superpose each other and any opaline features. Only two samples contain possible opal-CT, though neither exhibit the classic bifurcated opal-CT peak at 4.1 Å. Instead, these potential "opal-CT" peaks are poorly developed and appear slightly peaked, being too narrow for opal-A but too broad to be attributed to crystalline phases **(Figure 2)**. We also cannot rule out the presence of other amorphous phases such as allophane or hisingerite, the XRD patterns of which may exhibit narrower humps than opal-A [Milliken and Bish, 2014].

The Hawaii sample suite can be split into two mineralogic subgroups on the basis of opal content. The first subgroup comprises 29 samples from the Ka'u Desert (KD), Mauna Loa (ML), and Mauna Ulu (MU), that are commonly dark rocks with orange or brown discoloration. XRD patterns indicate that these samples lack a significant amorphous component and only exhibit a modest broad hump when opal-A is present. Opaque coatings of variable thickness are present on several rocks, but the presence of a coating did not uniquely correlate with discernable opal content for the bulk powders. Cristobalite is the only crystalline silica phase identified and it is found in nearly all samples within this subgroup. Few other minerals are present but include hematite, gibbsite, gypsum, jarosite, and akaganeite, the presence of which is largely consistent

with previous studies [Mathews, 1983 BS thesis; Morris et al., 2000; Seelos et al., 2010; Chemtob et al., 2010; Chemtob and Rossman, 2014].

In contrast, the 18 samples in the second subgroup from the Sulphur Banks (SB) and Steam Vents (SV) stand out as having significantly higher opal content and diversity of other accessory minerals based on their XRD patterns. Almost all samples contain substantial opal-A as indicated by prominent XRD humps, and two samples from Sulphur Banks may contain opal-CT **(Figure 2)**. Rocks from these sites tend to be grey or white with some orange or yellow coloration and the few samples lacking opal tend to be brownish in color. Crystalline silica occurs as quartz and tridymite in addition to cristobalite, in contrast to the latter being the only crystalline silica phase found at the KD, ML, and MU locations. The SB and SV samples also host a range of Ti-bearing phases (e.g., anatase, rutile, and ilmenite) and alteration minerals, including sulfates (jarosite, alunite, gypsum), kaolinite, hematite, and sulfur. Measurements of rock coatings and bulk powders from two samples (HISB 1 and HISB 2) appear to show segregation of opal-A in the thick white coating and opal-CT in the bulk (red colored) powder. Overall, the samples in this subgroup tend to exhibit greater opal content and diversity of accessory minerals compared with the other subgroup, possibly indicating more advanced alteration and/or chemical leaching processes at these sites.

5.1.2 Yellowstone Suite

The suite of Yellowstone hot spring sinter samples is characterized by higher opal-A contents and less mineral diversity compared with samples in the Hawaii suite. The Octopus Springs (OS), Steep Cone (SC), and Sentinel Meadow (SM) sites are

neutral-alkaline environments, whereas the Nymph Lake (NL) and Rabbit Creek (RCM and RCF, collected on two separate trips) locations have known acidity. We observe that samples from alkaline sites tend to contain purer opal-A compared with samples from more acidic sites that incorporate kaolinite. Opal-CT is not readily identified in any of our samples, although some have been reported in the literature (**Section 3.2**). Crystalline silica phases such as quartz, cristobalite, and tridymite are prevalent throughout all sites but may be detrital components from the rhyolitic country rock [e.g., Bishop et al., 2004].

Fifteen samples from the acidic Nymph Lake and Rabbit Creek (RCM) sites are characterized by low to moderate opal-A content, with NL samples exhibiting shallow XRD humps and RCM samples containing a greater opal-A component. Kaolinite is present in many of the RCM samples but is less common in the NL samples. Coincidentally, orthoclase is found only in samples from the NL site in our Yellowstone suite, and it is likely retained from the rhyolitic country rock. We note that the XRD data do not preclude the possibility that the observed kaolinite may be detrital and originate from weathering of surrounding country rock. The presence of orthoclase, infrequent occurrence of kaolinite (which can form from weathering of orthoclase), and lack of significant opal-A at Nymph Lake suggests that alteration processes at this site are relatively incipient. More uncommon phases include one occurrence of gypsum at NL, two carbonate identifications at RCM, and several instances of Ti-bearing phases (titanite, anatase, ilmenite) at both sites. Kaolinite and calcite are observed in one RCM sample, similar to previous observations at acidic and alkaline sites in this location [Mills et al., 2011].

Twenty-one samples from Octopus Spring (OS), Steep Cone (SC), and Sentinel Meadow (SM) come from alkaline environments and all contain significant opal-A exhibiting prominent XRD humps. Six SC samples are pure opal-A with no accessory minerals present. The RCF group of seven samples similarly contains opal-A, in addition to one opal-A/CT sample with incipient development of an opal-CT peak. In contrast to the acidic NL and RCM sites, these alkaline sinters lack kaolinite (except in one SC sample) and tend to contain halite or calcite. Ti-minerals (anatase, titanite) are still uncommon in these samples, although one OS sample also contains Zn-bearing sphalerite.

5.1.3 New Zealand Suite

The New Zealand sample suite exhibits the greatest diversity in opal type out of our three suites, with opal-A, -A/CT, and -CT identified in addition to quartz. Samples from most locations contain more than one opal type, allowing for observation of the opal maturation sequence at individual sites. Discrete cristobalite and quartz are found throughout the suite, although cristobalite and tridymite peaks may be obscured in some sample patterns by the presence of opal-CT. Like at Yellowstone, these sinter deposits can be sorted into acidic and neutral-alkaline settings, and kaolinite is again found in samples from acidic hot spring sinters.

Sixteen samples from Sinter Island (SI) and Te Kopia (TK) comprise the acidic settings represented in the New Zealand suite. The Sinter Island samples contain opal-A, opal-A/CT, and opal-CT and document the early stages of diagenesis, though the full diagenetic sequence up to quartz has been previously documented [Lynne et al., 2007].

Quartz is present in all SI samples and could be the result of in situ opal maturation or represent a detrital component. Te Kopia samples contain both opal-A and opal-CT as well as subsidiary quartz and cristobalite. Kaolinite is present in only the acidic SI and TK samples, though interestingly it is found only in the four opal-CT samples from TK and the three opal-A/CT samples from SI that show incipient conversion to opal-CT, and it is not present in samples with only opal-A. This association of kaolinite with opal-CT may indicate acceleration of diagenesis by these acidic alteration events [Lynne et al., 2007]. Ti- and Zn-bearing phases are uncommon, though titanite and sphalerite are identified in two Te Kopia samples.

Twenty-two samples from Umukuri (UM) and Tahunaatara (TH) represent less acidic conditions. Samples from Umukuri contain only opal-CT and subordinate quartz, with two samples consisting of pure quartz from the lowermost strata at the southern end of the sinter. The notable lack of other accessory minerals is consistent with in situ observations of halted alteration due to uplift of the sinter [Campbell et al., 2001]. Our Tahunaatara (TH) samples contain only opal-A, though opal-CT has previously been documented in lower horizons [Rodgers et al., 2004]. Crystalline quartz and cristobalite are also present, as are Ti-phases (titanite, ilmenorutile) in three separate samples. Some of these minerals are likely detrital given the incorporation of fluvial and volcanic materials in the sinter deposit [Campbell et al., 2003]. Previous workers have also identified kaolinite formed from acidic steam condensate alteration at Tahunaatara, though we do not observe this in our samples. Seven other samples come from the Orakei Korako Boardwalk's Tim and Terry Pool, Lakeside Soda Mountain, and an unknown location. The samples from known localities are primarily opal-A with minor quartz and

titanite, whereas the two unknown samples are primarily opal-CT with quartz and other minor phases.

5.2 Distinguishing Opal Types from XRD Parameters

Beyond the binary categorization of opal type (e.g., A vs. CT), the degree of opal maturity is also measurable using XRD parameters such as the 4.1 Å FWHM, the 4.1 Å peak position, and the tridymite/cristobalite (4.32 Å/4.1 Å) intensity ratio (see S**ection 2.2** above). In this analysis we focus on those samples dominated by opaline silica and exclude samples that contain overwhelming amounts of non-opaline (particularly igneous) minerals, as they have peaks in the 4.1 Å region which often swamp any meaningful measurement related to the opal-A and -CT component (e.g., HISB 1 red in **Figure 2)**.

5.2.1 XRD Parameter Values

FWHM values for our samples overall average 7.25˚ 2θ (range: 6.25-8.06˚ 2θ) for opal-A, 0.88˚ 2θ (range: 0.59-1.91˚ 2θ) for opal-CT, and 0.16˚ 2θ (range: 0.14-0.18˚ 2θ) for quartz **(Table 2)**. These measurements are in line with those established in the general literature for XRD measurements of opal (**Section 2.2**) as well as published values specific to New Zealand locations **(Table 3)**. Slight discrepancies may arise where the delineation between opal-CT and -C is not clear (**Section 2.2**). Variations exist amongst our sample suites for opal-A; Hawaii samples tend to have the largest FWHM and New Zealand the smallest. Significant variations occur within the New Zealand suite for opal-

CT as well; FWHM values are generally lower (0.59-0.71˚ 2θ) for neutral-alkaline sites and higher (0.91-1.91˚ 2θ) for more acidic sites (more in **Section 6.1**).

Peak positions average 4.01 Å (ranging 3.93-4.15 Å) for opal-A, 4.10 Å (ranging 4.08-4.13 Å) for opal-CT, and 4.27 Å for quartz **(Table 2)**. These also agree with the published literature, though the range of accepted values varies widely **(Table 3)**. Again, discrepancies may occur due to differences in methodology; for example, discrete cristobalite and quartz peaks in our samples were removed prior to parameter calculations to make sure the peak is not attributed to a detrital non-opal mineral. The tridymite/cristobalite intensity ratio averages to 0.84 for opal-A, 0.34 for opal-CT, and zero for quartz. We are not aware of previously published values for this parameter for our sample sites, but the T/C ratio is expected to decrease as opals mature and eliminate tridymite stacking in favor of cristobalite stacking.

5.2.2 Opal Maturation Trends

Plots of the 4.1 Å FWHM, peak position, and the T/C ratio show the separation of opal types in this parameter space **(Figure 3A-C)**. As opal crystallinity increases, the FWHM predictably decreases. The 4.1 Å peak position and T/C ratio both behave in a more complicated manner, first increasing with increasing opal-A crystallinity, and then decreasing when opal-CT starts to develop and eventually convert to opal-C. While the FWHM remains the standard for measuring opal crystallinity, additional insight into the maturation process can be gained from the 4.1 Å peak position and T/C ratio parameters.

Within the opal-A continuum, the 4.1 Å peak position tends to increase with increasing opal-A crystallinity, as samples with higher peak positions tend to have

smaller FWHM **(Figure 3A)**. However, once the opal-A is converted to opal-CT (coinciding with a peak position of approximately 4.15 Å), the peak position will decrease towards the ~4.04 Å cristobalite peak as documented in the literature [Murata and Nakata, 1974]. The four opal-A/CT samples help illustrate this transition, as they have intermediate FWHM between opal-A and opal-CT but have higher peak positions compared to opal-A and most opal-CT. The peak shift within opal-A was previously observed in similar New Zealand samples by Lynne and Campbell [2004], and these results extend the trend to peak positions below 4.0 Å using the Hawaii and Yellowstone samples. This opal maturation trend can be used to suggest, for example, that our Hawaii opal-A are immature in comparison to New Zealand opal-A (discussed further in **Section 6.1**).

The T/C intensity ratio also shows separate trends for opal-A and opal-CT. As opal-A becomes more crystalline and increases in peak position, its T/C ratio appears to increase slightly **(Figure 3B, C)**. This may indicate some preliminary tridymite formation in opal-A leading up to the beginning of opal-CT formation, consistent with microscale observations of tridymite forming prior to opal-CT peak development in XRD [Lynne and Campbell, 2004]. During the subsequent conversion of opal-CT to opal-C, the T/C ratio then decreases due to preferential cristobalite stacking. We note that the T/C ratio is greatly affected by the presence of quartz, which has a reflection at 4.26 Å close to the 4.32 Å tridymite reflection, thereby artificially increasing the perceived tridymite component of the sample and causing it to appear closer to opal-CT than opal-C. However, this is unlikely to affect the overall trends that are observed in this parameter, as quartz does not appear to be preferentially associated with opal-A or opal-CT samples.

In summary, samples from Hawaii are generally poorer in opaline silica compared with samples from Yellowstone and New Zealand. This is not entirely surprising given that the former result from alteration and chemical weathering of basaltic materials whereas the latter are precipitates from hot springs. However, for Hawaii and Yellowstone samples that do contain opaline silica we observe that they are dominated by opal-A, whereas samples from New Zealand span the range of opal-A to opal-CT. Additional insights into crystallinity gradients within the opal-A and opal-CT subgroups can also be obtained from the XRD parameters described in this section.

5.3 Major Element Chemistry from ICP-AES

Chemical results can be categorized into two subgroups for each of the Hawaii, Yellowstone, and New Zealand suites (**Table 4)** and correspond with the distinct mineralogic subgroups presented in **Section 5.1**. The chemical index of alteration (CIA) can be used as a proxy for the degree of chemical weathering, with values of 30-35 for unaltered basalt, 45-55 for unaltered granite, and increasing up to 100 with further chemical weathering [Nesbitt and Young, 1982]. Within the Hawaii suite, samples in the opal-poor group (KD, ML, MU) yield an average chemical composition consistent with relatively unaltered basaltic material and a modest CIA value of 56.96. The average composition for the opal-rich group (SV, SB) is considerably more altered from a mineralogic perspective as well as a chemical perspective and has a higher CIA index of 76.08.

Titanium content, which may reflect pH conditions **(Section 2.3),** also varies between the sample groups **(Figure 4A, D)**. The Hawaii samples as a whole tend to have

the highest Ti values, ranging from 1.71-4.34 wt% TiO_2 for the opal-poor group and 0.53-5.23 wt% for the opal-rich Sulphur Banks group. Acidic sinters range in TiO_2 content from 0.02-0.25 wt% for Yellowstone and 0.03-0.14 wt% for New Zealand. Alkaline sinters from Yellowstone have a lower range of 0.003-0.06 wt% compared to their acidic counterparts, as do New Zealand alkaline sinters with a range of 0.03-0.07 wt%. Though the sinters are not as Ti-rich as the Hawaii samples, six acidic sinters have Ti contents as high as 0.16, 0.18, 0.25, and 0.51 wt% (the latter from a sample contributed by Steve Ruff). These samples were all sourced from the acidic Rabbit Creek, Nymph Lake, Te Kopia, and Sylvan Springs (for the 0.51 wt% TiO_2 sample) sites. These values are on par with previous sinter measurements by Preston et al. [2008], whose data are also consistent with acidic sinters generally containing higher Ti content.

We observe no systematic correlation between Ti and P **(Figure 4B, E)** in any of the sample groups. While Hawaii samples tend to have the highest P values, there is considerable overlap between them and the sinter samples with respect to P. A correlation between Ti and P would be expected in the case of Ti complexing with P under reducing and acidic conditions [Pe-Piper et al., 2011]. P is also expected to decrease under acidic conditions, but we see no evidence of this between the altered and (relatively) unaltered Hawaii samples, and between acidic and neutral-alkaline sinters. Similarly, no distinctions are observed in Ni content, which is mobile at pH<6 [Degryse et al., 2009], between the sample groups **(Figure 4C, F)**.

However, there are general trends in Mn content, which is highest for the opal-poor Hawaii group, moderate for the opal-rich Hawaii group, and low for the sinter samples **(Figure 4C, F)**. The lower Mn of the acid-leached and opal-rich Sulphur Banks

group is consistent with Mn being a mobile element at pH<6 at oxidizing conditions [Degryse et al., 2009]. The low Mn content of the sinter samples can be attributed to sinter precipitation at neutral-alkaline conditions (after which acidic leaching is experienced at several sites). No systematic variations in Mn are observed between acidic and neutral-alkaline sinter settings.

6. Mineralogic and Chemical Characteristics of Acidic/Alkaline Environments

We observe differences in mineralogy and chemistry depending on formation environment (fumarole vs. sinter) and pH (acidic vs. neutral-alkaline). We categorize the Hawaii locations, Yellowstone Nymph Lake and Rabbit Creek (RCM), and New Zealand Tahunaatara, Te Kopia, and Sinter Island sites as acidic environments. The Yellowstone Octopus Spring, Rabbit Creek (RCF), Sentinel Meadow, and Steep Cone and New Zealand Orakei Korako Boardwalk, Lakeside Soda Mt., and Umukuri locations are considered to be more neutral/alkaline.

6.1 XRD Parameter Variations

Our samples appear to cluster in the XRD parameter space with some dependence on their association with acidic or neutral/alkaline settings **(Figure 3D-F)**. Previous work described in the New Zealand opal literature has shown that the 4.1 Å FWHM parameter is typically higher for acidic samples. Lynne et al. [2006] introduced opal-A samples into an active fumarole and found an overall increase in FWHM from 7.2 to 8.6° 2θ over 86 weeks. Opals from the very acidic Rotokawa geothermal field have larger FWHM (up to 9.5° 2θ), attributed to a higher disorder within opals deposited or reworked by acidic

fluids [Rodgers et al., 2002]. Rodgers et al. [2004] also noted that weathered opal-A samples would have asymmetric 4.1 Å humps and a larger FWHM range (6.1-7.6° 2θ) while unweathered samples would have smaller FWHM range (6.5-7° 2θ). Our results are not completely consistent with this previous work, but we propose that diagenetic progress and overall opal maturity can explain our observed trends (**Section 5.2.2**).

Among the opal-A samples, the acidic Hawaii Sulphur Banks group has the largest average FWHM and peak positions at relatively low d-spacing even in comparison to acidic samples from Yellowstone and New Zealand. Their position in this plot **(Figure 3D)** suggests that they are relatively immature on the scale of opal-A diagenesis, which may be due to their formation via acid-sulfate leaching of basalt. In contrast, acidic processes at Yellowstone and New Zealand represent secondary alteration events acting on previously deposited sinters. Another possibility is that the accessory minerals in the Hawaii samples overlap in the 4.1 Å bump region and may contribute to artificial FWHM broadening, despite our efforts to remove discrete crystalline peaks from the parameter calculation.

The highest FWHM tend to belong to the alkaline sinters (particularly from Yellowstone), while the lowest FWHM belong to acidic sinters. On the maturation trend, these acidic samples plot on the more mature end of the opal-A continuum and with further diagenesis start forming incipient opal-CT peaks, reflected in the four opal-A/CT samples, which are all found in acidic environments. This is consistent with a previous proposal that acidic conditions may accelerate opal diagenesis [Lynne et al., 2007].

Opal-CT samples from New Zealand suite at first appear to show the opposite trend, where acidic samples from the Sinter Island deposit tend to have higher FWHM

and appear less mature than the alkaline Umukuri samples. However, this crystallinity difference is likely controlled by age rather than pH. The Umukuri sinter is known for being in the later stages of opal diagenesis (opal-CT to –C to quartz) with no reported opal-A occurrence, while the Sinter Island deposit is comparatively young and still retains opal-A despite having experienced rapid diagenesis through quartz.

The fact that these different sampling locations occupy different portions of the XRD parameter space offers a basis of comparison for XRD measurements by Mars rovers or landers. For example, a martian sample that plots near the alkaline Umukuri opal-CT cluster could be interpreted as a relatively old and mature deposit that has likely undergone significant diagenesis. While this application is a possibility, more opal samples from a variety of sites are needed to fill out this parameter space and provide more points of comparison.

6.2 Diagnostic Mineralogy

Distinct mineralogic and chemical differences are observed in our samples and reflect both pH and the type of environment (i.e. acidic fumarole-leached basalt vs. acidic-leached sinter vs. neutral-alkaline sinter). The two groups of Hawaii samples both represent acidic fumarole environments, where opals are commonly produced as coatings or rinds from the acidic leaching of basalt. However, samples from the Sulphur Banks have undergone more pervasive aqueous alteration, as evidenced by their higher CIA values. This results in a high abundance of opal that is observed as large amorphous components in XRD and also in high Si content of up to 85 wt% SiO_2. Some conversion to opal-CT is possible (e.g., in HISB 1 red and HISB 2 red), though rare. These opal-rich

samples are also accompanied by an assemblage of traditionally acidic minerals like kaolinite, jarosite, and alunite. In contrast, alteration in more semiarid regions, such as the Ka'u Desert, Mauna Loa, and Mauna Ulu, produces less opal, which manifests as small XRD-amorphous bumps and a modest Si content ranging from 26-53 wt% SiO_2, not much different from unaltered basalt.

The sinter samples from Yellowstone and New Zealand can represent opal precipitation from neutral-alkaline waters (Octopus Spring, Rabbit Creek RCF, Steep Cone, Sentinel Meadow, Umukuri, Tahunaatara) or opals that have since been affected by acidic leaching processes (Nymph Lake, Rabbit Creek RCM, Sinter Island, Te Kopia). The alkaline sinters tend to be pure opal-A, or opal-CT in the case of some NZ sites, with a few accessory minerals like calcite and halite. The acidic sinters tend to be accompanied by kaolinite. Ti-bearing minerals are present, but similarly uncommon, in both acidic and alkaline sinters. To summarize, acid-leaching of basalt produces many accessory minerals that are commonly associated with acidic environments (jarosite, sulfates, kaolinite); acidic sinters are also accompanied by kaolinite but in general sinter deposits tend to have fewer accessory phases.

6.3 Diagnostic Chemistry

Amongst our samples, no clear chemical trends are observed that might be considered diagnostic hallmarks of a particular formation environment. Titanium has been commonly used in the martian literature as a diagnostic of pH conditions, with higher Ti content indicating acidic conditions that have leached away more mobile elements. In this manner, opal deposits at Home Plate in Gusev crater have been

interpreted as the result of acidic leaching of basalt, as they have TiO_2 contents up to ~1.5 wt% [Morris et al., 2008; Squyres et al., 2008]. High Ti content, up to 1.57 wt%, has also been observed at Gale crater and inferred to represent acidic conditions at the time of formation [Rampe et al., 2017]. Although we do observe generally higher Ti content in acid-altered samples, there are several reasons why Ti content is not a reliable indicator of formation environment, at least from our samples.

On average, the altered Sulphur Banks samples tend to have higher Ti content compared to the less-altered, opal-poor group of Hawaii samples. However, there is significant overlap in the value ranges for the opal-poor group and the opal-rich SB group **(Figure 4A)**. Hawaiian basalts are also inherently enriched in Ti [Prytulak and Elliott, 2007], as indicated by the already high Ti values (upwards of 1.71 wt%) in the less-altered Hawaiian samples. Thus, Ti values for acid-leached Hawaiian basalts are not necessarily appropriate analogs for what we may observe on Mars. As noted previously by Preston et al. [2008] and Ruff et al. [2011], sinters are capable of achieving TiO_2 as high as 0.9 wt% from Preston et al. [2008] and 0.25-0.51 wt% in our samples, though it is still the acidic sinters that tend to have the higher Ti values. Given these considerations, it can be difficult to unambiguously identify an acid-leached basaltic environment based on Ti content alone.

The general lack of systematic trends or correlations in other elements also suggests that chemical data should not be interpreted alone. We observe no trends between Ti and P [e.g., Pe-Piper et al., 2011], or in P content itself, which is expected to be low in acidic samples. We also do not see any trends associated with Ni content, although we do see some systematic variations in Mn content. Mn decreases for the opal-

rich Sulphur Banks samples as the result of Mn mobility at pH<6 at oxidizing conditions [Degryse et al., 2009], and is very low in the sinter samples. However, it is also important to note that the Yellowstone and New Zealand hot spring sites are hosted in rhyolitic country rock, which is again not necessarily an appropriate analog for basaltic Mars.

To summarize, Ti content may not be unique diagnostic of formation conditions, as we observe a significant overlap in Ti values between opal-rich samples and relatively unaltered samples from Hawaii, as well as relatively high Ti content in sinter samples. With the exception of Mn, we do not observe diagnostic trends in any other elements. These results suggest that chemical data are not necessarily reliable indicators of formation environment without additional observations of geologic context and macro/micro-scale textures. Commonly studied terrestrial analog sites in Hawaii, Yellowstone National Park, and New Zealand, such as those analyzed in this work, may also not be ideal analogs. The former site produces basalts that are inherently enriched in Ti, and the hot springs in the latter two sites are hosted in rhyolitic, not basaltic, country rock.

7. Conclusion

We have conducted a systematic analysis of the mineralogy and chemistry of opal-bearing samples from acidic fumarole, acidic sinter, and neutral-alkaline sinter sites as terrestrial analogs to martian opal deposits. From our samples, it appears that an opal deposit formed from acidic fumarolic leaching of basalt would be accompanied by a variety of different alteration phases like kaolinite, jarosite, and other sulfates. Opals from hot spring sinters would have fewer accessory minerals, which would likely be

calcite or halite in alkaline settings and kaolinite in more acidic settings. XRD parameters, such as those depicted in **Figure 3**, illustrate the trend in opal maturation and could be a basis of comparison for future martian samples that plot near clusters from certain sampling sites.

Although we observe some distinctions in Ti and Mn content between samples from basaltic fumarole versus sinter environments, we do not observe any other chemical trends that are suggestive of acidic or neutral-alkaline formation conditions. Even when interpreting Ti content, it should be recognized that Hawaiian basalts, while popular terrestrial analog materials for Mars, are inherently enriched in Ti content regardless of whether they have experienced acid sulfate-leaching. We also observe significant overlap in the Ti content between unaltered samples and opal-rich, acid sulfate-leached samples, suggesting that high Ti values do not necessarily correlate with exposure to acidic conditions. Sinter samples can also exhibit relatively high Ti values, as demonstrated by some of our samples as well as those from previous studies. Overall, we caution against solely using chemical data to interpret formation environment, which likely requires integrating the full suite of chemical, mineralogic, microtextural, and geologic properties. Future work for determining the chemical signatures of specific opal-forming environments may benefit from analysis of samples from more analogous terrestrial sites, such as basaltic hot spring environments in Iceland, etc. [Preston et al., 2008].

Acknowledgements

The authors are extremely appreciative to Gregg Swayze for several Hawaii samples and David Bish for providing a pure opal-CT sample to benchmark the other

opal-CT samples. We also gratefully thank Terik Daly, Joe Orchado, Dave Murray, Laura Messier, and Rachel Sheppard for assistance with flux fusion and ICP-AES methods. This work was funded by a MSL Participating Scientist grant.

References

Allen, C. C., J. L. Gooding, M. Jercinovic, and K. Keil (1981), Altered basaltic glass: A terrestrial analog to the soil of Mars, *Icarus*, *45*(2), 347–369, doi:10.1016/0019-1035(81)90040-3.

Bandfield, J. L. (2008), High-silica deposits of an aqueous origin in western Hellas Basin, Mars, *Geophysical Research Letters*, *35*(12), doi:10.1029/2008GL033807.

Bishop, J. L., E. Murad, M. D. Lane, and R. L. Mancinelli (2004), Multiple techniques for mineral identification on Mars:: a study of hydrothermal rocks as potential analogues for astrobiology sites on Mars, *Icarus*, *169*(2), 311–323, doi:10.1016/j.icarus.2003.12.025.

Cady, S. L., and J. D. Farmer (1996), Fossilization processes in siliceous thermal springs: trends in preservation along thermal gradients, *Ciba Found. Symp.*, *202*, 150-170; discussion 170-173.

Campbell, K. A., K. Sannazzaro, K. A. Rodgers, N. R. Herdianita, and P. R. L. Browne (2001), Sedimentary Facies and Mineralogy of the Late Pleistocene Umukuri Silica Sinter, Taupo Volcanic Zone, New Zealand, *Journal of Sedimentary Research*, *71*(5), 727–746, doi:10.1306/2DC40964-0E47-11D7-8643000102C1865D.

Campbell, K. A., T. F. Buddle, and P. R. L. Browne (2003), Late Pleistocene siliceous sinter associated with fluvial, lacustrine, volcaniclastic and landslide deposits at

Tahunaatara, Taupo Volcanic Zone, New Zealand, *Earth and Environmental Science Transactions of The Royal Society of Edinburgh*, *94*(4), 485–501, doi:10.1017/S0263593300000833.

Campbell, K. A., B. Y. Lynne, K. M. Handley, S. Jordan, J. D. Farmer, D. M. Guido, F. Foucher, S. Turner, and R. S. Perry (2015), Tracing Biosignature Preservation of Geothermally Silicified Microbial Textures into the Geological Record, *Astrobiology*, *15*(10), 858–882, doi:10.1089/ast.2015.1307.

Chemtob, S. M., and G. R. Rossman (2014), Timescales and mechanisms of formation of amorphous silica coatings on fresh basalts at Kīlauea Volcano, Hawai'i, *Journal of Volcanology and Geothermal Research*, *286*, 41–54, doi:10.1016/j.jvolgeores.2014.08.029.

Chemtob, S. M., B. L. Jolliff, G. R. Rossman, J. M. Eiler, and R. E. Arvidson (2010), Silica coatings in the Ka'u Desert, Hawaii, a Mars analog terrain: A micromorphological, spectral, chemical, and isotopic study, *J. Geophys. Res.*, *115*(E4), E04001, doi:10.1029/2009JE003473.

Curtiss, B., J. B. Adams, and M. S. Ghiorso (1985), Origin, development and chemistry of silica-alumina rock coatings from the semi-arid regions of the island of Hawaii, *Geochimica et Cosmochimica Acta*, *49*(1), 49–56, doi:10.1016/0016-7037(85)90190-5.

Degryse, F., E. Smolders, and D. R. Parker (2009), Partitioning of metals (Cd, Co, Cu, Ni, Pb, Zn) in soils: concepts, methodologies, prediction and applications – a review, *European Journal of Soil Science*, *60*(4), 590–612, doi:10.1111/j.1365-2389.2009.01142.x.

Ehlmann, B. L. et al. (2016), Discovery of alunite in cross crater, terra sirenum, mars: evidence for acidic, sulfurous waters, *American Mineralogist*, *101*(7), 1527–1542, doi:10.2138/am-2016-5574.

Elzea, J. M., and S. B. Rice (1996), TEM and X-ray diffraction evidence for cristobalite and tridymite stacking sequences in opal, *Clays and Clay Minerals*, *44*(4), 492–500.

Farr, T. G., and J. B. Adams (1984), Rock coatings in Hawaii, *Geological Society of America Bulletin*, *95*(9), 1077–1083, doi:10.1130/0016-7606(1984)95<1077:RCIH>2.0.CO;2.

Galvez, M. E., O. Beyssac, K. Benzerara, N. Menguy, S. Bernard, and S. C. Cox (2012), Micro- and nano-textural evidence of Ti(–Ca–Fe) mobility during fluid–rock interactions in carbonaceous lawsonite-bearing rocks from New Zealand, *Contrib Mineral Petrol*, *164*(5), 895–914, doi:10.1007/s00410-012-0780-2.

Graetsch, H., H. Gies, and I. Topalović (1994), NMR, XRD and IR study on microcrystalline opals, *Phys Chem Minerals*, *21*(3), 166–175, doi:10.1007/BF00203147.

Greenwood, R. (1973), Cristobalite: Its Relationship to Chert Formation in Selected Samples from the Deep Sea Drilling Project, *Journal of Sedimentary Research*, *43*(3).

Grotzinger, J. P. et al. (2015), Deposition, exhumation, and paleoclimate of an ancient lake deposit, Gale crater, Mars, *Science*, *350*(6257), aac7575, doi:10.1126/science.aac7575.

Guidry, S. A., and H. S. Chafetz (2003), Anatomy of siliceous hot springs: examples from Yellowstone National Park, Wyoming, USA, *Sedimentary Geology*, *157*(1–2), 71–106, doi:10.1016/S0037-0738(02)00195-1.

Guthrie, G. D., D. L. Dish, and R. C. Reynolds (1995), Modeling the X-ray diffraction pattern of opal-CT, *American Mineralogist*, *80*(7–8), 869–872, doi:10.2138/am-1995-7-834.

Hanna, B. T. (2003), Mineralogical and geochemical characterization of two Sulfolobales harboring hot spring systems : Rabbit Creek and Ragged Hills, Yellowstone National Park, WY, USA, Thesis, Montana State University - Bozeman, College of Letters & Science.

Herdianita, N. R., P. R. L. Browne, K. A. Rodgers, and K. A. Campbell (2000a), Mineralogical and textural changes accompanying ageing of silica sinter, *Mineral. Deposita*, *35*(1), 48–62, doi:10.1007/s001260050005.

Herdianita, N. R., K. A. Rodgers, and P. R. L. Browne (2000b), Routine instrumental procedures to characterise the mineralogy of modern and ancient silica sinters, *Geothermics*, *29*(1), 65–81, doi:10.1016/S0375-6505(99)00054-1.

Inagaki, F., Y. Motomura, K. Doi, S. Taguchi, E. Izawa, D. R. Lowe, and S. Ogata (2001), Silicified Microbial Community at Steep Cone Hot Spring, Yellowstone National Park, *Microbes and Environments*, *16*(2), 125–130, doi:10.1264/jsme2.2001.125.

Jones, B., and R. W. Renaut (2003), Hot spring and geyser sinters: the integrated product of precipitation, replacement, and deposition, *Can. J. Earth Sci.*, *40*(11), 1549–1569, doi:10.1139/e03-078.

Jones, J. B., and E. R. Segnit (1971), The nature of opal I. nomenclature and constituent phases, *Journal of the Geological Society of Australia*, *18*(1), 57–68, doi:10.1080/00167617108728743.

Jutras, P., R. S. Quillan, and M. J. LeForte (2009), Evidence from Middle Ordovician paleosols for the predominance of alkaline groundwater at the dawn of land plant radiation, *Geology*, *37*(1), 91–94, doi:10.1130/G25447A.1.

Kastner, M., J. B. Keene, and J. M. Gieskes (1977), Diagenesis of siliceous oozes—I. Chemical controls on the rate of opal-A to opal-CT transformation—an experimental study, *Geochimica et Cosmochimica Acta*, *41*(8), 1041–1059, doi:10.1016/0016-7037(77)90099-0.

Konhauser, K. O., B. Jones, A.-L. Reysenbach, and R. W. Renaut (2003), Hot spring sinters: keys to understanding Earth's earliest life forms, *Can. J. Earth Sci.*, *40*(11), 1713–1724, doi:10.1139/e03-059.

Krauskopf, K. B. (1956), Dissolution and precipitation of silica at low temperatures, *Geochimica et Cosmochimica Acta*, *10*(1), 1–26, doi:10.1016/0016-7037(56)90009-6.

Kyle, J. E., and P. A. Schroeder (2007), Role of smectite in siliceous-sinter formation and microbial-texture preservation: Octopus Spring, Yellowstone National Park, Wyoming, USA, *Clays and Clay Minerals*, *55*(2), 189–199, doi:10.1346/CCMN.2007.0550208.

Lee, M. R., I. MacLaren, S. M. L. Andersson, A. Kovács, T. Tomkinson, D. F. Mark, and C. L. Smith (2015), Opal-A in the Nakhla meteorite: A tracer of ephemeral liquid water in the Amazonian crust of Mars, *Meteorit Planet Sci*, *50*(8), 1362–1377, doi:10.1111/maps.12471.

Lynne, B. Y., and K. A. Campbell (2003), Diagenetic transformations (opal-A to quartz) of low- and mid-temperature microbial textures in siliceous hot-spring deposits,

Taupo Volcanic Zone, New Zealand, *Can. J. Earth Sci.*, *40*(11), 1679–1696, doi:10.1139/e03-064.

Lynne, B. Y., and K. A. Campbell (2004), Morphologic and Mineralogic Transitions From Opal-A to Opal-CT in Low-Temperature Siliceous Sinter Diagenesis, Taupo Volcanic Zone, New Zealand, *Journal of Sedimentary Research*, *74*(4), 561–579, doi:10.1306/011704740561.

Lynne, B. Y., K. A. Campbell, R. S. Perry, P. R. L. Browne, and J. N. Moore (2006), Acceleration of sinter diagenesis in an active fumarole, Taupo volcanic zone, New Zealand, *Geology*, *34*(9), 749–752, doi:10.1130/G22523.1.

Lynne, B. Y., K. A. Campbell, B. J. James, P. R. L. Browne, and J. Moore (2007), Tracking crystallinity in siliceous hot-spring deposits, *Am J Sci*, *307*(3), 612–641, doi:10.2475/03.2007.03.

Martin, R., K. A. Rodgers, and P. R. L. Browne (1999), The nature and significance of sulphate-rich, aluminous efflorescences from the Te Kopia geothermal field, Taupo Volcanic Zone, New Zealand, *Mineralogical Magazine*, *63*(3), 413–413, doi:10.1180/002646199548501.

Martin, R., D. C. Mildenhall, P. R. L. Browne, and K. A. Rodgers (2000), The age and significance of in-situ sinter at the Te Kopia thermal area, Taupo Volcanic Zone, New Zealand, *Geothermics*, *29*(3), 367–375, doi:10.1016/S0375-6505(00)00008-0.

Mathews, C. A. (1983), Fumarolic alteration of basalt on Mauna Ulu, Kilauea Volcano, Hawaii, *McMaster University B.S. Thesis*.

McLennan, S. M. (2003), Sedimentary silica on Mars, *Geology*, *31*(4), 315–318, doi:10.1130/0091-7613(2003)031<0315:SSOM>2.0.CO;2.

Meyer-Dombard, D. R., E. L. Shock, and J. P. Amend (2005), Archaeal and bacterial communities in geochemically diverse hot springs of Yellowstone National Park, USA, *Geobiology*, *3*(3), 211–227, doi:10.1111/j.1472-4669.2005.00052.x.

Milliken, R. E., and D. L. Bish (2014), Distinguishing Hisingerite from Other Clays and its Importance for Mars, vol. 45, p. 2251.

Milliken, R. E. et al. (2008), Opaline silica in young deposits on Mars, *Geology*, *36*(11), 847–850, doi:10.1130/G24967A.1.

Mills, V. W., J. D. Farmer, S. W. Ruff, J. Nunez, and L. L. Jahnke (2011), Systematic variations in sinter mineralogy, microtexture and diagenesis in modern siliceous hot springs: Clues for interpreting depositional conditions in ancient deposits, *AGU Fall Meeting Abstracts*, *33*.

Minitti, M. E., C. M. Weitz, M. D. Lane, and J. L. Bishop (2007), Morphology, chemistry, and spectral properties of Hawaiian rock coatings and implications for Mars, *J. Geophys. Res.*, *112*(E5), E05015, doi:10.1029/2006JE002839.

Mizutani, S. (1977), Progressive ordering of cristobalitic silica in the early stage of diagenesis, *Contrib. Mineral. Petrol.*, *61*(2), 129–140, doi:10.1007/BF00374363.

Morris, R. V. et al. (2000), Mineralogy, composition, and alteration of Mars Pathfinder rocks and soils: Evidence from multispectral, elemental, and magnetic data on terrestrial analogue, SNC meteorite, and Pathfinder samples, *J. Geophys. Res.*, *105*(E1), 1757–1817, doi:10.1029/1999JE001059.

Morris, R. V. et al. (2008), Iron mineralogy and aqueous alteration from Husband Hill through Home Plate at Gusev Crater, Mars: Results from the Mössbauer instrument

on the Spirit Mars Exploration Rover, *J. Geophys. Res.*, *113*(E12), E12S42, doi:10.1029/2008JE003201.

Morris, R. V. et al. (2016), Silicic volcanism on Mars evidenced by tridymite in high-SiO2 sedimentary rock at Gale crater, *PNAS*, *113*(26), 7071–7076, doi:10.1073/pnas.1607098113.

Murata, K. J., and J. K. Nakata (1974), Cristobalitic Stage in the Diagenesis of Diatomaceous Shale, *Science*, *184*(4136), 567–568, doi:10.1126/science.184.4136.567.

Nesbitt, H. W., and G. M. Young (1989), Formation and Diagenesis of Weathering Profiles, *The Journal of Geology*, *97*(2), 129–147.

Payne, J. H., and K. T. Mau (1946), A Study of the Chemical Alteration of Basalt in the Kilauea Region of Hawaii, *The Journal of Geology*, *54*(6), 345–358, doi:10.1086/625375.

Pe-Piper, G., A. Karim, and D. J. W. Piper (2011), Authigenesis of Titania Minerals and the Mobility of Ti: New Evidence From Pro-Deltaic Sandstones, Cretaceous Scotian Basin, Canada, *Journal of Sedimentary Research*, *81*(10), 762–773, doi:10.2110/jsr.2011.63.

Preston, L. J., G. K. Benedix, M. J. Genge, and M. A. Sephton (2008), A multidisciplinary study of silica sinter deposits with applications to silica identification and detection of fossil life on Mars, *Icarus*, *198*(2), 331–350, doi:10.1016/j.icarus.2008.08.006.

Prytulak, J., and T. Elliott (2007), TiO2 enrichment in ocean island basalts, *Earth and Planetary Science Letters*, *263*(3–4), 388–403, doi:10.1016/j.epsl.2007.09.015.

Rampe et al., E. B. (2017), Mineralogical trends in mudstone deposits from the Murray formation, Gale crater, Mars, *in revision at Earth and Planetary Science Letters*.

Rodgers, K. A., and G. Cressey (2001), The occurrence, detection and significance of moganite (SiO2) among some silica sinters, *Mineralogical Magazine*, *65*(2), 157–167, doi:10.1180/002646101550181.

Rodgers, K. A., K. L. Cook, P. R. L. Browne, and K. A. Campbell (2002), The mineralogy, texture and significance of silica derived from alteration by steam condensate in three New Zealand geothermal fields, *Clay Minerals*, *37*(2), 299–322, doi:10.1180/0009855023720035.

Ruff, S. W. et al. (2011), Characteristics, distribution, origin, and significance of opaline silica observed by the Spirit rover in Gusev crater, Mars, *Journal of Geophysical Research: Planets*, *116*(E7), n/a–n/a, doi:10.1029/2010JE003767.

Ruff, S. W., and J. D. Farmer (2016), Silica deposits on Mars with features resembling hot spring biosignatures at El Tatio in Chile, *Nature Communications*, *7*, 13554, doi:10.1038/ncomms13554.

Schiffman, P., R. Zierenberg, N. Marks, J. L. Bishop, and M. D. Dyar (2006), Acid-fog deposition at Kilauea volcano: A possible mechanism for the formation of siliceous-sulfate rock coatings on Mars, *Geology*, *34*(11), 921–924, doi:10.1130/G22620A.1.

Seelos, K. D., R. E. Arvidson, B. L. Jolliff, S. M. Chemtob, R. V. Morris, D. W. Ming, and G. A. Swayze (2010), Silica in a Mars analog environment: Ka'u Desert, Kilauea Volcano, Hawaii, *J. Geophys. Res.*, *115*(E4), E00D15, doi:10.1029/2009JE003347.

Siever, R. (1962), Silica Solubility, 0°-200° C., and the Diagenesis of Siliceous Sediments, *The Journal of Geology*, *70*(2), 127–150.

Skok, J. R., J. F. Mustard, B. L. Ehlmann, R. E. Milliken, and S. L. Murchie (2010), Silica deposits in the Nili Patera caldera on the Syrtis Major volcanic complex on Mars, *Nature Geosci*, *3*(12), 838–841, doi:10.1038/ngeo990.

Smith, M. R., J. L. Bandfield, E. A. Cloutis, and M. S. Rice (2013), Hydrated silica on mars: combined analysis with near-infrared and thermal-infrared spectroscopy, *Icarus*, doi:10.1016/j.icarus.2013.01.024.

Smith, M. R., and J. L. Bandfield (2012), Geology of quartz and hydrated silica-bearing deposits near Antoniadi Crater, Mars, *Journal of Geophysical Research: Planets*, *117*(E6), n/a–n/a, doi:10.1029/2011JE004038.

Squyres, S. W. et al. (2003), Athena Mars rover science investigation, *J.-Geophys.-Res.*, *108*(E12), 8062, doi:10.1029/2003JE002121.

Squyres, S. W. et al. (2008), Detection of Silica-Rich Deposits on Mars, *Science*, *320*(5879), 1063–1067, doi:10.1126/science.1155429.

Summons, R. E., J. P. Amend, D. Bish, R. Buick, G. D. Cody, D. J. Des Marais, G. Dromart, J. L. Eigenbrode, A. H. Knoll, and D. Y. Sumner (2011), Preservation of Martian Organic and Environmental Records: Final Report of the Mars Biosignature Working Group, *Astrobiology*, *11*(2), 157–181, doi:10.1089/ast.2010.0506.

Sun, V. Z., and R. E. Milliken (2015), Ancient and recent clay formation on Mars as revealed from a global survey of hydrous minerals in crater central peaks, *J. Geophys. Res. Planets*, *120*(12), 2015JE004918, doi:10.1002/2015JE004918.

Sun, V. Z., R. E. Milliken, and K. M. Robertson (2017), Distinguishing Opal Types and Their Water Distributions from Near-Infrared Spectroscopy for Applications to Mars, *in prep*.

Thompson, L. M. et al. (2016), Potassium-rich sandstones within the Gale impact crater, Mars: The APXS perspective, *J. Geophys. Res. Planets*, *121*(10), 2016JE005055, doi:10.1002/2016JE005055.

Tokashiki, Y., and K. Wada (1975), Weathering implications of the mineralogy of clay fractions of two Ando soils, Kyushu, *Geoderma*, *14*(1), 47–62, doi:10.1016/0016-7061(75)90012-9.

Tosca, N. J., and A. H. Knoll (2009), Juvenile chemical sediments and the long term persistence of water at the surface of Mars, *Earth and Planetary Science Letters*, *286*(3–4), 379–386, doi:10.1016/j.epsl.2009.07.004.

Vitale, M. (2002), Factors controlling the formation of mineral precipitates lining the channel in Rabbit Creek Yellowstone National Park Wyoming, *Theses, Dissertations, Professional Papers*.

Walter, M. R., and D. J. Des Marais (1993), Preservation of Biological Information in Thermal Spring Deposits: Developing a Strategy for the Search for Fossil Life on Mars, *Icarus*, *101*(1), 129–143, doi:10.1006/icar.1993.1011.

Williams, L. A., and D. A. Crerar (1985), Silica Diagenesis, II. General Mechanisms, *Journal of Sedimentary Research*, *55*(3).

Williams, L. A., G. A. Parks, and D. A. Crerar (1985), Silica Diagenesis, I. Solubility Controls, *Journal of Sedimentary Research*, *55*(3).

Wilson, M. J. (2014), The structure of opal-CT revisited, *Journal of Non-Crystalline Solids*, *405*, 68–75, doi:10.1016/j.jnoncrysol.2014.08.052.

Weitz, C. M., J. L. Bishop, P. Thollot, N. Mangold, and L. H. Roach (2011), Diverse mineralogies in two troughs of Noctis Labyrinthus, Mars, *Geology*, *39*(10), 899–902, doi:10.1130/G32045.1.

Wray, J. J. et al. (2011), Columbus crater and other possible groundwater-fed paleolakes of Terra Sirenum, Mars, *Journal of Geophysical Research: Planets*, *116*(E1), n/a–n/a, doi:10.1029/2010JE003694.

Young, G. M., and H. W. Nesbitt (1998), Processes Controlling the Distribution of Ti and Al in Weathering Profiles, Siliciclastic Sediments and Sedimentary Rocks, *Journal of Sedimentary Research*, *68*(3).

Tables

Table 1. Summary of the opaline and crystalline minerals in our sample suites. The number of samples containing each phase is also indicated. “Pure” opal-A or opal-CT indicates that those samples contain no other accessory minerals.

Suite	Locale	Opal	Crystalline Si	2.2 µm Phase	Ti/Zn	Igneous	Other
HI	**Ka'u Desert (KD): 5**	None: 5	Cristobalite: 5		Spinel: 1	Pyroxene: 5 Plagioclase: 5	Hematite: 3
	Mauna Loa (ML): 15	Slight opal-A: 6 None: 9	Cristobalite: 14	Gibbsite: 2	Spinel: 1	Olivine: 5 Pyroxene: 14 Plagioclase: 14	Hematite: 1 Pyrite: 2
	Mauna Ulu (MU): 9	Slight opal-A: 5 None: 4	Cristobalite: 6	Gypsum: 2 Jarosite: 1		Olivine: 8 Pyroxene: 6 Plagioclase: 2	Hematite: 1 Akaganeite: 1
	Steam Vents (SV): 4	Slight opal-A: 1 None: 3	Cristobalite: 3 Quartz: 1	Kaolinite: 3 Gibbsite: 1 Hisingerite/halloysite: 1	Spinel: 2	Olivine: 1 Pyroxene: 4 Plagioclase: 3	Goethite: 1 Molybdenite: 1 Magnesite: 2
	Sulphur Banks (SB): 14	Opal-CT: 1 Opal-A/CT: 1 Opal-A: 12 None: 1	Cristobalite: 11 Quartz: 7 Tridymite: 2 Stishovite: 1	Jarosite: 4 Gypsum: 4 Kaolinite: 2 Alunite: 1 Hisingerite/halloysite: 2	Anatase: 9 Ilmenite: 4 Rutile: 5 Titanite: 1 Spinel: 1 Sphalerite: 1	Olivine: 2 Pyroxene: 7 Plagioclase: 6	Hematite: 4 Pyrite: 1 Lizardite: 2 Magnetite: 4 Antigorite: 1 Calcite: 1 Sulfur: 4 Magnesite: 3
YS	**Nymph Lake (NL): 8**	Slight opal-A: 6 Opal-A: 2	Cristobalite: 8 Quartz: 7 Tridymite: 7	Kaolinite: 2 Gypsum: 1	Titanite: 1	Orthoclase: 6	
	Octopus Spring (OS): 5	Opal-A: 5	Cristobalite: 3 Quartz: 5		Titanite: 1 Anatase: 1 Sphalerite: 1		Halite: 2
	Rabbit Creek M (RCM): 7	Slight opal-A: 1 Opal-A: 5 None: 1	Cristobalite: 7 Quartz: 7 Tridymite: 2 Stishovite: 1	Kaolinite: 6	Titanite: 1 Anatase: 1 Ilmenite: 1		Calcite: 1 Magnesite: 1
	Rabbit Creek F (RCF): 7	Opal-A: 6 Opal-A/CT: 1	Quartz: 7				Calcite: 2
	Steep Cone (SC): 11	Pure opal-A: 6 Opal-A: 5	Cristobalite: 4 Quartz: 3 Tridymite: 1	Kaolinite: 1	Spinel: 1		Halite: 1

	Sentinel Meadow (SM): 5	Opal-A: 5	Cristobalite: 3 Quartz: 4		Rutile: 1	Plagioclase: 1	Halite: 1
NZ	**Umukuri (UM): 16**	Opal-CT: 14 Pure quartz: 2	Quartz: 14				
	Sinter Island (SI): 10	Opal-A: 3 Opal-A/CT: 3 Opal-CT: 4	Cristobalite: 1 Quartz: 10	Kaolinite: 3			
	Tahunaatara (TH): 6	Opal-A: 6	Cristobalite: 4 Quartz: 6		Titanite: 3 Ilmenorutile: 1 Spinel: 1	Pyroxene: 1 Plagioclase: 2	Hematite: 1
	Te Kopia (TK): 6	Opal-A: 2 Opal-CT: 4	Cristobalite: 1 Quartz: 6	Kaolinite: 4	Titanite: 1 Sphalerite: 1		
	Other: 7	Opal-A: 3 Pure opal-A: 2 Opal-CT: 2	Cristobalite: 1 Quartz: 5		Titanite: 1	Beryl: 2	
D. Bish	**Humboldt County, NV**	Pure opal-CT: 1					

Table 2. Summary of FWHM, peak position, and T/C ratio values for the opal types in our sample suites.

Opal Type (Suite, # samples)	FWHM Range (˚2θ)	FWHM Average (˚2θ)	Peak Position Range (Å)	Peak Position Average (Å)	T/C Ratio Range	T/C Ratio Average
A (HI, 5)	7.84-7.94	7.88	3.96-3.98	3.97	0.78-0.85	0.83(2)
A (YS, 27)	6.67-8.06	7.31	3.93-4.04	4.00	0.78-0.86	0.82(9)
A (NZ, 16)	6.25-7.36	6.95	4.00-4.15	4.04	0.83-0.89	0.86
A/CT (YS, 1)	-	5.84	-	4.11	-	0.80
A/CT (NZ, 3)	1.38-3.37	2.06	4.12-4.13	4.13	0.44-0.61	0.50
CT (NZ, 24)	0.59-1.91	0.88	4.08-4.13	4.10	0.26-0.52	0.34
CT (D. Bish)	-	1.98	-	4.10	-	0.57
Quartz (NZ, 2)	0.14-0.18	0.16	4.26(8)-4.27(2)	4.27	0	0

Table 3. Comparison of FWHM and peak positions for New Zealand samples used in our study and in previously published works. See **Section 3.3** for references to previously published measurements. Note that any discrepancies between the numbers of samples reported here and in **Table 2** are caused by omission of samples containing significant accessory minerals, etc.

Suite	Opal Type (# samples)	FWHM (Literature, ˚2θ)	FWHM (This study, ˚2θ)	Peak Position (Literature, Å)	Peak Position (This study, Å)
Umukuri	CT (14)	0.54-0.69	**0.63-0.71**	4.05-4.13	**4.08-4.11**
	C	0.43-0.8	**absent**	-	**absent**
	Quartz (2)	0.2	**0.14-0.18**	-	**4.27**
Sinter Island	A (3)	6.1-7.15	**6.25-7.16**	-	**4.02-4.15**
	A/CT (3)	3.55-6.0	**1.38-3.37**	-	**4.12-4.13**
	CT (4)	0.86-2.5	**0.91-1.17**	-	**4.10-4.12**
	C	0.7-0.85	**absent**	-	**absent**
	Quartz	0.2-0.4	**absent**	-	**absent**
Tahunaatara	A (6)	6.0-9.0	**6.68-7.14**	4.01-4.17	**4.04-4.07**
Te Kopia	A (2)	5.65-7.4, 7.95	**6.63-6.96**	4.03, 4.08-4.13	**4.05-4.06**
	A/CT	1.35-4.8	**absent**	4.09-4.1	**absent**
	CT (4)	1.15	**1.44-1.91**	4.08	**4.11-4.13**
Other	A (5)	-	**7.02-7.36**	-	**4.00-4.04**
	CT (2)	-	**0.59-0.65**	-	**4.10-4.11**

Table 4. Average major element chemistry for our sample suites, values in oxide weight percent or CIA percent. The Hawaii suite is split into two groups, KD/ML/MU and SV/SB as described in **Section 5.1.1.** The Yellowstone and New Zealand samples are all sinters from acidic or neutral-alkaline environments and have been divided as such **(Sections 5.1.2-3)**. Steve Ruff also provided chemistry for additional samples from Hawaii and Yellowstone; these are included in the grey boxes for comparison with our samples.

Suite (# samples)	Al_2O_3	CaO	Cr_2O_3	Fe_2O_3	K_2O	MgO	MnO	Na_2O	NiO	P_2O_5	SiO_2	TiO_2	CIA
HI opal-poor: KD/ML/MU (11)	13.49	8.1	0.07	13.38	0.3	7.86	0.16	1.68	0.03	0.16	46.84	2.31	56.96
HI opal-rich: SV/SB (11)	4.27	1.06	0.05	8.14	0.14	1.51	0.04	0.17	0.01	0.12	63.15	3.08	76.08
S. Ruff HI-SV/SB (7)	4.66	1.79	-	4.29	0.14	2.45	0.05	0.27	-	0.15	70.19	3.82	75.49
YS acidic: NL/RCM (5)	6.27	0.17	<0.01	1.43	1.18	0.03	<0.01	0.86	<0.01	0.07	84.6	0.13	68.73
YS alkaline: OS/RCF/SC/SM (6)	0.85	0.26	<0.01	0.1	0.24	0.03	0.01	1.07	<0.01	0.06	90.87	0.02	37.15
S. Ruff YS acid. (11)	4.44	0.45	-	0.64	1.15	0.12	0.02	1.13	-	0.02	82.29	0.15	61.82
S. Ruff YS alk. (10)	0.51	0.14	-	0.15	0.18	0.05	0.02	0.42	-	0.01	90.06	0.03	42.37
NZ acidic: SI/TK (4)	1.69	0.27	0.04	0.3	0.4	0.09	0.01	0.31	0.05	0.07	92.51	0.08	60.67
NZ alkaline: UM/TH (7)	1.39	0.21	0.03	0.3	0.37	0.04	0.01	0.34	0.03	0.07	95.04	0.05	60.44

Figures

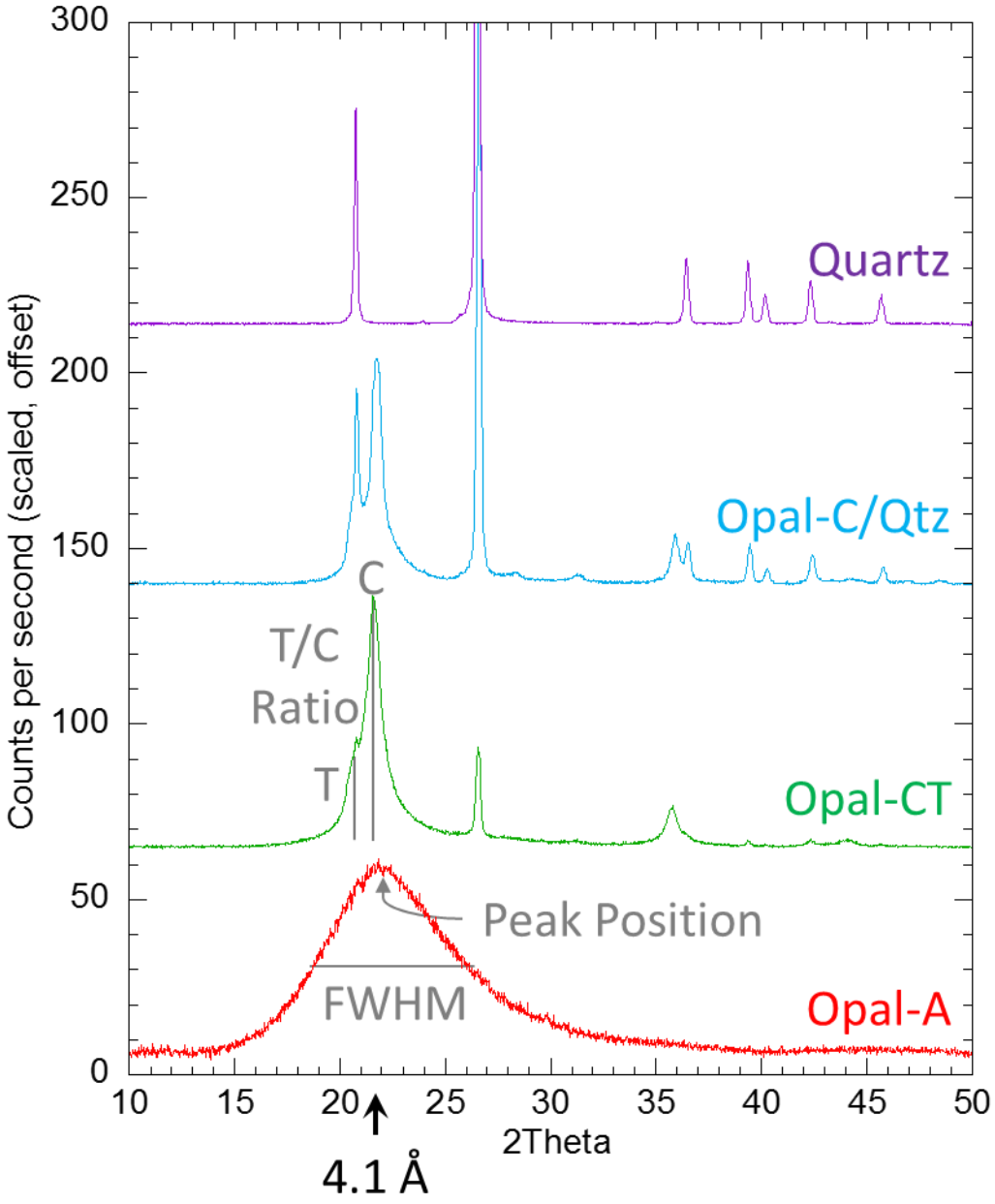

Figure 1. Representative XRD patterns of opal-A, opal-CT, opal-C with quartz, and quartz. Annotations indicate the parameters that are related to opal crystallinity: the 4.1 Å FWHM, peak position, and tridymite/cristobalite intensity ratio.

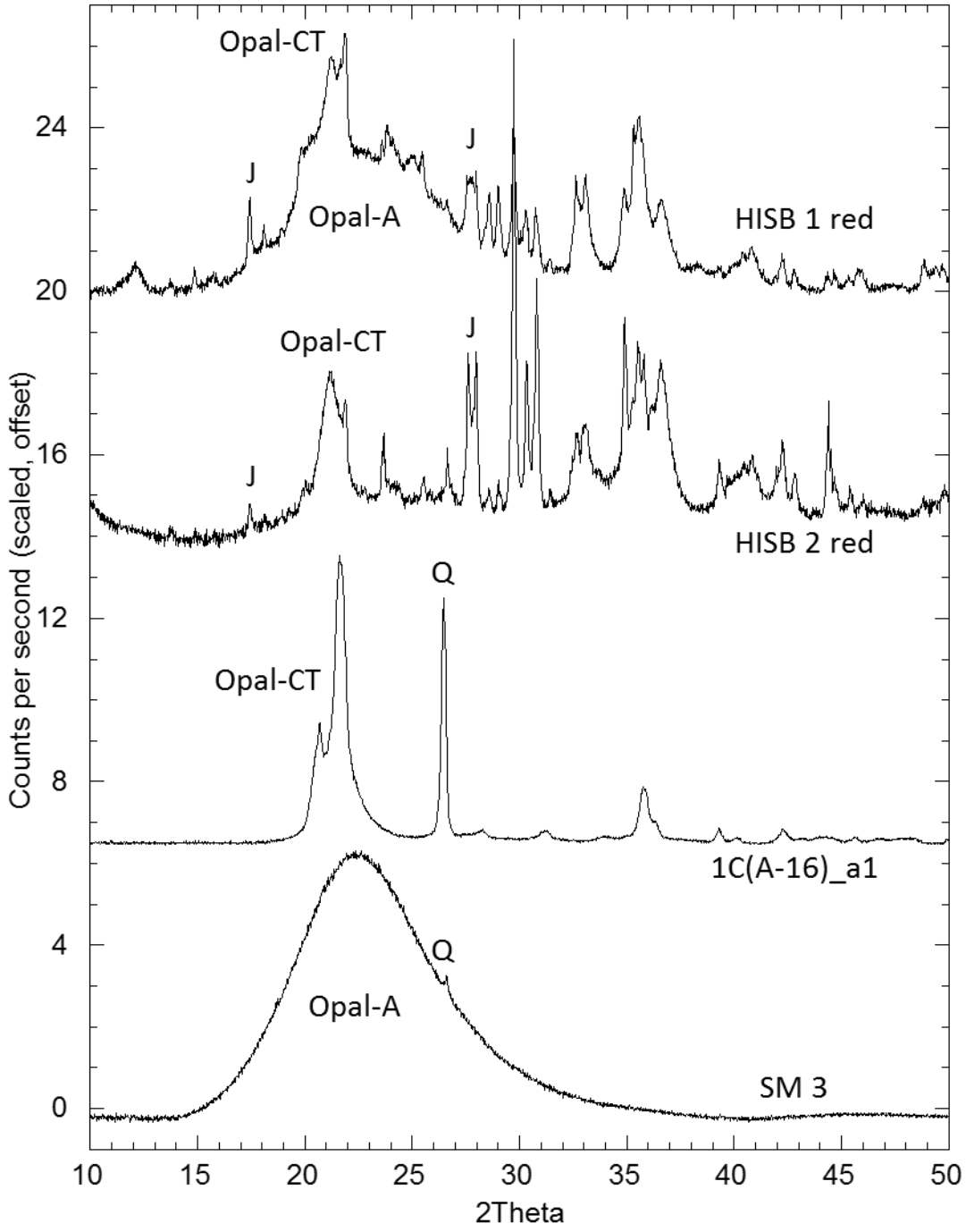

Figure 2. XRD patterns showing putative opal-CT peaks in the Hawaii sample suite, with a Yellowstone opal-A and New Zealand opal-CT for comparison. Sharp discrete peaks represent quartz (Q), jarosite (J), and other igneous minerals. A broad shoulder at 20˚ 2θ in the HISB 2 red sample may be attributed to halloysite or hisingerite.

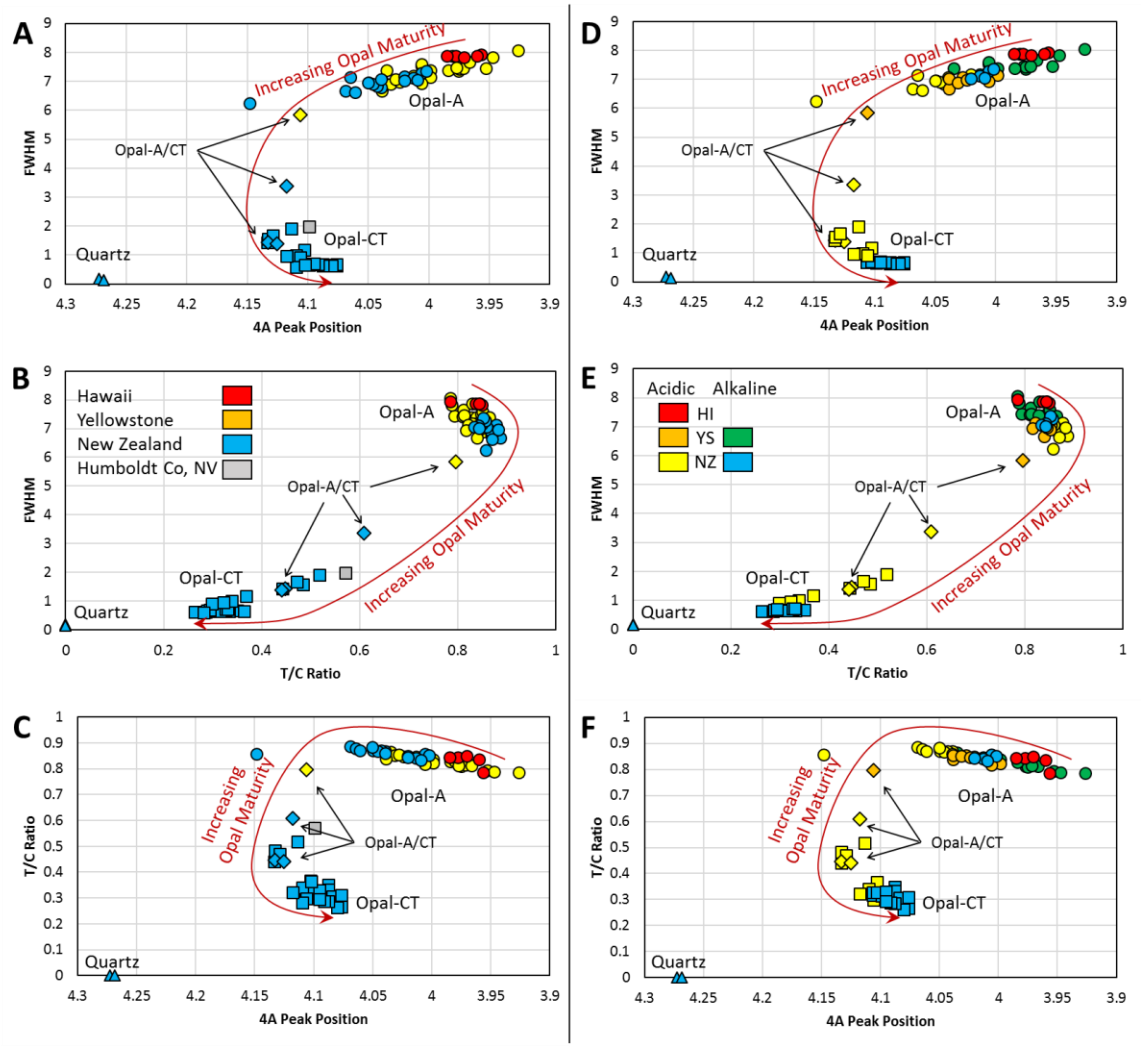

Figure 3. Plots of FWHM, 4.1 Å peak position, and tridymite/cristobalite intensity ratio against each other. Colors in **A-C** indicate sample suite (HI, YS, NZ, opal-CT from D. Bish), while those in **D-F** indicate acidic (warm colors) or neutral-alkaline (cool colors) environments. Circles indicate opal-A, diamonds opal-A/CT, squares opal-C, and triangles quartz. Curves indicate the inferred opal maturation sequence in this parameter space. Note that the x-axis is reversed for the top and bottom plots.

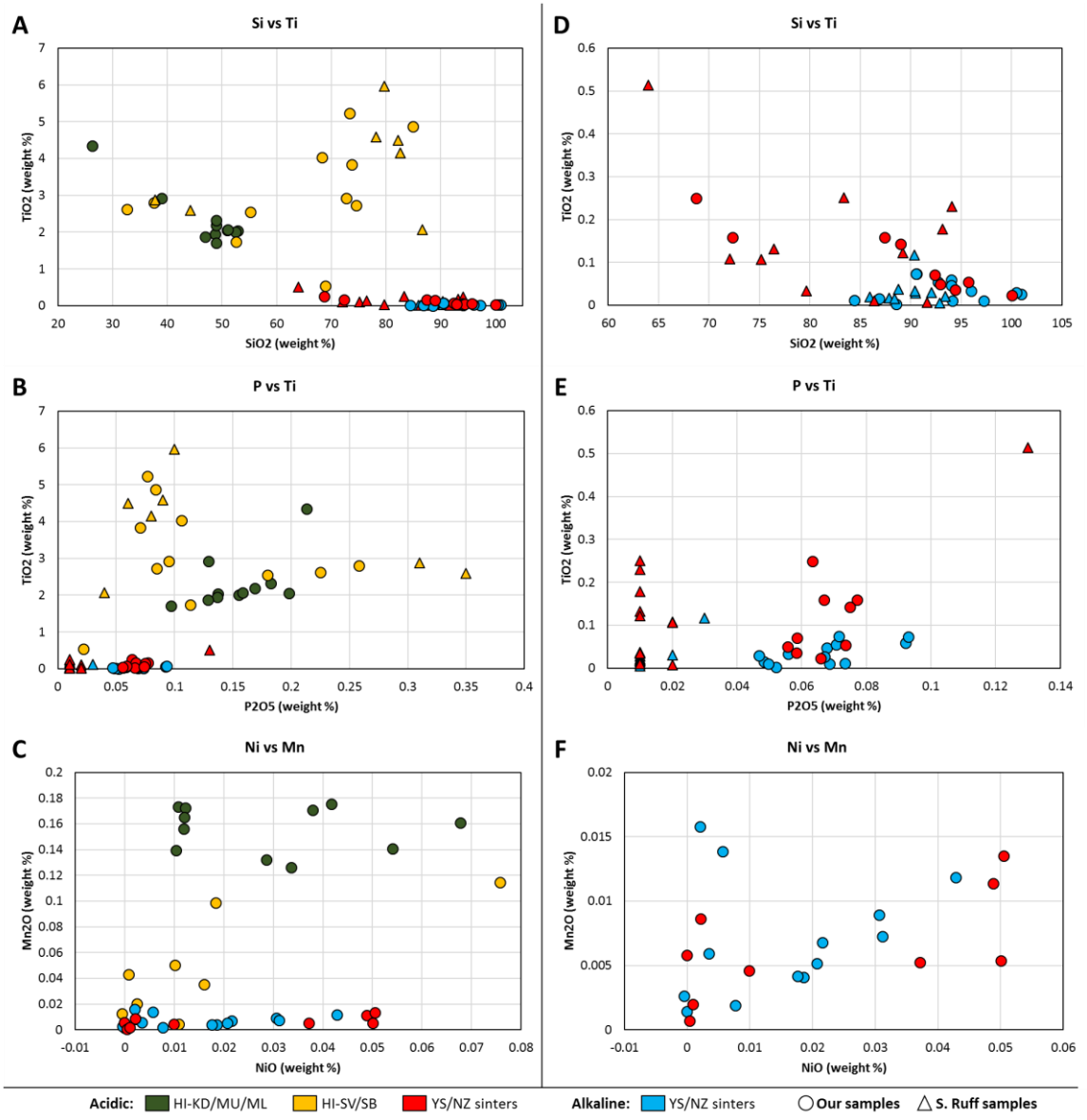

Figure 4. Chemical oxide trends from all of our and S. Ruff's samples for **A)** Si vs. Ti, **B)** P vs. Ti, and **C)** Ni vs Mn. Colors indicate sample suite and approximate environmental pH represented by that suite. Figures **D-F** show the same trends, but only for the YS/NZ sinters, sorted by acidic or alkaline environment.

CHAPTER 4:

Distinguishing Opal Types and Their Water Distributions from Near-Infrared Spectroscopy for Applications to Mars

Vivian Z. Sun,

Ralph E. Milliken, Kevin M. Robertson

Department of Earth, Environmental, and Planetary Sciences, Brown University,

Providence, RI 02912, USA

To be submitted:

Summer 2017

Abstract

Identification of opal type can reveal information about the geochemical maturity and extent of aqueous alteration in an environment. Although orbital infrared spectroscopy has identified opaline silica across Mars, it has been difficult to distinguish between different opal types (e.g., opal-A versus opal-CT), which are spectrally similar despite containing different distributions of water. In this work we develop spectral parameters to characterize opal's 1.4, 1.9, and 2.2 μm absorptions for a suite of terrestrial opal-A and opal-CT samples. Band position, depth, area, and Gaussian fits were used to quantify variations in these features, which each consist of a short-wavelength absorption due to structural SiOH or H_2O and a long-wavelength absorption indicative of H-bonding to H_2O. We find that opal-A and opal-CT can be distinguished by a longer-wavelength 1.4 μm band position for opal-CT and a higher ratio of the 2.26/2.21 μm band depths or Gaussian amplitudes for opal-A. These parameters work for both powder and rock samples, can identify materials with >80 wt% opal, and are additionally advantageous when applied to orbital Mars data because they are less affected by atmospheric absorptions and the presence of other H_2O-bearing minerals at 1.9 μm. Another new finding from this work is that opal-CT tends to adsorb H_2O in multiple layers with H-bonding to other H_2O, whereas opal-A adsorbs more H_2O as a monolayer bonded to SiOH. These results demonstrate a fundamental difference in the H_2O-bonding environments between opal-A and opal-CT and may guide interpretations of orbital opal detections on Mars.

1. Introduction

Hydrated or opaline silica has been widely detected on Mars by orbital spectrometers [e.g., Milliken et al., 2008; Bandfield, 2008], confirming early predictions of widespread secondary silica phases on this basaltic planet [McLennan, 2003]. These opal occurrences are evidence of past aqueous conditions, but the nature of their formation environments with regards to pH and water availability is still uncertain. Information such as accessory mineralogy and opal type can help resolve some of these conditions and are attainable through orbital spectroscopy. In particular, visible-near-infrared hyperspectral spectrometers such as CRISM (Compact Reconnaissance Imaging Spectrometer for Mars) [Murchie et al., 2007] allow for identification of these hydrated phases at spatial resolutions (~18 m/pixel) sufficient for correlating with high-resolution imagery.

Inorganic opal forms in a variety of acidic to alkaline environments, initially precipitating as amorphous opal-A and converting or "maturing" to more crystalline opal-CT, opal-C, and microcrystalline quartz with subsequent aqueous alteration [Krauskopf, 1956; Siever, 1962; Williams and Crerar, 1985]. This diagenetic opal sequence therefore provides a metric for measuring water longevity, with the presence of mature opals indicating more intense or prolonged aqueous conditions. For example, the apparent prevalence of opal-A and lack of opal-CT/C on Mars has been taken to suggest limited water availability [Tosca and Knoll, 2009; Smith et al., 2013]. Opals also enable microfossil preservation [Cady and Farmer, 1996; Konhauser et al., 2003], with immature opals offering better preservation quality [Jones and Renaut, 2003; Campbell et al., 2015]. The ability to discern aqueous activity and identify regions with the best

biopreservation potential are compelling reasons to distinguish between the different opal types.

Orbital spectroscopy is the predominant method of identifying opaline silica on Mars on a global scale, but distinguishing specific opal types has proved difficult. Identifying opals at thermal infrared wavelengths is possible but may be confounded by emission features from other silicate minerals, particularly at the coarser spatial resolutions of current orbital thermal infrared spectrometers [e.g., Michalski et al., 2003; Goryniuk et al., 2004]. However, at near-infrared (NIR) wavelengths, opal has characteristic hydration absorptions at 1.4, 1.9, and 2.2 μm whose shapes are likely to vary due to different water distributions within different opal types [Langer and Florke, 1974]. Rice et al. [2013] were the first to parameterize opal's NIR absorptions for application to Mars data. They found that silica phases (e.g., quartz versus opal) were differentiable from their 1.4 and 1.9 μm absorptions, and opal types (e.g., opal-A vs. opal-CT) were distinguishable only by the band depth ratio of the 2.2 to 1.9 μm absorptions.

However, several complications may arise from using the 1.9 μm absorption to distinguish between opal types. The 1.9 μm H_2O absorption is not unique to opals and could be affected by the presence of any hydrated mineral bearing H_2O. CRISM data are also affected by residual atmospheric absorptions in the 2 μm region, which occlude the longer wavelength portions of the 1.9 μm absorption (e.g., ~1.96 μm). Subsequent work by Robertson et al. [2013] also showed that these parameters could be heavily influenced by opal water content, regardless of opal type. In comparison, the 2.2 μm feature is more indicative of opal's silanol (SiOH) groups but has not been studied in detail except by

Langer and Florke [1974] and Rice et al. [2013]. Still, the broad shape of the 2.2 μm feature has not been fully characterized by parameters used in previous work.

In this study we build on previous work by Rice et al. [2013] and Robertson et al. [2013] to determine the best NIR spectral parameters for distinguishing between specific opal types. Here we focus on the 1.4 and 2.2 μm features, which are more unique to opal, and also employ Gaussian modeling, as suggested by Langer and Florke [1974] and Rice et al. [2013], to better characterize opal's broad absorption features. These results will enable identification of particular opal types and therefore inferences of water activity in opal-rich environments on Mars.

2. Background

The amorphous structure of opaline silica allows water to exist within structural imperfections and bonded to surfaces, in contrast to the compact crystalline structures of nominally anhydrous silica phases such as quartz, cristobalite, and tridymite. Water is incorporated in opaline silica as two chemical groups – molecular water (H_2O) and silanol (SiOH) – that each may occur in two bonding scenarios depending on the influence of H-bonding **(Figure 1)**. The terminology for these groups differs throughout the literature, but the following classifications from Langer and Florke [1974] will be used in this work.

Structurally bound water is referred to as Type A; for silanols this includes surficial and internal SiOH that are not H-bonded to H_2O (but may be H-bonded to other silanols). Type A H_2O can be completely isolated in voids [Langer and Florke, 1974] or H-bonded to SiOH [Anderson and Wickersheim, 1964; Burneau et al., 1990], but is not

H-bonded to additional H_2O that is adsorbed as subsequent layers. There is some inconsistency in the literature as to which definition of Type A H_2O is adopted, but in this work we define Type A H_2O to include both isolated H_2O and the first layer of H_2O bound to SiOH. Type B describes chemical groups that are H-bonded to H_2O. For example, Type B SiOH can be H-bonded to Type A H_2O at the surface or in inclusions. Type B H_2O is H-bonded to other H_2O molecules, either within inclusions or adsorbed in multiple layers at the silica surface.

Distinguishing these four groups (Type A SiOH, Type A H_2O, Type B SiOH, and Type B H_2O) is important because they are distributed differently within the various opal types. The absorptions related to each group manifest at different wavelengths, allowing for assessment of their population distributions, and thereby opal type, from NIR spectroscopy. The term "total water" or, more generically, "water", will hereafter refer to the sum of Type A and B H_2O and SiOH. We note again that the aforementioned terms are not universally adopted throughout the literature. Many studies refer to Type A and B or Type I and II to distinguish between structural and H-bonded groups or surficial and internal groups.

2.1 Opal Water Content and Distribution

Total water generally decreases with opal crystallinity. Surveys of opaline sinters document upwards of 4-10 wt% water in opal-A, <7 wt% water in opal-CT/C, and <0.2 wt% water in microcrystalline quartz [Herdianita et al., 2000a; Campbell et al., 2001]. Synthetic silica gels, which are more amorphous than opal-A, can have as much as 20-30 wt% water [Krauskopf, 1956]. However, water content can vary from sample to sample,

and it is not uncommon to find an opal-CT with more water than an opal-A or a volcanic agate (a microcrystalline quartz) with as much as 1-2 wt% water [Florke et al., 1982]. Different water contents can even be found within the same opal phase in the same sample. Jones and Renaut [2004] reported two opal-A varieties that likely precipitated or dehydrated under different conditions, with the "dry" opal (5-9 wt% water) cemented by "wet" opal (10-14 wt% water). We direct the reader to **Appendix A** for more information on the methods and uncertainties associated with quantifying water content in opals.

Quantifying SiOH and H_2O and their Type A and Type B subdivisions across the different opal types is similarly nebulous. Opal-CT tends to have less SiOH than opal-A, but their H_2O content varies widely [Langer and Florke, 1974]. The lower SiOH content of opal-CT may be attributed to conversion of silanol to siloxane, resulting in the increase of short-range structural order as observed in XRD [Rodgers et al., 2004; Day and Jones, 2008]. Silanols can be further subdivided into single and geminal SiOH, referring respectively to one or two hydroxyls attached to a single silicon atom, with opal-CT containing a higher proportion of geminal SiOH compared to opal-A [Brown et al., 2003; Bobon et al., 2011]. Silanol and H_2O populations have also been studied for other silica polymorphs like microcrystalline quartz [Graetsch et al., 1985; Yamagishi et al., 1997] and glasses [Stolper, 1982], but do not seem to follow any trends in relation to opal.

The proportion of Type A to Type B H_2O also decreases with increasing opal crystallinity. Langer and Florke [1974] found opal-A to have relatively more Type A H_2O than opal-CT, and Campbell et al. [2001] similarly reported more Type A water in opal-CT/C relative to microcrystalline quartz. The complementary statement is that the proportion of Type B H_2O, which is often adsorbed, increases with crystallinity; for

instance, almost all of the H_2O in microcrystalline quartz is adsorbed [Florke et al., 1982]. In opal-CT this increased H_2O adsorption may be attributed to its large and irregular internal surface and microstructure [Langer and Florke, 1974]. Alternatively, Bobon et al. [2011] proposed that opal-CT's higher proportion of geminal silanols facilitate H_2O adsorption, while opal-A's higher proportion of single silanols limits the number of adsorption sites **(Figure 1)**. Despite the literature on Type A and B H_2O, not much is specifically reported on Type A and B SiOH.

To briefly summarize, opal's total water content, SiOH content, and proportion of Type A to Type B H_2O tends to decrease with increasing crystallinity. However, there does not seem to be a consensus in the literature on H_2O content or the proportion of Type A to Type B SiOH within the opal continuum.

2.2 Opal Absorptions at Near-Infrared Wavelengths (1-4 μm)

Opal's spectral features in the NIR wavelengths reflect absorptions due to the H_2O and SiOH groups described previously **(Table 1)**. The 1.4, 1.9, and 2.2 μm features have been documented throughout the opal literature (references 1-8 in **Table 1**) and are understood to consist of at least two sub-absorptions at a shorter wavelength (1.4, 1.9, 2.2 μm) and at a longer wavelength (1.46, 1.96, 2.26 μm) [e.g., Anderson and Wickersheim, 1964; Langer and Florke, 1974].

The shorter wavelength features correspond to Type A water. Silanol that is not H-bonded to H_2O will manifest at 2.2 μm, and H_2O that is isolated or H-bonded to SiOH (but not to additional H_2O) will appear at 1.9 μm. The absorption at 1.4 μm is an overtone of the fundamental OH stretch in both SiOH and H_2O, found in the 2.7-2.8 μm

region. The longer wavelength Type B features are attributed to the effects of H_2O that is H-bonded to SiOH or H_2O. The 2.26 μm feature indicates SiOH that is H-bonded to H_2O, which shifts the frequency of the Si-OH bond to this longer wavelength. The 1.96 μm absorption is due to H-bonding between multiple H_2O, which produces weaker bonds compared to Type A H_2O bonded to SiOH and results in a longer wavelength, lower energy absorption. This is sometimes referred to as "polymeric", "networked", or "molecular" H_2O, much like in liquid water, and occurs within H_2O inclusions and when atmospheric H_2O is adsorbed as multiple layers. The 1.46 μm feature is also an overtone of the OH stretch in both SiOH and H_2O but again reflects the effects of H-bonded H_2O.

The above absorptions have been identified in opals, but additional insights have been gained from spectroscopy of silica gels and glasses in the material science field, where silica is of interest due to the flexibility of its Si-O-Si bond and its use in electronic devices, solar cells, and optical fibers. Many of these works (references 9-25 in **Table 1**) studied synthetic silica gels and employed additional experiments to understand water bonding environments (e.g., heating and thermoanalytical methods, reaction with chlorosilane, deuterium exchange, ab initio studies) [e.g., Gallego-Gomez et al., 2011]. These studies revealed more nuanced absorptions, for instance, due to H-bonding between adjacent SiOH that vary slightly depending on whether the O or H is perturbed [Van Roosmalen and Mol, 1978; Tsuchiya, 1982; Hoffman and Knozinger, 1987; Burneau et al., 1990; Tielens et al., 2008]. Making these distinctions is beyond the scope of this work but the general delineation of silanol absorptions in the 2.6-4 μm range is relevant to distinguishing opal types.

A sharp absorption at 2.68 μm is attributed to "isolated" or "free" SiOH that is not H-bonded to H_2O or other SiOH **(Figure 1)**. However, this absorption disappears upon further hydration, indicating that free SiOH are located at the mineral surface and available for bonding with adsorbed H_2O. This 2.68 μm feature is paralleled at 1.36, 1.88, and 2.18 μm, though they are rarely discussed in the opal literature.

Silanols that experience H-bonding have fundamental OH stretch absorptions in the 2.69-2.86 μm range that can be further subdivided into single, geminal, and adjacent SiOH features. Care must be taken when interpreting the literature, as single SiOH are also inconsistently referred to as "vicinal", "isolated", or "terminal". Among studies that distinguish between single and geminal (or "twin" or "double") SiOH absorptions, the geminal species is typically at slightly longer wavelengths [Hockey and Pethica, 1961; Hair and Hertl, 1968; Jones and Segnit, 1969; Van Roosmalen and Mol, 1978; Hoffman and Knozinger, 1987; Bunker et al., 1989]. Single SiOH may appear at 2.7-2.74 μm, whereas geminal SiOH appear at 2.82-2.86 μm; both species reflect the influence of H-bonding to H_2O. This distinction offers potential for discerning opal type as opal-CT may have proportionally more geminal SiOH compared to opal-A [Brown et al., 2003; Bobon et al., 2011].

Silanols that are H-bonded to each other **(Figure 1)** are called "adjacent", "vicinal", "bridged", or "polymeric" and have been assigned to features throughout the entire 2.69-2.86 μm range, depending on the study. This wide range is likely due to the diverse bonding environments that can occur between adjacent combinations of both single and geminal SiOH. Polymeric H_2O absorbs at wavelengths above 2.8 μm, with

their longer wavelength positions indicating their loosely bound nature and lower energy of removal.

2.3 Previous Work on Spectral Differentiation of Opal-A and Opal-CT

While general opal absorptions have been well-documented, few studies have focused on distinguishing between natural opal-A and opal-CT using NIR spectroscopy. Langer and Florke [1974] determined opal-CT to have proportionally more Type B H_2O from its 1.9 and 1.96 μm features, but did not explicitly compare the 2.2-2.26 μm SiOH absorptions between opal-A and opal-CT. Bobon et al. [2011] similarly focused on the 1.9-1.96 μm absorption to propose that opal-CT has a higher proportion of geminal SiOH sites than opal-A.

Recently, Rice et al. [2013] initiated the study of spectral opal differentiation for application to Mars datasets. This study used band positions and band depth ratios to parameterize the Type A and Type B absorptions at 1.4, 1.9, and 2.2 μm for a comprehensive suite of natural and synthetic silica samples. They found that the 1.4 μm absorption position and 1.91/1.96 μm band depth ratio could distinguish between silica phases, such as between opal and microcrystalline quartz, but not between specific opal types. The ratio of the 2.2 to 1.9 μm band depths proved to be more discerning as it is generally, though not uniquely, higher for opal-A than opal-CT.

Relying on the 1.9 μm feature to indicate opal type has additional limitations. Opal-A dehydration experiments by Robertson et al. [2013] showed that the 1.4 and 1.9 μm parameters can reflect water content rather than opal type, which is a concern due to the widely varying water contents in natural opals **(Section 2.1)**. In relevance to Mars applications, interpretation of the 1.9 μm absorption is also complicated by its presence in

other H_2O-bearing minerals that may be found mixed with opal. The longer wavelength feature at >1.96 μm may also be obscured in Mars spectra due to atmospheric absorptions in the 2 μm range.

With these concerns in mind, this study extends from these previous works to determine NIR spectral parameters that can distinguish between opal types, specifically opal-A and opal-CT. In particular, we focus on the 2.2 μm SiOH feature, as it is more diagnostic of opals than the 1.9 μm feature. We explore the use of Gaussian models, as suggested by Langer and Florke [1974] and Rice et al. [2013] to characterize opal's broad absorptions and also study absorptions in the 2.6-4 μm range to help interpret the 1.4, 1.9, and 2.2 μm features.

3. Experimental Methods

A total of 135 samples were collected from Mars-analog sites and measured for their spectra (0.4-25 μm) at Brown University's Reflectance Experiment Laboratory (RELAB) facility. These materials were sourced from Hawaii, Yellowstone, and New Zealand and their chemistry and mineralogy were characterized in a previous study [Sun et al., 2017]. An additional pure opal-CT sample from Humboldt County, Nevada was provided courtesy of David Bish. These samples are known to contain opal-A, opal-CT, and microcrystalline quartz from X-ray diffraction (XRD) patterns, which will be used to corroborate the spectral observations in this work. Sample chips were first measured for their spectra and then hand-ground and sieved to <45 μm using a mortar and pestle, after which the resulting powders were measured. An effort was made to separate coatings and weathering rinds from rock interiors when possible, particularly for some Hawaii

samples. Of these samples, 73 were spectrally pure opals in that they contained opal and no other 2.2 µm-absorbing minerals **(Table 2)**; the remaining samples either contained no opal or opal mixed with other 2.2 µm-absorbing phases.

3.1 Spectral Measurements from 0.4-25 µm

Reflectance spectra of both rock chips and powders were obtained from 0.4-2.5 µm on an Analytical Spectral Devices (ASD) spectrometer at a sampling resolution of 1 nm. Measurements were taken over approximately 0.5 cm diameter spot sizes for powders, with incidence and emergence angles of 30° and 0° respectively. For rock chips, spectra were acquired over a spot size spanning the entire chip to reduce the effects of heterogeneously distributed minerals. The data were taken with respect to a Spectralon standard and later corrected for absolute reflectance by multiplication with a Spectralon spectrum obtained from the RELAB bidirectional spectrometer.

A Fourier Transform Infrared (FTIR) spectrometer was also used to take spectra from 1-4.7 µm using a CaF2 beam splitter and 1.5-25 µm using a KBr beam splitter. Reflectance data were obtained at a sampling resolution of 0.482 cm^{-1} and then converted to wavelength units. All spectra were acquired under ambient conditions, which were typically 50% relative humidity at lab temperature (22°C) at the time of these measurements. Fluctuations in relative humidity can influence the amount of water adsorbed to mineral surfaces and thereby affect spectral absorptions related to water in the NIR. Although lab conditions were relatively consistent, samples from a single location suite (i.e. Hawaii, Yellowstone, New Zealand) were measured in succession on the same day to minimize the effects of atmospheric variations.

3.2 NIR Spectral Parameters

Based on the terrestrial geologic and material science literature **(Section 2.2)**, we focus on the three major opal features at 1.4, 1.9, and 2.2 μm. We assume that each of these features are composed of two distinct individual absorptions related to different populations of water in the opal structure. In each pair of absorptions, the shorter wavelength absorptions at 1.41, 1.91, and 2.21 μm are attributed to Type A H_2O or SiOH and the longer wavelength absorptions at 1.46, 1.96, and 2.26 μm are attributed to Type B H_2O or SiOH that is affected by H-bonding of H_2O. To characterize the relative amounts of these water species in our opal samples, we adopt four spectral parameters that were applied to each of the 1.4, 1.9, and 2.2 μm features: 1) the position of the absorption minimum, 2) band depth and band depth ratios, 3) band area and band area ratios, and 4) Gaussian amplitude ratios **(Figure 2)**. Our ratio calculations for band depth and Gaussian amplitudes are presented as the ratio of the longer wavelength absorption to the shorter wavelength absorption. Note that these parameters are largely correlated to one another; for instance, an absorption position at longer wavelengths will correspond to higher band depth ratios and Gaussian ratios.

To perform these calculations, each ASD spectrum was first continuum-corrected to measure the true band minimums and depths. The 1.4, 1.9, and 2.2 μm features were separately fit and divided by linear continuums with endpoints that were allowed to float between 1.3-1.35 μm and 1.5-1.7 μm for the 1.4 μm feature, 1.8-1.9 μm and 2.0-2.2 μm for the 1.9 μm feature, and 2.1-2.2 μm and 2.3-2.4 μm for the 2.2 μm feature. These endpoint ranges were determined through trial-and-error and continuums were calculated iteratively until all values in the divided spectrum were less than 1. Calculations of band

position, depth, and area were straightforward using the continuum-corrected spectra. The 1.4, 1.9, and 2.2 μm features were then modeled with two Gaussians centered at the shorter wavelength absorption (1.41, 1.91, and 2.21 μm) and the longer wavelength absorption (1.46, 1.96, and 2.26 μm). All calculated parameters were verified by visual inspection and omitted from analyses if appropriate (e.g., some samples entirely lack hydration absorptions).

3.3 Controlled Opal Mixtures

Binary mixtures of pure opal-A and montmorillonite or kaolinite were created to investigate the performance of our spectral parameters on materials that contain other 2.2 μm-absorbing minerals. Three Yellowstone samples – SM 1, OS 2, and NL 1 – were chosen as opal-A endmembers to span the range of observed 2.26/2.21 μm ratios. The montmorillonite and kaolinite are SAz-1 and KGa-1 from The Clay Minerals Society. Montmorillonite was chosen because the shapes of its spectral features are very similar to those of opal's, though montmorillonite absorptions are narrower. Kaolinite has distinctive doublets at 1.4 and 2.2 μm, but was included as another endmember due to its prevalence in our natural samples and in orbital detections on Mars.

For SM 1, 26 opal-montmorillonite and opal-kaolinite mixtures were prepared to represent 0, 5, 10, 20, 30, 40, 50, 60, 70, 80, 90, 95, and 100% Al-clay by mass. For OS 2 and NL 1, a total of 16 mixtures were created with 0, 5, 10, and 20% Al-clay by mass. All components were powdered to <45 μm, weighed for a total of 0.2 g per mixture, and mixed together at ambient laboratory conditions. Each mixture was measured three times on the ASD spectrometer, with unloading and repacking of the sample in between each

measurement to account for heterogeneities in the mixtures. Parameter calculations were performed on the three repeated measurements and then averaged together to obtain final parameter values for each mixture.

4. Results for Distinguishing Opal-A and Opal-CT

Here we assess the performance of our spectral parameters in distinguishing between opal-A and opal-CT. The 1.4 and 2.2 μm opal absorptions are the focus of this section, but we discuss the 1.9 μm and 2.6-4 μm absorptions in relation to opal's water content in **Section 5**. In **Sections 4.1 and 4.2** we focus on spectrally pure opal samples (powders and rock chips, respectively) whose XRD patterns do not contain other minerals that also absorb at 2.2 μm. In **Section 4.3** we apply our parameters to natural and lab-controlled mixtures of opal and other 2.2 μm-absorbing minerals to determine the detection limits of this methodology. In **Section 4.4**, we compare our results with those of Rice et al. [2013], which was the first study to establish this type of spectral analysis for application to Martian opals. The complete set of spectral data are available in **Appendix F**.

4.1 Distinguishing Opal Types using the 1.4 and 2.2 μm Parameters

The 1.4 μm band position and the 2.26/2.21 μm Gaussian ratio appear to be the most effective for diagnosing opal type in powdered opal samples **(Figure 3A)**. The other parameter variations for these features (described in **Section 3.2**) were also explored but only confirm the results presented here. In particular, using a band depth ratio in place of the Gaussian ratio achieves similar results **(Figure 3B)**, but we adopt Gaussian modeling

for the 2.2 μm feature in order to account for the entire absorption and avoid capturing noise in the data.

Opal-A tends to have absorption minima centered around 1.41 μm (ranging from 1.408-1.413 μm), while opal-CT minima span the range of 1.413-1.445 μm. Two quartz samples in our sample suite show even longer-wavelength minima ranging from 1.434-1.462 μm. Opals have distinct 2.2 μm Gaussian ratios as well, with opal-A values ranging from 1-3.24, opal-CT from 0.3-1, and quartz at ~0.2. In general, as opal crystallinity increases, the 1.4 μm absorption minimum shifts to longer wavelengths, while the 2.26/2.21 μm Gaussian ratio decreases.

It is notable that maturity or crystallinity gradients were observed within the opal-A and opal-CT groups for these samples based on their XRD patterns [Sun et al., 2017]. For instance, opal-A from the Hawaii suite had broader XRD-amorphous humps compared to some New Zealand opal-A and were inferred to be less crystalline or less mature opal-A. However, no similar trends are observed in this spectral parameter space. Therefore, although it may be tempting to interpret the gradation in the spectral parameters as correlating to relative maturity, these parameters can only distinguish opal-A from opal-CT, not a very amorphous opal-A from a more crystalline opal-A.

4.2 Effects of Rock Chip versus Powder Measurements

The results presented thus far show that powdered opal-A and opal-CT samples are distinguishable using the 1.4 and 2.2 μm parameters. However, for application to orbital Mars data, many targets of interest may be of exposed rock outcrops rather than fine particulates. Whole rock spectra may differ from powder spectra due to

heterogeneous distribution of minerals (e.g., as a coating; Smith et al., 2017) or due to different H_2O adsorption properties of bedrock and particulate material. In this section, we therefore assess the performance of the 1.4 and 2.2 μm parameters in identifying opal-A and opal-CT from rock chips of the same samples studied in **Section 4.1**.

Opal-A rock samples vary little in their 1.4 μm position, but can differ in the 2.26/2.21 μm ratio value by +0.5 and up to -1.5 **(Figure 3D)**. The Hawaii rock values deviate the most from their powder values, likely due to the heterogeneous and complex basaltic mineralogy present in the Hawaii samples. By contrast, the Yellowstone and New Zealand samples are predominantly and homogenously opal with few other accessory phases, which helps minimize differences between the rock and powder spectra. Individual opal-CT samples show a similar range of variation in their 2.2 μm parameter and may differ in their 1.4 μm positions by as much as 0.02 μm. The most significant changes occur for the two quartz samples, which shift into the opal-CT field **(Figure 3C)**. However, despite the differences observed for individual samples, the opal-A and opal-CT fields are still distinct and preserved in this parameter space (compare **Figure 3A and 3C**). This suggests that the 1.4 and 2.2 μm parameters will still successfully identify opal-A and opal-CT when analyzing whole rock spectra.

4.3 Identifying Opal Type in Mixed Samples

We have shown that NIR spectroscopy can provide a rapid and effective mechanism for identifying opal type in relatively "pure" samples, i.e. those that do not contain other minerals that also absorb at 1.4, 1.9, and 2.2 μm. However, terrestrial opals are often mixed with spectrally similar minerals like kaolinite, jarosite, alunite, and

gypsum, and these assemblages have also been identified on Mars [e.g., Milliken et al., 2008; Wray et al., 2011]. Mixtures of these materials may result in improper characterization of opal type, which is particularly concerning for Mars as spectrally ambiguous mineralogy can influence geologic interpretations. In this section we apply the 1.4 and 2.2 μm parameters to natural and controlled opal mixtures to assess their effectiveness in identifying opal type in more complex samples.

4.3.1 Natural Samples with Other 2.2 μm-Absorbing Minerals

Here we apply the 1.4 and 2.2 μm parameters to natural samples that either contain no opal or are a mixture of opal, kaolinite, jarosite, alunite, and gypsum. All of the non-opal samples plot outside of the pure opal-A and opal-CT fields **(Figure 4)**, indicating that these parameters should not produce false detections of opal when there is none present. Some opal mixtures plot on the edges of the pure opal fields, although many are well outside these fields. There are notably few mixed samples with 1.4 μm positions beyond 1.415 μm; this likely shows the effects of minerals like kaolinite that have fixed absorption positions in the 1.4 μm region and can pull the overall absorption to the 1.41-1.415 μm range. Several opal-A mixtures plot within the opal-CT field, suggesting that mixed opal-A might be mistaken for opal-CT, although the opposite is not true from these samples. Overall, these spectral parameters are capable of distinguishing between opal-rich and non-opal materials, and still can provide some indication of the opal type in mixed samples.

4.3.2 Controlled Binary Mixtures of Opal-A and Kaolinite/Montmorillonite

Our spectral parameters were also applied to binary mixtures of opal-A and kaolinite or montmorillonite **(Table 3)** to determine the purity of samples plotting in the pure opal fields. For these binary mixtures, the 1.4 and 2.2 μm parameters can reliably identify materials with >80 wt% opal-A, although the exact amount depends on parameter values for the pure opal-A (**Figure 5**).

Mixtures with opal-A that have initially higher 2.2 μm ratios are able to "hide" more Al-clays in their spectra before they plot outside the pure opal fields. For example, mixtures with samples OS 2 (diamonds in **Figure 5**) or NL 1 (triangles in **Figure 5**) can contain up to 5 wt% kaolinite or 10-20 wt% montmorillonite and still be mistaken for pure opal-A (at <5 wt% clay) or pure opal-CT (at 10-20 wt% montmorillonite). In contrast, mixtures with sample SM 1, which has a lower initial 2.2 μm ratio (circles in **Figure 5**), are much easier to identify as impure opal mixtures. Less than 5 wt% montmorillonite or an even smaller amount of kaolinite will pull a SM1 mixture well out of the pure opal fields.

However, in either case, higher abundances of Al-clays (>10-20 wt%) will cause mixtures to converge at 2.2 μm ratios approaching zero and 1.4 μm positions approaching 1.412 μm for kaolinite and 1.416 μm for montmorillonite. Our opal-CT samples were not available in sufficient quantity to produce mixtures, but the current results suggest that the 1.4 and 2.2 μm parameters will have similar, if not better, success in identifying pure opal-CT samples. In particular, opal-CT has a much weaker 2.2 μm absorption compared to opal-A that may be more susceptible to overprinting by other Al-clay absorptions.

We also note that our methods do not incorporate thresholds like the root-mean-square error (RMSE) for identifying poor Gaussian fits, which would likely decrease the tolerance for Al-clays in our parameters. The influence of even 5 wt% kaolinite or montmorillonite is obviously apparent in the spectra, as both clays have sharp 2.2 µm features compared to opal's broader absorption **(Figure 5C)**. However, the calculated 2.26/2.21 µm ratio for the best-fit Gaussians will still have these mixtures plotting within the pure opal fields. For example, a mixture with 5 wt% montmorillonite is calculated as having the same 2.2 µm ratio as an opal-CT sample (B3_b1), yet the shapes of the 2.2 µm features are not the same **(Figure 5C)**. Implementing RMSE thresholds could reduce these occurrences, although we choose not to in order to simulate a "blind" scenario such as if these parameters were applied to orbital Mars data.

4.4 Comparison with Rice et al. [2013]

Our results differ from those of Rice et al. [2013] in several aspects. The 1.4 µm position appears capable of distinguishing between opal-A and quartz in both studies, though the exact values are not necessarily the same **(Figure 6)**. Rice et al. report positions ranging from 1.405-1.411 µm for opal-A and 1.418-1.421 µm for chert and chalcedony. The opal-A values are consistent between the two studies, but our positions for quartz occur at significantly longer wavelengths than those observed for chert and chalcedony in their study. Still, these two endmember groups are distinct from one another in the data from both studies. The biggest difference regarding the 1.4 µm position occurs in the opal-CT samples, where Rice et al. report a range of 1.407-1.431 µm that is split into 1.425-1.431 µm for sinter opal-CT and 1.407-1.411 µm for opal-CT

from unspecified localities. We note that opal-A and opal-CT would be distinguishable in their work if only sinter opal-CT were considered.

Differences between the two studies also exist in the assessment of the 2.2 μm feature. Rice et al. find opal-A and opal-CT to overlap in their 2.26/2.21 μm parameters (their Figure 21), but in our work both band depth and Gaussian ratios for 2.26/2.21 μm show a clear delineation of opal-A and opal-CT **(Figure 3A, B)**. A comparison of the band depth and Gaussian ratios shows that the two parameters perform differently, though systematically, with the Gaussian method capturing more influence from the 2.26 μm sub-absorption in opal-A **(Figure 7)**. However, discrepancies between the two studies cannot be due to the use of different parameters, as our opal-A and opal-CT samples are still distinguished using same band depth parameters as Rice et al. **(Figure 3B)**.

Sampling methods could cause some of these differences, as alluded to by Rice et al. [2013]. We only study natural opal samples and Rice et al. surveyed a more comprehensive set of synthetic and natural silica samples that included opals. This is suggested by the distinction of opal-A and opal-CT at 1.4 μm in both studies, if only natural sinter samples are considered. Importantly, our observations for the 1.4 and 1.9 μm features are consistent with Rice et al. (details in **Section 5.2**), suggesting that the 2.2 μm feature holds additional insight in distinguishing the difference opal types.

5. Implications for Opal Water Content and Distribution

The spectral distinctions between opal-A and opal-CT indicate that their water contents are distributed differently in their structures. It is understood that opal-CT generally contains less SiOH and total water content than opal-A, although both groups

span wide and overlapping ranges in values **(Section 2.1)**. Opal-CT also contains proportionally more Type B H_2O than opal-A [Langer and Florke, 1974], possibly enabled by its greater population of geminal SiOH [Bobon et al., 2011]. However, less is known about differences in H_2O content or the proportion of Type A to Type B SiOH between opal-A and opal-CT. The results from our work may help address these issues, as the 1.4, 1.9, and 2.2 μm absorptions indicate SiOH (1.4, 2.2 μm) and H_2O (1.4, 1.9 μm) content and their short and long wavelength sub-absorptions are proxies for the proportion of Type A and Type B water respectively. In this section we confirm previous observations of water content and present a model to explain the different distribution of SiOH and H_2O in opal-A and opal-CT.

5.1 H_2O, SiOH, and Total Water Content

Absolute water content is typically determined by techniques such as the Penfield method or thermogravimetric analyses [Herdianita et al., 2000], but band depths and areas can provide a qualitative comparison of water content within opal-A and opal-CT. Band areas of the 1.9 μm H_2O absorption show that opal-A and opal-CT have similar amounts of H_2O **(Figure 8A)**, although the Type A and Type B distribution of that H_2O differs and is discussed in **Section 5.2**. In contrast, band areas of the 2.2 μm SiOH absorption indicate that opal-A consistently has more SiOH than opal-CT. Opal-A also typically has greater total water content (SiOH + H_2O) as seen in the band area of the 3 μm absorption and in the sum of the 1.9 and 2.2 μm band areas **(Figure 8B)**. These results are consistent with Langer and Florke [1974], as both opal types have overlapping ranges of H_2O content and opal-A has more SiOH and total water content than opal-CT.

Our work is also in agreement with a similar study conducted by Day and Jones [2008], despite differences in absorption fitting methods.

5.2 Distribution of Type A and Type B H_2O and SiOH

The proportion of Type B to Type A water can be indicated either by ratios of the longer to the shorter wavelength absorptions in each 1.4, 1.9, and 2.2 μm feature or by band positions, which shift to longer wavelengths with increasing Type B water. The separation of opal-A and opal-CT in the parameter space of **Figure 3** indicates that opal-CT tends to have a higher proportion of Type B H_2O due to its longer wavelength band positions for the 1.4 μm feature. This is corroborated by opal-CT's higher 1.46/1.41 μm and 1.96/1.91 μm band depth ratios compared to opal-A (**Figure 8C**, note that ratios are inverted to directly compare with Rice et al.'s Figure 20). The higher proportion of Type B H_2O in opal-CT has been previously documented to suggest that opal-CT has an increased propensity to adsorb multiple layers of H_2O [Langer and Florke, 1974], possibly facilitated by a larger population of geminal silanols at the surface [Bobon et al., 2011].

However, opal-CT has lower 2.26/2.21 μm band depth **(Figure 8D)** and Gaussian ratios **(Figure 3A)**, indicating a lower proportion of Type B SiOH, or silanols that are H-bonded to H_2O. Similar results are observed in the opal data of Day and Jones [2008] despite differences in our band fitting methodologies. This implies that opal-CT has fewer SiOH sites that are available to bond with adsorbing H_2O at the surface **(Figure 9)**, resulting in a stronger 2.21 μm absorption due to structural SiOH that is not bonded to H_2O (Type A) and a weaker 2.26 μm absorption (Type B). Reconciling this with opal-

CT's higher proportion of Type B H_2O suggests that H_2O experiences limited bonding with surficial SiOH but produces more "layers" or "networks" of H_2O in opal-CT. This produces a stronger 1.96 μm absorption due to molecular H_2O (Type B) and a weaker 1.91 μm absorption due to the first layer of H_2O that is bonded to SiOH (Type A). Conversely, opal-A's SiOH sites bond more readily with adsorbing H_2O (producing a stronger 2.26 μm Type B absorption), but additional layers of H_2O are more difficult to adsorb (weakening the 1.96 μm Type B absorption). Thus, while opal types can have similar amounts of H_2O **(Figure 8A)**, the distribution of that H_2O is the distinguishing factor between opal-A and opal-CT **(Figure 9)**.

These differences in H_2O adsorption between opal-A and opal-CT occur despite opal-CT having a larger geminal SiOH population, which would allow it to nominally adsorb more Type A H_2O and produce Type B SiOH absorptions [Brown et al., 2003; Bobon et al., 2011]. In an exaggerated example, an opal-A with only single SiOH would have 4.6 OH nm^{-2}, whereas an opal-CT with only geminal SiOH would have 7.9 OH nm^{-2} [Iler, 1979; Burneau et al., 1990 and references therein]. There is also some suggestion that multiple layers of H_2O, such as those in opal-CT, only form when there is high surface hydroxylation (>5 OH nm^{-2}) [Bogdan et al., 1998]. However, this speculation is at odds with observations of opal-CT containing less total SiOH than opal-A **(Figure 8A)** [Rodgers et al., 2004; Day and Jones, 2008].

Assuming that opal-CT does in fact have a larger geminal SiOH population, Type A H_2O is also easier to desorb from geminal sites, possibly due to nonlinearities in the H-bonds [Burneau et al., 1990]. This may be reflected spectroscopically in the longer wavelengths and lower energies associated with geminal SiOH absorptions [e.g., Hockey

and Pethica, 1961; Jones and Segnit, 1969]. Adsorbed H_2O therefore may be relatively unstable on an opal-CT surface, leaving SiOH sites that are free of any H-bonding. Evidence for these free, or isolated, SiOH sites occurs in a sharp feature at 2.68 μm, which is observed in opal-CT even at ambient lab conditions but is not seen in ambient opal-A **(Figure 10)**. However, this 2.68 μm feature appears in opal-A upon dehydration via heating, demonstrating that these SiOH sites are present in opal-A but are H-bonded to adsorbed water at ambient conditions. The presence of this 2.68 μm free SiOH feature in ambient opal-CT supports the hypothesis that opal-CT surfaces are less likely to produce bonds between Type B SiOH and Type A H_2O. We note that our interpretations of the H_2O distribution in opal-A and opal-CT are consistent regardless of whether or not opal-CT does in fact have a higher proportion of geminal SiOH, as per Bobon et al.'s [2011] model.

6. Conclusion

Our spectroscopic study of natural opal samples demonstrates that opal-A and opal-CT can be distinguished by parameters describing their 1.4 and 2.2 μm absorptions. The 1.4 μm feature in opal-A tends to be centered at 1.408-1.413 μm, while opal-CT ranges from 1.413-1.445 μm. The ratio of the 2.26 to 2.21 μm absorptions, using either band depth or Gaussian amplitudes, is higher for opal-A than for opal-CT. These parameters work equally well for powder and rock chip samples, and are capable of identifying opal-rich materials with >80% opal in mixtures with other 2.2 μm-absorbing minerals. Focusing on the 1.4 and 2.2 μm absorptions is also advantageous for

application to Mars data, as these features are less affected by the presence of other H_2O-bearing minerals and atmospheric absorptions in orbital data.

Additional analyses of opal's 1.9 and 2.6-4 μm absorptions confirm and contribute to our understanding of differences in water content and distribution within opal-A and opal-CT. We confirm previous observations of higher SiOH and total water content in opal-A, and similar H_2O content in both opal types. Opal-CT is observed to have a higher proportion of Type B H_2O and a lower proportion of Type B SiOH than opal-A, suggesting different distributions and interactions of SiOH and H_2O. We propose that opal-CT has fewer SiOH that can sustain H-bonding to adsorbed H_2O, but simultaneously has a higher propensity to adsorb multiple layers of networked H_2O. In contrast, more of opal-A's H_2O content is adsorbed onto SiOH rather than as additional networks of H_2O. This hypothesis is supported by studies of H_2O desorption from geminal SiOH (as may be more common in opal-CT) as well as observations of free, non-H-bonded SiOH in opal-CT spectra taken at ambient laboratory conditions.

Our work shows that it is indeed possible to unambiguously identify different opal types using spectral data, at least at ambient terrestrial conditions. Future work will focus on conducting similar spectral analyses of opal-C and microcrystalline quartz samples to fully characterize and distinguish between phases in the full opal diagenetic sequence. Application of these parameters to Martian data would require spectral measurements at Mars-relevant conditions (low pressure, temperature, and varying relative humidity), which is the subject of ongoing study. These results may aid in interpretations of orbital opal detections on Mars, as knowledge of opal type can be used to infer water longevity and locate areas of high biopreservation potential.

Acknowledgements

The authors would like to thank Hannah Kaplan for assistance with Gaussian modeling. This work was funded by a MSL Participating Scientist grant.

References

Anderson, J. H., and K. A. Wickersheim (1964), Near infrared characterization of water and hydroxyl groups on silica surfaces, *Surface Science*, *2*, 252–260, doi:10.1016/0039-6028(64)90064-0.

Bandfield, J. L. (2008), High-silica deposits of an aqueous origin in western Hellas Basin, Mars, *Geophysical Research Letters*, *35*(12), doi:10.1029/2008GL033807.

Boboň, M., A. A. Christy, D. Kluvanec, and L. Illášová (2011), State of water molecules and silanol groups in opal minerals: a near infrared spectroscopic study of opals from Slovakia, *Phys Chem Minerals*, *38*(10), 809–818, doi:10.1007/s00269-011-0453-0.

Bogdan, A., M. Kulmala, and N. Avramenko (1998), Reduction of Enthalpy of Fusion and Anomalies during Phase Transitions in Finely Divided Water, *Phys. Rev. Lett.*, *81*(5), 1042–1045, doi:10.1103/PhysRevLett.81.1042.

Bolis, V., B. Fubini, L. Marchese, G. Martra, and D. Costa (1991), Hydrophilic and hydrophobic sites on dehydrated crystalline and amorphous silicas, *J. Chem. Soc., Faraday Trans.*, *87*(3), 497–505, doi:10.1039/FT9918700497.

Brown, L. D., A. S. Ray, and P. S. Thomas (2003), 29Si and 27Al NMR study of amorphous and paracrystalline opals from Australia, *Journal of Non-Crystalline Solids*, *332*(1–3), 242–248, doi:10.1016/j.jnoncrysol.2003.09.027.

Bunker, B. C., D. M. Haaland, T. A. Michalske, and W. L. Smith (1989), Kinetics of dissociative chemisorption on strained edge-shared surface defects on dehydroxylated silica, *Surface Science*, *222*(1), 95–118, doi:10.1016/0039-6028(89)90337-3.

Burneau, A., and C. Carteret (2000), Near infrared and ab initio study of the vibrational modes of isolated silanol on silica, *Physical Chemistry Chemical Physics*, *2*(14), 3217–3226, doi:10.1039/b002863k.

Burneau, A., O. Barres, J. P. Gallas, and J. C. Lavalley (1990), Comparative study of the surface hydroxyl groups of fumed and precipitated silicas. 2. Characterization by infrared spectroscopy of the interactions with water, *Langmuir*, *6*(8), 1364–1372, doi:10.1021/la00098a008.

Cady, S. L., and J. D. Farmer (1996), Fossilization processes in siliceous thermal springs: trends in preservation along thermal gradients, *Ciba Found. Symp.*, *202*, 150-170; discussion 170-173.

Campbell, K. A., K. Sannazzaro, K. A. Rodgers, N. R. Herdianita, and P. R. L. Browne (2001), Sedimentary Facies and Mineralogy of the Late Pleistocene Umukuri Silica Sinter, Taupo Volcanic Zone, New Zealand, *Journal of Sedimentary Research*, *71*(5), 727–746, doi:10.1306/2DC40964-0E47-11D7-8643000102C1865D.

Campbell, K. A., B. Y. Lynne, K. M. Handley, S. Jordan, J. D. Farmer, D. M. Guido, F. Foucher, S. Turner, and R. S. Perry (2015), Tracing Biosignature Preservation of Geothermally Silicified Microbial Textures into the Geological Record, *Astrobiology*, *15*(10), 858–882, doi:10.1089/ast.2015.1307.

Christy, A. A. (2010), New insights into the surface functionalities and adsorption evolution of water molecules on silica gel surface: A study by second derivative near

infrared spectroscopy, *Vibrational Spectroscopy*, *54*(1), 42–49, doi:10.1016/j.vibspec.2010.06.003.

Dyar, M. D., C. A. Hibbitts, and T. M. Orlando (2010), Mechanisms for incorporation of hydrogen in and on terrestrial planetary surfaces, *Icarus*, *208*(1), 425–437, doi:10.1016/j.icarus.2010.02.014.

Flörke, O. W., B. Köhler-Herbertz, K. Langer, and I. Tönges (1982), Water in microcrystalline quartz of volcanic origin: Agates, *Contr. Mineral. and Petrol.*, *80*(4), 324–333, doi:10.1007/BF00378005.

Gallego-Gómez, F., A. Blanco, D. Golmayo, and C. López (2011), Three Regimes of Water Adsorption in Annealed Silica Opals and Optical Assessment, *Langmuir*, *27*(23), 13992–13995, doi:10.1021/la203529s.

Goryniuk, M. C., B. A. Rivard, and B. Jones (2004), The reflectance spectra of opal-A (0.5–25 μm) from the Taupo Volcanic Zone: Spectra that may identify hydrothermal systems on planetary surfaces, *Geophys. Res. Lett.*, *31*(24), L24701, doi:10.1029/2004GL021481.

Graetsch, H., O. W. Flörke, and G. Miehe (1985), The nature of water in chalcedony and opal-C from brazilian agate geodes, *Phys Chem Minerals*, *12*(5), 300–306, doi:10.1007/BF00310343.

Hair, M. L. (1975), Hydroxyl groups on silica surface, *Journal of Non-Crystalline Solids*, *19*, 299–309, doi:10.1016/0022-3093(75)90095-2.

Herdianita, N. R., P. R. L. Browne, K. A. Rodgers, and K. A. Campbell (2000), Mineralogical and textural changes accompanying ageing of silica sinter, *Mineral. Deposita*, *35*(1), 48–62, doi:10.1007/s001260050005.

Hertl, W., and M. L. Hair (1968), Hydrogen bonding between adsorbed gases and surface hydroxyl groups on silica, *J. Phys. Chem.*, *72*(13), 4676–4682, doi:10.1021/j100859a053.

Hockey, J. A., and B. A. Pethica (1961), Surface hydration of silicas, *Trans. Faraday Soc.*, *57*(0), 2247–2262, doi:10.1039/TF9615702247.

Hoffmann, P., and E. Knözinger (1987), Novel aspects of mid and far IR Fourier spectroscopy applied to surface and adsorption studies on SiO2, *Surface Science*, *188*(1–2), 181–198, doi:10.1016/S0039-6028(87)80150-4.

Iler, R. K. (1979), *The chemistry of silica*, Wiley, New York.

Inaki, Y., H. Yoshida, T. Yoshida, and T. Hattori (2002), Active Sites on Mesoporous and Amorphous Silica Materials and Their Photocatalytic Activity: An Investigation by FTIR, ESR, VUV−UV and Photoluminescence Spectroscopies, *J. Phys. Chem. B*, *106*(35), 9098–9106, doi:10.1021/jp025768f.

Jones, B., and R. W. Renaut (2003), Hot spring and geyser sinters: the integrated product of precipitation, replacement, and deposition, *Can. J. Earth Sci.*, *40*(11), 1549–1569, doi:10.1139/e03-078.

Jones, B., and R. W. Renaut (2004), Water Content of Opal-A: Implications for the Origin of Laminae in Geyserite and Sinter, *Journal of Sedimentary Research*, *74*(1), 117–128, doi:10.1306/052403740117.

Jones, J. B., and E. R. Segnit (1969), Water in sphere-type opal, *Mineralogical Magazine*, *37*(287), 357–361.

Konhauser, K. O., B. Jones, A.-L. Reysenbach, and R. W. Renaut (2003), Hot spring sinters: keys to understanding Earth's earliest life forms, *Can. J. Earth Sci.*, *40*(11), 1713–1724, doi:10.1139/e03-059.

Krauskopf, K. B. (1956), Dissolution and precipitation of silica at low temperatures, *Geochimica et Cosmochimica Acta*, *10*(1), 1–26, doi:10.1016/0016-7037(56)90009-6.

Langer, K., and O. W. Flörke (1974), Near infrared absorption spectra (4000–9000 cm− 1) of opals and the role of "water" in these SiO 2· nH 2 O minerals., *Fortschritte der Mineralogie*, *52*(1), 17–51.

McDonald, R. S. (1958), Surface Functionality of Amorphous Silica by Infrared Spectroscopy, *J. Phys. Chem.*, *62*(10), 1168–1178, doi:10.1021/j150568a004.

McLennan, S. M. (2003), Sedimentary silica on Mars, *Geology*, *31*(4), 315–318, doi:10.1130/0091-7613(2003)031<0315:SSOM>2.0.CO;2.

Michalski, J. R., M. D. Kraft, T. Diedrich, T. G. Sharp, and P. R. Christensen (2003), Thermal emission spectroscopy of the silica polymorphs and considerations for remote sensing of Mars, *Geophys. Res. Lett.*, *30*(19), 2008, doi:10.1029/2003GL018354.

Milliken, R. E. et al. (2008), Opaline silica in young deposits on Mars, *Geology*, *36*(11), 847–850, doi:10.1130/G24967A.1.

Murchie, S. et al. (2007), Compact Reconnaissance Imaging Spectrometer for Mars (CRISM) on Mars Reconnaissance Orbiter (MRO), *Journal of Geophysical Research: Planets*, *112*(E5), n/a–n/a, doi:10.1029/2006JE002682.

Pelto, C. R. (1956), A study of chalcedony, *Am J Sci*, *254*(1), 32–50, doi:10.2475/ajs.254.1.32.

Rice, M. S., E. A. Cloutis, J. F. Bell III, D. L. Bish, B. H. Horgan, S. A. Mertzman, M. A. Craig, R. W. Renaut, B. Gautason, and B. Mountain (2013), Reflectance spectra diversity of silica-rich materials: Sensitivity to environment and implications for detections on Mars, *Icarus*, *223*(1), 499–533, doi:10.1016/j.icarus.2012.09.021.

Robertson, K. M., R. E. Milliken, S. W. Ruff, J. D. Farmer, and E. L. Shock (2013), Can VIS-NIR reflectance spectra be used to assess formation environments of opaline silica on Mars?, *Lunar Planet. Sci., XLIV*, Abstract 1612.

Siever, R. (1962), Silica Solubility, 0°-200° C., and the Diagenesis of Siliceous Sediments, *The Journal of Geology*, *70*(2), 127–150.

Smith, M. R., J. L. Bandfield, E. A. Cloutis, and M. S. Rice (2013), Hydrated silica on mars: combined analysis with near-infrared and thermal-infrared spectroscopy, *Icarus*, doi:10.1016/j.icarus.2013.01.024.

Smith, R. J., B. H. N. Horgan, P. Mann, E. A. Cloutis, and P. R. Christensen (2017), Acid weathering of basalt and basaltic glass: 2. Effects of microscopic alteration textures on spectral properties, *J. Geophys. Res. Planets*, *122*(1), 2016JE005112, doi:10.1002/2016JE005112.

Stolper, E. (1982), Water in silicate glasses: An infrared spectroscopic study, *Contr. Mineral. and Petrol.*, *81*(1), 1–17, doi:10.1007/BF00371154.

Sun, V. Z., R. E. Milliken, K. M. Robertson, S. W. Ruff, and J. D. Farmer (2017), Mineralogy and Chemistry of Opal-Rich Mars Analog Sites and Implications for Rover Observations, *in prep*.

Tielens, F., C. Gervais, J. F. Lambert, F. Mauri, and D. Costa (2008), Ab Initio Study of the Hydroxylated Surface of Amorphous Silica: A Representative Model, *Chem. Mater.*, *20*(10), 3336–3344, doi:10.1021/cm8001173.

Tosca, N. J., and A. H. Knoll (2009), Juvenile chemical sediments and the long term persistence of water at the surface of Mars, *Earth and Planetary Science Letters*, *286*(3–4), 379–386, doi:10.1016/j.epsl.2009.07.004.

Tsuchiya, I. (1982), Infrared spectroscopic study of hydroxyl groups on silica surfaces, *J. Phys. Chem.*, *86*(21), 4107–4112, doi:10.1021/j100218a005.

Van Roosmalen, A. J., and J. C. Mol (1978), An infrared study of the silica gel surface. 1. Dry silica gel, *J. Phys. Chem.*, *82*(25), 2748–2751, doi:10.1021/j100514a026.

Voort, P. V. D., I. Gillis-D'Hamers, and E. F. Vansant (1990), Estimation of the distribution of surface hydroxyl groups on silica gel, using chemical modification with trichlorosilane, *J. Chem. Soc., Faraday Trans.*, *86*(22), 3751–3755, doi:10.1039/FT9908603751.

Williams, L. A., and D. A. Crerar (1985), Silica Diagenesis, II. General Mechanisms, *Journal of Sedimentary Research*, *55*(3).

Wray, J. J. et al. (2011), Columbus crater and other possible groundwater-fed paleolakes of Terra Sirenum, Mars, *Journal of Geophysical Research: Planets*, *116*(E1), n/a–n/a, doi:10.1029/2010JE003694.

Yamagishi, H., S. Nakashima, and Y. Ito (1997), High temperature infrared spectra of hydrous microcrystalline quartz, *Phys Chem Min*, *24*(1), 66–74, doi:10.1007/s002690050018.

Zhdanov, S. P., L. S. Kosheleva, and T. I. Titova (1987), IR study of hydroxylated silica, *Langmuir*, *3*(6), 960–967, doi:10.1021/la00078a014.

Zhuravlev, L. T. (2000), The surface chemistry of amorphous silica. Zhuravlev model, *Colloids and Surfaces A: Physicochemical and Engineering Aspects*, *173*(1–3), 1–38, doi:10.1016/S0927-7757(00)00556-2.

Tables

Table 1. Compilation of opal features in the 1-4 μm region. References 1-8 report absorptions from natural opal and chalcedony samples, references 9-25 report absorptions from synthetic silica gel or glass, and reference 26 reports general H_2O absorptions.

References for Table 1:

1. Pelto [1956]
2. Jones and Segnit [1969]
3. Langer and Florke [1974]
4. Graetsch et al. [1985]
5. Yamagishi et al. [1997]
6. Goryniuk et al. [2004]
7. Bobon et al. [2011]
8. Rice et al. [2013]
9. McDonald [1958]
10. Hockey and Pethica [1961]
11. Anderson and Wickersheim [1964]
12. Hair and Hertl [1968]
13. Hair [1975]
14. Van Roosmalen and Mol [1978]
15. Stolper [1982]
16. Tsuchiya [1982]
17. Zhdanov et al. [1987]
18. Hoffman and Knozinger [1987]
19. Bunker et al. [1989]
20. Bolis et al. [1991]
21. Burneau et al. [1990]
22. Van Der Voort et al. [1990]
23. Burneau and Carteret [2000]
24. Inaki et al. [2002]
25. Christy [2010]
26. Dyar et al. [2010]

Table 1.

Abs (um)	Molecule (Type)	Action	H-bonded?	References
1.4-1.41	SiOH, H_2O (A)	OH stretch overtone in SiOH and H_2O	to SiOH but not H_2O	6-8, 11, 15, 21, 25, 26
1.45-1.46	SiOH, H_2O (B)	OH stretch overtone in SiOH and H_2O	yes (to H_2O)	6-8, 11, 21, 25
1.90-1.92	H_2O (A)	combination bend and stretch of H_2O	to SiOH but not H_2O	3, 4, 5-8, 11, 15, 21, 25, 26
1.93-1.96	H_2O (B)	combination bend and stretch of H_2O	yes (to H_2O)	3, 6-8, 11, 21, 25
2.20-2.22	SiOH (A)	combination OH stretch and SiOH or SiOSi bend	to SiOH but not H_2O	3, 4, 5-8, 11, 15, 21, 25, 26
2.25-2.26	SiOH (B)	combination OH stretch and SiOH or SiOSi bend	yes (to H_2O)	3, 5-8, 11, 21, 25
2.67-2.68	SiOH (isolated/free, A)	fundamental OH stretch	no	4, 5, 9, 11, 12, 14, 16, 18-20, 22-24
2.7-2.74	SiOH (single, B)	fundamental OH stretch	yes (to H_2O)	2, 10
2.82-2.86	SiOH (geminal, B)	fundamental OH stretch	yes (to H_2O)	2, 10
2.69-2.86	SiOH (adjacent)	fundamental OH stretch	yes (to SiOH)	1-6, 13, 14, 17-22, 24
>2.8	H_2O (B)	fundamental OH stretch	yes (to H_2O)	3, 4, 9-13, 15, 17, 20-22, 26

Table 2. Spectrally pure opal samples and their calculated spectral parameters for the 1.4, 1.9, 2.2, and 3 μm features. Abbreviations for table headers are as follows: BD = Band Depth, BA = Band Area, GR = Gaussian Ratio.

Suite	Locale	Sample ID	Opal Type	**1.4 μm Position**	1.4 μm BD	1.46/ 1.41 μm BD Ratio	1.4 μm BA	1.9 μm Position	1.9 μm BD	1.96/ 1.91 μm BD Ratio	1.9 μm BA	2.26/ 2.21 μm BD Ratio	2.2 μm BA	**2.26/ 2.21 μm GR**	3 μm BA
Hawaii	Sulphur Banks	HISB 2 white bulk	A	**1.411**	0.058	0.796	0.008	1.904	0.175	0.626	0.016	1.152	0.006	**2.445**	0.841
		HISB2 01	A	**1.412**	0.106	0.715	0.013	1.906	0.241	0.617	0.024	0.919	0.006	**1.358**	1.073
		HISB2 02	A	**1.412**	0.075	0.738	0.010	1.907	0.181	0.625	0.018	0.854	0.004	**1.101**	0.886
		HISB2 03	A	**1.411**	0.046	0.844	0.009	1.905	0.144	0.554	0.012	1.026	0.004	**1.639**	0.813
		HISB2 05	A	**1.412**	0.062	0.738	0.009	1.906	0.184	0.573	0.016	0.961	0.005	**1.420**	0.884
Yellow-stone National Park	Nymph Lake	NL 1	A	**1.410**	0.048	0.706	0.006	1.903	0.150	0.591	0.013	1.148	0.005	**3.244**	0.783
		NL 3	A	**1.410**	0.021	0.724	0.003	1.903	0.083	0.486	0.006	1.111	0.002	**1.900**	-
		3B2_a1	A	**1.412**	0.078	0.789	0.010	1.905	0.207	0.689	0.021	1.296	0.005	**3.178**	0.684
		3B2_b1	A	**1.411**	0.079	0.734	0.010	1.905	0.219	0.648	0.021	1.268	0.005	**2.615**	0.801
		2A_1	A	**1.409**	0.140	0.663	0.015	1.903	0.283	0.614	0.026	1.081	0.008	**2.084**	0.823
		2C2_1	A	**1.411**	0.054	0.777	0.007	1.905	0.153	0.670	0.015	1.221	0.003	**2.749**	0.545
	Octopus Spring	OS 1	A	**1.413**	0.143	0.768	0.018	1.906	0.331	0.655	0.034	0.998	0.004	**1.367**	0.813
		OS 2	A	**1.410**	0.097	0.678	0.011	1.903	0.231	0.576	0.020	1.161	0.005	**2.218**	0.789
		OS 3	A	**1.413**	0.135	0.747	0.017	1.907	0.304	0.607	0.029	1.029	0.005	**1.525**	0.725
		OS 4	A	**1.409**	0.087	0.639	0.010	1.903	0.207	0.547	0.017	1.177	0.003	**1.972**	0.716
		OS 5	A	**1.410**	0.068	0.730	0.009	1.904	0.206	0.613	0.019	1.209	0.004	**2.515**	0.728
	Rabbit	1E_a1	A	**1.408**	0.122	0.607	0.013	1.902	0.265	0.556	0.022	0.945	0.009	**1.594**	0.774

	Creek	1E_b1	A	**1.409**	0.129	0.619	0.014	1.903	0.293	0.571	0.025	0.949	0.010	**1.578**	0.832
		4E_a1	A	**1.409**	0.089	0.665	0.010	1.903	0.212	0.567	0.018	1.090	0.003	**1.831**	0.771
		4E_b1	A	**1.409**	0.125	0.611	0.012	1.903	0.288	0.575	0.025	0.993	0.007	**1.630**	0.786
		1C1_1	A	**1.408**	0.134	0.675	0.016	1.902	0.290	0.632	0.028	0.870	0.009	**1.328**	0.797
		4D_1	A	**1.410**	0.135	0.711	0.016	1.904	0.316	0.644	0.031	0.996	0.006	**1.535**	0.657
		1D_1	A/CT	**1.409**	0.134	0.752	0.017	1.904	0.310	0.689	0.032	0.929	0.010	**1.516**	-
	Sentinel Meadow	SM 1	A	**1.408**	0.090	0.568	0.010	1.902	0.195	0.473	0.014	0.967	0.003	**1.360**	0.809
		SM 2	A	**1.410**	0.117	0.713	0.014	1.903	0.282	0.615	0.026	1.220	0.005	**2.308**	0.931
		SM 3	**A**	**1.410**	0.116	0.721	0.014	1.903	0.248	0.607	0.023	1.356	0.004	**2.803**	0.823
		4B_a1	A	**1.409**	0.129	0.633	0.013	1.903	0.278	0.587	0.024	1.302	0.006	**2.973**	0.724
		4B_b1	A	**1.409**	0.134	0.673	0.014	1.903	0.282	0.609	0.026	1.300	0.006	**2.927**	0.806
	Steep Cone	5A_a1	A	**1.409**	0.194	0.677	0.021	1.903	0.382	0.636	0.036	1.108	0.012	**2.337**	0.957
		5A_b1	A	**1.408**	0.141	0.657	0.016	1.902	0.279	0.594	0.024	1.051	0.008	**1.960**	0.773
		5B_a1	A	**1.409**	0.131	0.668	0.014	1.903	0.273	0.611	0.025	1.081	0.006	**1.961**	0.825
		5B_b1	A	**1.409**	0.143	0.678	0.016	1.903	0.288	0.622	0.026	1.099	0.008	**2.037**	0.841
		5C_a1	A	**1.409**	0.161	0.686	0.018	1.903	0.323	0.640	0.030	1.090	0.010	**2.234**	0.874
		5C_b1	A	**1.409**	0.156	0.711	0.019	1.903	0.299	0.637	0.028	1.108	0.009	**2.153**	0.835
		5D_a1	A	**1.408**	0.144	0.650	0.015	1.902	0.288	0.604	0.026	1.051	0.008	**1.968**	0.798
		5D_b1	A	**1.409**	0.168	0.695	0.019	1.903	0.329	0.643	0.031	1.090	0.009	**2.094**	0.845
		5E_a1	A	**1.408**	0.143	0.628	0.015	1.902	0.293	0.584	0.025	1.068	0.008	**2.012**	0.776
		5E_b1	A	**1.408**	0.152	0.632	0.016	1.902	0.301	0.588	0.026	1.069	0.007	**2.201**	0.814
New Zealand	-	4A(A-15)_a1	CT	**1.414**	0.027	0.694	0.004	1.909	0.106	0.533	0.009	0.473	0.001	**0.303**	0.498
		4A(A-15)_b1	CT	**1.417**	0.027	0.773	0.004	1.911	0.095	0.593	0.009	0.664	0.002	**0.531**	0.526
	Lakeside Soda Mt.	6A(A-17)_a1	A	**1.411**	0.097	0.823	0.013	1.905	0.251	0.691	0.026	0.995	0.006	**1.545**	0.867
		6A(A-	A	**1.411**	0.093	0.829	0.013	1.905	0.245	0.696	0.026	0.984	0.004	**1.465**	0.885

		17)_b1													
		6A(A-17)_c1	A	**1.411**	0.090	0.831	0.012	1.906	0.237	0.703	0.026	0.928	0.004	**1.257**	0.855
	OK Boardwalk Tim and Terry Pool	5(A-12)_a1	A	**1.410**	0.062	0.642	0.006	1.904	0.191	0.650	0.017	1.157	0.005	**2.554**	0.744
		5(A-12)_b1	A	**1.410**	0.071	0.755	0.009	1.904	0.208	0.644	0.019	1.086	0.006	**1.973**	0.831
	Sinter Island	1A(A-21)_a1	A	**1.408**	0.078	0.530	0.008	1.903	0.206	0.468	0.015	0.820	0.007	**1.112**	0.779
		1A(A-21)_b1	A	**1.408**	0.074	0.555	0.008	1.903	0.194	0.486	0.015	0.815	0.007	**1.077**	-
		5(A-4)A_c1	A/CT	**1.413**	0.099	0.857	0.014	1.907	0.234	0.725	0.027	0.604	0.003	**0.703**	-
		1B(A-23)_a1	CT	**1.416**	0.086	0.875	0.010	1.909	0.236	0.774	0.028	0.479	0.001	**0.565**	0.755
		1B(A-23)_b1	CT	**1.419**	0.056	0.985	0.009	1.911	0.178	0.770	0.022	0.598	0.001	**0.661**	0.747
		1B(A-23)_c1	CT	**1.445**	0.081	1.107	0.012	1.919	0.212	0.849	0.028	0.597	0.001	**0.584**	0.731
		5(A-4)B_b1	CT	**1.421**	0.074	1.004	0.011	1.911	0.213	0.786	0.027	0.605	0.001	**0.644**	0.735
	Tahumatara	B4_a1	A	**1.409**	0.031	0.715	0.004	1.903	0.127	0.575	0.011	0.872	0.005	**1.260**	0.682
		B4_b1	A	**1.408**	0.035	0.741	0.005	1.903	0.137	0.590	0.012	0.840	0.005	**1.150**	0.739
		B5_a1	A	**1.408**	0.052	0.541	0.006	1.902	0.150	0.447	0.010	0.823	0.006	**1.160**	0.657
		B5_b1	A	**1.408**	0.049	0.545	0.006	1.902	0.145	0.448	0.010	0.824	0.006	**1.193**	0.688
		B6_a1	A	**1.409**	0.025	0.637	0.003	1.903	0.093	0.469	0.006	0.871	0.003	**1.291**	0.670
		B6_b1	A	**1.409**	0.056	0.551	0.005	1.903	0.172	0.593	0.014	0.931	0.005	**1.622**	0.700
	TeKopia	(B-10)B_a1	A	**1.410**	0.049	0.811	0.007	1.905	0.142	0.668	0.014	0.822	0.005	**1.121**	0.751
		(B-10)B_b1	A	**1.410**	0.073	0.818	0.011	1.905	0.182	0.705	0.019	0.826	0.006	**1.094**	0.814
	Umukuri	1C(A-16)_a1	CT	**1.415**	0.017	0.796	0.003	1.908	0.054	0.497	0.004	0.781	0.001	**0.551**	0.447

		1C(A-16)_b1	CT	**1.445**	0.043	1.144	0.007	1.920	0.128	0.844	0.016	0.663	0.001	**0.672**	0.558
		1D(A-9)_a1	CT	**1.445**	0.022	1.034	0.004	1.914	0.079	0.733	0.009	0.754	0.001	**0.651**	0.469
		1D(A-9)_c1	CT	**1.419**	0.035	1.034	0.006	1.914	0.118	0.748	0.014	0.690	0.001	**0.689**	0.570
		1D(A-9)_d1	CT	**1.445**	0.076	1.105	0.011	1.917	0.209	0.840	0.027	0.642	0.001	**0.671**	0.672
		2C(A-8)_b1	**CT**	**1.419**	0.029	1.001	0.004	1.914	0.118	0.739	0.014	0.501	0.001	**0.492**	0.576
		2D(B-8)_b1	CT	**1.419**	0.019	1.017	0.003	1.913	0.086	0.721	0.009	0.736	0.001	**0.737**	0.524
		B3_a1	CT	**1.418**	0.035	0.940	0.005	1.911	0.140	0.701	0.016	0.711	0.001	**0.721**	0.600
		B3_b1	CT	**1.416**	0.031	0.896	0.004	1.909	0.121	0.698	0.013	0.814	0.001	**0.988**	0.569
		B3_c1	CT	**1.413**	0.026	0.781	0.004	1.908	0.107	0.578	0.009	0.895	0.001	**1.040**	0.541
		4C(A-11)_a1	Q	**1.462**	0.011	1.309	0.002	1.920	0.041	0.817	0.004	0.481	0.001	**0.172**	-
		4C(A-11)_b1	Q	**1.434**	0.013	1.257	0.002	1.918	0.042	0.760	0.004	0.567	0.001	**0.112**	-
D. Bish	Humboldt County, Nevada	46E5885	CT	**1.412**	0.111	0.795	0.015	1.907	0.229	0.690	0.024	0.794	0.002	**0.959**	0.728

Table 3. Binary mixtures of opal-A and kaolinite or montmorillonite. The mass fraction of Al-clay in each mixture is shown as the ideal target mass fraction and the mass fraction actually achieved in the mixture. The 1.4 and 2.2 µm parameter values are averaged from the three measurements of each mixture.

Mixture (Opal/Al-clay)	Al-clay % (by mass, ideal)	Al-clay % (by mass, actual)	1.4 µm Position	2.26/2.21 µm Gaussian Ratio
SM 1/kaolinite	0	0.00	1.407	1.115
	5	5.57	1.409	0.478
	10	9.99	1.410	0.120
	20	20.00	1.412	0.002
	30	29.99	1.412	0.000
	40	39.89	1.412	0.000
	50	49.41	1.412	0.000
	60	59.14	1.412	0.000
	70	69.12	1.412	0.000
	80	79.88	1.412	0.000
	90	89.79	1.412	0.000
	95	92.82	1.412	0.000
	100	100.00	1.412	0.000
SM 1/ montmorillonite	0	0.00	1.407	1.100
	5	5.21	1.409	0.796
	10	10.40	1.411	0.502
	20	20.02	1.413	0.279
	30	29.64	1.414	0.212
	40	39.89	1.415	0.161
	50	49.83	1.416	0.139
	60	59.43	1.416	0.124
	70	69.35	1.416	0.115
	80	79.63	1.416	0.108
	90	89.58	1.416	0.103
	95	94.41	1.416	0.099
	100	100.00	1.416	0.097
NL 1/kaolinite	0	0.00	1.411	2.739
	5	5.02	1.412	0.909
	10	9.46	1.412	0.070
	20	20.08	1.413	0.002
NL 1/ montmorillonite	0	0.00	1.411	2.739
	5	5.48	1.413	0.994
	10	5.48	1.414	0.522
	20	5.48	1.415	0.220

OS 2/kaolinite	0	0.00	1.409	2.642
	5	5.25	1.411	1.082
	10	10.31	1.412	0.556
	20	19.91	1.412	0.007
OS 2/ montmorillonite	0	0.00	1.409	2.642
	5	5.02	1.411	1.347
	10	10.42	1.413	0.826
	20	20.06	1.414	0.403

Figures

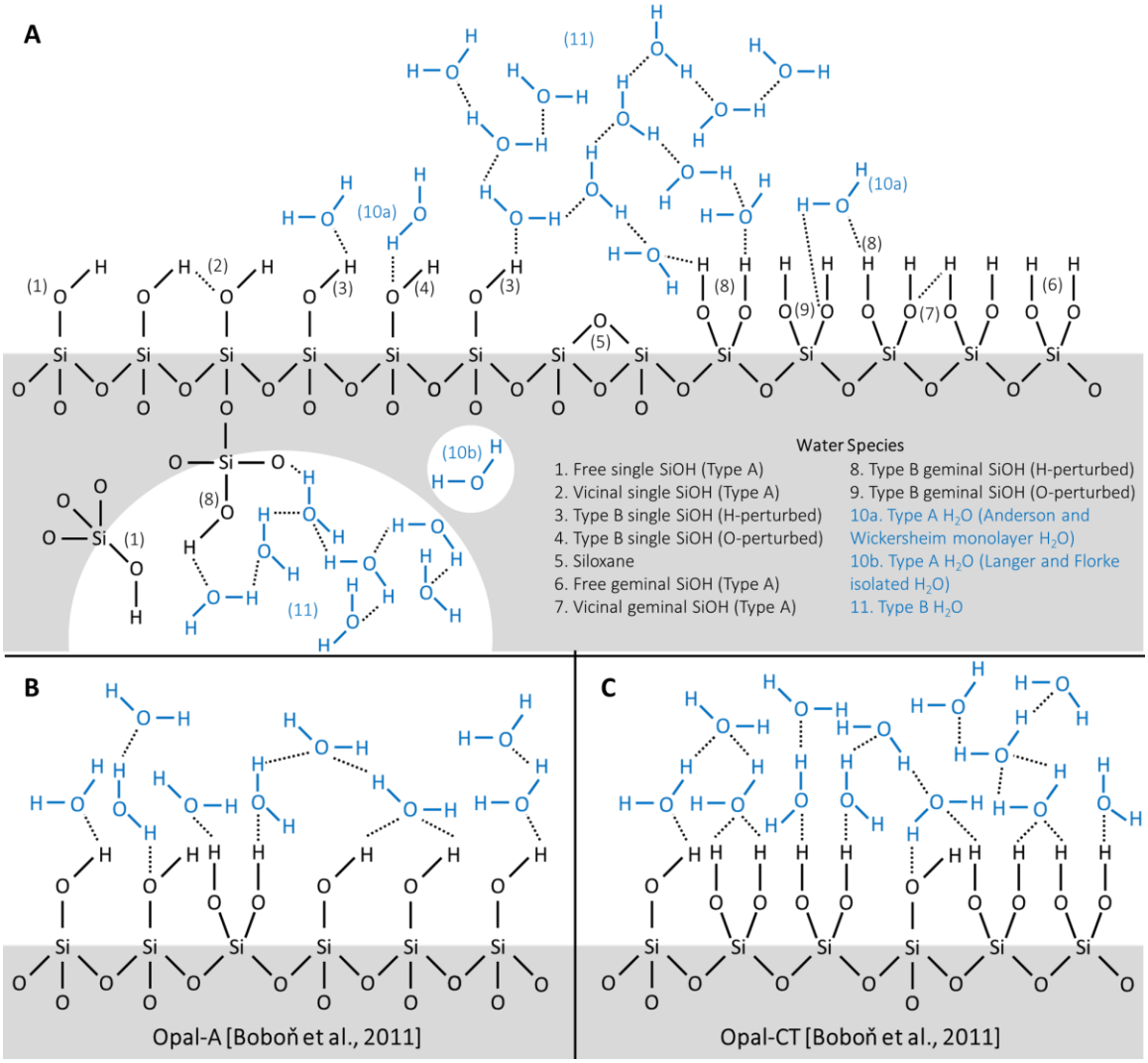

Figure 1. A) Depiction of Type A and B H_2O and SiOH (single, geminal, adjacent, free) species. **B)** H_2O adsorption model for opal-A and **C)** opal-CT according to Bobon et al. [2011], illustrating different proportions of geminal to single SiOH groups and the effect on amount of adsorbed H_2O. Figures are adapted from Anderson and Wickersheim [1964], Langer and Florke [1974], Van Der Voort et al. [1990], Zhuravlev [2000], and Bobon et al. [2011].

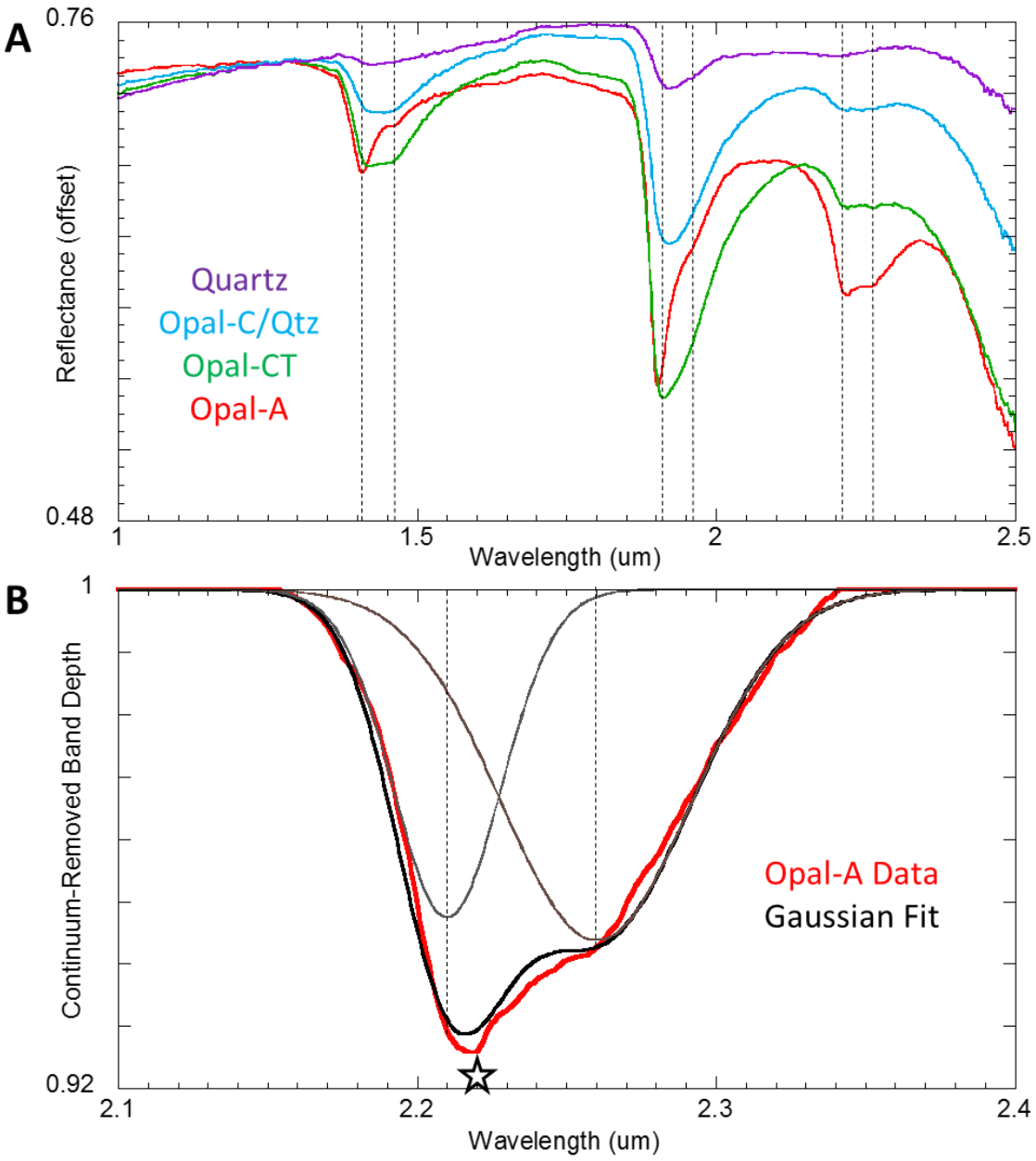

Figure 2. A) NIR spectra for opal samples from New Zealand, showing the shorter and longer wavelength absorptions that make up the 1.4, 1.9, and 2.2 µm features. Dashed lines indicate 1.41 (Type A SiOH or H_2O), 1.46 (Type B SiOH or H_2O), 1.91 (Type A H_2O), 1.96 (Type B H_2O), 2.21 (Type A SiOH), and 2.26 µm (Type B SiOH). **B)** An example of a Gaussian fit for the 2.2 µm feature in the opal-A sample. Dashed lines indicate band depths at 2.21 and 2.26 µm, and a star indicates the band position of the overall 2.2 µm feature. The band area is the entire area enclosed by the red curve. The 1.4 and 1.9 µm features were assessed in the same manner as depicted here.

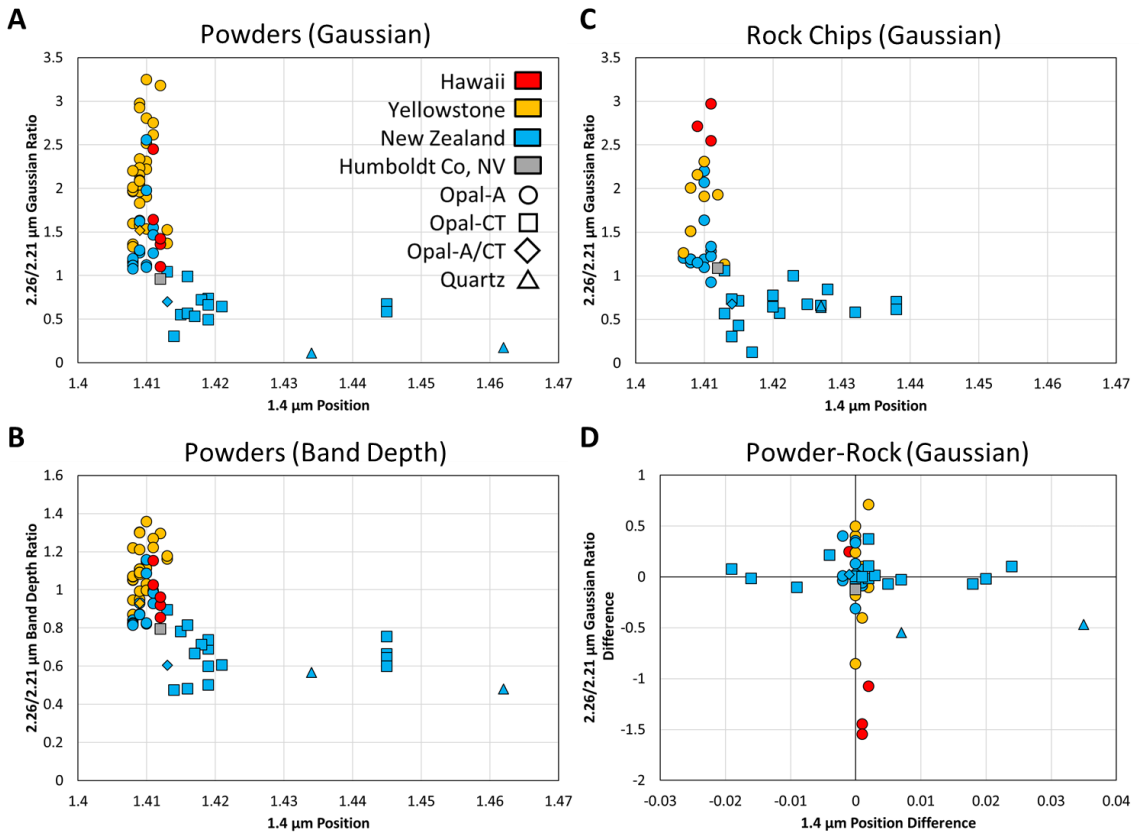

Figure 3. A) Powdered opal-A and opal-CT are distinguishable from their 1.4 µm position and 2.26/2.21 µm Gaussian ratio. **B)** Similar results are obtained when using the 2.26/2.21 µm band depth ratio in place of the Gaussian ratio. **C)** Whole rock opal-A and opal-CT are also distinguishable using these parameters. **D)** Differences in the 1.4 and 2.2 µm parameters for individual samples, presented as the difference of the rock value from the powder value. Note that some Yellowstone samples were measured only as powders and are therefore not represented in **C** and **D**.

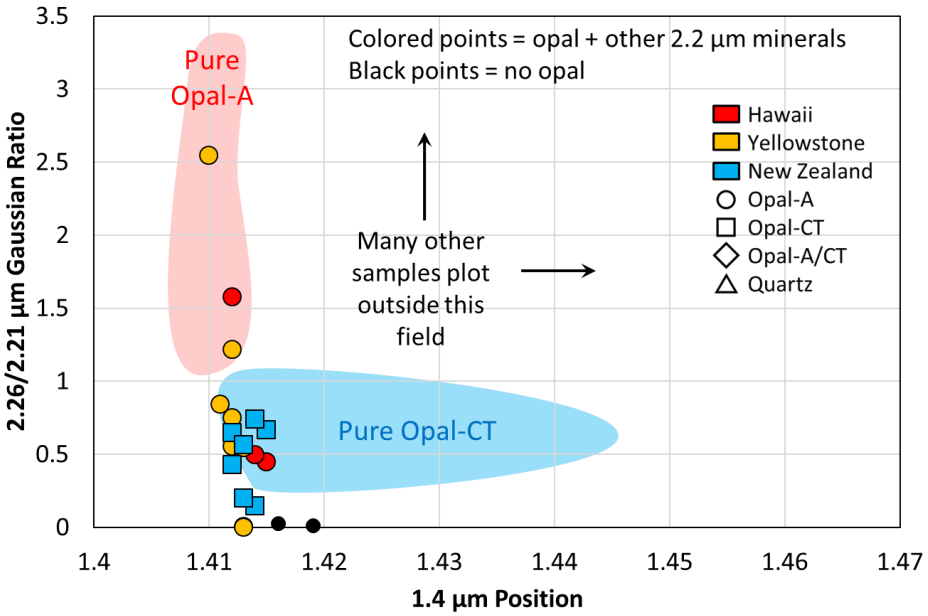

Figure 4. Plot of the 1.4 against the 2.2 µm parameter showing the pure opal-A and opal-CT fields from **Figure 3** and data points of samples containing opal and other 2.2 µm-absorbing minerals (colored by sample suite as in **Figure 3**) and non-opal samples (black).

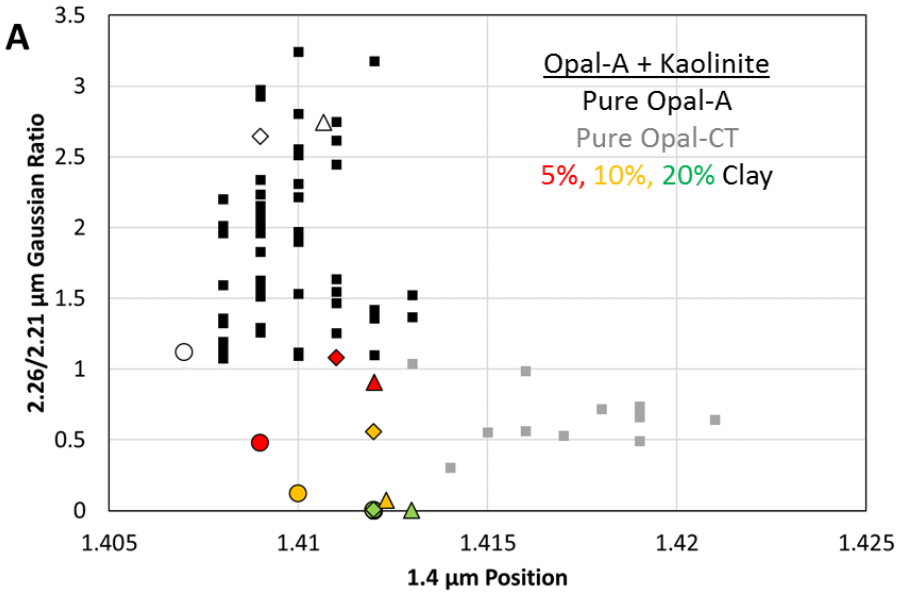
A
Opal-A + Kaolinite
Pure Opal-A
Pure Opal-CT
5%, 10%, 20% Clay
2.26/2.21 µm Gaussian Ratio
1.4 µm Position
3.5
3
2.5
2
1.5
1
0.5
0
1.405
1.41
1.415
1.42
1.425

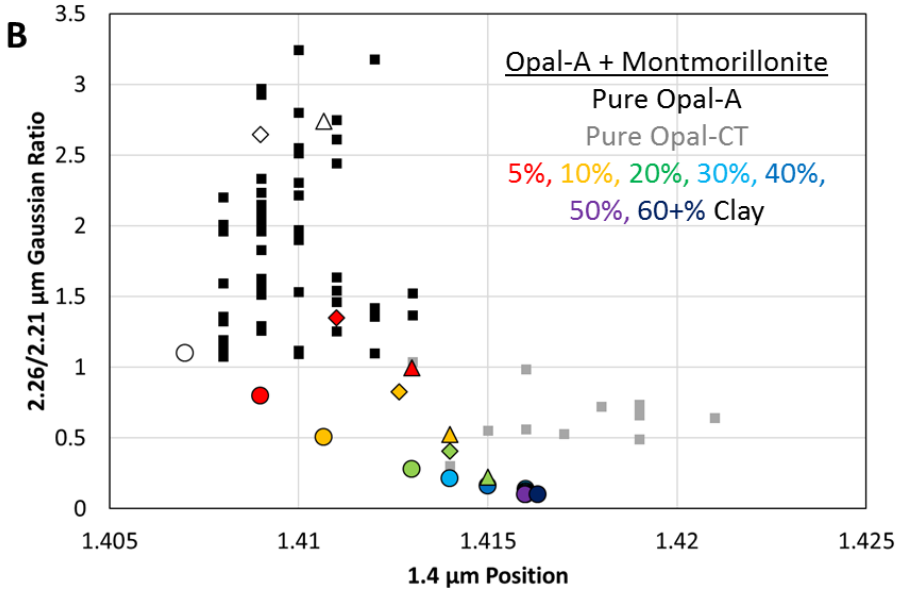
B
Opal-A + Montmorillonite
Pure Opal-A
Pure Opal-CT
5%, 10%, 20%, 30%, 40%,
50%, 60+% Clay
2.26/2.21 µm Gaussian Ratio
1.4 µm Position
3.5
3
2.5
2
1.5
1
0.5
0
1.405
1.41
1.415
1.42
1.425

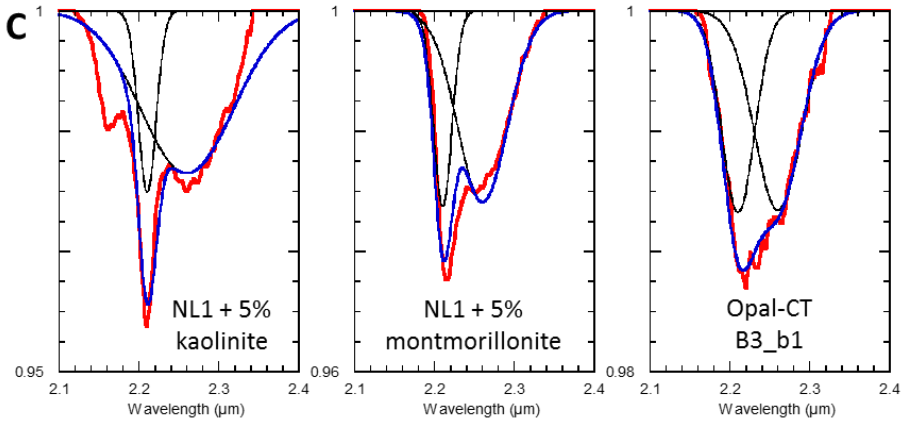
C
NL1 + 5%
kaolinite
NL1 + 5%
montmorillonite
Opal-CT
B3_b1
Wavelength (µm)
2.1
2.2
2.3
2.4

Figure 5. Plot of the 1.4 against the 2.2 µm parameter for the binary **A)** opal-kaolinite and **B)** opal-montmorillonite mixtures, compared to pure opal-A (black squares) and pure opal-CT (grey squares). The pure opal endmembers are plotted as white markers, and their mixtures are shown as a function of clay fraction (indicated by color) and opal sample: SM 1 (circles), OS 2 (diamonds), NL 1 (triangles). **C)** Examples of 2.2 µm Gaussian fits for opal-A (NL 1) mixtures with 5 wt% kaolinite and montmorillonite, and an opal-CT sample that has a similar 2.2 µm Gaussian ratio as the 5% montmorillonite mixture. Spectral data are in red, and modeled Gaussian fits are in blue and black.

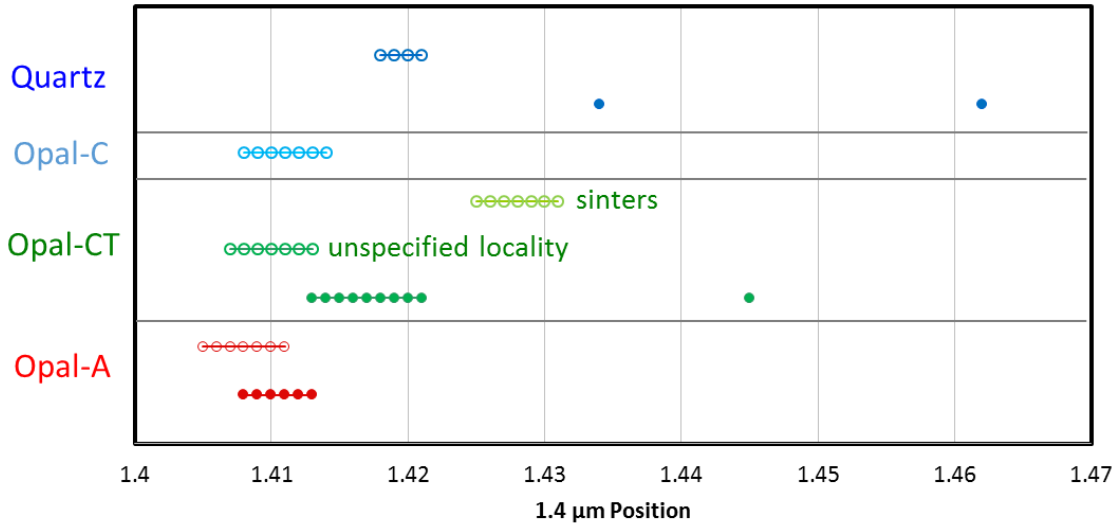

Figure 6. Comparison of values for the 1.4 µm position for our study (solid circles) and Rice et al. [2013] (their Table 16; open circles). The opal-CT samples from Rice et al. [2013] are split into those found in sinters and those with unspecified origins.

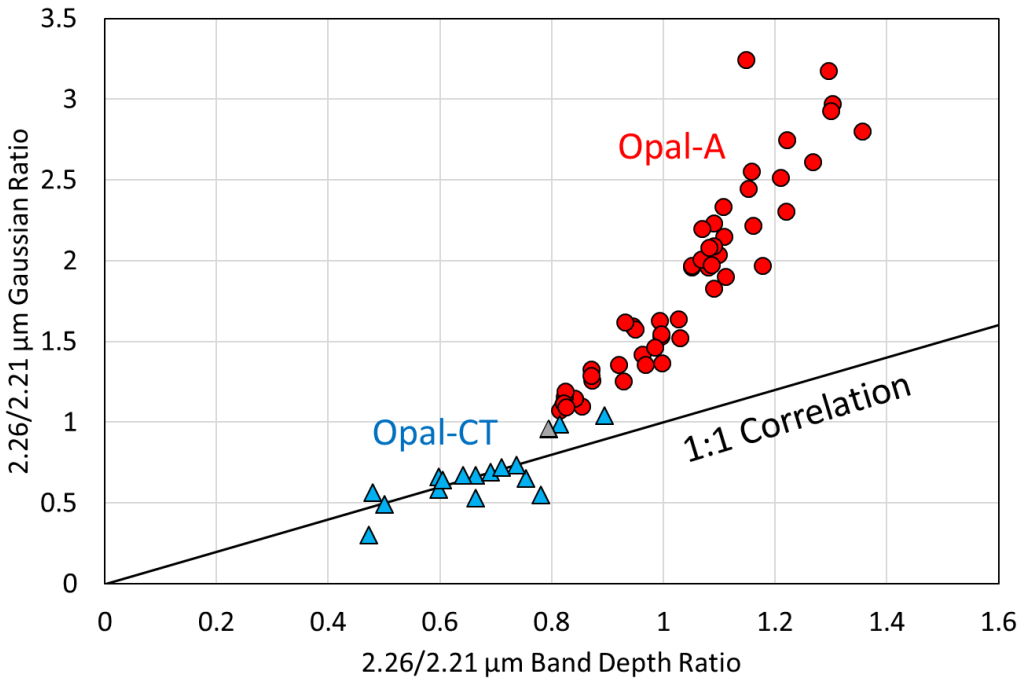

Figure 7. Comparison of the 2.26/2.21 µm band depth ratio and the 2.26/2.21 µm Gaussian ratio for opal-A (red) and opal-CT samples (blue, grey for D. Bish's sample). Opal-CT samples generally fall on the 1:1 correlation line while opal-A samples fall above the line. The deviation of the opal-A samples indicates that the Gaussian ratio is more influenced by the 2.26 µm sub-absorption than the band depth ratio. The slope of the opal-A trend is approximately 3.82.

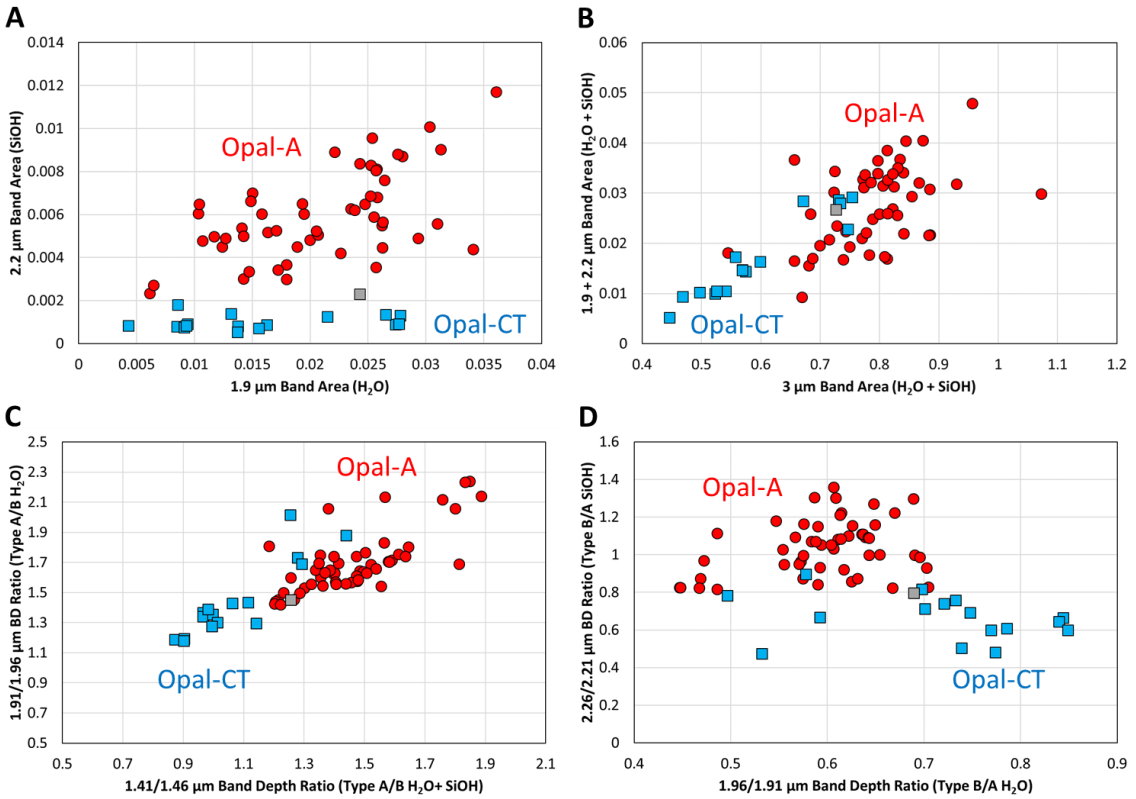

Figure 8. Plots of inferred water content for opal-A (red) and opal-CT (blue, grey for D. Bish's sample). **A)** H_2O and SiOH content are indicated by the 1.9 and 2.2 µm band areas, respectively. **B)** Total SiOH and H_2O content is reflected in the band area of the broad 3 µm feature, and is approximated by the sum of the 1.9 and 2.2 µm band areas. **C)** The proportion of Type A to Type B H_2O is reflected in the 1.41/1.46 µm band depth ratio and the 1.91/1.96 band depth ratio. Note that these ratios are reversed from the norm of this paper, in order to directly compare with results from Rice et al. [2013] (their Figure 20). **D)** The proportion of Type B to Type A H_2O is indicated by the 1.96/1.91 µm band depth ratio, while the 2.26/2.21 µm band depth ratio indicates the proportion of Type B to Type A SiOH.

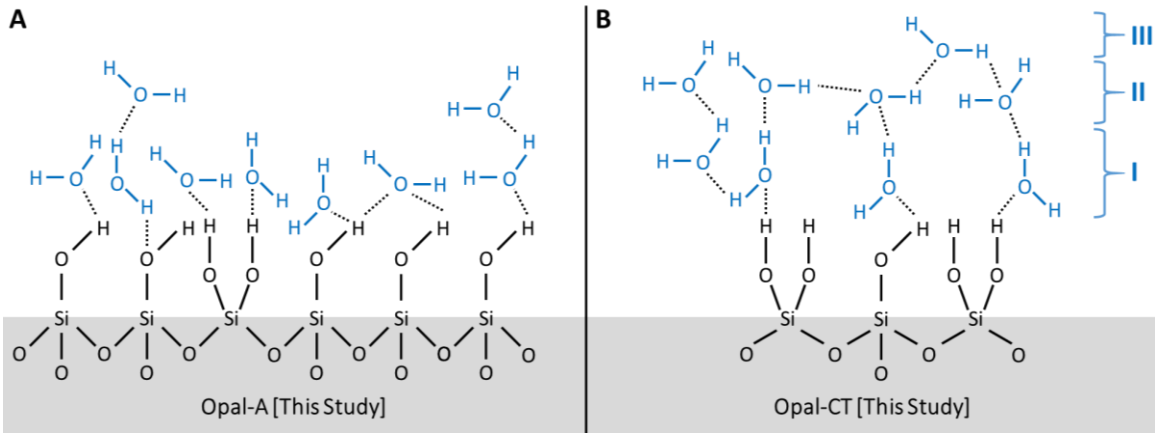

Figure 9. Model for **A)** opal-A and **B)** opal-CT from this study. On the right side, numerals indicate the number of adsorbed H_2O layers. Over the same surface area, opal-A has more SIOH content and more SiOH bonded to adsorbed H_2O (i.e. Type B SiOH). In contrast, opal-CT has more free SiOH and more adsorbed H_2O layers (i.e. Type B H_2O). Both opal types have the same H_2O content as measured in the number of H_2O molecules. Note that the depiction of opal-CT having more geminal SiOH than opal-A is inherited from the interpretations by Bobon et al. [2011]. Our interpretations of the different H_2O distribution between opal-A and opal-CT hold regardless of the true distribution of single versus geminal SiOH in opal-A and opal-CT.

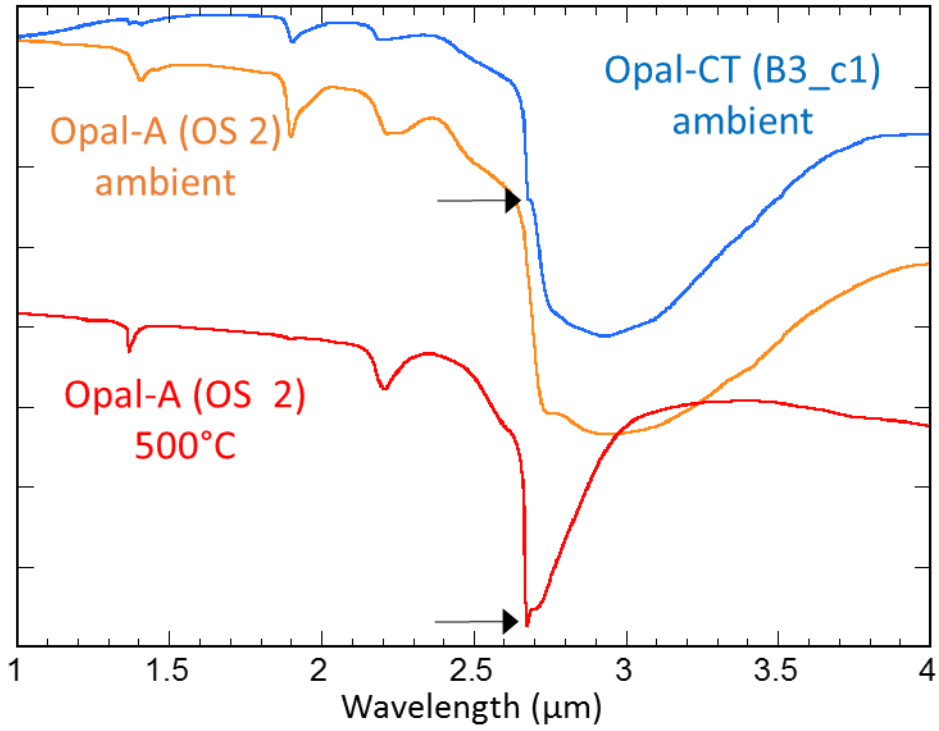

Figure 10. Spectrum of an opal-CT and opal-A sample taken at ambient conditions and the same opal-A immediately after heating to 500°C. Black arrows point to the sharp 2.68 µm absorption assigned to free SiOH that do not experience any H-bonding. Note the absence of this 2.68 µm in the ambient opal-A spectrum but its appearance upon dehydrating the same opal-A at 500°C.

CHAPTER 5:

Constraining the Hydration Behavior of Opaline Silica at Mars-Relevant Conditions from Laboratory Experiments

Vivian Z. Sun,

Ralph E. Milliken, Kevin M. Robertson

Department of Earth, Environmental, and Planetary Sciences, Brown University,

Providence, RI 02912, USA

To be submitted:

Summer 2017

Abstract

Spectral variations have been observed in martian opals using orbital data and are inferred to represent differences in crystallinity. Most opal detections have previously been compared with ambient spectra of terrestrial opals, though spectra are expected to be different at martian surface conditions due to differences in water content. Different opal types also exhibit different H_2O adsorption properties that may affect how they hydrate and cycle water on Mars and influence their near-infrared (NIR) reflectance spectra. To address these questions we performed hydration/dehydration experiments on several terrestrial opals at Mars-like pressure, temperature, and relative humidity (RH), while collecting reflectance spectra at NIR wavelengths. We monitored changes in characteristic absorptions at 1.4, 1.9, 2.2, and 3 μm to determine if opal-A and opal-CT are spectrally distinguishable at martian surface conditions and if they are likely to adsorb/desorb H_2O on diurnal or seasonal timescales. Measurements at low pressure constrain the position of the 1.4 μm feature to 1.37-1.41 μm for martian opal-A and 1.41-1.45 μm for opal-CT. Low temperature experiments indicate different hydration behavior for opal-A and opal-CT. Opal-A readily hydrates at -85°C and >90% RH and dehydrates at -55°C and ~15% RH, suggesting that despite slow kinetics, martian opal-A should be capable of atmospheric water exchange and may show observable variations at 2.2 μm over hour-long timescales. Opal-CT also adsorbs and desorbs H_2O but develops ice-like spectral features at temperatures below -45°C due to its greater population of multilayer H_2O and associated higher degree of H-bonding. This suggests that martian opal-CT occurrences may exhibit ice-like features, particularly in the 3 μm wavelength region, a hypothesis that may be testable within existing or future spacecraft data.

1. Introduction

Visible-near infrared (VIS-NIR) reflectance spectra acquired by orbital spectrometers over the past two decades have confirmed that aqueous minerals, including those with exchangeable H_2O, are widespread across Mars [e.g., Bibring et al., 2006] despite previous speculation that such minerals may not be hydrated at Mars' lower pressures and temperatures [e.g., Zent et al., 2001; also discussed in Bish et al., 2003]. Water species in these minerals can occur as structurally bound OH and/or H_2O, structurally adsorbed H_2O that is weakly coordinated to specific regions in a crystal structure, and/or surface adsorbed H_2O. The abundance of the latter two forms may be particularly sensitive to changes in relative humidity (RH) and can also be affected by slower water adsorption rates at the low pressures and temperatures on the martian surface [e.g., Bishop and Pieters, 1995].

Many experiments have been performed for materials such as sulfates, zeolites, clays, and palagonitic dust to investigate changes in their hydration states at Mars-relevant conditions [Bishop and Pieters, 1995; Zent et al., 2001; Bish et al., 2003; Janchen et al., 2006; 2009; Frinak et al., 2005; Cloutis et al., 2008; Pommerol et al., 2009]. Results from these studies largely suggest that while these minerals are less hydrated at Mars-like conditions, H_2O may exchange with the atmosphere on kinetically rapid timescales, even for weakly adsorbing materials [Beck et al., 2010]. Hydrated minerals may therefore comprise a significant reservoir of water on Mars [Mustard et al., 2012] and could help regulate diurnal or seasonal variations in atmospheric H_2O [Bish et al., 2003; Milliken et al., 2007; Pommerol et al., 2009].

However, drawing clear interpretations from existing lab data is complicated because very few studies have controlled T, P, and RH simultaneously and at Mars-like conditions. Previous mineral reflectance measurements at low T and P were summarized by Dalton [2010], who also noted that there is a clear lack of experimental work at the temperature range typical of Mars (e.g., ~150-250 K), an issue that was also pointed out by Jamieson et al. [2014] in their study of the Mg-sulfate kieserite. In addition, RH was not controlled or monitored in many previous NIR experiments, and in many studies where RH was controlled, the samples were removed from the environment during sample analysis. A number of X-ray diffraction (XRD) and Raman studies consist of phase stability measurements performed *in-situ* through controlling RH at low temperature [e.g., Vaniman et al., 2004; Wang et al., 2011; Robertson and Bish, 2013], but common Mars-like temperatures (<250 K) and associated RH values are rarely achieved, thus many results must be greatly extrapolated to conditions that typify the martian surface. In addition, these experiments did not systematically cycle through T and RH ranges experienced during martian diurnal or seasonal cycles. As a result, it is not yet clear which minerals are actually able to cycle water over the appropriate timescales on Mars, and kinetic factors for these changes remain poorly quantified at such low temperatures.

Near-infrared (NIR) spectroscopy is an excellent tool for studying hydration changes in minerals as it is highly sensitive to vibrational absorptions associated with H_2O and OH-bonding environments, and changes in absorption width and shape at low pressures and temperatures have already been observed in several previous studies [Bishop and Pieters, 1995; Frinak et al., 2005; Pommerol et al., 2009]. In addition,

laboratory NIR measurements are appropriate because the majority of hydrated mineral detections on Mars are based on measurements acquired by orbital NIR spectrometers such as the Mars Express OMEGA (Observatoire pour la Minéralogie, l'Eau, les Glaces et l'Activité) and Mars Reconnaissance Orbiter CRISM (Compact Reconnaissance Imaging Spectrometer for Mars) instruments [Bibring et al., 2006; Mustard et al., 2008]. Measuring NIR reflectance spectra of hydrated minerals under Mars-like conditions is therefore not only informative of potential mineral stability, water reservoirs, and water cycling, but it also facilitates direct comparison between laboratory and spacecraft data.

Of the many hydrated phases that have been observed on Mars over the past decade, opaline silica ($SiO_2 \cdot nH_2O$) has been identified in a wide variety of locations and geologic settings across the planet using orbital NIR reflectance data [Milliken et al., 2008; Ehlmann et al., 2009; Skok et al., 2010; Weitz et al., 2011] as well as in Gusev and Gale craters using thermal infrared (TIR) spectra and X-ray diffraction (XRD) by the Spirit and Curiosity rovers, respectively [Squyres et al., 2008; Ruff et al., 2011; Morris et al., 2016]. These detections are consistent with geochemical arguments that suggest opaline silica should be a common weathering product on Mars [McLennan, 2003]. Thus, understanding the water cycling potential of opaline silica and how to correctly identify different maturation states of opal (e.g., opal-A from opal-CT or opal–C) has important implications for water-rock interaction on that planet in both the past and present.

Previous studies have used data such as CRISM to identify different forms of silica ranging from opal-A to more crystalline forms such as opal-CT and quartz [e.g., Milliken et al., 2008; Rice et al., 2013; Smith et al., 2013]. This is possible because different forms of silica are distinguished by their structures, distribution of silanol

(SiOH) groups, and effects these properties have on H_2O adsorption, all of which affect spectral properties at NIR and TIR wavelengths [e.g., Langer and Florke 1974; Rice et al., 2013; Sun et al., 2017b]. However, though some observed variations in spectral absorptions are likely attributed to silica type, particularly for Si-O vibrations at wavelengths >6 μm, Si-OH and H_2O absorptions that dominate NIR wavelengths may be strongly affected by H_2O content. However, the H_2O content of opal may vary as a function of RH, and most CRISM-based detections of opal on Mars have relied on comparison with laboratory spectra of terrestrial opals acquired under ambient conditions or low P-T conditions where RH was not controlled [Milliken et al., 2008; Rice et al., 2013]. Therefore, although it is possible that some of the spectral variations observed in NIR data for martian opal occurrences are due to differences in opal type, they may also be the result of differences in H_2O content as a function of diurnal or seasonal variations in RH and/or H_2O adsorption kinetics of opal under martian atmospheric conditions.

We address this issue by examining the hydration state and water cycling potential of opaline silica through *in situ* laboratory reflectance measurements acquired under ambient, heated, and Mars-relevant conditions. We focus on whether or not opal hydration state may differ between ambient and martian atmospheric conditions for opal-A and opal-CT samples and assess the water cycling potential of these materials as a function of RH at low temperature. We report results from a series of hydration and dehydration experiments and discuss effects on NIR absorptions in the 1.4, 1.9, 2.2, and 3 μm wavelength regions, the properties of which have previously been characterized for these samples in Sun et al. [2017b]. These results help clarify if different opal types (specifically, opal-A versus opal-CT) are spectrally distinguishable on Mars' surface with

CRISM and OMEGA data and provide constraints on whether or not opaline silica is capable of atmospheric H_2O exchange on diurnal or seasonal timescales under the low temperatures that typify the martian surface.

2. Background

2.1 Opal Types: Structures, Water Speciation, and Spectral Characteristics

Opals can be divided into subgroups on the basis of their crystallinity [Jones and Segnit, 1971], water speciation, and consequently their spectral characteristics [Langer and Florke, 1974; Rice et al., 2013; Sun et al., 2017b]. Opal-A is the most amorphous phase in the opal sequence, and through repeated dissolution and reprecipitation will convert to more crystalline phases such as opal-CT, opal-C, and microcrystalline quartz [Siever, 1962]. Comparative studies of water speciation in different opal types and associated spectral features are most extensive for opal-A and opal-CT [e.g., Langer and Florke, 1974; Bobon et al., 2011]. These studies divided the "total water" of opals into molecular water (H_2O) and silanol (SiOH) groups, which can each be further categorized into "Type A" and "Type B" depending on their H-bonding interactions with H_2O **(Figure 1)**.

Type A refers to structurally bound water, which can take the form of SiOH groups that are not H-bonded to H_2O molecules, or H_2O that is completely isolated in voids [Langer and Florke, 1974] or H-bonded to SiOH as a monolayer (i.e., not H-bonded to networked or polymerized H_2O) [Anderson and Wickersheim, 1964; Burneau et al., 1990]. Type B species experience H-bonding to H_2O, such as SiOH that is bonded to Type A H_2O or H_2O that is H-bonded to other H_2O molecules as part of a network, much

like in liquid H_2O or in multiple layers of adsorbed H_2O. In a general sense, Type B water species in opal are consistent with increased degrees of H-bonding relative to Type A species, and it is well documented that water absorptions shift to longer wavelengths (lower energy) with increasing degree of H-bonding [e.g., Lippincott and Schroeder, 1955].

These different water species are discernable in NIR absorptions located in the 1.4, 1.9, 2.2, and 3 μm wavelength regions (references in **Table 1**). Absorptions centered near 1.9 μm reflect the combination H_2O bending plus stretching mode, whereas the features at 2.2 μm result from stretching vibrations associated with SiOH. Weaker absorptions near ~1.4 μm represent overtones of the fundamental OH stretches in both SiOH and H_2O. The 1.4, 1.9, and 2.2 μm features are each composed of multiple absorptions that can be broadly characterized as a shorter wavelength component indicative of Type A water (at ~1.4, ~1.9, and ~2.2 μm) and a longer wavelength component indicative of Type B water (at ~1.46, ~1.96, and ~2.26 μm) [Langer and Florke, 1974].

Absorptions in the 3 μm region for opals are attributed to fundamental OH stretches in both SiOH and H_2O as well as the first overtone of the H_2O bending mode ($2v_2$, occurring near ~3.1 μm). Type B liquid-like H_2O molecules that are H-bonded to other H_2O commonly manifest at wavelengths longer than ~2.8 μm. Silanol, having either one (single) or two (geminal) OH groups available for H-bonding to H_2O, absorb between 2.67-2.86 μm but can be further distinguished into groups based on their observed wavelength ranges. A sharp absorption at 2.67-2.68 μm is indicative of "free" SiOH groups that are not H-bonded to H_2O, with free single SiOH absorbing at slightly

shorter wavelengths than free geminal SiOH [e.g., Burneau et al., 1990]. Silanol that experiences H-bonding with adjacent silanol is associated with absorptions throughout the wavelength range of 2.69-2.86 μm. SiOH groups that are H-bonded to H_2O (i.e. Type B SiOH) occupy a similar wavelength range, though some studies have distinguished single SiOH at 2.7-2.74 μm and geminal SiOH at 2.82-2.86 [Hockey and Pethica, 1961; Jones and Segnit, 1969]. These observations indicate that geminal silanol groups generally absorb at longer wavelengths than single silanol groups and that increased degree of H-bonding shifts SiOH vibrations to longer wavelengths. Thus, H_2O abundance and distribution is expected to have an effect on the position of SiOH absorptions in CRISM and other NIR data.

2.2 Distinguishing Opal-A and Opal-CT from NIR Spectroscopy

Spectra obtained at ambient laboratory conditions are not necessarily analogous to orbital spectra returned from Mars. Mars' reduced pressure, temperature, and atmospheric water vapor content can greatly influence the kinetics and amount of H_2O that is adsorbed on mineral surfaces [e.g., Zent et al., 2001]. This is particularly concerning for assessing NIR spectra of opal because different opal types are defined by their structures, which are linked to variations in water speciation and distribution of adsorbed H_2O as described above. NIR spectral variations of opal are thus expected to vary as a function of H_2O content and how this H_2O interacts with SiO and SiOH groups. As a result, spectra for opals at the martian surface may appear markedly different compared with those measured for opals in an ambient laboratory setting [e.g., Milliken et al., 2008; Rice et al., 2013]. However, the degree to which Mars-like conditions impact

our ability to properly distinguish opal-A, -CT, -C and their hydration/dehydration behavior is not well understood. We address this issue in this work, with a focus on previously characterized opal-A and opal-CT samples, and we provide below a brief overview of the differences in water distribution between these phases and how it relates to NIR absorptions.

Opal-A and opal-CT are reported to contain different proportions of Type A and B SiOH and H_2O groups, allowing for identification of opal type at NIR wavelengths. Opal-CT contains a lower proportion of Type B SiOH and a higher proportion of Type B H_2O relative to opal-A, the latter of which may be present as multiple layers of H_2O adsorbed at the opal surface (i.e. potentially exchangeable) or hosted within inclusions (i.e. unlikely to be lost except at high temperatures) [Langer and Florke, 1974; Campbell et al., 2001]. Adsorption of H_2O by opal-CT may be facilitated by its reported higher proportion of geminal SiOH groups compared with opal-A. This is because geminal SiOH groups have two OH sites available for H-bonding rather than one, which may also promote the building of a broader network of H-bonded H_2O if water is readily available (e.g., at high RH) [Brown et al., 2003; Bobon et al., 2011]. In addition, desorption of H_2O is also more likely to occur from geminal SiOH sites [Burneau et al., 1990]. In contrast, opal samples dominated by single (non-geminal) SiOH groups (as is potentially the case for opal-A) may exhibit a weaker propensity to adsorb H_2O or build a network of H-bonded H_2O molecules.

To reconcile opal-CT's lower proportion of Type B SiOH with its higher proportion of Type B H_2O, we hypothesized in our previous work that opal-CT tends to accumulate its adsorbed H_2O as multiple layers (i.e. Type B H_2O) **(Figure 1C)**. In

contrast, opal-A tends to adsorb H_2O as a single layer that is bonded to Type B SiOH at the mineral surface **(Figure 1B)**. This is strongly supported by observations of "free" (non-H-bonded) SiOH in opal-CT spectra acquired under ambient conditions, as indicated by a sharp, narrow absorption at 2.68 μm in these data [Sun et al., 2017b]. The retention of non-H-bonded SiOH even at moderate to high RH suggests the H_2O that is adsorbed prefers to bond with other H_2O molecules rather than free single SiOH at the surface [Sun et al., 2017b]. Alternatively, the presence of the 2.68 μm feature under these conditions may indicate a higher proportion of free, single SiOH in the opal-CT structure that is not accessible for H_2O adsorption.

Our previous work demonstrated that opal-A and opal-CT are spectrally distinguishable at ambient laboratory conditions due to their different structural and adsorption properties [Sun et al., 2017b; see also Langer and Florke, 1974 and Rice et al., 2013]. In particular, the position of the 1.4 μm absorption and the shape of the 2.2 μm feature are distinct for both opal types **(Figure 2A)**. The 1.4 μm absorption in opal-A commonly occurs at shorter wavelengths (<1.413 μm) than for opal-CT (>1.413 μm), reflecting a higher proportion of Type B H_2O (with a higher degree of H-bonding) in opal-CT. The 2.2 μm feature consists of multiple overlapping SiOH absorptions that are influenced by H-bonding to H_2O and that can be parameterized as a ratio of the strengths of the 2.26 to the 2.21 μm absorptions, where a higher ratio value indicates increased degrees of H-bonding of H_2O to the SiOH groups. Our previous work demonstrated that this ratio value was typically higher for opal-A compared with opal-CT, indicating a greater proportion of SiOH groups were affected by H-bonding to H_2O in opal-A (i.e., increased Type B SiOH). The shape and relative strengths of absorptions that contribute

to the 1.9 μm H_2O feature are also dependent on opal type and H_2O content [Sun et al., 2017b]. However, we do not focus on this feature here because it is not unique to opal (similar features occur in other hydrated minerals such as clays) and because it partially overlaps atmospheric absorptions on Mars, making it difficult to interpret this feature in CRISM or OMEGA data for materials with multiple hydrated phases or when residual atmospheric effects are present.

2.3 Mars Atmospheric Conditions and Effects on Water Adsorption and Kinetics

Atmospheric properties such as pressure, temperature, and relative humidity affect the amount of water that can be adsorbed onto a mineral surface and the rate at which adsorption or desorption occurs. With atmospheric pressures on the order of <1000 Pa [Hess et al., 1980] and nonpolar temperatures ranging from -90°C to -5°C [Kieffer, 1976; Davy et al., 2010; Martin-Torres et al., 2015], surface conditions on Mars are very different than those experienced on Earth. Previous studies have shown that hydrated materials at these lower pressures and temperatures tend to experience spectral changes associated with dehydration [e.g., Bishop and Pieters, 1995], but to our knowledge no previous studies have focused on monitoring or controlling RH at such low temperatures during the measurement of NIR spectra.

Atmospheric water content can be measured in terms of water vapor pressure (P_{H2O}) and relative humidity (RH). Water vapor pressure is temperature-dependent, and at low Mars-like temperatures (-70 to 0°C) the absolute water vapor pressure P_{H2O} can be approximated as a function of the dew point temperature T_d [Vaisala, 2013]:

$$P(H_2O) = 6.114742 * 10^{\frac{9.778707*T_d}{273.1466+T_d}} \qquad \text{(Equation 1)}$$

The saturation water vapor pressure over ice can be similarly approximated as a function of the temperature *T* and represents the maximum amount of moisture that the air can hold at that temperature [Vaisala, 2013]:

$$P(H_2O_{saturated}) = 6.114742 * 10^{\frac{9.778707*T}{273.1466+T}} \quad \text{(Equation 2)}$$

Relative humidity is then the ratio of the actual water vapor pressure (P_{H2O}) to the saturation water vapor pressure ($P_{H2O\ saturated}$), and thus a function of temperature:

$$\%RH = 100 * P_{H_2O}/P_{H_2O_{saturated}} \quad \text{(Equation 3)}$$

One hundred percent relative humidity occurs when the temperature *T* is equal to the dew point temperature T_d, and excess moisture will condense or freeze out when the air is completely saturated with water. Thus, although Mars' thinner atmosphere contains less water than Earth's atmosphere in an absolute sense, high RH and condensation can be achieved when temperatures drop sufficiently to reduce the saturation water vapor pressure. However, it remains that water vapor pressure values on Mars are relatively low compared with Earth, and measurements by the NASA Phoenix lander ranged from 0.05 to 2 Pa depending on the time of day, with lower values occurring overnight [Smith et al., 2009]. However, because the saturation vapor pressure is also lower on Mars due to low temperatures, 100% RH can be achieved during the winter or nighttime, as observed by the Phoenix lander and the Curiosity rover [Smith et al., 2009; Martin-Torres et al., 2015]. By comparison, the saturation vapor pressure of water at 20°C is 2340 Pa and the water vapor pressure at 30% RH at this temperature is ~700 Pa, several orders of magnitude higher than what is observed for Mars.

Relative humidity is likely the primary control on the saturated water content of hydrated minerals, as suggested by a study of water adsorption on Na-montmorillonite

[Frinak et al., 2005; Bish, personal communication]. Thus in a theoretical sense, the water content of martian hydrated minerals may be similar to their terrestrial analogs because of similar RH ranges on Mars and Earth, despite large differences in water vapor pressure. However, Mars' lower water vapor pressure and temperature can impede the kinetics of hydration and dehydration [Frinak et al., 2005; Beck et al., 2010], which may result in lower observed water contents if high RH is not sustained for sufficiently long periods of time. Diurnal and seasonal variations in atmospheric conditions on Mars can therefore have significant influence on a mineral's hydration state and determine whether it can exchange water with the atmosphere on timescales detectable by orbiters, landers, or rovers [Bish et al., 2003; Vaniman et al., 2004].

3. Experimental Methods

Three types of experiments were performed to understand opal's dehydration and hydration behavior at low pressures, temperatures, and RH **(Table 2)**. The first two types were designed to assess extreme variations in spectra as opals dehydrate from an initially hydrated state, which we consider to be achieved at ambient laboratory conditions (typically 22°C and 25-30% RH). We explored dehydration induced by 1) low pressure (i.e. a 0.016 mbar vacuum) as well as 2) heating up to 500°C. Exposure to low pressure is expected to partially dehydrate the opal and more closely mimic opal's hydration state on present-day Mars, whereas heating will more fully dehydrate the opal and can aid our understanding of how H_2O and SiOH are held in the opal structure throughout the dehydration process. The third type of experiment investigates if opal can hydrate or

dehydrate at >90%, ~15%, and ~0.2% RH respectively at Mars-relevant temperatures (-85 to -10°C) on timescales of hours.

The objective of this work is to constrain the range of opal spectral variations due to hydration changes, so the experiments are designed as endmember scenarios rather than exact replications of martian surface conditions. For example, we chose 0.016 mbar pressure (partly due to constraints in the experimental equipment), which is much lower than Mars' ~6 mbar atmospheric pressure, to observe dehydration on a faster timescale in the lab. The opal-A and opal-CT powders (sieved to <45 μm) used in these experiments were previously characterized for their opal type, chemistry, and spectral features at ambient lab conditions [Sun et al., 2017ab]. Spectral variations are quantified using absorption band positions and band depth ratios in the 1.4, 1.9, 2.2, and 3 μm regions as discussed in **Section 2.2**.

3.1 Dehydration at Low Pressure (0.016 mbar)

Our previous work demonstrated that opal-A and opal-CT are distinguishable at ambient laboratory conditions due to different H_2O and SiOH speciation expressed in NIR absorptions at 1.4, 1.9, and 2.2 μm [Sun et al., 2017b]. It is unknown if the H_2O and SiOH species will be disproportionately affected when opal samples are exposed to Mars-like conditions. Unlike dehydration by heating to high temperatures, dehydration via low pressure will not alter opal's crystalline structure and is not expected to completely remove H_2O (i.e. the 1.9 μm H_2O feature is likely to remain visible). This experiment type is meant to determine how opal spectra might appear on the current martian surface and, by proxy, if opal-A and opal-CT are spectrally distinguishable at low pressures and

lower hydration states. Temperature was not controlled in the low P experiments because it adds a confounding factor due to its effect on RH. However, with a weak vacuum pressure of 0.016 mbar and an ambient temperature of 22°C, the water vapor pressure inside the chamber is approximately 0.042 Pa (Equation 1 with constants at 22°C from Vaisala, 2013), which is on the lower end of values observed on Mars **(Section 2.3)**.

Eight opal-A and seven opal-CT samples were studied in this experiment suite and were selected to span a range of observed 1.4 and 2.2 μm parameter values (band positions and strengths) at ambient conditions **(Figure 2A)**. Approximately 10 mg of sample was loaded into an aluminum sample cup which was then tapped by hand to smooth the sample surface and placed into a Linkam THMS350V environmental chamber. An Edwards E2M1.5 rotary vacuum pump was attached to the Linkam stage, as well as a Pfeiffer Pirani gauge to report the sample chamber pressure **(Figure 3A)**. Reflectance spectra were obtained from 0.4-2.5 μm on an ASD (Analytical Spectral Devices) FieldSpec 3 spectroradiometer at a sampling resolution of 2 nm for a 0.5 cm diameter spot size with incidence and emergence angles of 30° and 0°, respectively. Sample reflectance measurements were taken relative to a Spectralon standard (from Labsphere) and later corrected to absolute reflectance by multiplying by a Spectralon spectrum obtained from the NASA RELAB bidirectional spectrometer. Spectra were first obtained at ambient laboratory conditions, after which the pressure was reduced to 0.016 mbar by turning on the vacuum pump. Spectra were taken every 24 hours until no obvious further changes were observed in the consecutive spectra; most samples were held in the vacuum for two to three days.

3.2 Dehydration via Heating (to 500°C)

Different water bonding environments are a key distinguishing factor between opal-A and opal-CT, as discussed above, thus dehydration trends may also be distinct between different types of opal. Compared to dehydration at low pressure, heating to 500°C will not only remove most if not all H_2O, but it will also begin to remove OH from silanol groups at the high end of this temperature range [e.g., Gallego-Gomez et al., 2011]. The motivation for this experiment is therefore to determine the behavior of opal's water from an initial hydrated state (i.e. at ambient laboratory conditions) to a dehydrated state beyond what is achieved by low pressures, providing information about the spectral properties when samples lack H_2O. The experimental setup used here also enables a higher temporal resolution in spectral measurements than in the previous experiments **(Section 3.1)**, allowing for a more detailed analysis of H_2O and OH behavior during opal dehydration.

Five opal-A, six opal-CT, and one opal-A/CT sample were selected for this experiment, again spanning the range of observed 1.4 and 2.2 μm parameter values at ambient conditions **(Figure 2A)**. Approximately 5 mg of sample were loaded in an aluminum sample cup, tapped by hand, and placed in a Linkam FTIR600 environmental chamber **(Figure 3B)**. Dry air was generated with a Parker-Balston purge gas generator with a reported dew point of -70°C, a value that was verified using a Vaisala low RH probe. The dry air was pumped into the Linkam stage through an inflow valve and evolved water was removed through an open outflow valve. The interior of the stage was maintained at slight positive pressure to insure continuous flow of dry air through the

chamber. The temperature was controlled using the LinkSys32 software included with the Linkam environment stage package.

Reflectance spectra were acquired from 1.6 to 16 μm using a Bruker LUMOS FTIR (Fourier Transform Infrared) microscope with a sampling resolution of 2 cm^{-1} over a 100 μm diameter spot size. Data were taken with respect to a KBr powder standard. The samples were initially held at 25°C with continuous flow of dry lab air for one minute prior to the first spectral measurement. After the first measurement, the sample chamber was heated to 500°C over four hours at a temperature ramp of 2°C/minute, with measurements taken at 5°C interval or every 150 seconds.

3.3 Hydration/Dehydration at Low Temperatures (-85 to -10°C)

Whereas the previous two types of experiments explored the behavior of H_2O in opal during dehydration, with the heated experiments providing an endmember scenario, the experiments described here focus on the kinetics or rates of hydration and dehydration at Mars-like temperatures and a range of RH. Specifically, we wish to determine if martian opal hydration may vary on sufficiently fast timescales to be observable on a diurnal or seasonal basis. Temperature, relative humidity, and water vapor pressure are contributing factors to water adsorption kinetics **(Section 2.3)**. In these experiments we controlled temperature and RH and did not specifically monitor total pressure, but the water vapor pressures at our experimental conditions are roughly analogous to conditions on Mars (~0.26 Pa for our dry air with a dew point temperature of -70°C) **(Section 5.3)**.

Two opal-A and two opal-CT samples were selected for this suite of low temperature experiments. These experiments use the same configuration as in **Section 3.2** with the Linkam FTIR600 stage and the Bruker LUMOS FTIR microscope, with the exception that an LN_2 dewar was attached to the Linkam stage to cool and regulate the chamber to low temperatures **(Figure 3B)**. Samples were first measured under ambient conditions (22°C, 25-30% RH), and subsequent procedures depended on the initial sample hydration state at the start of the experiment and whether the sample would be hydrated or dehydrated.

3.3.1 Hydration at -85°C and >90% RH

This experiment first simulates an endmember scenario to investigate if opal will rehydrate at -85°C and >90% RH, which is sometimes reached on Mars during the winter or night [Smith et al., 2009; Martin-Torres et al., 2015]. We investigate opal hydration starting from three initial hydration states: a very dehydrated, a partially dehydrated, and a hydrated opal. The very dehydrated opal was produced via heating at 200°C, which is approximately the temperature at which adsorbed H_2O is removed but SiOH will remain [Gallego-Gomez et al., 2011]. The sample chamber was heated at a rate of 30°C/minute from an ambient 22°C to 200°C, and was then held at 200°C with dry air for 30 minutes to stabilize; 30 minutes was chosen as the heating time since little spectral change is observed between 30 minutes and one hour. The partially hydrated opal was produced by holding the sample at room temperature with dry air running through the chamber for one hour. The hydrated opal was represented by an opal at ambient laboratory conditions, with no further preparation required.

After the initial hydration state of the sample was acquired, the chamber temperature was dropped to -85°C at a -30°C/minute ramp with dry lab air (dew point of -70°C) running through the chamber. Though the sample would nominally be at 100% RH at -70°C, the chamber temperature was dropped to -85°C to compensate for temperature differences between the sensor and the actual sample due to the conductivity of the aluminum sample cup. The lower temperature of -85°C ensures that the sample chamber achieves a high RH (>90%), particularly since the temperature typically fluctuates within 1°C and can result in nonlinear shifts in RH. The sample was then held at -85°C for twelve hours, with continuous spectral measurements every 150 seconds.

3.3.2 Dehydration at -55°C (~15% RH) and -10°C (~0.2% RH)

This experiment simulates a contrasting scenario to determine if a hydrated opal will dehydrate at a Mars-like temperature and RH of -55°C and 15% respectively, which can be achieved during martian summer or daytime [Smith et al., 2009; Martin-Torres et al., 2015]. We consider an opal at ambient conditions to be relatively hydrated and held it in the sample chamber at 22°C without dry air to avoid prematurely dehydrating the sample. The chamber temperature was then cooled to -55°C at a -30°C/minute ramp; the RH inside the chamber increased during this phase in the absence of dry air. After -55°C was reached, dry air was introduced into the chamber to produce 15% RH. The sample was then held at -55°C for eight hours or until no significant spectral changes were observed, with continuous spectral measurements every 150 seconds. Opal samples were also cycled between -85 and -10°C for several hours at each temperature to assess the longer-term effects of varying RH from >90% to 0%.

3.3.3 Hydration at 22°C and 100% RH

Analogous experiments can be conducted at room temperature to investigate the effects of faster kinetics. Most experiments at ambient conditions were not necessary due to hydration and dehydration reactions that are instantaneously observed at these warmer temperatures. For example, an opal sample that is heated in a furnace at 200°C to remove its 1.9 μm feature will regain some of the 1.9 μm feature as soon as it is exposed to the ambient air and measured. Dehydration by heating or flowing dry air over the sample also occurs rapidly at ambient conditions.

However, it is still uncertain if opals are saturated with adsorbed H_2O at ambient conditions. Samples were thus subject to 100% RH at room temperature to determine the spectral features of an H_2O-saturated opal. The opal was held within a sealed Linkam stage containing three additional sample cups filled with H_2O, which equilibrate with the chamber atmosphere to produce 100% RH. Atmospheric saturation of H_2O was confirmed by condensation droplets that formed within the chamber outside of the H_2O-bearing sample cups. Thus in these experiments, the atmosphere inside the sample chamber was able to reach 100% RH, in contrast to the low T experiments in **Section 3.3.1**, which were conducted at high RH (>90%) but not necessarily 100% RH.

4. Results: Opal Dehydration Behavior at Low Pressures and via Heating

4.1 Distinguishing Opal-A and Opal-CT at Low Pressures

Opal-A and opal-CT experience dehydration at 0.016 mbar (P_{H2O} = 0.042 Pa) that is reflected as decreases in the 1.4 μm position and the 2.26/2.21 μm band depth ratio **(Figure 2B and 2C**; spectral data available in **Appendix G)**. Both opal types are

distinguishable at low pressures, even though both opal fields move to new parts of the parameter space. However, the same general trends still hold, in that opal-A tends to have shorter 1.4 μm band positions and higher 2.26/2.21 μm band depth ratios than opal-CT. The exception is a group of two opal-A samples whose low pressure spectra did not change significantly from their ambient spectra and are discussed later in this section.

The decrease in the 1.4 μm position indicates a loss of Type B H_2O, which are loosely bonded to other H_2O molecules and therefore are easily removed with just low pressure. In contrast, Type A H_2O that are bound to SiOH are more tightly held and are not readily removed at low pressures. The decrease in Type B H_2O, which manifests at 1.46 μm, shifts the position of the overall 1.4 μm feature to shorter wavelengths where Type A H_2O absorbs. Similarly, the 2.26/2.21 μm band depth ratio decreases at lower pressures due to the loss of H_2O that is bound to SiOH, effectively converting Type B SiOH (2.26 μm) to Type A SiOH (2.21 μm).

Most low-pressure opal-A samples cluster tightly around a position of 1.38 μm and a 2.26/2.21 μm ratio value of 0.6, although two anomalous samples shift only slightly from their ambient positions **(Figure 2B and 2C)**. Low-pressure opal-CT samples do not shift as dramatically or uniformly as the opal-A samples, but still occupy a field with positions between 1.405 to 1.42 μm and 2.26/2.21 μm ratio values between 0.2 to 0.6. The more substantial shifts associated with most low-pressure opal-A suggest that the H_2O lost from opal-A, whether it was attached to SiOH or other H_2O, was more loosely held than in opal-CT.

The exclusion to the above trends is an anomalous pair of opal-A samples that show little change from their ambient spectra. This discrepancy may be attributed to

structural heterogeneities amongst the opal-A samples that can be quantified from their X-ray diffraction (XRD) patterns. The XRD pattern of opal-A is characterized by a broad amorphous hump spanning 2.6-5.9 Å (or 15-35˚ 2θ for CuKα) and centered at approximately 4.0 Å [Jones and Segnit, 1971]. As opal-A crystallinity increases, the position of this hump decreases (in °2θ space) as well as the full width at half-maximum intensity (FWHM). The anomalous opal-A pair have an average 4Å peak position of 21.93 °2θ and a FWHM of 6.65 °2θ, both of which are lower than the 22.41 °2θ peak position and 7.5 °2θ FWHM for the normal opal-A group. With the caveat of small sample sizes, these values suggest that the anomalous opal-A pair is slightly more crystalline than the normal opal-A group [Sun et al., 2017a], which may explain why they plot closer to the low-pressure opal-CT than the low-pressure opal-A.

Overall these observations suggest that opal-A and opal-CT are spectrally distinguishable at low pressures and can be differentiated in Mars orbital spectra. martian opals will likely plot in between the low pressure and ambient measurements, as our low pressure (0.016 mbar) conditions represent a more extreme dehydration scenario than would be present at Mars' 6 mbar atmosphere. Thus these results predict that martian opal-A will tend to fall at wavelengths short of 1.41 μm whereas opal-CT will fall at wavelengths past 1.41 μm. The delineation at 1.41 μm is bolstered by the fact that an opal-A sample (at least in our sample suite) will never move beyond the 1.41 μm position even if exposed to 100% RH at ambient conditions **(Section 5.1)**. The overall predicted range in the 1.4 μm position is consistent with observations from CRISM spectra, in which hydrated silica show a similar range in the 1.4 μm position (spanning 1.38 to 1.435

μm) [Smith et al., 2013; Sun and Milliken, 2015] as that predicted by our ambient and low pressure measurements.

4.2 Opal Dehydration Behavior via Heating to 500°C

Measurements of heated opal samples on the Bruker LUMOS FTIR microscope are acquired at higher temporal resolution than the low-pressure measurements and allow for detailed documentation of their dehydration trends (spectral data available in **Appendix H**). Opal-A and opal-CT again exhibit different dehydration behavior as they are heated to high temperatures due to their distinct water bonding environments. At ~200°C, adsorbed H_2O is readily lost while SiOH, and sometimes Type A H_2O bonded to SiOH, are largely unaffected. At higher temperatures, condensation and annealing of SiOH occurs as well as the removal of more tightly bound Type A H_2O [Gallego-Gomez et al., 2011]. The 3 μm feature for both opal-A and opal-CT are broad at ambient conditions, reflecting contributions at <2.86 μm from SiOH, which can be free or H-bonded to other SiOH (Type A) or H_2O (Type B), and at >2.8 μm from H_2O.

Upon heating to 200°C, the 3 μm feature in opal-A loses more of the long wavelength, or H_2O, component **(Figure 4A)**. This is paralleled in the disappearance of the 1.9 μm feature in most opal-A samples by 200°C, which indicates that most, if not all, H_2O has been removed from the opal-A. In contrast, opal-CT's 3 μm feature is less asymmetrical at 200°C and the 1.9 μm feature is still retained, indicating that H_2O still exists within the opal-CT structure at temperatures where it would be removed from opal-A **(Figure 4B)**. For both opal-A and opal-CT, the removal of H_2O is also reflected in the 2.2 μm feature, which skews towards shorter wavelengths as the 2.26 μm component (i.e.

Type B SiOH that experiences H-bonding to Type A H_2O) is decreased in favor of the 2.2 μm component (i.e. Type A SiOH with no H-bonding to H_2O).

At 500°C, the removal of some SiOH from opal-A is apparent in the decreased 2.2 and 3 μm absorptions. The minimum of the 3 μm feature also shifts to ~2.7 μm, reflecting the contribution of free, not H-bonded SiOH at 2.68 μm and H-bonded adjacent SiOH at <2.86 μm, but little, if any, influence from H_2O at >2.8 μm **(Figure 4A)**. Similar changes are observed in opal-CT, which has also lost its H_2O and 1.9 μm feature by 500°C **(Figure 4B)**. The 2.68 μm absorption is sharp and distinct for opal-CT, indicating that opal-CT has proportionally more free SiOH at 500°C than opal-A.

Overall, opal-CT retains more of its water content at higher temperatures than opal-A. The 3 μm band area for opal-A decreases almost linearly with temperature **(Figure 4C)**, whereas it initially decreases at a slower rate for opal-CT **(Figure 4D)**. Differences in H_2O retention are also apparent in the 2.85/2.68 μm band depth ratio, which acts as a proxy for the proportion of H_2O (2.85 μm) to free SiOH (2.68 μm), and the 2.26/2.2 μm band depth ratio, which indicates the proportion of Type B SiOH with H-bonding to H_2O (2.26 μm) to Type A SiOH that is not influenced by H_2O (2.2 μm). In this parameter space, opal-A shows well-defined trends as both ratios decrease with dehydration **(Figure 4E)**. The initial decrease of both ratios indicates that much of the removed H_2O seen at 2.85 μm was also bonded to Type B SiOH, which manifests at 2.26 μm. Several samples show kinks in their dehydration trends; the flatter portions of the trends suggest that more free SiOH is produced at higher temperatures than at lower temperatures, by breaking H-bonds between SiOH and H_2O as well as between adjacent SiOH. This is corroborated by an increase in the 2.68 μm band depth with temperature,

which passively decreases the 2.85/2.68 μm ratio while having little effect on the 2.26/2.2 μm ratio. In contrast, opal-CT shows much more diffuse trends, with its 2.85/2.68 μm ratio spanning the same range as opal-A but its 2.26/2.2 μm ratio decreasing only slightly **(Figure 4F)**. This confirms that opal-CT's SiOH are mostly not bonded to H_2O, as significant H_2O losses indicated by the decreasing 2.85/2.68 μm ratio are not paralleled by a similar decrease in the 2.26 μm band depth (which is indicative of SiOH that are influenced by H_2O).

5. Results: Opal Hydration and Dehydration Kinetics at Low Temperatures (-85 to -10°C)

Hydration and dehydration changes in opal occur rapidly at ambient laboratory conditions. For example, an opal dehydrated at 200°C with an absent 1.9 μm absorption will immediately adsorb H_2O and regain its 1.9 μm feature upon exposure to the ambient atmosphere. Similarly, dehydration of a hydrated opal, whether by vacuum, heating, or exposure to dry air, is essentially instantaneous and clearly observable in its spectra.

In this section we investigate if opal hydration changes are observable on short timescales at low Mars-relevant temperatures (-85 to -10°C), which will certainly slow the rates of water adsorption and desorption. Both opal-A and opal-CT show hydration and dehydration changes on kinetically fast timescales, typically over the course of several hours (spectral data available in **Appendix I**). However, both opal types have different sorption behaviors due to their different water bonding environments. These spectral changes are reflected in the 3 μm region but are also paralleled at 1.9 and 2.2 μm, allowing for hypothetical observation of these changes in martian orbital data.

5.1 Opal-A

5.1.1 Hydration Changes in Opal-A

At -85°C and >90% RH, initially dehydrated opal-A will clearly rehydrate over timescales as short as a few hours. When heated to 200°C for 30 minutes, opal-A loses most of its H_2O content and experiences a loss of the 1.9 μm feature and a significant reduction of the longer wavelength component of the 3 μm absorption (compare the black and red spectra in **Figure 5A**). However, after 12 hours at -85°C and >90% RH, the dehydrated opal-A regains some H_2O as seen in the reappearance of a small 1.9 μm absorption and a broadening of the 3 μm feature (blue spectrum in **Figure 5A**).

These gradual spectral changes can be tracked from the 3 μm band area, which shows a continuous increase of adsorbed H_2O throughout the entire 12 hour experiment (red in **Figure 5B**). Changes in the 2.2 μm feature are not immediately obvious from visual inspection of the spectra, but the 2.26/2.2 μm band depth ratio tracks trends in the 3 μm band area (red in **Figure 5C**). The increase in this parameter indicates that the adsorbing H_2O is bonding onto SiOH, resulting in an increase of Type B SiOH at 2.26 μm. This is corroborated by the hydration trend in the 2.85/2.68 μm and 2.26/2.2 μm parameter space (blue in **Figure 5D**), which falls above the dehydration (via heating) trend and suggests preferential formation of Type B SiOH with adsorbing H_2O and less formation of Type B H_2O multilayers. In other words, the first monolayer of H_2O is preferentially formed over additional H_2O multilayers in this experiment. Rehydration of partially dehydrated opal-A produces a trend consistent with the dehydration curve (yellow in **Figure 5D**), suggesting that typical water adsorption on opal-A resumes with increasing water content. This is consistent with previous observations of H_2O clusters

forming on silica surfaces during the early stages of adsorption, with H_2O merging and layering occurring only with more extensive adsorption [Bogdan et al., 1998].

The degree of observable hydration at -85°C likely varies with the initial hydration state of the opal-A. For example, a partially dehydrated opal-A (e.g., with a small 1.9 μm feature) will rehydrate with a slower increase in the 3 μm band area (yellow in **Figure 5B**). While we caution that increases in band depth or area are not necessarily linearly correlated with actual weight percent increases in water content, the rate of hydration likely slows as saturation of adsorbed H_2O is approached. For example, opal-A that is hydrated at ambient laboratory conditions will not hydrate further at >90% RH at -85°C. While this may be a kinetic issue, the same opal-A also does not show obvious additional hydration when exposed to 100% RH at 22°C (blue in **Figure 5B**), suggesting that the adsorbed H_2O content of opal-A at ambient conditions is close to saturation.

5.1.2 Dehydration Changes in Opal-A

Opal-A that is hydrated at ambient laboratory conditions will also dehydrate at -55°C and nominally 15% RH **(Figure 6A)**. These changes are subtler than those observed for the hydration experiments at -85°C, but slight reductions of the 1.9 and 3 μm features are still apparent in the spectra. The 3 μm band area and band depth ratios at 2.26/2.2 μm and 1.96/1.9 μm all decrease over time, illustrating the loss of Type B H_2O (at 1.96 μm) and Type A H_2O (bonded to Type B SiOH at 2.26 μm) **(Figure 6B)**.

Overall, hydration and dehydration changes are spectrally observed over the course of a few hours **(Figure 6C)**, suggesting that martian opal-A will likely show diurnal and/or seasonal hydration and spectral changes on kinetically fast timescales.

Importantly, these changes can likely be monitored in orbital CRISM data from the 2.26/2.2 μm band depth ratio and possibly the 1.96/1.9 μm band depth ratio if the 1.96 μm component is not affected by atmospheric absorptions. However, hydration changes in these experiments are poorly documented in the comparatively weaker 1.4 μm feature, which over a few hours at >90% RH shows only a band position shift on the order of 1 to 2 nm, well below the 6 nm sampling resolution of CRISM data. This is not to say that the 1.4 μm position will not exhibit larger shifts over longer timescales, for example over seasonal atmospheric variations on Mars, but longer-term experiments will be needed to assess this possibility.

5.2 Opal-CT

5.2.1 Formation of Ice in Opal-CT at -45°C

Unlike opal-A, opal-CT develops an ice-like spectrum at -85°C **(Figure 7A and 7B)**, resulting in less obvious hydration and dehydration trends. Ice likely forms in opal-CT due to opal-CT's higher proportion of Type B H_2O that is present as adsorbed multilayers, rather than as a single monolayer (Type A H_2O) bonded to SiOH as in opal-A. Multiple layers of H_2O can appear spectrally similar to liquid water and may freeze at low temperatures, whereas the first H_2O monolayer, and possibly the next two bound layers, can remain mobile and unfrozen at low temperatures [Hall et al., 1985; Overloop and van Gerven, 1992; Foster and Ewing, 2000]. This hypothesis would imply that opal-CT may contain three or more layers of adsorbed H_2O while opal-A contains at most one to three H_2O layers. Another explanation for why opal-CT develops ice-like spectra is that its surface structure enables ice formation whereas opal-A's structure does not. For

instance, kaolinite's lattice structure is similar to that of hexagonal ice and may facilitate nucleation of ice [Croteau et al., 2008]. Following this analogy, the distribution of surface SiOH on opal-A may not allow for H_2O to adsorb in the appropriate structures needed for ice formation.

The onset of ice-like spectra in opal-CT appears at approximately -45°C, which suggests either a depressed freezing point or a severe temperature discrepancy between the chamber stage and the actual opal sample. The latter is certainly a possibility, as our equipment only reports the temperature of the stage and not the sample itself, which is insulated by the aluminum sample cup. To counteract this effect, our hydration experiments were performed at -85°C even though -70°C would give a nominal RH of 100%. However, even if the temperature discrepancy is as much as 45°C, these results still indicate a fundamental difference between opal-A and opal-CT because both opals were subject to the same experimental conditions and showed different behaviors at freezing temperatures. There is also evidence to support that opal-CT's H_2O may freeze at temperatures well below the typical 0°C freezing point. Several studies of adsorbed water on silica materials have observed that the freezing temperature for bound H_2O layers can be depressed by as much as 50°C dependent on the number of bound layers [da Silva et al., 1992; Bogdan et al., 1998; Schreiber et al., 2001], which can wholly account for the discrepancy seen in our opal-CT samples.

5.2.2 Hydration Changes in Opal-CT

Despite the freezing of opal-CT's H_2O at -85°C, hydration changes are still observed over the course of 12 hours at >90% RH. During this time, the 3 μm band area

visibly increases **(Figure 7A)**, although its growth appears to stagnate after a few hours **(Figure 7C)**. This suggests that H_2O in the high RH chamber still adsorbs onto the opal-CT surface and its frozen H_2O multilayers. Further evidence of active H_2O adsorption is the decrease in the 2.68 μm feature **(Figure 7A)**, which indicates that free SiOH at the opal-CT surface are initially unbound but eventually H-bond to H_2O (or other SiOH) over the course of the experiment. The slight increase in the 2.26/2.2 μm band depth ratio also suggests that at least some of the newly adsorbed H_2O is bonding to SiOH and forming more Type B SiOH at 2.26 μm **(Figure 7C)**.

Opal-CT hydrates predictably faster at ambient laboratory conditions, but surprisingly adsorbs much more water than is observed in opal-A, which is likely near H_2O saturation at ambient conditions (compare **Figure 5B and 8C)**. Interestingly, as the 1.9 and 3 μm absorptions broaden and deepen with hydration, the 2.2 μm feature decreases in strength **(Figure 8A and 8B)**. The 2.26/2.21 μm band depth ratio also decreases as the 1.96/1.9 μm band depth ratio increases **(Figure 8D)**. These observations reinforce the model of opal-CT's preference to adsorb H_2O as Type B multilayers rather than as Type A monolayers attached to Type B SiOH.

5.2.3 Dehydration Changes in Opal-CT

Low-temperature dehydration of opal-CT was simulated at -40°C (~2.5% RH) instead of -55°C due to freezing of opal-CT's H_2O content at -45°C. A slight decrease in the 3 μm absorption is observed over the course of four hours **(Figure 9A and 9B)**, although this could simply be an artificial effect from continuum removal of the spectra. Active dehydration of opal-CT is possible, but not immediately obvious in the absence of

changes in the 1.9, 2.2, and 2.68 μm features, which can be used to corroborate changes in the 3 μm feature.

Overall, hydration and dehydration of opal-CT may occur on Mars but the associated spectral changes are much more subdued than for opal-A and may be difficult to observe from orbital data. The broader implications of these experiments are that martian opal-CT spectra will likely appear ice-like, given the freezing temperatures on Mars' surface.

5.3 Predicted Effects of Low Pressure on Water Adsorption Kinetics

Hydration kinetics may be affected by pressure in addition to temperature. A study of Na-montmorillonite showed that water adsorption followed a 1/e loading time dependent on the water vapor pressure [Frinak et al., 2005]. Low pressures were not specifically controlled in our low temperature experiments, but several factors suggest that our results are applicable to the current martian environment. From previous experimental and thermodynamic study of water adsorption onto smectites and zeolites, pressure did not appear to be the dominant factor controlling adsorption kinetics [David Bish, personal communication]. Our experimental conditions are also similar to those used in calibrations of the REMS (Rover Environmental Monitoring Station) instrument on the MSL (Mars Science Laboratory) rover, which were chosen to mimic atmospheric conditions at Gale crater [Harri et al., 2014].

We can also calculate the actual water vapor pressure in our experimental chamber by applying the dew point temperature T_d = -70°C of the dry air input to Equation 1 **(Section 2.3)**. For both the hydration (at -85°C) and dehydration (at -55°C)

experiments, the actual water vapor pressure in the hydration experiments is 0.2611 Pa. By comparison, the water vapor pressure on Mars has been measured from 0.05 to 2 Pa [Smith et al., 2009]. Because the calculated water vapor pressure in our experiments is comparable to present-day martian water vapor pressures, the kinetics of our experiments are likely similar to adsorption kinetics on Mars.

6. Conclusion

Hydration and dehydration experiments for opal-A and opal-CT at Mars-relevant pressure, temperature, and RH enable predictions for how martian opals may be distinguished from orbital data and how their spectra may vary with seasonal and diurnal atmospheric variations. Experiments at low pressure (0.016 mbar) simulate the long-term dehydration effects on opal due to Mars' thinner atmosphere. These measurements suggest that martian opal-A and opal-CT can be distinguished from orbital spectra; a key distinguishing feature is that opal-A's 1.4 μm feature is positioned at wavelengths short of 1.41 μm while opal-CT is positioned at wavelengths past 1.41 μm.

Experiments at low temperatures (-85 to -10°C) were also performed to assess opal hydration and dehydration kinetics on Mars and determine if hydration changes can be spectrally observed on diurnal or seasonal timescales. We find several differences in hydration behavior between opal-A and opal-CT, owing to their different structures and water adsorption properties. Hydration and dehydration changes are obvious for opal-A and are apparent after only a few hours. These results suggest that martian opal-A readily exchanges water with the atmosphere, even at low temperatures, and will likely show hydration variations in its spectra if observed during periods of different relative

humidity. Importantly, these spectral variations are likely best observed in CRISM data using the 2.26/2.21 μm band depth ratio, as atmospheric absorptions will obscure part of the 1.9 μm feature and changes in the 1.4 μm band position are below the sampling resolution of CRISM data, at least over the course of short-term experiments.

In contrast, changes for opal-CT are much more subdued and difficult to observe spectrally. In addition, the H_2O in opal-CT appear to freeze and produce ice-like spectra at temperatures below -45°C, likely due to opal-CT's higher proportion of Type B H_2O which occurs as multiple layers and can structurally and spectrally resemble liquid water. Conversely, opal-A's higher proportion of Type A, monolayer H_2O likely remains mobile and does not freeze at low temperatures. These results suggest that martian opal-CT are likely to exhibit ice-like spectra, particularly in the 3 μm region.

Acknowledgements

The authors thank David Bish for discussion of the effects of low pressure on hydration kinetics. This work was funded by a MSL Participating Scientist grant.

References

Anderson, J. H., and K. A. Wickersheim (1964), Near infrared characterization of water and hydroxyl groups on silica surfaces, *Surface Science*, *2*, 252–260, doi:10.1016/0039-6028(64)90064-0.

Beck, P., A. Pommerol, B. Schmitt, and O. Brissaud (2010), Kinetics of water adsorption on minerals and the breathing of the Martian regolith, *J. Geophys. Res.*, *115*(E10), E10011, doi:10.1029/2009JE003539.

Bibring, J.-P. et al. (2006), Global Mineralogical and Aqueous Mars History Derived from OMEGA/Mars Express Data, *Science*, *312*(5772), 400–404, doi:10.1126/science.1122659.

Bish, D. L., J. William Carey, D. T. Vaniman, and S. J. Chipera (2003), Stability of hydrous minerals on the martian surface, *Icarus*, *164*(1), 96–103, doi:10.1016/S0019-1035(03)00140-4.

Bishop, J. L., and C. M. Pieters (1995), Low-temperature and low atmospheric pressure infrared reflectance spectroscopy of Mars soil analog materials, *J. Geophys. Res.*, *100*(E3), 5369–5379, doi:10.1029/94JE03331.

Boboň, M., A. A. Christy, D. Kluvanec, and L. Illášová (2011), State of water molecules and silanol groups in opal minerals: a near infrared spectroscopic study of opals from Slovakia, *Phys Chem Minerals*, *38*(10), 809–818, doi:10.1007/s00269-011-0453-0.

Bogdan, A., M. Kulmala, and N. Avramenko (1998), Reduction of Enthalpy of Fusion and Anomalies during Phase Transitions in Finely Divided Water, *Phys. Rev. Lett.*, *81*(5), 1042–1045, doi:10.1103/PhysRevLett.81.1042.

Brown, L. D., A. S. Ray, and P. S. Thomas (2003), 29Si and 27Al NMR study of amorphous and paracrystalline opals from Australia, *Journal of Non-Crystalline Solids*, *332*(1–3), 242–248, doi:10.1016/j.jnoncrysol.2003.09.027.

Burneau, A., O. Barres, J. P. Gallas, and J. C. Lavalley (1990), Comparative study of the surface hydroxyl groups of fumed and precipitated silicas. 2. Characterization by infrared spectroscopy of the interactions with water, *Langmuir*, *6*(8), 1364–1372, doi:10.1021/la00098a008.

Campbell, K. A., K. Sannazzaro, K. A. Rodgers, N. R. Herdianita, and P. R. L. Browne (2001), Sedimentary Facies and Mineralogy of the Late Pleistocene Umukuri Silica Sinter, Taupo Volcanic Zone, New Zealand, *Journal of Sedimentary Research*, *71*(5), 727–746, doi:10.1306/2DC40964-0E47-11D7-8643000102C1865D.

Christy, A. A. (2010), New insights into the surface functionalities and adsorption evolution of water molecules on silica gel surface: A study by second derivative near infrared spectroscopy, *Vibrational Spectroscopy*, *54*(1), 42–49, doi:10.1016/j.vibspec.2010.06.003.

Cloutis, E. A., M. A. Craig, R. V. Kruzelecky, W. R. Jamroz, A. Scott, F. C. Hawthorne, and S. A. Mertzman (2008), Spectral reflectance properties of minerals exposed to simulated Mars surface conditions, *Icarus*, *195*(1), 140–168, doi:10.1016/j.icarus.2007.10.028.

Croteau, T., A. K. Bertram, and G. N. Patey (2008), Adsorption and Structure of Water on Kaolinite Surfaces: Possible Insight into Ice Nucleation from Grand Canonical Monte Carlo Calculations, *J. Phys. Chem. A*, *112*(43), 10708–10712, doi:10.1021/jp805615q.

Dalton, J. B. (2010), Spectroscopy of Icy Moon Surface Materials, *Space Sci Rev*, *153*(1–4), 219–247, doi:10.1007/s11214-010-9658-7.

Davy, R., J. A. Davis, P. A. Taylor, C. F. Lange, W. Weng, J. Whiteway, and H. P. Gunnlaugson (2010), Initial analysis of air temperature and related data from the Phoenix MET station and their use in estimating turbulent heat fluxes, *J. Geophys. Res.*, *115*(E3), E00E13, doi:10.1029/2009JE003444.

Ehlmann, B. L. et al. (2009), Identification of hydrated silicate minerals on Mars using MRO-CRISM: Geologic context near Nili Fossae and implications for aqueous alteration, *Journal of Geophysical Research: Planets*, *114*, E00D08, doi:10.1029/2009JE003339.

Foster, M. C., and G. E. Ewing (2000), Adsorption of water on the NaCl(001) surface. II. An infrared study at ambient temperatures, *The Journal of Chemical Physics*, *112*(15), 6817–6826, doi:10.1063/1.481256.

Frinak, E. K., C. D. Mashburn, M. A. Tolbert, and O. B. Toon (2005), Infrared characterization of water uptake by low-temperature Na-montmorillonite: Implications for Earth and Mars, *J. Geophys. Res.*, *110*(D9), D09308, doi:10.1029/2004JD005647.

Gallego-Gómez, F., A. Blanco, D. Golmayo, and C. López (2011), Three Regimes of Water Adsorption in Annealed Silica Opals and Optical Assessment, *Langmuir*, *27*(23), 13992–13995, doi:10.1021/la203529s.

Goryniuk, M. C., B. A. Rivard, and B. Jones (2004), The reflectance spectra of opal-A (0.5–25 μm) from the Taupo Volcanic Zone: Spectra that may identify hydrothermal systems on planetary surfaces, *Geophys. Res. Lett.*, *31*(24), L24701, doi:10.1029/2004GL021481.

Hall, P. G., R. T. Williams, and R. C. T. Slade (1985), Nuclear magnetic resonance and dielectric relaxation investigations of water sorbed by Spherisorb silica, *J. Chem. Soc., Faraday Trans. 1*, *81*(4), 847–855, doi:10.1039/F19858100847.

Harri, A.-M. et al. (2014), Mars Science Laboratory relative humidity observations: Initial results, *J. Geophys. Res. Planets*, *119*(9), 2132–2147, doi:10.1002/2013JE004514.

Hertl, W., and M. L. Hair (1968), Hydrogen bonding between adsorbed gases and surface hydroxyl groups on silica, *J. Phys. Chem.*, *72*(13), 4676–4682, doi:10.1021/j100859a053.

Hess, S. L., J. A. Ryan, J. E. Tillman, R. M. Henry, and C. B. Leovy (1980), The annual cycle of pressure on Mars measured by Viking Landers 1 and 2, *Geophys. Res. Lett.*, *7*(3), 197–200, doi:10.1029/GL007i003p00197.

Hockey, J. A., and B. A. Pethica (1961), Surface hydration of silicas, *Trans. Faraday Soc.*, *57*(0), 2247–2262, doi:10.1039/TF9615702247.

Hoffmann, P., and E. Knözinger (1987), Novel aspects of mid and far IR Fourier spectroscopy applied to surface and adsorption studies on SiO2, *Surface Science*, *188*(1–2), 181–198, doi:10.1016/S0039-6028(87)80150-4.

Jamieson, C. S., E. Z. Noe Dobrea, J. B. Dalton, K. M. Pitman, and W. J. Abbey (2014), The spectral variability of kieserite (MgSO4·H2O) with temperature and grain size and its application to the Martian surface, *J. Geophys. Res. Planets*, *119*(6), 2013JE004489, doi:10.1002/2013JE004489.

Jänchen, J., D. L. Bish, D. T. F. Möhlmann, and H. Stach (2006), Investigation of the water sorption properties of Mars-relevant micro- and mesoporous minerals, *Icarus*, *180*(2), 353–358, doi:10.1016/j.icarus.2005.10.010.

Jänchen, J., R. V. Morris, D. L. Bish, M. Janssen, and U. Hellwig (2009), The H2O and CO2 adsorption properties of phyllosilicate-poor palagonitic dust and smectites under

martian environmental conditions, *Icarus*, *200*(2), 463–467, doi:10.1016/j.icarus.2008.12.006.

Jones, J. B., and E. R. Segnit (1969), Water in sphere-type opal, *Mineralogical Magazine*, *37*(287), 357–361.

Jones, J. B., and E. R. Segnit (1971), The nature of opal I. nomenclature and constituent phases, *Journal of the Geological Society of Australia*, *18*(1), 57–68, doi:10.1080/00167617108728743.

Kieffer, H. H. (1976), Soil and Surface Temperatures at the Viking Landing Sites, *Science*, *194*(4271), 1344–1346, doi:10.1126/science.194.4271.1344.

Langer, K., and O. W. Flörke (1974), Near infrared absorption spectra (4000–9000 cm− 1) of opals and the role of "water" in these SiO 2· nH 2 O minerals., *Fortschritte der Mineralogie*, *52*(1), 17–51.

Lippincott, E. R., and R. Schroeder (1955), One-Dimensional Model of the Hydrogen Bond, *The Journal of Chemical Physics*, *23*(6), 1099–1106, doi:10.1063/1.1742196.

Martín-Torres, F. J. et al. (2015), Transient liquid water and water activity at Gale crater on Mars, *Nature Geosci*, *8*(5), 357–361, doi:10.1038/ngeo2412.

McDonald, R. S. (1958), Surface Functionality of Amorphous Silica by Infrared Spectroscopy, *J. Phys. Chem.*, *62*(10), 1168–1178, doi:10.1021/j150568a004.

McLennan, S. M. (2003), Sedimentary silica on Mars, *Geology*, *31*(4), 315–318, doi:10.1130/0091-7613(2003)031<0315:SSOM>2.0.CO;2.

Milliken, R. E., J. F. Mustard, F. Poulet, D. Jouglet, J.-P. Bibring, B. Gondet, and Y. Langevin (2007), Hydration state of the Martian surface as seen by Mars Express

OMEGA: 2. H2O content of the surface, *Journal of Geophysical Research: Planets*, *112*(E8), n/a–n/a, doi:10.1029/2006JE002853.

Morris, R. V. et al. (2016), Silicic volcanism on Mars evidenced by tridymite in high-SiO2 sedimentary rock at Gale crater, *PNAS*, *113*(26), 7071–7076, doi:10.1073/pnas.1607098113.

Mustard, J. F. et al. (2008), Hydrated silicate minerals on Mars observed by the Mars Reconnaissance Orbiter CRISM instrument, *Nature*, *454*(7202), 305–309, doi:10.1038/nature07097.

Mustard, J. F., F. Poulet, B. L. Ehlmann, R. E. Milliken, and A. Fraeman (2012), Sequestration of volatiles in the Martian crust through hydrated minerals: A significant planetary reservoir of water, *Lunar Planet. Sci. XLIII*, Abstract No. 1539.

Overloop, K., and L. van Gerven (1992), NMR relaxation in adsorbed water, *Journal of Magnetic Resonance (1969)*, *100*(2), 303–315, doi:10.1016/0022-2364(92)90263-7.

Pommerol, A., B. Schmitt, P. Beck, and O. Brissaud (2009), Water sorption on martian regolith analogs: Thermodynamics and near-infrared reflectance spectroscopy, *Icarus*, *204*(1), 114–136, doi:10.1016/j.icarus.2009.06.013.

Rice, M. S., E. A. Cloutis, J. F. Bell III, D. L. Bish, B. H. Horgan, S. A. Mertzman, M. A. Craig, R. W. Renaut, B. Gautason, and B. Mountain (2013), Reflectance spectra diversity of silica-rich materials: Sensitivity to environment and implications for detections on Mars, *Icarus*, *223*(1), 499–533, doi:10.1016/j.icarus.2012.09.021.

Robertson, K., and D. Bish (2013), Constraints on the distribution of CaSO4·nH2O phases on Mars and implications for their contribution to the hydrological cycle, *Icarus*, *223*(1), 407–417, doi:10.1016/j.icarus.2012.10.028.

Ruff, S. W. et al. (2011), Characteristics, distribution, origin, and significance of opaline silica observed by the Spirit rover in Gusev crater, Mars, *Journal of Geophysical Research: Planets*, *116*(E7), n/a–n/a, doi:10.1029/2010JE003767.

Schreiber, A., I. Ketelsen, and G. H. Findenegg (2001), Melting and freezing of water in ordered mesoporous silica materials, *Phys. Chem. Chem. Phys.*, *3*(7), 1185–1195, doi:10.1039/B010086M.

Siever, R. (1962), Silica Solubility, 0°-200° C., and the Diagenesis of Siliceous Sediments, *The Journal of Geology*, *70*(2), 127–150.

da Silva, A., P. Donoso, and M. A. Aegerter (1992), Properties of water adsorbed in porous silica aerogels, *Journal of Non-Crystalline Solids*, *145*, 168–174, doi:10.1016/S0022-3093(05)80450-8.

Skok, J. R., J. F. Mustard, B. L. Ehlmann, R. E. Milliken, and S. L. Murchie (2010), Silica deposits in the Nili Patera caldera on the Syrtis Major volcanic complex on Mars, *Nature Geosci*, *3*(12), 838–841, doi:10.1038/ngeo990.

Smith, M. R., J. L. Bandfield, E. A. Cloutis, and M. S. Rice (2013), Hydrated silica on mars: combined analysis with near-infrared and thermal-infrared spectroscopy, *Icarus*, doi:10.1016/j.icarus.2013.01.024.

Smith, P. H. et al. (2009), H2O at the Phoenix Landing Site, *Science*, *325*(5936), 58–61, doi:10.1126/science.1172339.

Squyres, S. W. et al. (2008), Detection of Silica-Rich Deposits on Mars, *Science*, *320*(5879), 1063–1067, doi:10.1126/science.1155429.

Stolper, E. (1982), Water in silicate glasses: An infrared spectroscopic study, *Contr. Mineral. and Petrol.*, *81*(1), 1–17, doi:10.1007/BF00371154.

Sun, V. Z., and R. E. Milliken (2015), Ancient and recent clay formation on Mars as revealed from a global survey of hydrous minerals in crater central peaks, *J. Geophys. Res. Planets*, *120*(12), 2015JE004918, doi:10.1002/2015JE004918.

Sun, V. Z., R. E. Milliken, and K. M. Robertson (2017a), Distinguishing Opal Types and Their Water Distributions from Near-Infrared Spectroscopy for Applications to Mars, *in prep*.

Sun, V. Z., R. E. Milliken, K. M. Robertson, S. W. Ruff, and J. D. Farmer (2017b), Mineralogy and Chemistry of Opal-Rich Mars Analog Sites and Implications for Rover Observations, *in prep*.

Vaisala (2013), Humidity Conversion Formulas

Vaniman, D. T., D. L. Bish, S. J. Chipera, C. I. Fialips, J. William Carey, and W. C. Feldman (2004), Magnesium sulphate salts and the history of water on Mars, *Nature*, *431*(7009), 663–665, doi:10.1038/nature02973.

Voort, P. V. D., I. Gillis-D'Hamers, and E. F. Vansant (1990), Estimation of the distribution of surface hydroxyl groups on silica gel, using chemical modification with trichlorosilane, *J. Chem. Soc., Faraday Trans.*, *86*(22), 3751–3755, doi:10.1039/FT9908603751.

Wang, A., J. J. Freeman, I.-M. Chou, and B. L. Jolliff (2011), Stability of Mg-sulfates at −10°C and the rates of dehydration/rehydration processes under conditions relevant to Mars, *J. Geophys. Res.*, *116*(E12), E12006, doi:10.1029/2011JE003818.

Weitz, C. M., J. L. Bishop, P. Thollot, N. Mangold, and L. H. Roach (2011), Diverse mineralogies in two troughs of Noctis Labyrinthus, Mars, *Geology*, *39*(10), 899–902, doi:10.1130/G32045.1.

Zent, A. P., D. J. Howard, and R. C. Quinn (2001), H2O adsorption on smectites: Application to the diurnal variation of H2O in the Martian atmosphere, *J. Geophys. Res.*, *106*(E7), 14667–14674, doi:10.1029/2000JE001394.

Zhdanov, S. P., L. S. Kosheleva, and T. I. Titova (1987), IR study of hydroxylated silica, *Langmuir*, *3*(6), 960–967, doi:10.1021/la00078a014.

Zhuravlev, L. T. (2000), The surface chemistry of amorphous silica. Zhuravlev model, *Colloids and Surfaces A: Physicochemical and Engineering Aspects*, *173*(1–3), 1–38, doi:10.1016/S0927-7757(00)00556-2.

Tables

Table 1. Compilation of opal features in the 1-4 μm region. References 1-5 report absorptions from natural opal and chalcedony samples, references 6-15 report absorptions from synthetic silica gel or glass. A more complete list of references is available in Table 1 of Sun et al. [2017b].

References for Table 1:
1. Jones and Segnit [1969]
2. Langer and Florke [1974]
3. Goryniuk et al. [2004]
4. Bobon et al. [2011]
5. Rice et al. [2013]
6. McDonald [1958]
7. Hockey and Pethica [1961]
8. Anderson and Wickersheim [1964]
9. Hair and Hertl [1968]
10. Stolper [1982]
11. Zhdanov et al. [1987]
12. Hoffman and Knozinger [1987]
13. Burneau et al. [1990]
14. Van Der Voort et al. [1990]
15. Christy [2010]

Abs (um)	Molecule (Type)	Action	H-bonded?	References
1.4-1.41	SiOH, H_2O (A)	OH stretch overtone in SiOH and H_2O	no, yes (to SiOH but not H_2O)	3-5, 8, 10, 13, 15
1.45-1.46	SiOH, H_2O (B)	OH stretch overtone in SiOH and H_2O	yes (to H_2O)	3-5, 8, 13, 15
1.90-1.92	H_2O (A)	combination bend and stretch of H_2O	no, yes (to SiOH but not H_2O)	2-5, 8, 10, 13, 15
1.93-1.96	H_2O (B)	combination bend and stretch of H_2O	yes (to H_2O)	2-5, 8, 13, 15
2.20-2.22	SiOH (A)	combination OH stretch and SiOH or SiOSi bend	no	2-5, 8, 10, 13, 15
2.25-2.26	SiOH (B)	combination OH stretch and SiOH or SiOSi bend	yes (to H_2O)	2-5, 8, 13, 15
2.67-2.68	SiOH (isolated/free, A)	fundamental OH stretch	no	6, 8, 9, 12, 14
2.7-2.74	SiOH (single, B)	fundamental OH stretch	yes (to H_2O)	1, 7
2.82-2.86	SiOH (geminal, B)	fundamental OH stretch	yes (to H_2O)	1, 7
2.69-2.86	SiOH (adjacent)	fundamental OH stretch	yes (to SiOH)	1-3, 11-14
>2.8	H_2O (B)	fundamental OH stretch	yes (to H_2O)	2, 6-10, 11, 14

Table 2. Summary of the experiments performed in this work and the opal-A and opal-CT samples studied in each experiment.

	Opal-A Samples	**Opal-CT Samples**
Low Pressure Experiments (all ASD)	(B-10)B_a1 1C1_1 3B2_b HISB2_white OS2 OS3 SM1 SM3	B3_a1 4A(A-15)_a1 1C(A-16)_b1 2C(A-8)_b1 46E5885 5(A-4)B_b1 B3_c1
Heating Experiments (all FTIR)	2C2_1 4D_1 HISB2_1 OS3 SM3 5(A-4)A_c1 (opal-A/CT)	1B(A-23)_a1 1B(A-23)_b1 1C(A-16)_b1 2C(A-8)_b1 5(A-4)B_b1 B3_a1
Low Temperature and Relative Humidity Experiments (FTIR unless otherwise noted)		
Hydration at -85°C, nominal 100% RH from a very dehydrated state	SM3 OS3 (ASD and FTIR)	B3_a1 46E5885 (ASD)
Hydration at -85°C, nominal 100% RH from a partially dehydrated state	SM3 (ASD and FTIR)	-
Hydration at -85°C, nominal 100% RH from a hydrated state	SM3	-
Dehydration at -55°C, ~15% RH from a hydrated state	SM3	N/A, not possible due to freezing
Dehydration at -40°C, ~2.5% RH from a hydrated state	-	B3_a1
Cycling between nominal 100% RH (-85°C) and ~0% RH (-10°C)	SM3	N/A, not possible due to freezing
Hydration at 22°C, 100% RH from a hydrated state	SM3 OS3	B3_a1 (ASD and FTIR) 46E5885 (ASD and FTIR)

Figures

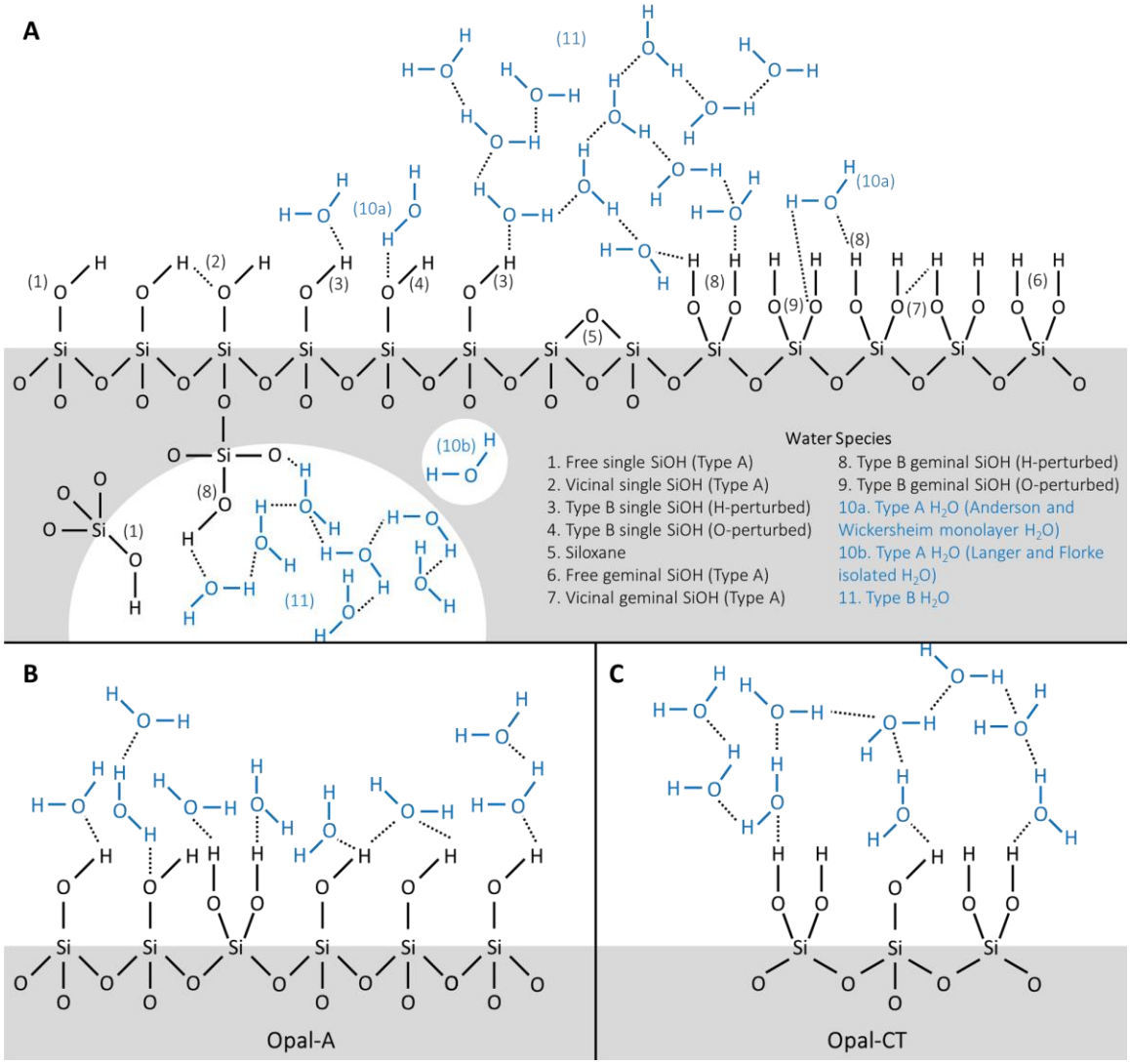

Figure 1. A) Depiction of Type A and B H_2O and SiOH (single, geminal, adjacent, free) species. **B)** H_2O adsorption model for opal-A and **C)** opal-CT incorporating the models of Bobon et al. [2011] and Sun et al. [2017b]. Compared to opal-A, opal-CT has a greater proportion of geminal to single SiOH groups and also preferentially adsorbs H_2O in multiple layers, rather than as a single layer attached to SiOH. Figures are adapted from Anderson and Wickersheim [1964], Langer and Florke [1974], Van Der Voort et al. [1990], Zhuravlev [2000], and Bobon et al. [2011].

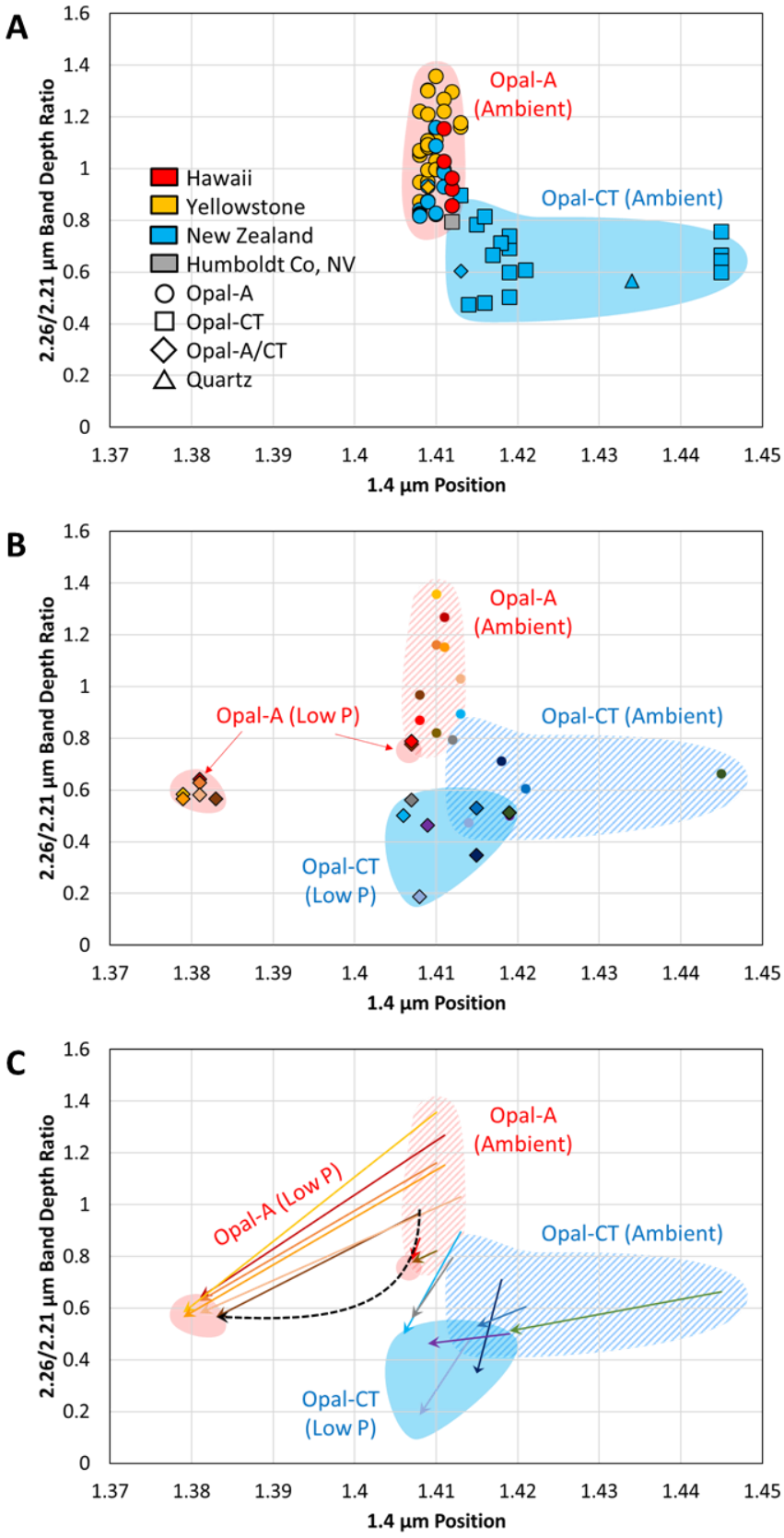
A
B
C
2.26/2.21 µm Band Depth Ratio
1.4 µm Position
Opal-A (Ambient)
Opal-CT (Ambient)
Opal-A (Low P)
Opal-CT (Low P)
Hawaii
Yellowstone
New Zealand
Humboldt Co, NV
Opal-A
Opal-CT
Opal-A/CT
Quartz

Figure 2. A) Opal-A and opal-CT are spectrally distinguishable at ambient laboratory conditions by the position of their 1.4 μm absorption and the 2.26/2.21 μm band depth ratio [Sun et al., 2017b]. **B)** At low pressure (0.016 mbar), the 1.4 μm position and the 2.26/2.21 μm ratio both decrease for opal-A and opal-CT. Opals measured at ambient conditions are shown as circles, while opals measured at low pressure are shown as diamonds. Both opal types are still distinguishable, although the opal-A samples plot as two groups, one of which does not significantly deviate from the ambient opal-A samples. **C)** The same plot as **B**, but with lines connecting the ambient and low pressure points for each sample to illustrate their migration in this parameter space when a vacuum is pulled. Note that these lines are shown for clarity and do not represent actual dehydration trends, which are nonlinear. For reference, an example of such a dehydration trend is depicted for sample SM 1 in the curved, dotted black line.

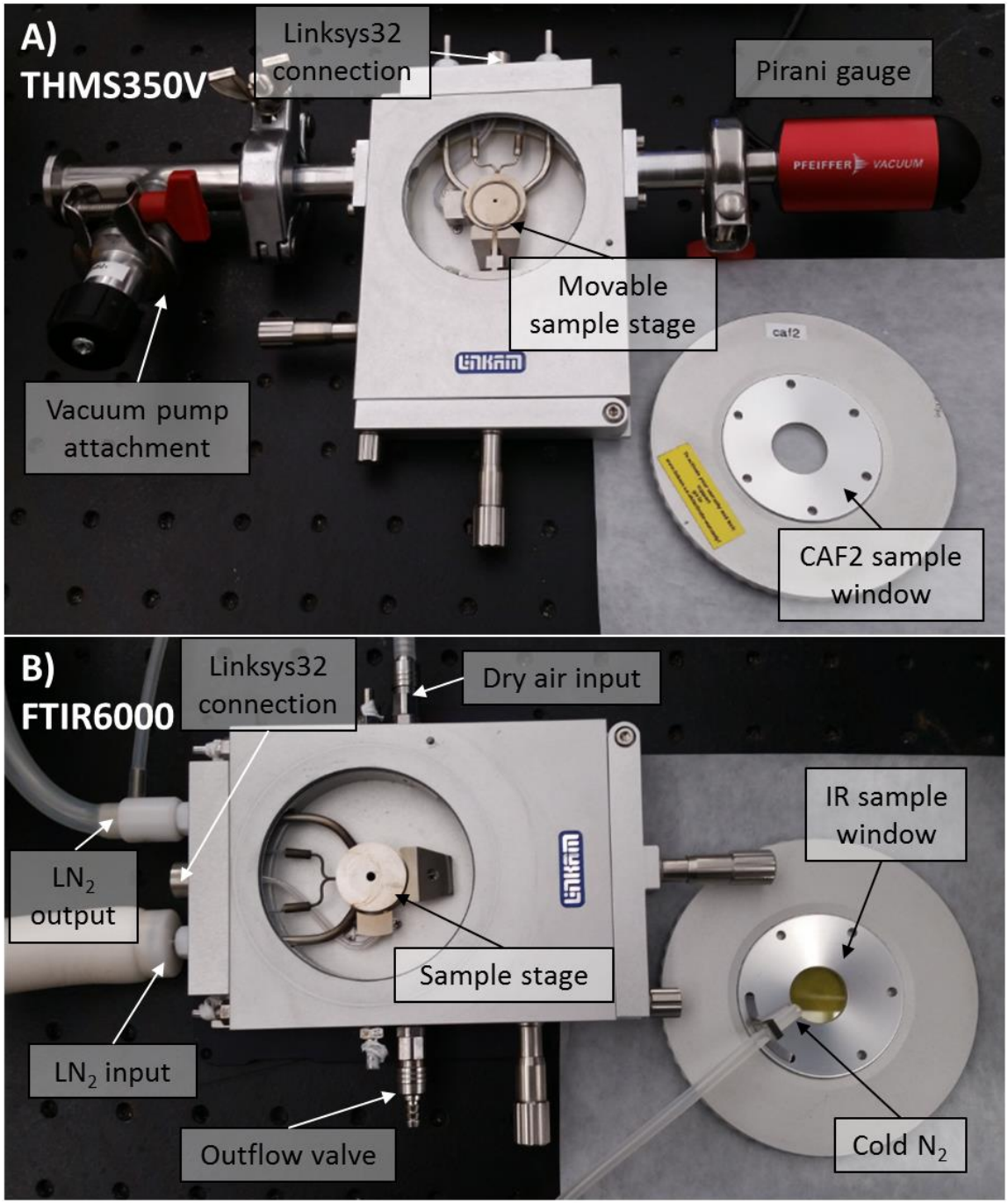

Figure 3. Experimental setup for both Linkam stages. For scale, the sample stage is 22 mm in diameter. **A)** The THMS350V stage is used for low pressure experiments, with its attached vacuum pump and pirani gauge. **B)** The FTIR6000 stage is used for heating and low temperature experiments, the latter enabled by a connection to a LN_2 dewar. Dry air with a dewpoint of -70°C can be passed through the chamber and removed through an outflow valve. During low temperature experiments, cold air is blown over the sample window to prevent condensation.

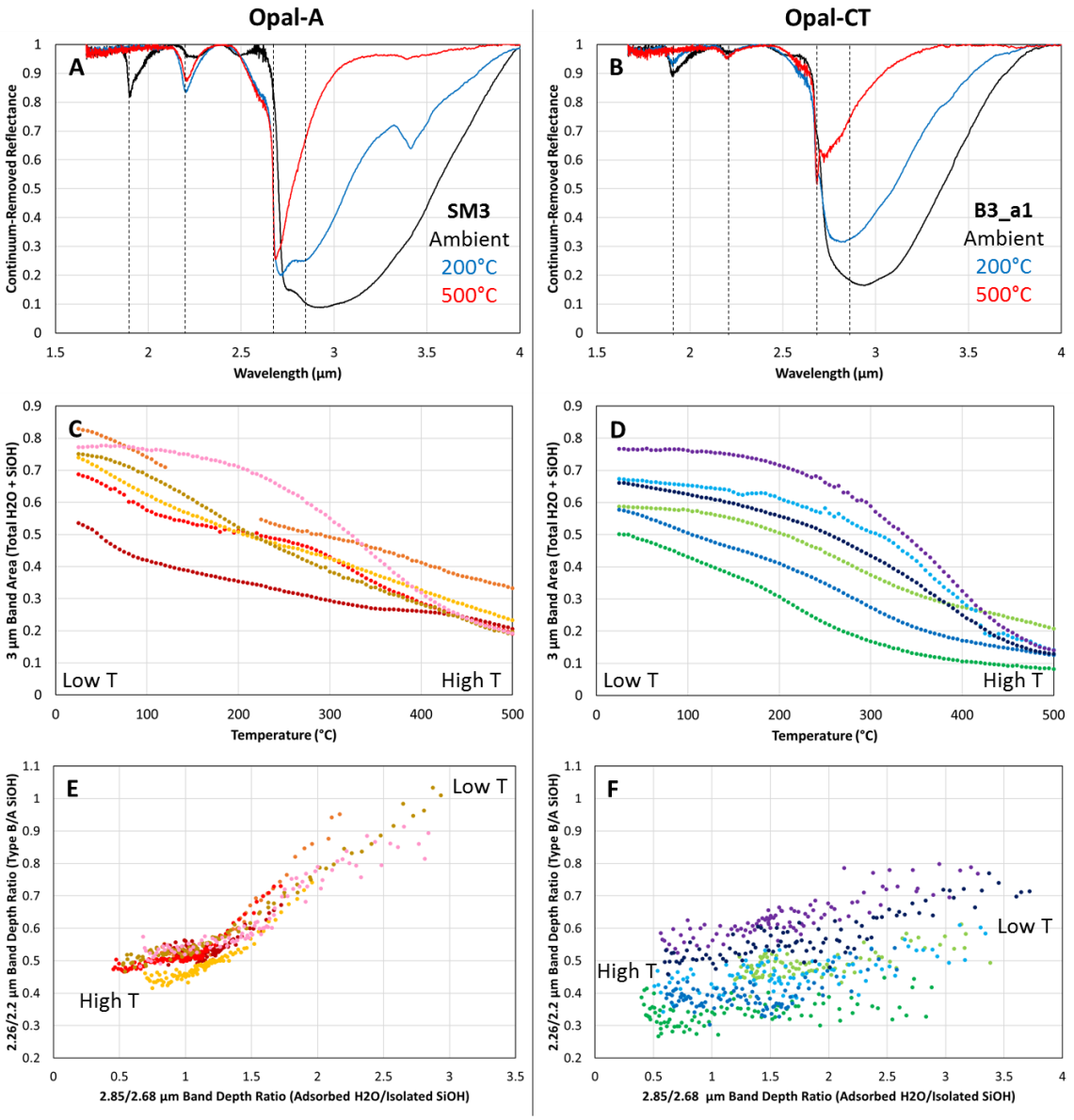

Figure 4. Continuum-removed **s**pectra of **A)** an opal-A sample SM 3 and **B)** an opal-CT sample B3_a1 at ambient laboratory conditions (black) and after heating to 200°C (blue) and 500°C (red). **C)** The band area of the broad 3 µm feature, indicating total H_2O and SiOH content, decreases with increasing temperature for five opal-A samples and an opal-A/CT sample (pink) and **D)** six opal-CT samples. A gap in the orange opal-A spectrum is due to missing data from this temperature interval. **E)** The 2.85/2.68 µm band depth ratio is a proxy for the proportion of H_2O to free SiOH, while the 2.26/2.2 µm band depth ratio is a proxy for the proportion of Type A SiOH (not H-bonded to H_2O) to Type B SiOH (H-bonded to H_2O). Opal-A shows clear dehydration trends in this parameter space and shows significant change in the 2.26/2.2 µm band depth ratio, whereas **F)** opal-CT dehydration trends are more diffuse and do not show as much change in the 2.26/2.2 µm band depth ratio.

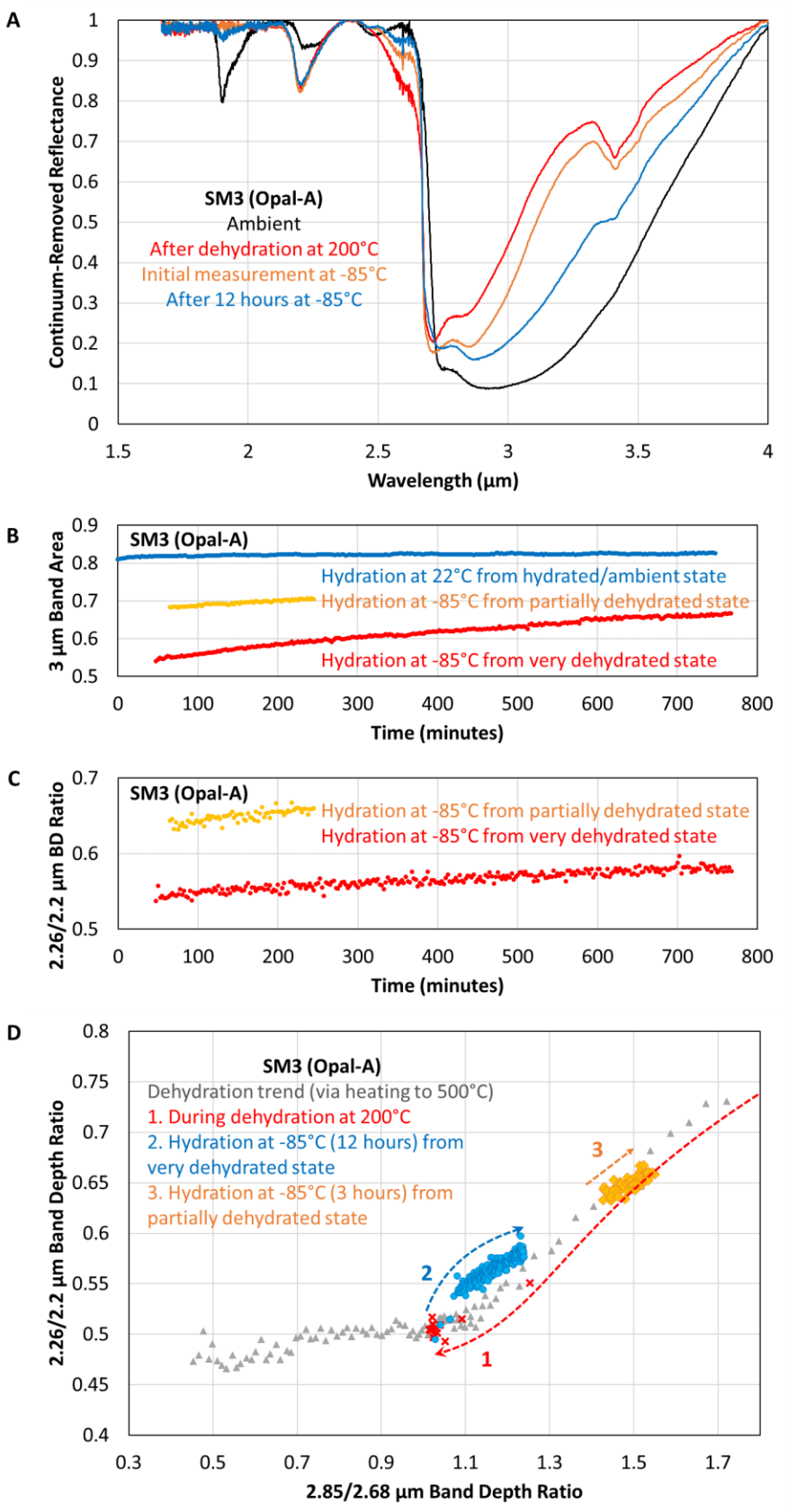
A
Continuum-Removed Reflectance
Wavelength (µm)
SM3 (Opal-A)
Ambient
After dehydration at 200°C
Initial measurement at -85°C
After 12 hours at -85°C
B
3 µm Band Area
Time (minutes)
SM3 (Opal-A)
Hydration at 22°C from hydrated/ambient state
Hydration at -85°C from partially dehydrated state
Hydration at -85°C from very dehydrated state
C
2.26/2.2 µm BD Ratio
Time (minutes)
SM3 (Opal-A)
Hydration at -85°C from partially dehydrated state
Hydration at -85°C from very dehydrated state
D
2.26/2.2 µm Band Depth Ratio
2.85/2.68 µm Band Depth Ratio
SM3 (Opal-A)
Dehydration trend (via heating to 500°C)
1. During dehydration at 200°C
2. Hydration at -85°C (12 hours) from very dehydrated state
3. Hydration at -85°C (3 hours) from partially dehydrated state
1
2
3

Figure 5. A) Continuum-removed spectra of opal-A sample SM 3 at ambient conditions, after dehydration at 200°C, and after hydration at -85°C (>90% RH). Absorptions at ~3.4 µm are attributed to organic material in the sample. **B)** Behavior of the 3 µm band area and the **C)** 2.26/2.2 µm band depth ratio as opal-A is (red) hydrated at -85°C for 12 hours from a very dehydrated state, (yellow) hydrated at -85°C for three hours from a partially dehydrated state, and (blue) hydrated at 22°C for 12 hours from an initially hydrated state at ambient laboratory conditions. No discernable trend is observed in the 2.26/2.2 µm band depth ratio during the hydration experiment at 22°C, thus it is not shown in C). Datapoints lacking in the first ~50 minutes of the red and yellow trends correspond to dehydration of the sample via heating or dry air. **D)** Behavior of the 2.85/2.68 µm and 2.26/2.2 µm band depth ratios as opal-A is 1) dehydrated at 200°C (red) and 2) hydrated at -85°C (blue) from the very dehydrated state. 3) The hydration trend for an initially partially dehydrated opal is also shown for comparison. Dotted lines correspond to progression of the parameters with time.

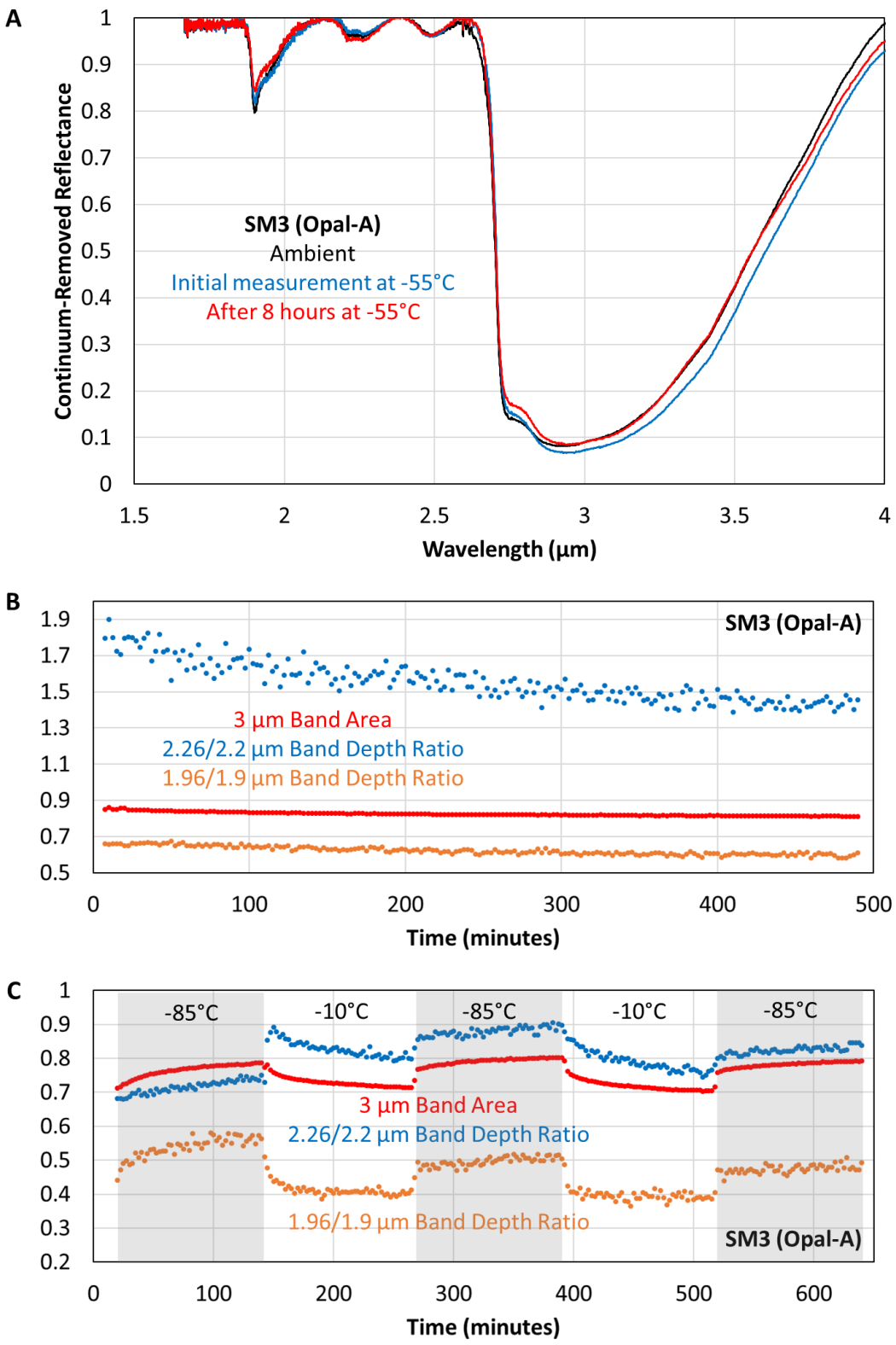

Figure 6. A) Continuum-removed spectra of opal-A sample SM 3 at ambient condition and after dehydration at -55°C (15% RH). The initial measurement at -55°C (blue) shows

a slight increase in hydration relative to the ambient spectrum (black) due to the RH increase as the temperature is decreased from 22°C to -55°C. **B)** Behavior of the 3 µm band area and 2.26/2.2 and 1.96/1.9 µm band depth ratios as opal-A is dehydrated at -55°C for eight hours. **C)** Behavior of the 3 µm band area and the 2.26/2.2 and 1.96/1.9 µm band depth ratios as opal-A is cycled between -85°C (>90% RH) and -10°C (~0% RH) in two hour intervals.

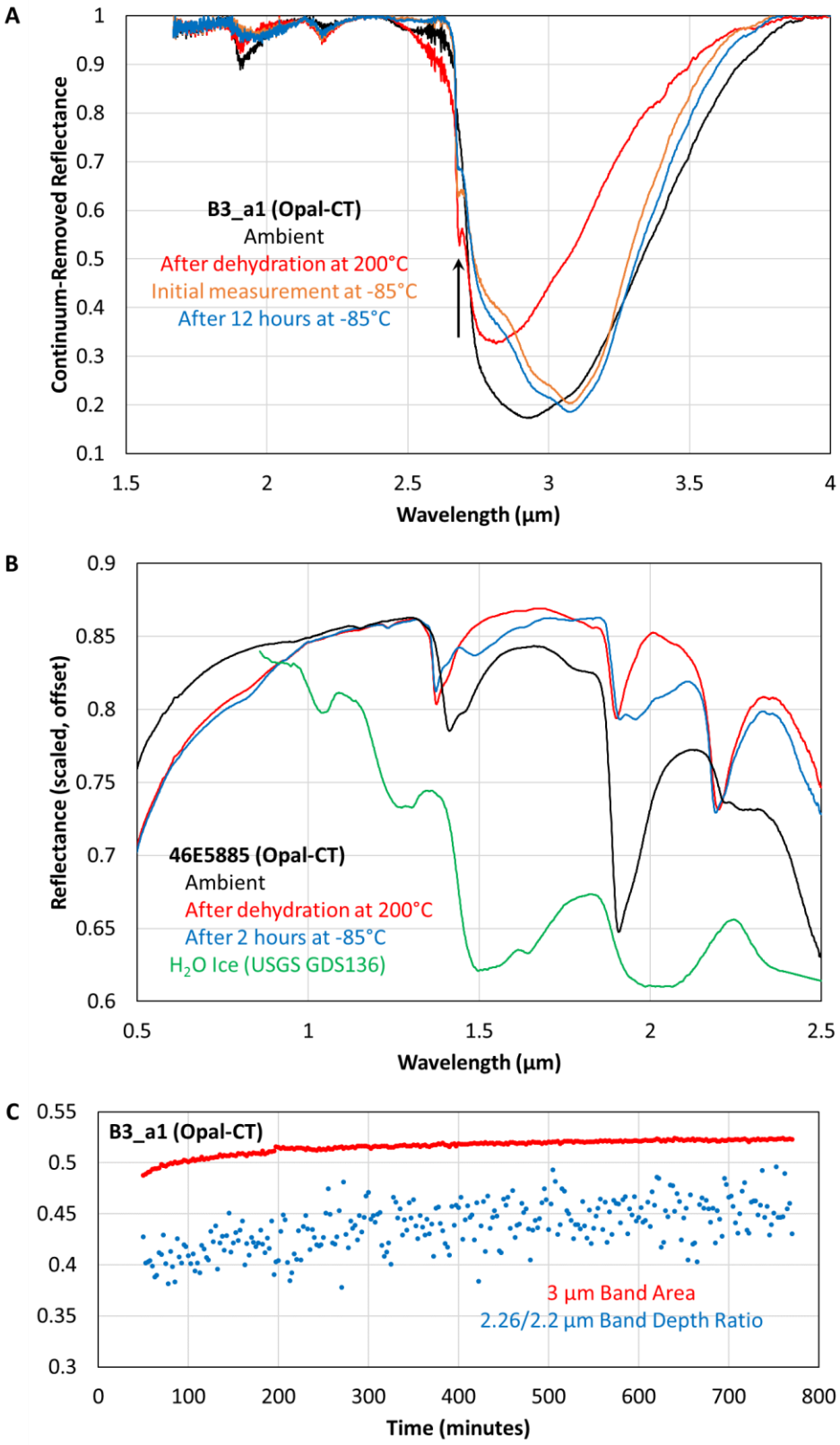
A
Continuum-Removed Reflectance
Wavelength (µm)
B3_a1 (Opal-CT)
Ambient
After dehydration at 200°C
Initial measurement at -85°C
After 12 hours at -85°C
B
Reflectance (scaled, offset)
Wavelength (µm)
46E5885 (Opal-CT)
Ambient
After dehydration at 200°C
After 2 hours at -85°C
H2O Ice (USGS GDS136)
C
B3_a1 (Opal-CT)
3 µm Band Area
2.26/2.2 µm Band Depth Ratio
Time (minutes)

Figure 7. A) Continuum-removed spectra of opal-CT sample B3_a1 at ambient conditions, after dehydration at 200°C, and after hydration at -85°C (>90% RH). Note the presence of ice at ~3.1 µm in the two spectra taken at -85°C and the black arrow indicating a decrease in the 2.68 µm absorption attributed to free SiOH. **B)** ASD spectra of opal-CT sample 46E5885 at ambient conditions, after dehydration at 200°C, and after hydration at -85°C. The opal-CT spectra are offset (but not scaled) such that the reflectance values are the same at 1.32 µm. A library spectrum of water ice from the USGS is scaled and shown for comparison. The presence of ice in the -85°C opal-CT spectrum (blue) is especially apparent at 1.5 µm. **C)** Behavior of the 3 µm band area and the 2.26/2.2 µm band depth ratio as opal-CT is hydrated at -85°C for 12 hours. The first 50 minutes correspond to dehydration of the sample at 200°C and the temperature ramp down to -85°C.

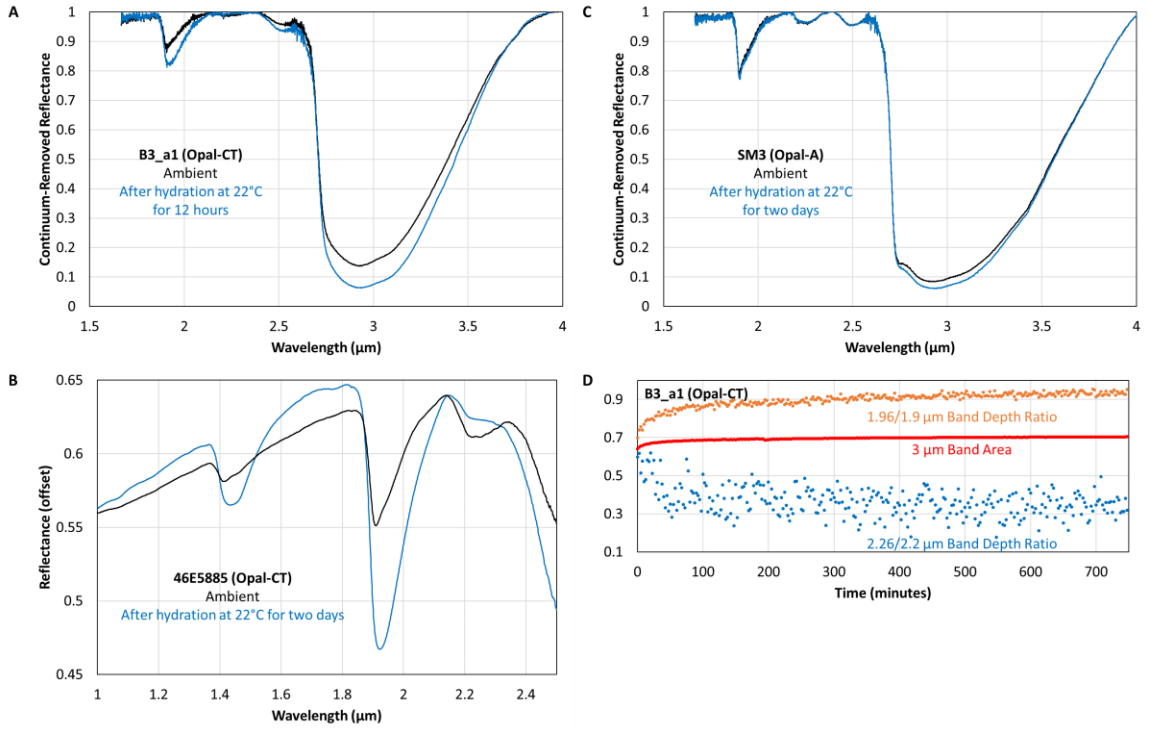

Figure 8. A) Spectra of opal-CT sample B3_a1 at ambient conditions and after hydration at 22°C (100% RH). **B)** ASD spectra of opal-CT sample 46E5885 at ambient conditions and after hydration at 22°C (100% RH). The spectra are offset such that the reflectance values are the same at 2.13 µm. **C)** For comparison, spectra of opal-A sample SM3 at ambient conditions and after hydration at 22°C (100% RH), showing little difference in hydration. **D)** Behavior of the 3 µm band area and 2.26/2.2 and 1.96/1.9 µm band depth ratios as opal-CT sample B3_a1 is hydrated at -40°C for 12 hours, corresponding to the spectra in **A**.

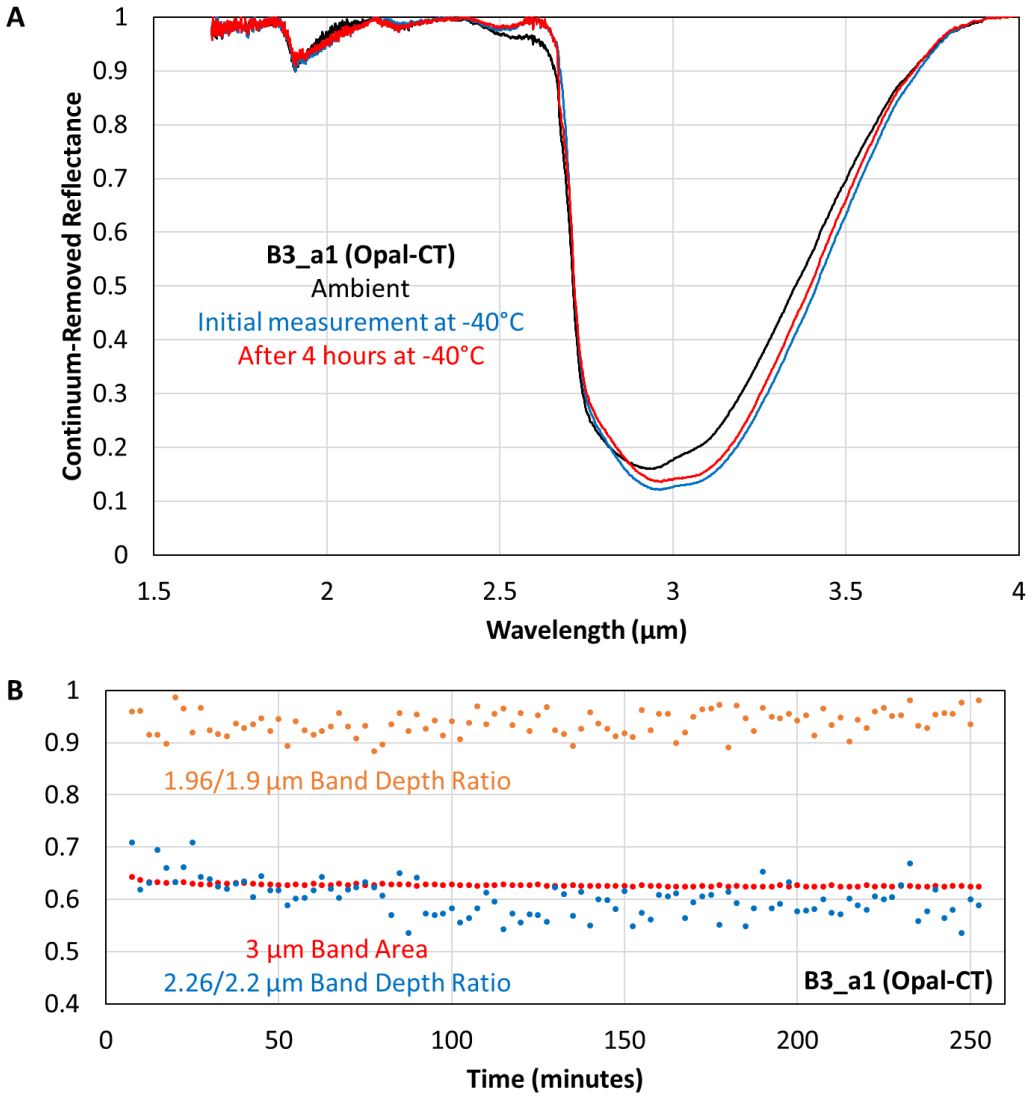

Figure 9. A) Continuum-removed spectra of opal-CT sample B3_a1 at ambient condition and after dehydration at -40°C. The initial measurement at -40°C (blue) shows an increase in hydration relative to the ambient spectrum (black) due to the RH increase as the temperature is decreased from 22°C to -40°C. **B)** Behavior of the 3 µm band area and 2.26/2.2 and 1.96/1.9 µm band depth ratios as opal-CT is dehydrated at -40°C for four hours.

CHAPTER 6:

Hydrated Silica on Mars: Geologic Settings and Orbital Evidence for Opal Maturity and Seasonal Cycling of Water with the Atmosphere

Vivian Z. Sun

and

Ralph E. Milliken

Department of Earth, Environmental, and Planetary Sciences, Brown University,

Providence, RI 02912, USA

To be submitted:

Summer 2017

Abstract

Widespread hydrated or opaline silica has been detected on Mars from orbital spectroscopy and reflect water-rock interactions in diverse environments. Spectral variations have long been observed in the 1.4, 1.9, and 2.2 μm features of these detections and are interpreted to represent differences in silica crystallinity. However, most orbital detections are compared to laboratory spectra acquired under ambient conditions and specific opal types have not yet been conclusively identified on Mars from orbital data. Here we document the geologic settings of martian opals and determine the opal types present by comparison of CRISM data with laboratory measurements of opals at Mars-like conditions. Based on the 1.4 μm feature, we find that bedrock silica occurrences are consistent with opal-A while eolian silica occurrences are consistent with opal-CT on a global scale. This could reflect differences in exposure age between the two geologic settings or indicate slow opal maturation in particulate materials. We also observe temporal variations in the 2.2 μm absorption, which may result from opal exchanging H_2O with seasonally changing atmospheric water content. This is a kinetically feasible process based on laboratory experiments and suggests that opals may play a role in regulating the present-day atmospheric water cycle. Overall, these results add to the growing documentation of more mature silica phases on Mars, indicating more extensive aqueous processes than previously thought. However, the association of opal type with geologic context suggests that caution and detailed geomorphologic and stratigraphic study is needed when interpreting martian paleoenvironments from opal detections.

1. Introduction

Orbital detections of hydrated or opaline silica across Mars provide evidence for widespread water-rock interaction in a variety of aqueous environments. These occurrences are associated with diverse geologic settings, and their hypothesized formation mechanisms include sedimentary deposition [Milliken et al., 2008], direct precipitation [Skok et al., 2010; Ruff et al., 2011; Bandfield et al., 2013], and acidic leaching [Bishop et al., 2008]. On Earth, the diagenetic sequence of opal-A to opal-CT to opal-C to microcrystalline quartz is known to represent an increasing degree of aqueous activity and can be used to assess water longevity in an environment [e.g., Siever, 1962; Williams and Crerar, 1985]. The apparent prevalence of opal-A may indicate limited water availability on Mars post-formation, as any opal-A exposed to aqueous conditions at the martian surface should convert completely to quartz within 400 million years [Tosca and Knoll, 2009]. Recently, however, more mature silica phases such as opal-CT [Morris et al., 2016] or other relatively crystalline opals [Smith et al., 2013] and secondary quartz [Smith and Bandfield, 2012] have been identified on Mars, indicating regions where more extensive aqueous activity may have occurred. Opals on Earth are also recognized as excellent host materials for preserving biomarkers [Cady and Farmer, 1996; Konhauser et al., 2003], and immature opals like opal-A are noted to offer better preservation quality, as more mature opals like opal-CT/C result from further aqueous processing that may overprint the original biosignatures [e.g., Jones and Renaut, 2003; Campbell et al., 2015]. Discerning opal type on Mars therefore allows for further assessment of aqueous activity in past environments as well as identification of regions with high biosignature preservation potential.

Near-infrared spectral variations in opals have been observed from orbital data and are hypothesized to represent differences in opal crystallinity or type [Milliken et al., 2008; Smith et al., 2013]. Opal's hydration features at 1.4, 1.9, and 2.2 μm reflect different H-bonding environments of SiOH and H_2O associated with the opal structure. Different opal types exhibit different bonding behaviors and therefore spectral features, particularly with regard to H-bonding of adsorbed H_2O on the opaline surface [Langer and Florke, 1974; Bobon et al., 2011; Sun et al., 2017b]. Spectroscopic studies of terrestrial opals have shown that it is possible to distinguish opal types (e.g., A versus CT) by using spectral parameters to characterize its 1.4 and 2.2 μm features at both ambient laboratory [Rice et al., 2013; Sun et al., 2017b] and Mars-like atmospheric conditions [Sun et al., 2017c].

Through these spectral parameterization methods, regional variations in opal crystallinity or type have been identified on Mars using CRISM (Compact Reconnaissance Imaging Spectrometer for Mars) data [Smith et al., 2013]. There is also evidence for different opal types on much smaller scales, with the most striking known contrast in hydrated silica spectra coming from Elorza crater **(Figure 1)**. At Elorza's central pit, hydrated and relatively dehydrated silica are observed four kilometers apart in the same CRISM image [Sun and Milliken, 2015]. These detections are also observed in different geologic contexts, with the hydrated silica associated with eolian material and the dehydrated silica occurring in a bedrock unit. Thus several variables could be contributing to this spectral contrast and to hydrated silica's spectral variability in general on Mars: opal type, host material, and possible opal hydration as induced by changes in atmospheric water content.

The observations at Elorza suggest that some of the regional opal variability observed by Smith et al. [2013] may be due to opals in different host materials which may not necessarily represent local in situ aqueous activity. This is particularly true if the silica is hosted in mobile eolian sediments that may have originated elsewhere, and this caveat has previously been recognized by Smith et al. [2013]. Spectral variabilities may also occur from seasonal atmospheric water variations, which affect H_2O adsorption on opals. Though kinetics on Mars are slower due to lower pressures and temperatures, laboratory experiments have demonstrated that opals can exchange water with a Mars-like atmosphere on very short timescales (on the order of hours) [Sun et al., 2017c]. In this work we explore the possible causes for these variations in CRISM hydrated silica spectra by comparison with laboratory measurements of opals [from Sun et al., 2017bc]. We distinguish the opal types and/or hydration states that are present on Mars, discuss the relation to their geologic settings, and investigate the possibility of seasonal cycling of water between opal and the martian atmosphere.

2. Background

2.1 The Hydrated Silica Group

The "hydrated silica" class comprises a broad group of aqueous phases with the chemical formula $SiO_2 \cdot nH_2O$ and more than 1 wt% H_2O [Jones and Segnit, 1971]. This group can include hydrated silica-rich glasses of volcanic or impact origin, opaline silica (opal-A, opal-CT, opal-C), and microcrystalline quartz (e.g., chalcedony). These phases can be distinguished in terrestrial samples due to the more comprehensive measurements that can be obtained in a laboratory through techniques such as X-ray diffraction and

nuclear magnetic resonance spectroscopy (see Wilson, 2014 for a summary of techniques used to distinguish between opal types). In spectroscopic observations of Mars from orbit, it is often not possible to distinguish between, for instance, hydrated glass and opal-A. Thus the term "hydrated silica" is often used as a catchall phrase to encompass the aforementioned silica phases and is also sometimes used interchangeably with "opaline silica". In this work we will adopt a similar practice and refer to characteristics of opaline silica in relation to hydrated silica.

The opaline silica family follows a sequence of increasing crystallinity in the order of opal-A, opal-CT, and opal-C. In most scenarios, silica precipitates out as amorphous opal-A and undergoes an Ostwald ripening process with subsequent aqueous activity, whereby repeated dissolution and reprecipitation will form more crystalline opal-CT, then opal-C, and ultimately microcrystalline quartz [e.g., Williams and Crerar, 1985]. Full conversion of opal-A to microcrystalline quartz is predicted to occur within 400 million years in the presence of liquid water at martian surface conditions [Tosca and Knoll, 2009]. Though some martian opal has been identified as opal-A [e.g., Ruff et al., 2011; Lee et al., 2015], recent observations of opal's NIR spectra have hinted at more crystalline opal phases on Mars [Rice et al., 2013; Smith et al., 2013].

2.2 Distinguishing Opal Types from NIR Spectroscopy

Hydrated silica-rich phases all share broad absorptions at 1.4, 1.9, and 2.2 μm but show slight differences in band position and shape due to variations in the distribution of their H_2O and SiOH content. Despite a wealth of literature on the spectral features of hydrated silica phases, in both the geologic and material science fields, only a handful of

studies have focused on the NIR spectral differences between different opal types (specifically, opal-A and opal-CT). Pioneering work in this area was performed by Langer and Florke [1974], which categorized opal's water content into four chemical groups called Type A and Type B SiOH and H_2O. Type A can indicate either SiOH that is not influenced by H-bonded H_2O or H_2O that is isolated or bonded only to SiOH **(Figure 2A)**. Type B refers to water groups that experience H-bonding to H_2O, for instance SiOH that is bonded to H_2O at the silica surface or H_2O that is bonded to other H_2O, much like in liquid water.

Vibrations of SiOH molecules are attributed to absorptions at 2.2 μm, a combination bend and stretch of H_2O molecules causes absorptions at 1.9 μm, and OH stretch overtones (from both SiOH and H_2O) are present at 1.4 μm **(Figure 2B)**. Each of these three features are comprised of two subabsorptions, with the shorter wavelength absorption attributed to Type A water and the longer wavelength absorption to Type B water, reflecting the lower bond energies of the relatively weak H-bonds. The relative proportions of these Type A and B SiOH and H_2O populations vary for the different opal types, allowing for their differentiation in NIR spectra. For example, opal-CT contains a higher proportion of Type B H_2O [Langer and Florke, 1974] and Type A SiOH, indicating that much of its H_2O content is present as adsorbed multilayers [Sun et al., 2017b]. In contrast, opal-A has a greater proportion of Type A H_2O [Langer and Florke, 1974] and Type B SiOH, suggesting that adsorbed H_2O preferentially forms bonds with SiOH rather than with other H_2O at the silica surface [Sun et al., 2017b].

Recently, Rice et al. [2013] presented a comprehensive spectral study of silica phases, including opals, to determine how silica-rich materials could be distinguished on

Mars from orbital NIR spectra. They found that general silica groups (i.e. opals versus quartz) were distinguishable, particularly from the position of the 1.4 μm feature. Though they also found that opal-A and opal-CT may be differentiated by opal-A's higher ratio of the 2.2 μm band depth to the 1.9 μm band depth (their Figure 20), the latter may be difficult to obtain from orbital CRISM data, which often shows atmospheric absorptions at ~2 μm that may prohibit valid calculation of the 1.9 μm band depth.

Our previous work [Sun et al., 2017b] expanded on these previous studies and demonstrated that opal-A and opal-CT can be distinguished from the position of their 1.4 μm absorption and the band depth (or Gaussian amplitude) ratio of the 2.26 to 2.21 μm features **(Figure 3)**. Similar to the results of Rice et al. [2013], we also found that the position of the 1.4 μm feature shifts to longer wavelengths with increasing silica crystallinity and were able to specifically constrain positions short of 1.413 μm to opal-A and positions past 1.413 μm to opal-CT. The shape of the 2.2 μm feature was also diagnostic, with higher 2.26/2.21 μm band depth ratios occurring for opal-A. These trends were maintained for spectral measurements at ambient laboratory conditions as well as those obtained at low pressures to simulate martian surface conditions. Together, the ambient and low pressure measurements constrain this parameter space for martian opals, which are expected to occupy band positions at 1.37-1.41 μm for opal-A and at 1.41-1.45 μm for opal-CT **(Figure 3B)**.

2.3 Opal Hydration Behavior on Mars

Hydration kinetics at martian conditions have been studied for a number of hydrated minerals (e.g., smectites, zeolites, sulfates) and have demonstrated that

adsorption and desorption processes on martian minerals can occur on kinetically fast timescales despite lower temperatures and pressures [e.g., Bish et al., 2003; Beck et al., 2010]. Recent low temperature hydration experiments on opals suggest that such processes are also relevant for martian opaline silica and may account for some spectral variations observed in orbital data [Sun et al., 2017c]. These laboratory experiments suggest promise for mineral-atmosphere water exchange on present-day Mars, and hydrated minerals have been hypothesized to help regulate diurnal or seasonal atmospheric water variations [e.g., Bish et al., 2003]. However, there has yet to be confirmation of a specific mineral exhibiting diurnal or seasonal variations in water content, despite an effort to detect hydration changes in sulfate deposits at Valles Marineris over several years [Roach et al., 2009].

In laboratory experiments, opal-A will readily adsorb or desorb H_2O at temperatures as low as -55 to -85°C, resulting in observable spectral changes within an hour of exposure to these simulated martian conditions. These spectral variations are most obvious in the large 3 µm absorption associated with OH stretching in SiOH and H_2O, while spectral variations at 1.4, 1.9, and 2.2 µm are subtler. Of the opal-related spectral parameters discussed in **Section 2.2**, the 2.26/2.21 µm band depth ratio appears to be best-suited for tracking these hydration changes. The position of the 1.4 µm feature only shows shifts on the order of 1-2 nm, at least over the course of short-term experiments, well below the sampling resolution of CRISM data. Martian opal-A are therefore likely to react to atmospheric water content variations on kinetically fast timescales that may be observable in the 2.2 µm feature in CRISM data. In contrast, hydration changes for opal-CT are more difficult to observe particularly because its H_2O

content, most of which is present as multiple liquid H_2O-like layers, freezes at temperatures below -45°C. As a result, opal-CT on Mars are likely to exhibit ice-like spectra, especially in the 3 μm region.

3. Methods

The objectives of this work are to identify the opal types present on Mars, their geologic contexts, and assess the possibility of water exchange between opals and the seasonally changing martian atmosphere. This work thus requires correlating mineralogy from high-resolution spectral data with geomorphologic units defined in high-resolution images. We used data acquired by a suite of instruments on the Mars Reconnaissance Orbiter (MRO): Compact Reconnaissance Imaging Spectrometer for Mars (CRISM) spectral data, Context Camera (CTX) images, and High Resolution Imaging Science Experiment (HiRISE) images.

3.1 Opal Identification in CRISM Data

In this work we use CRISM data from the 1.0-2.6 μm wavelength region, which captures the 1.4, 1.9, and 2.2 μm absorptions diagnostic of hydrated silica [Murchie et al., 2007]. Data cubes were processed in ENVI using the CRISM Analysis Toolkit v6.6, which was used to apply photometric corrections by dividing the data by the cosine of the solar incidence angle and minimize atmospheric effects using the volcano scan method [McGuire et al., 2009]. Vertical striping effects and spectral spikes were then reduced [Parente, 2008] prior to map-projecting each image cube, and standard parameter maps [Pelkey et al., 2007] were generated to guide mineral identification.

Each CRISM scene was first examined using the BD1900 and BD2210 parameter maps, which respectively indicate absorptions at 1.9 μm due to H_2O and at 2.2 μm due to Al-OH or Si-OH vibrations from Al-clays or hydrated silica. Regions highlighted in these parameters were then manually inspected to confirm or refute the presence of hydrated silica. Al-bearing clays like kaolinite and montmorillonite also absorb at 2.2 μm but can be distinguished from hydrated silica by their narrower features, where the longer wavelength edge of the absorption ends short of 2.3 μm. All regions of interest (ROI) were ratioed to a spectrally bland background region to enhance spectral features and reduce atmospheric and instrumental noise. CRISM false color images were also investigated pixel-by-pixel, as some silica detections (as small as tens of pixels) were not highlighted in the parameter maps but did appear as blue-green tones in false color (R/G/B: 2.5295/1.5066/1.0800 μm). Lastly, individual ROIs with similar absorption features were combined into larger ROIs to produce higher signal-to-noise spectra and enable subsequent parameterization of the 1.4 and 2.2 μm features.

3.2 CRISM Sampling Methodology

While conducting a global survey is beyond the scope of this work, we aim to achieve a globally representative sampling of hydrated silica detections in diverse geologic settings. Hydrated silica spectra were therefore collected via three procedures:

1) Detections were taken from our previous global survey of central peak craters [Sun and Milliken, 2015], which provides a relatively complete compilation of hydrated silica occurrences in crater environments.

2) Regional surveys were conducted over locations previously identified as bearing hydrated silica [Carter et al., 2013; Ehlmann and Edwards, 2014]. These regions include:

    a. Ganges Chasma and surrounding plains [Milliken et al., 2008]
    b. Nili Patera [Skok et al., 2010]
    c. Western Hellas Basin [Bandfield, 2008; Bandfield et al., 2013]
    d. Acidalia Planitia [Pan and Ehlmann, 2014]
    e. Confirmed detections from around Valles Marineris and Noctis Labyrinthus [Milliken et al., 2008; Bishop et al., 2009; Metz et al., 2009; Roach et al., 2010; Le Deit et al., 2012; Weitz et al., 2011; 2013]
    f. Confirmed detections from Terra Sirenum [Wray et al., 2011; Ehlmann et al., 2016]
    g. Confirmed detections from Gale crater [Seelos et al., 2014; Fraeman et al., 2016]

    For each of these regions, CRISM analysis spanned all images within a predetermined study area that encompassed data studied by the cited works. For regions with exceptional mineralogic diversity or an abundance of CRISM data, we only assessed images that are confirmed to contain hydrated silica in the literature. Several regions are known to contain hydrated silica but were not assessed in this study due to the complex mineral assemblages present and the amount of CRISM images available: Nili Fossae [Ehlmann et al., 2009; Smith and Bandfield, 2012; Amador and Bandfield, 2016], Mawrth Vallis [Bishop et al.,

2008; McKeown et al., 2009; Noe Dobrea et al., 2010], and Claritas Rise [Viviano-Beck et al., 2017].

3) CRISM images whose default BD2210 maps have high BD2210 parameter values are examined for the presence of hydrated silica. Care was taken to distinguish hydrated silica from Al-clays, as both are highlighted in the BD2210 parameter. A total of 121 images had high BD2210 parameters and did not overlap with those studied from the first two procedures. Of these, 37 were confirmed as bearing hydrated silica, 63 contained Al-clays rather than hydrated silica, and the remainder did not contain any 2.2 μm-bearing minerals. Areas identified through this process as having hydrated silica were investigated further in more extensive regional studies, including: Arcadia Planitia, Chryse Planitia, Elysium Planitia, Hesperia Planum, Kasei Vallis, Mamers Vallis, and Eastern Terra Cimmeria.

A list of the CRISM images studied is provided in **Appendix J**. From the images identified through this survey as containing hydrated silica, groups of overlapping images were selected to study temporal spectral variations. Spectra were obtained from the same silica units and ratioed to the same background region in all images in an overlapping set of images. This minimizes extraneous factors that may cause spectral variations, such as different surface roughness or topographic slopes from different background regions.

3.3 Correlation to Geologic Settings

Hydrated silica detections were then correlated to geomorphologic units observed in HiRISE (0.25-0.50 cm/pixel resolution; McEwen et al., 2007) and CTX (5-6.5 m/pixel;

Malin et al., 2007) images. Units were defined on the basis of their tone, texture, and stratigraphic relations as described in Section 3.4 of Sun and Milliken [2015]. The general categories used in this work are: bedrock, eolian or unconsolidated materials, and periglacial materials. The bedrock group describes coherent units that appear lithified, and can encompass rock outcrops, sedimentary bedrock (when in association with fluvial landforms), and impact melt or uplifted bedrock associated with impact craters. Eolian or unconsolidated deposits appear as mobile materials that do not appear to be indurated and may have eolian features like dunes or ripples. Periglacial materials are similar to unconsolidated deposits, except that they tend to occur at higher latitudes and are characterized by lobate morphologies. Examples of these broad geomorphologic classes are shown in **Section 4.**

3.4 Comparison of CRISM Spectra to Laboratory Spectra

We use spectral parameters to quantify variations in the 1.4 and 2.2 μm features of hydrated silica in both CRISM and laboratory data. Spectra are continuum-removed and the band position of the 1.4 μm minimum is calculated. The 2.2 μm feature is modeled with two Gaussians centered at 2.21 and 2.26 μm, indicative of SiOH that are not H-bonded to H_2O and those that do experience H-bonding with H_2O, respectively [Langer and Florke, 1974]. Subtle variations in the 2.2 μm feature are then characterized using the ratio of the 2.26 to the 2.21 μm Gaussian amplitudes. These parameters at 1.4 and 2.2 μm were shown in our previous work to be capable of distinguishing between opal-A and opal-CT at ambient lab conditions as well as at low pressures **(Figure 3)**. Due to noise in the CRISM data, all calculation results were manually inspected to ensure that

the parameters were capturing real absorptions and not noise. Gaussian fits for the 2.26/2.21 μm ratio were inspected for goodness of fit and the calculated position of the 1.4 μm feature was verified to indicate a real absorption minimum rather than single data spikes. The latter criteria proved to be very restricting because a detection with a clear 2.2 μm feature (i.e. the requirement for the detection to classify as hydrated silica) may not necessarily have a discernable 1.4 μm feature. As a result, a number of detections were not included in the final parameter results because their spectra, while sufficient to identify the presence of hydrated silica, were too noisy to produce meaningful parameter values.

The shape of opal's 1.9 μm feature also varies with opal type and can be quantified through similar parameterization [Rice et al., 2013]. However, we focus on the 1.4 and 2.2 μm features as the 1.9 μm feature is a ubiquitous absorption in all H_2O-bearing minerals and its shape is also distorted at longer wavelengths (~1.96 μm) due to residual atmospheric absorptions in CRISM data [Murchie et al., 2007]. These specific parameters are also relatively sensitive to the presence of other minerals that also absorb at 1.4 and 2.2 μm, thus materials that plot within the pure opal fields are expected to be relatively opal-rich (>80 wt% opal) when mixed with other 2.2- μm absorbing phases [Sun et al., 2017b].

4. Results: Geologic Settings of Martian Opals

This section describes the general geomorphologic units that host hydrated silica and synthesizes possible formation mechanisms proposed in the literature. These geologic settings are broadly grouped into bedrock units, eolian or unconsolidated

deposits, and periglacial deposits **(Figure 4)**, but can be further subdivided based on high resolution imagery and the regional geologic context. Though many of these locations have been previously studied, we confirm past detections and report new detections of hydrated silica as well, particularly in the regions of Ganges and Melas Chasmata, Nili Patera, and Arcadia Planitia.

4.1 Bedrock

Bedrock units are generally characterized in CTX and HiRISE imagery by their lithified and cohesive appearance, but can have additional features when occurring in fluvial, volcanic, or impact settings. Fluvial or sedimentary bedrock often contains layering, appears stratigraphically confined, or is associated with fluvial landforms. Bedrock in volcanic settings is oftentimes massive (rather than layered) and sometimes occurs within mounds or domes that may have volcanic origins. Within impact craters, bedrock units are varied in their appearance and origin as they may be excavated from depth or formed in situ as impact melt. Bedrock in nondescript outcrops cannot be placed into any of the aforementioned groups.

4.1.1 Fluvial and Sedimentary Settings

Hydrated silica-bearing bedrock that has an inferred fluvial and sedimentary origin often shows layering **(Figure 5B)** or appears confined to a single stratum **(Figure 5C, D)**. In the absence of observable layering, a bedrock unit may appear massive but still be considered sedimentary when associated with a fluvial landform such as a fan deposit **(Figure 5E)**. Because sedimentary bedrock can also form from eolian and

volcanic processes, in this section we only infer units to have a fluvial origin if they have a clear association with fluvial landforms or features.

Hydrated silica associated with fluvial sedimentary bedrock is prevalent in the plains near Valles Marineris, where orbital evidence for opaline silica was first identified [Milliken et al., 2008]. The silica-bearing bedrock in this region appears both light-toned and dark-toned (e.g., **Figure 5B-D**) and its expanse ranges from Ganges Chasma to the east and towards Noctis Labyrinthus to the west. It is not yet understood whether these strata are discrete or continuous throughout the entire region. The many channels and fan deposits observed on these plains have favored a fluvial origin for these silica occurrences, implying either a detrital origin or authigenic formation [Metz et al., 2009]. Due to their stratigraphic position above Hesperian-age lava flows and their occurrence within pits that formed during the Hesperian, the emplacement or formation of this hydrated silica likely occurred during the Hesperian or Amazonian [Milliken et al., 2008]. Some co-located occurrences of jarosite [Milliken et al., 2008], Fe/Mg and Al clays [Le Deit et al., 2010], and various other sulfates [Roach et al., 2010] indicate a complex aqueous history in the Valles Marineris region and suggest that the hydrated silica here may have formed through pedogenic leaching or other acidic processes. Hydrated silica in the nearby pits of Noctis Labyrinthus also occur along a similar assemblage of Fe/Mg and Al clays and jarosite, but these minerals exhibit even more complex stratigraphic relations that point to a complicated alteration history [Weitz et al., 2011; 2013].

Hydrated silica occurs within sedimentary bedrock at several other notable regions on Mars. Hydrated silica units in Acidalia Planitia are found in knobby terrains in

close association with Fe/Mg smectite and jarosite or "doublet material" [Pan and Ehlmann, 2014]. The silica appears restricted to discrete strata, and is interpreted to have formed during a second alteration event after Fe/Mg smectite formation. Formation mechanisms proposed include leaching or precipitation under more acidic conditions, as suggested by the co-occurrence of jarosite or doublet material [Pan and Ehlmann, 2014]. Terra Sirenum is another region recognized for hosting hydrated silica occurrences amongst acidic mineral assemblages that include Al-clays, jarosite, and alunite. Silica occurrences at Columbus crater [Wray et al., 2011] and Cross crater [Ehlmann et al., 2016] are also inferred to have formed from groundwater precipitation or other alteration under acidic conditions.

Other instances of sedimentary hydrated silica in the southern highlands are less regional, but include fan deposits within craters (e.g., **Figure 5E**), in knobby terrains in Terra Cimmeria, and along the bottom of fluvial channels like Kasei and Mamers Valles. At these locations Fe/Mg clays are often the only other hydrated phase in the vicinity and may be co-located with hydrated silica, as in the case of Mamers Valles and Terra Cimmeria, or unassociated with silica, like at Kasei Valles **(Figure 5F)**. One last location of note is Gale crater, the site of ongoing investigations by the Curiosity rover, which has identified opaline silica using the CheMin X-ray diffractometer [Morris et al., 2016]. Hydrated silica has also been detected from CRISM data [Seelos et al., 2014; Fraeman et al., 2016] and from orbit is observed within bedrock units **(Figure 5G)** that are likely sedimentary given the depositional history at Gale crater [Grotzinger et al., 2015]. Though none of these detections have yet been groundtruthed by rover observations,

formation hypotheses for the opaline silica identified by Curiosity are complex and varied [e.g., Rampe et al., 2017; Hurowitz et al., 2017].

4.1.2 Volcanic Settings

The first orbital detection of hydrated silica associated with a volcanic setting was made by Skok et al. [2010], who identified remarkably dehydrated silica, with a weak-to-absent 1.9 μm absorption, near the cone of Nili Patera in light-toned, high-relief bedrock **(Figure 6A)**. Dehydrated silica appears restricted to the Nili Patera cone, as silica elsewhere in this region and at Meroe Patera appears more hydrated with a visible 1.9 μm feature at all other locations. The most interesting of these hydrated silica detections are occurrences within a dune field 20 km south of the dehydrated silica at the volcanic cone (**Figure 7B,** also discussed further in **Section 4.2**). With the notable variations in hydration state, hydrated silica is the sole hydrated phase detected in the immediate vicinity of Nili and Meroe Patera. In the greater Syrtis Major and Nili Fossae region, however, hydrated silica is detected alongside kaolinite, Fe/Mg smectite, chlorite/prehnite, zeolite, and possibly illite and carbonate [e.g., Ehlmann et al., 2009]. The silica occurs primarily in bedrock (but is also in light-toned cover) and is found on the edges of the lava flows or exposed in craters, suggesting that it pre-dates volcanic activity **(Figure 7A)**. The sparse distribution of hydrated silica and lack of accessory mineralogy at Nili Patera proper may suggest high-temperature volcanic hydrothermal alteration as opposed to acid-fog alteration or fumarolic leaching [Skok et al., 2010]. Thus hydrated silica in this region may have formed during at least two alteration episodes, with the first episode occurring prior to flow emplacement at Nili Patera and

possibly producing the mélange of other alteration minerals. The second episode produced only hydrated silica, likely during or after the last flow emplacement at 3.7 Ga [Hiesinger and Head, 2004; Werner, 2009].

More ambiguously, hydrated silica in Arcadia Planitia is associated with mound structures that have been proposed to be of volcanic origin **(Figure 6B)**. Farrand et al. [2011] interpreted these features to be cryptodomes formed from Hesperian volcanism in the northern plains, though they acknowledge other possible dome formation mechanisms including mud volcanism, pingos, and rootless cones. Although they did not identify hydrated silica in their study, Farrand et al. [2011] did detect olivine, high-Ca pyroxene, and glassy compositions in association with these mound structures. At five locations in this region, we find hydrated silica in debris aprons surrounding these mounds (discussed further in **Section 4.2**) and at times on the flanks of the mound structures **(Figure 6B)**. Aside from the hypothesized volcanic setting, these detections are similar to those at Nili Patera in the sense that hydrated silica is the sole hydrated phase detected.

4.1.3 Uplifted Bedrock and Impact Melt in Craters

Hydrated silica occurs in almost a quarter of central peaks bearing hydrous mineralogy, with many of these detections occurring in bedrock units [Sun and Milliken, 2015]. These units can be further separated into bedrock that is uplifted from depth or lithified impact melt. Bedrock that is locally the stratigraphically lowest unit is likely to consist of uplifted materials, and can appear either massive **(Figure 6C, D)** or layered. Hydrated silica in these units could represent ancient alteration products that have been brought to the surface, but authigenesis induced by impact hydrothermalism or simply

post-impact surface alteration cannot be ruled out. Coherent bedrock units that superpose other materials, but cannot be traced to a fluvial origin, are interpreted as impact melt **(Figure 6E, F)**. The hydrated silica in these putative melt deposits is inferred to have formed authigenically post-impact, but may also represent pre-impact materials that have simply mixed into the impact melt. Authigenic formation of this hydrated silica could result from impact-shocking of Fe/Mg clays [Friedlander et al., 2015], which is supported by observations of increasing hydrated silica frequency with crater diameter and at the expense of Fe/Mg clay frequency [Sun and Milliken, 2015]. A full description of bedrock units associated with impact craters can be found in Section 5 of Sun and Milliken [2015].

4.1.4 Other Bedrock Outcrops

Although not examined in further detail in this work, many hydrated silica detections occur in rock outcrops in Noachian-age highland terrains like Noachis Terra and Terra Cimmeria. These generic bedrock units occur along scarps, some of which are associated with crater walls but were not discussed in the previous section. The complex geology and stratigraphy in these regions often complicates further interpretation of these bedrock units and further genetic classification into sedimentary or volcanic settings is not possible. However, bedrock exposures in impact craters can be considered analogous (and appear morphologically similar) to many of these intercrater outcrops as they could be excavating similar crustal layers.

4.2 Eolian or Unconsolidated Deposits

A surprising outcome from a global survey of central peaks bearing hydrous mineralogy is that more than half of those hydrated silica detections are associated with unconsolidated deposits, suggesting a global occurrence of mobile hydrated silica-bearing sediments [Sun and Milliken, 2015]. These unconsolidated deposits are characterized by smooth surfaces, poor crater retention, and a generally unlithified appearance **(Figure 8C-F)**. Such deposits in the Nili Fossae region have been interpreted as lag [Ehlmann et al., 2009] or material transported from a local source region [Smith and Bandfield, 2012]. However, in most cases, it is difficult to constrain the origins of these materials unless an obvious transport pathway is observed. Hereafter we use the term "eolian" to refer to these unconsolidated and mobile deposits.

In addition to the global distribution of these eolian silica within craters, two sites at Nili Patera and Arcadia Planitia host hydrated silica in eolian material and in spatial proximity to hydrated silica hosted in bedrock units. In contrast to the dehydrated bedrock silica at the Nili Patera cone **(Section 4.1.2)**, hydrated silica is detected within a dune field that lies 20 kilometers south of the cone **(Figure 7B and 8A)**. More specifically, the hydrated silica occurs only on the light-toned lee sides of the dunes, which may be actively migrating [Silvestro et al., 2010]. These dunes are at times superposed on top of light-toned patches that may be dacitic igneous flows [Christensen et al., 2005; Wray et al., 2013; see also Rogers and Nekvasil, 2015]. In Arcadia Planitia, unconsolidated hydrated silica is not associated with clear eolian landforms, but appears within debris aprons surrounding mound structures that sometimes contain hydrated silica

themselves **(Figure 8F)**. In some cases, periglacial polygonal textures can be observed in portions of these deposits.

4.3 Periglacial Deposits

Hydrated silica associated with periglacial materials is found at only a few locations in our search **(Figure 9)**, likely due to the latitudinal constraints of these mantling units and obscuration or dilution of spectral signatures from covering or mixing with these deposits. These units are characterized by their mantled appearance, smooth surfaces with few retained craters, and lobate flow-like morphologies. The largest expanse of these periglacial hydrated silica occurrences is the original detection by Bandfield [2008] and Bandfield et al. [2013] at the western edge of Hellas Basin **(Figure 9A)**. These silica occurrences are hypothesized to have formed authigenically through direct precipitation from nonacidic groundwater, though other mechanisms such as transportation and lag formation are also possible [Bandfield et al., 2013]. Fe/Mg smectite and chlorite are also detected on the outer margins of the basin but do not appear to be obviously associated with the hydrated silica.

5. Results: Correlation of Opal Spectral Variations with Geologic Setting

Comparison of CRISM hydrated silica spectra with lab spectra show that there is an association of opal maturity, hydration, or both, with geologic setting that is observable on a global scale **(Figures 10-12)**. Compared to bedrock silica, silica in unconsolidated eolian or periglacial deposits tends to have higher values in the 1.4 and 2.2 μm parameters despite some overlap between the two fields around 1.41-1.42 μm

(Figure 13). The obvious delineation in the 1.4 μm parameter suggests that eolian and periglacial silica has a composition similar to opal-CT, whereas bedrock silica has a composition closer to opal-A. An alternative explanation could be that, disregarding opal type, eolian silica is more hydrated than bedrock silica.

In this section we first discuss how this interpretation of opal maturity and hydration might be geologically possible and then propose and discount alternate explanations for these spectral variations. Spectral variations are also observed in the 2.26/2.21 μm ratio within all geologic settings, but will be discussed further in **Section 6** as it may be more affected by seasonal atmospheric water variations.

5.1 Opal Type

The delineation between martian bedrock silica and eolian silica occurs at a position of 1.41 to 1.42 μm, coinciding with the measured divide at 1.41 μm between laboratory spectra of terrestrial opal-A and opal-CT **(Figure 3)**. The position of the 1.4 μm feature has proven to be a robust diagnostic for distinguishing between opal-A and opal-CT. Hydration experiments on opal-A show that the 1.4 μm position of opal-A will never progress beyond 1.41 μm even when exposed to 100% relative humidity for several days at room temperature [Sun et al., 2017c]. Similarly, dehydration of opal-CT via exposure to dry lab air (with a dew point of -70°C) indicates that its 1.4 μm feature is unlikely to shift to wavelengths below 1.41 μm at very low pressure conditions. As an aside, extreme dehydration at high temperatures makes it possible to achieve positions as low as 1.37 μm, even for opal-CT, though these effects are likely temporary over geologic timescales **(Section 7.3)**. These experiments suggest that a martian silica deposit

plotting with a position of 1.43 μm **(Figure 13)** is highly unlikely to indicate opal-A since the 1.4 μm position of terrestrial opal-A never progresses beyond 1.41 μm even when fully hydrated.

Differences in martian opal type are therefore an attractive explanation for the spectral variations observed in CRISM data. Comparison with the laboratory data from **Figure 3** suggests that hydrated silica in lithified bedrock units is spectrally similar to opal-A, whereas silica in eolian and periglacial deposits is closer to opal-CT. If true, this implies that eolian and periglacial silica is more geochemically mature and aqueously altered than bedrock silica, which could result from several geologic processes. Within periglacial environments, it is not unexpected that silica may be relatively geochemically mature. These opals could be mixed with thin films of ice whose seasonal melting enables diagenetic alteration and maturation of these silica deposits over time, similar to what has been observed for carbonates in glacial sediments on Earth [Fairchild et al., 1993].

More globally, the preferential occurrence of opal-CT in eolian or unconsolidated deposits and opal-A in bedrock suggests differences in the exposure ages of martian hydrated silica. Silica in unconsolidated deposits likely represent older material that was aqueously altered to opal-CT either in the precursor rock or after erosion to their current particulate form. In the first scenario, the surface of a precursor opal-A rock could be chemically altered to opal-CT, after which physical weathering (either coincident or facilitated by the chemical weathering) would erode the opal-CT surface to the present-day eolian deposit, leaving behind a fresh opal-A surface. Eolian silica deposits in Nili Fossae were interpreted as lag deposits and proposed to have formed in a similar manner

[Ehlmann et al., 2009]. Bedrock silica would therefore represent a fresher exposure that has not yet undergone chemical weathering and thus retains an opal-A composition. This would suggest that bedrock silica units with higher 1.4 μm positions experience a faster rate of weathering to opal-CT than the erosion rate, which would remove the surficial opal-CT. Conversely, erosion rates for bedrock silica with lower 1.4 μm positions should outpace the rate of chemical weathering to opal-CT, thus preventing accumulation of surficial opal-CT and exposing fresher opal-A.

Granular eolian materials could also be subject to enhanced chemical weathering due to their greater surface areas compared to a single bedrock unit. For instance, if bedrock and eolian materials begin as opal-A and are exposed to the same aqueous conditions, the eolian silica will more efficiently convert to opal-CT. Studies of terrestrial eolian materials suggest that they are better able to retain water after a wet period and could facilitate dissolution and reprecipitation of silica [Folk, 1978], resulting in eventual opal maturation. The idea of eolian materials trapping water and volatiles has been previously related to dunes on Mars [Fenton et al., 2003]. Periods of precipitation on Mars were likely limited or entirely lacking, so this alteration would possibly rely on cycles of frosting and defrosting that are restricted to higher latitudes, similar to our proposed mechanism for opal maturation in periglacial deposits. However, these eolian materials are mobile and could be lofted to lower and mid-latitudes where we observe them today.

We must note that although the eolian silica detections on Mars are spectrally consistent with opal-CT, it is also possible that they may represent even more mature silica phases like opal-C or microcrystalline quartz. On Earth, sand grains are known to

be rich in quartz due to its greater resistance to physical weathering [Edgett and Lancaster, 1993; Muhs, 2004 and references therein]. Though quartz is nominally anhydrous, microcrystalline quartz may show hydration features from water at structural defect sites [Graetsch et al., 1987]. Microcrystalline quartz tends to have 1.4 μm positions at even longer wavelengths than opal-CT, as well as lower 2.26/2.21 μm Gaussian amplitude ratios [Sun et al., 2017b]. Pending further spectral characterization of opal-C and microcrystalline quartz in laboratory data, these more mature silica phases could also account for a number of silica detections in **Figure 13A**, particular those with high 1.4 μm positions and low 2.26/2.21 μm Gaussian amplitude ratios.

5.2 Opal Hydration Variations

Water content is inherently linked to opal type **(Section 2.2)**, but hydration variations can still exist within the same opal type particularly since silica crystallinity is gradational, rather than discrete, within the opal sequence. In this section we discuss hydration variations due to heterogeneities in opal structure, not variations due to adsorbed H_2O content, which is discussed in **Section 6**. Despite the compelling explanation that eolian silica is more geochemically mature than bedrock silica, the relative trend between opal-A and opal-CT in martian silica **(Figure 13A)** is the opposite of that predicted from laboratory measurements **(Figure 3)**. Laboratory opal-A shows low 1.4 μm positions and high 2.26/2.21 μm ratios, while opal-CT shows high 1.4 μm positions and low 2.26/2.21 μm ratios. In contrast, martian opals seem to follow a trend where the 1.4 μm position is directly correlated to the 2.26/2.21 μm ratio. This is similar to dehydration trends obtained through heating of opals, which yields high 1.4 and 2.2

μm parameter values with high H_2O content and low 1.4 and 2.2 μm parameter values with low H_2O content **(Figure 13B)**. These spectral variations induced by dehydration are independent of opal type. We also note that an alternative explanation for the trend in the martian opals could be mixing with another hydrated phase, specifically gypsum, which is discussed in **Section 7.2**.

The similarity of the observed CRISM trend and the laboratory dehydration trend suggests that variable H_2O content can account for some of the CRISM variations without needing to invoke differences in opal type. One possibility is that eolian silica has more H_2O inclusions, which will shift the 1.4 μm feature to longer wavelengths due to increased H-bonding between H_2O molecules but will not significantly affect the 2.2 μm SiOH feature. However, this explanation is somewhat contrived as it would require a process by which all eolian silica occurrences on Mars are opal-A with sufficient H_2O inclusions to produce longer-wavelength 1.4 μm features, which has not been observed in terrestrial samples to our knowledge. The explanation for silica occurrences in periglacial environments is more straightforward, as they may appear more hydrated because thin films of ice mixed with the opal can contribute towards a longer wavelength 1.4 μm feature since the analogous feature in ice is positioned at 1.5 μm. Overall, however, variable H_2O content cannot explain the entire range of CRISM spectral variations, and opal type is still necessary to account for the full range of observed parameter values, particularly in the position of the 1.4 μm feature.

6. Results: Temporal Changes in Hydrated Silica Spectra

6.1 Spectral Variations Over Time from Overlapping CRISM Images

Observations of the same silica units throughout multiple overlapping CRISM images **(Figure 14)** show that spectral variations are also observed as a function of martian season **(Figures 15-16)**. The 2.26/2.21 μm ratio is shown to increase and decrease at several locations in the southern and equatorial latitudes. This could reflect the effects of H_2O adsorption and desorption as atmospheric relative humidity (RH) increases and decreases during the winter and summer, respectively. Variations in the 1.4 μm position are only sometimes observed, and even then are difficult to discern with confidence over the noise in the CRISM data. The spectral variations at 2.2 μm are unlikely to indicate active opal maturation, which is unlikely to occur on present-day Mars on the short month or year timescales of the CRISM data. Opal maturation is also an irreversible process and any "cycling" of the 2.2 μm parameter, such as the decrease and increase observed at a Terra Cimmeria site (red in **Figure 16B**), negates this hypothesis.

Due to Mars' low temperatures, hydration and dehydration kinetics are relatively slow and may not necessarily occur over observable timescales [e.g., Zent et al., 2001; Roach et al., 2009]. However, laboratory experiments at Mars-relevant temperatures (-85 to -10°C) and water vapor pressures (0.2611 Pa) indicate that opal-A spectra can show hydration changes over timescales as short as hours [Sun et al., 2017c]. In particular, opal-A will tend to adsorb H_2O onto surface SiOH sites, resulting in an increase in the 2.26/2.21 μm ratio but very little change in the 1.4 μm band position, at least during the course of these relatively short experiments. These laboratory observations are consistent

with the temporal changes in the 2.26/2.21 μm ratio for martian opals in **Figure 16**, which we note mostly depict silica from bedrock units (with the exception of craters 51EE and 9BCE), which are implied to be opal-A following the analysis in **Section 5.1**.

In contrast, hydration changes and their associated spectral changes are not easily observed for opal-CT at the same Mars-like experimental conditions. This is primarily due to the freezing of opal-CT's H_2O content at temperatures below -45°C, which produces ice-like features at 3 μm. However, some H_2O adsorption and desorption was still observed on opal-CT at temperatures down to -85°C, suggesting that opal-CT may still be capable of exchanging H_2O with the atmosphere on Mars. In fact, eolian silica occurrences within two craters are interpreted as opal-CT, on the basis of their longer wavelength 1.4 μm features, and still show spectral variability over time **(Figure 15C, D and 16B)**. If opal-CT does in fact hydrate during periods of high RH, laboratory observations predict that opal-CT will prefer to adsorb H_2O onto other H_2O and form multiple layers (like in liquid water) [Sun et al., 2017c].

Although laboratory experiments have shown that temporal variations in CRISM data may represent real H_2O exchange between opal and the martian atmosphere, the observed trends do not appear to perfectly correlate with martian season **(Figure 16)**. For example, RH is expected to be lowest during the summer [e.g., Martin-Torres et al., 2015] and should correspond to lower opal hydration, yet high 2.26/2.21 μm ratios are observed in a Terra Cimmeria deposit (red in **Figure 16B**). Conversely, high RH during the winter should result in higher 2.26/2.21 μm ratios, but a detection at Noctis Labyrinthus (dark blue in **Figure 16A**) is observed with a low 2.26/2.21 μm value during one winter and a high 2.26/2.21 μm value during the next winter. Such inconsistencies

may result from a seasonal "lag" caused by the presence of other buffering minerals in these opal units. Alternatively, we could be imposing an overly simplistic interpretation of seasonal effects on RH when in reality these effects can be very complicated and localized.

Finally, it is necessary to note that although seasonal H_2O adsorption and desorption can account for some of the observed CRISM spectral variations **(Figure 3)**, this result does not contradict the previous interpretation of spectral variations induced by different opal types. As explained in **Section 5.1**, it is difficult to explain the full range of 1.4 μm positions without invoking opal type, particularly since it is difficult to hydrate opal-A to the point where its feature shifts past 1.41 μm. The example at Elorza crater **(Figure 1)** also provides further support for different opal types on Mars, as both silica spectra occur within the same CRISM image and show markedly different spectra despite being acquired at similar atmospheric conditions. Even though the two detections are separated by four kilometers of lateral distance and 400 meters of elevation, RH conditions are unlikely to be different enough to produce such distinct spectra at the two sites.

The combined effects of opal type **(Section 5.1)** and changing atmospheric conditions on the spectral variations of martian opals **(Figure 3)** is therefore summarized as follows. Opal type largely controls the position of the 1.4 μm feature and the laboratory-derived delineation between opal-A and opal-CT at 1.41 μm also coincides with a distinction in the geologic host material. However, within the opal-A and opal-CT (or bedrock and eolian) groups, variable atmospheric conditions between different CRISM images may account for variations in the 2.26/2.21 μm ratio.

6.2 Uncertainties Due to Methodology

As the temporal variations in hydrated silica spectra are subtle and require quantification via the 2.26/2.21 μm ratio parameter, we must also consider factors related to our methods and datasets that could produce artificial spectral differences. In this section we discuss the possible sources of uncertainty involved in the calculation of the 1.4 μm position and the 2.26/2.21 μm ratio parameter.

CRISM data are known to be affected by "spectral smile", which can cause cross-track wavelength shifts across the image on the order of ~10 nm [Ceamanos and Doute, 2010] and possibly affect the true position of the 1.4 μm absorption. However, the trends observed in our CRISM detections **(Figure 13)** span a range of 70 nm, and the bedrock and eolian silica fields are distinct enough that spectral smile cannot account for these differences.

Differences in albedo or viewing geometry (e.g., phase angle) may also influence spectral variations by imposing slopes (e.g., "phase reddening") that may affect spectral continua and absorption shapes. This is particularly a concern for the 2.26/2.21 μm ratio parameter, which characterizes subtleties in the shape of the 2.2 μm feature. To test the effect of different albedos and slopes on our spectral modeling results, we calculated linear mixtures of an opal-A spectrum with a flat line (to adjust albedo) as well as positive and negative sloped lines. Our continuum removal and Gaussian modeling methods were then applied to these modified spectra and only slight deviations from the original 2.2 μm parameter values were observed. These deviations are on the order of ~0.1, which are less than many of the temporal changes in the 2.2 μm ratio observed in **Figure 16**.

As a related case study, we also investigated the effects of ratioing CRISM spectra to different background ROIs, which may have different albedos and topographic slopes. However, no appreciable changes were observed in either the 1.4 or 2.2 μm parameters (again on the order of ~0.1 for the 2.2 μm ratio), suggesting that the choice of the background spectrum should not have a significant effect on our observed CRISM trends (within limits, i.e. a silica spectrum is not being ratioed to a Fe/Mg clay "background" spectrum). It is also possible that differences in viewing geometry or phase angle could cause variations in the 2.26/2.21 μm ratio and invalidate the seasonal variations observed in overlapping CRISM images **(Figure 16)**. However, a plot of the phase angle and the 2.26/2.21 μm ratio value for each CRISM image shows no discernable trend, indicating that phase angle variations are unlikely to systematically contribute to the spectral variations at 2.2 μm.

Future work will focus on quantifying the limits above which perceived temporal changes in the 2.2 μm ratio can be considered robust and legitimate (for example, parameter value differences of 0.2 or greater may be considered above the threshold of error). This will include conducting a similar study of overlapping CRISM images for minerals (e.g., kaolinite) whose spectra are not expected to vary significantly with changes in atmospheric water content. We will also explore the use of more sophisticated atmospheric correction algorithms [Wiseman et al., 2016] to increase signal-to-noise in the CRISM spectra and produce more accurate calculations of the 2.2 μm ratio. The 2.2 μm ratio will also be calculated for entire CRISM scenes on a pixel-by-pixel basis to determine the range of parameter variability due to inherent noise in the CRISM data [e.g., Kaplan et al., 2016].

7. Other Possible Causes of Spectral Variations

We favor differences in opal type and atmospheric conditions as the primary causes for spectral variations in orbital hydrated silica spectra. However, several other factors can contribute to general spectral variations, to varying degrees of plausibility, and are further discussed in this section.

7.1 Spectral and Physical Properties of the Host Material

Independent of chemical or physical weathering processes, it is possible that particulate eolian materials and bedrock units may have different spectral and physical properties due to particle size. However, while particle size scattering is known to affect band depths [Milliken and Mustard, 2007], it cannot completely remove absorptions nor cause shifts in absorption features. For example, it is not possible for particle size scattering to completely remove the 1.9 um feature or cause the 1.4 and 2.2 um features to shift or skew to shorter wavelengths in Elorza's bedrock spectrum (red in **Figure 1**).

A second possibility related to particle size is that eolian particulates may more readily adsorb water compared to bedrock materials due to their increased surface area. However, this is not supported by the analogous comparison of powder and rock chip spectra of the same opal samples in the lab. Our 1.4 and 2.2 um parameters yield the same distinctions between opal-A and opal-CT for both powder and chip samples (Figure 3 in Sun et al., 2017b). In addition, although rocks may have comparatively less adsorption surface area than particulates, they still have some degree of porosity and are still able to adsorb water on its surface, resulting in at least some absorption features, particularly at 1.9 um.

7.2 Mixtures with Other Hydrated Phases (i.e. Gypsum)

We also cannot rule out the possibility of opal mixtures with other hydrated phases to explain why eolian silica has a longer wavelength 1.4 μm absorption. One possible phase is gypsum, which has previously been observed in dunes at northern latitudes [Langevin et al., 2005]. Though pure gypsum grains are likely too fragile to saltate large distances, they could be a globally occurring material that can become incorporated in eolian sediments [e.g., Fishbaugh et al., 2007]. Gypsum and similar sulfates have previously been proposed to exist in light-toned dunes [Thomas et al., 1999], and eolian hydrated silica is, perhaps coincidentally, also often found in lighter-toned material. Gypsum has absorptions at 1.45, 1.95, and 2.22 μm, similar to those of opal, although gypsum's features have a characteristic triplet shape and are broader towards longer wavelengths. A mixture with gypsum would therefore pull opal's absorptions to longer wavelengths and could be a compelling explanation for the longer wavelength 1.4 μm feature and the higher 2.2 μm ratio values for eolian silica **(Figure 13)**. However, more work is needed to determine the amounts of gypsum necessary to produce these spectral effects in opal-gypsum mixtures while minimizing the appearance of gypsum's very characteristic triplet features.

Other minerals that could be physically mixed with silica while preserving the 1.4, 1.9, and 2.2 μm features are Al-clays like kaolinite and montmorillonite. However, kaolinite and montmorillonite have 1.4 μm features that are fixed at approximately 1.41 μm and, in physical lab mixtures with opal, will pull the overall 1.4 μm feature towards 1.41 μm [Sun et al., 2017b]. Al-clays are therefore unlikely to contribute to the observed

features in eolian silica but gypsum, with its broader, longer wavelength absorptions, is a much more plausible candidate.

7.3 Dehydration from Impact or Other Heating Events

Impacts and volcanic events are ubiquitous across Mars and could produce extreme environmental conditions that may affect silica hydration and spectra. An earlier survey of hydrated silica detections at central peaks of impact craters also found a possible correlation of impact crater size with hydrated silica occurrence frequency, suggesting that impact events could facilitate hydrated silica formation [Sun and Milliken, 2015]. Impact events can also dehydrate or dehydroxylate minerals [e.g., Che et al., 2011] and result in possibly permanent changes to the opal structure and water content. For example, heating opal-A to 800°C will remove its characteristic 1.4, 1.9, and 2.2 μm features. At lower temperatures, such as 200 to 500°C, both opal-A and opal-CT will still exhibit features at 1.4 and 2.2 μm [Sun et al., 2017c], similar to the spectrum observed at Elorza crater **(Figure 1)**.

However, all dehydrated samples, even those heated to 800°C, will eventually adsorb H_2O when exposed to ambient laboratory conditions. These experiments suggest that even if opals become dehydrated through a heating event, they will eventually equilibrate with the martian atmosphere and regain at least a 1.9 μm absorption. As further evidence, an opal-A sample that is dehydrated at 200°C and shows no 1.9 μm absorption will adsorb enough H_2O (at >90% RH) to regain an observable 1.9 μm feature within hours, even at -85°C [Sun et al., 2017c]. Thus while impacts and other heating events may cause dehydration of opaline silica, these effects are likely temporary given

equilibration of opal's water content with Mars' atmosphere over geologic timescales. Impact effects also are not likely to explain spectral variations observed in opal occurrences that are not found within craters. However, this analysis does highlight the mystery of the dehydrated silica spectrum at Elorza crater **(Figure 1)**, as no mechanism proposed thus far is capable of maintaining an absent 1.9 µm feature.

8. Summary and Conclusions

We have conducted a survey of martian hydrated silica spectra from CRISM data, studied their geologic contexts, quantified the variations in their 1.4 and 2.2 µm features, and assessed the possible causes for these spectral variations. We find that martian hydrated silica show significant variability in their 1.4 and 2.2 µm features, which we have parameterized as the band position of the 1.4 µm feature and the ratio of the 2.26 to 2.21 µm Gaussian amplitudes, respectively. Variations in the 1.4 µm band position are likely to represent differences in opal type, whereas changes in the 2.26/2.21 µm ratio can be influenced by seasonal variations in atmospheric water.

When distinguished by geologic unit, we observe a clear contrast where hydrated silica in bedrock tends to exhibit 1.4 µm features positioned at <1.42 µm, while silica in eolian or periglacial deposits will have features centered at >1.41 µm. This distinction between the bedrock and eolian silica coincides with the delineation between opal-A and opal-CT, which occurs at 1.41 µm on the basis of laboratory measurements. The association of immature opal-A with bedrock and mature opal-CT with eolian material may indicate differences in exposure age, where bedrock silica may represent fresher opal-A exposures that have not yet altered to more mature opal-CT and eroded away.

Alternatively, the particulate nature of eolian materials may facilitate maturation of opal-A to opal-CT for silica occurrences in unconsolidated deposits. Although observations of varying silica maturity have previously been made [Smith et al., 2013], in this work we are able to specifically constrain features <1.41 μm as characteristic of opal-A and features >1.41 μm as characteristic of opal-CT, while also linking these opal types to different geologic contexts on a global scale.

Variations in the 2.26/2.21 μm ratio are more likely to be affected by martian opals adsorbing or desorbing H_2O as seasonal atmospheric conditions change. Laboratory experiments have shown that opal-A can adsorb and desorb H_2O at Mars-like pressure and temperature and produce the associated spectral changes at 2.2 μm on kinetically fast timescales. On Mars, the 2.2 μm ratio is similarly observed to change over time at several sites where the same hydrated silica deposit can be monitored throughout overlapping CRISM images. These results may represent the first evidence for H_2O exchange between a specific mineral and the martian atmosphere and support hypotheses of hydrated minerals helping to regulate atmospheric water variations. However, further work is needed to quantify the uncertainties in the calculation of the 2.26/2.21 μm ratio and assess the robustness of these possible temporal variations in hydrated silica spectra.

The inferred distinction between bedrock opal-A and eolian opal-CT carries several implications for our interpretations of Mars' aqueous history. The spectral identification of opal-CT, with 1.4 μm features centered at >1.41 μm, indicates that mature silica phases may be more prevalent on Mars than originally thought [e.g., Tosca and Knoll, 2009]. These observations are also consistent with recent identification by the Curiosity rover of diverse silica phases across short length scales [Morris et al., 2016] and

of global variations in silica maturity [Smith et al., 2013]. However, the association of opal type with geologic context suggests that the identified opal type perhaps should not be interpreted at face value with regards to their implications for past aqueous activity. For example, identification of opal-CT may not necessarily indicate that a region experienced more extensive aqueous alteration if that opal-CT is hosted in a mobile eolian deposit. Similarly, a detection of opal-A in bedrock may not indicate limited aqueous alteration in that environment if that opal-A is a fresher bedrock surface resulting from high erosion rates that erode away previously altered opal-CT at the surface.

In summary, several factors can cause variations in martian hydrated silica spectra, the most notable of which are differences in opal type and hydration changes induced by varying atmospheric water content. These results indicate that aqueous alteration on Mars could have been prolonged enough for substantial opal maturation and that opals could still play a role in present-day atmospheric water cycling. However, caution and further work is still needed to determine how to best interpret opal type in their geologic contexts to make meaningful inferences about paleoenvironments on Mars.

Acknowledgements

The authors would like to thank Shuai Li for discussion of viewing geometries and their possible effects on spectral variations, and Kevin Robertson for discussion of opal mixtures with other minerals. This work was funded by a MSL Participating Scientist grant.

References

Amador, E. S., and J. L. Bandfield (2016), Elevated bulk-silica exposures and evidence for multiple aqueous alteration episodes in Nili Fossae, Mars, *Icarus*, *276*, 39–51, doi:10.1016/j.icarus.2016.04.015.

Bandfield, J. L. (2008), High-silica deposits of an aqueous origin in western Hellas Basin, Mars, *Geophysical Research Letters*, *35*(12), doi:10.1029/2008GL033807.

Bandfield, J. L., E. S. Amador, and N. H. Thomas (2013), Extensive hydrated silica materials in western Hellas Basin, Mars, *Icarus*, *226*(2), 1489–1498, doi:10.1016/j.icarus.2013.08.005.

Beck, P., A. Pommerol, B. Schmitt, and O. Brissaud (2010), Kinetics of water adsorption on minerals and the breathing of the martian regolith, *J. Geophys. Res.*, *115*(E10), E10011, doi:10.1029/2009JE003539.

Bish, D. L., J. William Carey, D. T. Vaniman, and S. J. Chipera (2003), Stability of hydrous minerals on the martian surface, *Icarus*, *164*(1), 96–103, doi:10.1016/S0019-1035(03)00140-4.

Bishop, J. L. et al. (2008), Phyllosilicate Diversity and Past Aqueous Activity Revealed at Mawrth Vallis, Mars, *Science*, *321*(5890), 830–833, doi:10.1126/science.1159699.

Bishop, J. L. et al. (2009), Mineralogy of Juventae Chasma: Sulfates in the light-toned mounds, mafic minerals in the bedrock, and hydrated silica and hydroxylated ferric sulfate on the plateau, *J. Geophys. Res.*, *114*(E2), E00D09, doi:10.1029/2009JE003352.

Boboň, M., A. A. Christy, D. Kluvanec, and L. Illášová (2011), State of water molecules and silanol groups in opal minerals: a near infrared spectroscopic study of opals from Slovakia, *Phys Chem Minerals*, *38*(10), 809–818, doi:10.1007/s00269-011-0453-0.

Cady, S. L., and J. D. Farmer (1996), Fossilization processes in siliceous thermal springs: trends in preservation along thermal gradients, *Ciba Found. Symp.*, *202*, 150-170; discussion 170-173.

Campbell, K. A., B. Y. Lynne, K. M. Handley, S. Jordan, J. D. Farmer, D. M. Guido, F. Foucher, S. Turner, and R. S. Perry (2015), Tracing Biosignature Preservation of Geothermally Silicified Microbial Textures into the Geological Record, *Astrobiology*, *15*(10), 858–882, doi:10.1089/ast.2015.1307.

Carter, J., F. Poulet, J.-P. Bibring, N. Mangold, and S. Murchie (2013), Hydrous minerals on Mars as seen by the CRISM and OMEGA imaging spectrometers: Updated global view, *J. Geophys. Res. Planets*, *118*(4), 831–858, doi:10.1029/2012JE004145.

Ceamanos, X., and S. Doute (2010), Spectral Smile Correction of CRISM/MRO Hyperspectral Images, *IEEE Transactions on Geoscience and Remote Sensing*, *48*(11), 3951–3959, doi:10.1109/TGRS.2010.2064326.

Che, C., T. D. Glotch, D. L. Bish, J. R. Michalski, and W. Xu (2011), Spectroscopic study of the dehydration and/or dehydroxylation of phyllosilicate and zeolite minerals, *J. Geophys. Res.*, *116*(E5), E05007, doi:10.1029/2010JE003740.

Christensen, P. R. et al. (2005), Evidence for magmatic evolution and diversity on Mars from infrared observations, *Nature*, *436*(7050), 6, doi:10.1038/nature03639.

Edgett, K. S., and N. Lancaster (1993), Volcaniclastic aeolian dunes: terrestrial examples and application to martian sands, *Journal of Arid Environments*, *25*(3), 271–297, doi:10.1006/jare.1993.1061.

Ehlmann, B. L., and C. S. Edwards (2014), Mineralogy of the Martian Surface, *Annual Review of Earth and Planetary Sciences*, *42*(1), 291–315, doi:10.1146/annurev-earth-060313-055024.

Ehlmann, B. L. et al. (2009), Identification of hydrated silicate minerals on Mars using MRO-CRISM: Geologic context near Nili Fossae and implications for aqueous alteration, *Journal of Geophysical Research: Planets*, *114*, E00D08, doi:10.1029/2009JE003339.

Ehlmann, B. L. et al. (2016), Discovery of alunite in cross crater, terra sirenum, mars: evidence for acidic, sulfurous waters, *American Mineralogist*, *101*(7), 1527–1542, doi:10.2138/am-2016-5574.

Fairchild, I. J., L. Bradby, and B. Spiro (1993), Carbonate diagenesis in ice, *Geology*, *21*(10), 901–904, doi:10.1130/0091-7613(1993)021<0901:CDII>2.3.CO;2.

Farrand, W. H., M. D. Lane, B. R. Edwards, and R. Aileen Yingst (2011), Spectral evidence of volcanic cryptodomes on the northern plains of Mars, *Icarus*, *211*(1), 139–156, doi:10.1016/j.icarus.2010.09.006.

Fenton, L. K., J. L. Bandfield, and A. W. Ward (2003), Aeolian processes in Proctor Crater on Mars: Sedimentary history as analyzed from multiple data sets, *J.-Geophys.-Res.*, *108*(E12), 5129, doi:10.1029/2002JE002015.

Fishbaugh, K. E., F. Poulet, V. Chevrier, Y. Langevin, and J.-P. Bibring (2007), On the origin of gypsum in the Mars north polar region, *J. Geophys. Res.*, *112*(E7), E07002, doi:10.1029/2006JE002862.

Folk, R. L. (1978), Angularity and Silica Coatings of Simpson Desert Sand Grains, Northern Territory, Australia, *Journal of Sedimentary Research*, *48*(2).

Fraeman, A. et al. (2016), Iron oxides in the Murray Formation: Investigating with orbiter and rover datasets, *MSL Science Discussion presentation*.

Friedlander, L. R., T. D. Glotch, D. L. Bish, M. D. Dyar, T. G. Sharp, E. C. Sklute, and J. R. Michalski (2015), Structural and spectroscopic changes to natural nontronite induced by experimental impacts between 10 and 40 GPa, *J. Geophys. Res. Planets*, *120*(5), 2014JE004638, doi:10.1002/2014JE004638.

Graetsch, H., O. W. Flörke, and G. Miehe (1987), Structural defects in microcrystalline silica, *Phys Chem Minerals*, *14*(3), 249–257, doi:10.1007/BF00307990.

Grotzinger, J. P. et al. (2015), Deposition, exhumation, and paleoclimate of an ancient lake deposit, Gale crater, Mars, *Science*, *350*(6257), aac7575, doi:10.1126/science.aac7575.

Hiesinger, H., and J. W. Head (2004), The Syrtis Major volcanic province, Mars: Synthesis from Mars Global Surveyor data, *J. Geophys. Res.*, *109*(E1), E01004, doi:10.1029/2003JE002143.

Hurowitz et al., J. A. (2017), Redox stratification of an ancient lake in Gale Crater, Mars, *in revision*.

Jones, B., and R. W. Renaut (2003), Hot spring and geyser sinters: the integrated product of precipitation, replacement, and deposition, *Can. J. Earth Sci.*, *40*(11), 1549–1569, doi:10.1139/e03-078.

Jones, J. B., and E. R. Segnit (1971), The nature of opal I. nomenclature and constituent phases, *Journal of the Geological Society of Australia*, *18*(1), 57–68, doi:10.1080/00167617108728743.

Kaplan, H. H., R. E. Milliken, D. Fernández-Remolar, R. Amils, K. Robertson, and A. H. Knoll (2016), Orbital evidence for clay and acidic sulfate assemblages on Mars based on mineralogical analogs from Rio Tinto, Spain, *Icarus*, *275*, 45–64, doi:10.1016/j.icarus.2016.03.019.

Konhauser, K. O., B. Jones, A.-L. Reysenbach, and R. W. Renaut (2003), Hot spring sinters: keys to understanding Earth's earliest life forms, *Can. J. Earth Sci.*, *40*(11), 1713–1724, doi:10.1139/e03-059.

Langer, K., and O. W. Flörke (1974), Near infrared absorption spectra (4000–9000 cm− 1) of opals and the role of "water" in these SiO 2· nH 2 O minerals., *Fortschritte der Mineralogie*, *52*(1), 17–51.

Langevin, Y., F. Poulet, J.-P. Bibring, and B. Gondet (2005), Sulfates in the North Polar Region of Mars Detected by OMEGA/Mars Express, *Science*, *307*(5715), 1584–1586, doi:10.1126/science.1109091.

Le Deit, L., J. Flahaut, C. Quantin, E. Hauber, D. Mège, O. Bourgeois, J. Gurgurewicz, M. Massé, and R. Jaumann (2012), Extensive surface pedogenic alteration of the Martian Noachian crust suggested by plateau phyllosilicates around Valles Marineris, *J. Geophys. Res.*, *117*(E11), E00J05, doi:10.1029/2011JE003983.

Lee, M. R., I. MacLaren, S. M. L. Andersson, A. Kovács, T. Tomkinson, D. F. Mark, and C. L. Smith (2015), Opal-A in the Nakhla meteorite: A tracer of ephemeral liquid water in the Amazonian crust of Mars, *Meteorit Planet Sci*, *50*(8), 1362–1377, doi:10.1111/maps.12471.

Malin, M. C. et al. (2007), Context Camera Investigation on board the Mars Reconnaissance Orbiter, *Journal of Geophysical Research: Planets*, *112*, E05S04, doi:10.1029/2006JE002808.

Martín-Torres, F. J. et al. (2015), Transient liquid water and water activity at Gale crater on Mars, *Nature Geosci*, *8*(5), 357–361, doi:10.1038/ngeo2412.

McEwen, A. S. et al. (2007), Mars Reconnaissance Orbiter's High Resolution Imaging Science Experiment (HiRISE), *Journal of Geophysical Research: Planets*, *112*, E05S02, doi:10.1029/2005JE002605.

McGuire, P. C. et al. (2009), An improvement to the volcano-scan algorithm for atmospheric correction of CRISM and OMEGA spectral data, *Planetary and Space Science*, *57*(7), 809–815, doi:10.1016/j.pss.2009.03.007.

McKeown, N. K., J. L. Bishop, E. Z. Noe Dobrea, B. L. Ehlmann, M. Parente, J. F. Mustard, S. L. Murchie, G. A. Swayze, J.-P. Bibring, and E. A. Silver (2009), Characterization of phyllosilicates observed in the central Mawrth Vallis region, Mars, their potential formational processes, and implications for past climate, *J. Geophys. Res.*, *114*(E2), E00D10, doi:10.1029/2008JE003301.

Metz, J. M., J. P. Grotzinger, D. Mohrig, R. Milliken, B. Prather, C. Pirmez, A. S. McEwen, and C. M. Weitz (2009), Sublacustrine depositional fans in southwest Melas Chasma, *J. Geophys. Res.*, *114*(E10), E10002, doi:10.1029/2009JE003365.

Milliken, R. E., and J. F. Mustard (2007), Estimating the water content of hydrated minerals using reflectance spectroscopy: II. Effects of particle size, *Icarus*, *189*(2), 574–588, doi:10.1016/j.icarus.2006.12.028.

Milliken, R. E. et al. (2008), Opaline silica in young deposits on Mars, *Geology*, *36*(11), 847–850, doi:10.1130/G24967A.1.

Morris, R. V. et al. (2016), Silicic volcanism on Mars evidenced by tridymite in high-SiO2 sedimentary rock at Gale crater, *PNAS*, *113*(26), 7071–7076, doi:10.1073/pnas.1607098113.

Muhs, D. R. (2004), Mineralogical maturity in dunefields of North America, Africa and Australia, *Geomorphology*, *59*(1–4), 247–269, doi:10.1016/j.geomorph.2003.07.020.

Murchie, S. et al. (2007), Compact Reconnaissance Imaging Spectrometer for Mars (CRISM) on Mars Reconnaissance Orbiter (MRO), *Journal of Geophysical Research: Planets*, *112*(E5), n/a–n/a, doi:10.1029/2006JE002682.

Noe Dobrea, E. Z. et al. (2010), Mineralogy and stratigraphy of phyllosilicate-bearing and dark mantling units in the greater Mawrth Vallis/west Arabia Terra area: Constraints on geological origin, *J. Geophys. Res.*, *115*(E7), E00D19, doi:10.1029/2009JE003351.

Pan, L., and B. L. Ehlmann (2014), Phyllosilicate and hydrated silica detections in the knobby terrains of Acidalia Planitia, northern plains, Mars, *Geophys. Res. Lett.*, *41*(6), 1890–1898, doi:10.1002/2014GL059423.

Parente, M. (2008), A new approach to denoising CRISM images, *Lunar Planet. Sci., XXXIX*, Abstract 2528.

Pelkey, S. M. et al. (2007), CRISM multispectral summary products: Parameterizing mineral diversity on Mars from reflectance, *Journal of Geophysical Research: Planets*, *112*(E8), n/a–n/a, doi:10.1029/2006JE002831.

Rampe et al., E. B. (2017), Mineralogical trends in mudstone deposits from the Murray formation, Gale crater, Mars, *in revision at Earth and Planetary Science Letters*.

Rice, M. S., E. A. Cloutis, J. F. Bell III, D. L. Bish, B. H. Horgan, S. A. Mertzman, M. A. Craig, R. W. Renaut, B. Gautason, and B. Mountain (2013), Reflectance spectra diversity of silica-rich materials: Sensitivity to environment and implications for detections on Mars, *Icarus*, *223*(1), 499–533, doi:10.1016/j.icarus.2012.09.021.

Roach, L. H., J. F. Mustard, S. L. Murchie, J.-P. Bibring, F. Forget, K. W. Lewis, O. Aharonson, M. Vincendon, and J. L. Bishop (2009), Testing evidence of recent hydration state change in sulfates on Mars, *J. Geophys. Res.*, *114*(E2), E00D02, doi:10.1029/2008JE003245.

Roach, L. H., J. F. Mustard, G. Swayze, R. E. Milliken, J. L. Bishop, S. L. Murchie, and K. Lichtenberg (2010), Hydrated mineral stratigraphy of Ius Chasma, Valles Marineris, *Icarus*, *206*(1), 253–268, doi:10.1016/j.icarus.2009.09.003.

Rogers, A. D., and H. Nekvasil (2015), Feldspathic rocks on Mars: Compositional constraints from infrared spectroscopy and possible formation mechanisms, *Geophys. Res. Lett.*, *42*(8), 2015GL063501, doi:10.1002/2015GL063501.

Ruff, S. W. et al. (2011), Characteristics, distribution, origin, and significance of opaline silica observed by the Spirit rover in Gusev crater, Mars, *Journal of Geophysical Research: Planets*, *116*(E7), n/a–n/a, doi:10.1029/2010JE003767.

Seelos, K. D., F. P. Seelos, C. E. Viviano-Beck, S. L. Murchie, R. E. Arvidson, B. L. Ehlmann, and A. A. Fraeman (2014), Mineralogy of the MSL Curiosity landing site in Gale crater as observed by MRO/CRISM, *Geophys. Res. Lett.*, *41*(14), 2014GL060310, doi:10.1002/2014GL060310.

Silvestro, S., L. K. Fenton, D. A. Vaz, N. T. Bridges, and G. G. Ori (2010), Ripple migration and dune activity on Mars: Evidence for dynamic wind processes, *Geophys. Res. Lett.*, *37*(20), L20203, doi:10.1029/2010GL044743.

Skok, J. R., J. F. Mustard, B. L. Ehlmann, R. E. Milliken, and S. L. Murchie (2010), Silica deposits in the Nili Patera caldera on the Syrtis Major volcanic complex on Mars, *Nature Geosci*, *3*(12), 838–841, doi:10.1038/ngeo990.

Smith, M. R., and J. L. Bandfield (2012), Geology of quartz and hydrated silica-bearing deposits near Antoniadi Crater, Mars, *Journal of Geophysical Research: Planets*, *117*(E6), n/a–n/a, doi:10.1029/2011JE004038.

Smith, M. R., J. L. Bandfield, E. A. Cloutis, and M. S. Rice (2013), Hydrated silica on mars: combined analysis with near-infrared and thermal-infrared spectroscopy, *Icarus*, doi:10.1016/j.icarus.2013.01.024.

Sun, V. Z., and R. E. Milliken (2015), Ancient and recent clay formation on Mars as revealed from a global survey of hydrous minerals in crater central peaks, *J. Geophys. Res. Planets*, *120*(12), 2015JE004918, doi:10.1002/2015JE004918.

Sun, V. Z., R. E. Milliken, and K. M. Robertson (2017b), Distinguishing Opal Types and Their Water Distributions from Near-Infrared Spectroscopy for Applications to Mars, *in prep*.

Sun, V. Z., R. E. Milliken, and K. M. Robertson (2017c), Constraining the Hydration Behavior of Opaline Silica at Mars-Relevant Conditions from Laboratory Experiments, *in prep*.

Thomas, P. C. et al. (1999), Bright dunes on Mars, *Nature*, *397*(6720), 592–594, doi:10.1038/17557.

Tosca, N. J., and A. H. Knoll (2009), Juvenile chemical sediments and the long term persistence of water at the surface of Mars, *Earth and Planetary Science Letters*, *286*(3–4), 379–386, doi:10.1016/j.epsl.2009.07.004.

Viviano-Beck, C. E., S. L. Murchie, A. W. Beck, and J. M. Dohm (2017), Compositional and structural constraints on the geologic history of eastern Tharsis Rise, Mars, *Icarus*, *284*, 43–58, doi:10.1016/j.icarus.2016.09.005.

Weitz, C. M., J. L. Bishop, P. Thollot, N. Mangold, and L. H. Roach (2011), Diverse mineralogies in two troughs of Noctis Labyrinthus, Mars, *Geology*, *39*(10), 899–902, doi:10.1130/G32045.1.

Weitz, C. M., J. L. Bishop, and J. A. Grant (2013), Gypsum, opal, and fluvial channels within a trough of Noctis Labyrinthus, Mars: Implications for aqueous activity during the Late Hesperian to Amazonian, *Planetary and Space Science*, *87*, 130–145, doi:10.1016/j.pss.2013.08.007.

Werner, S. C. (2009), The global martian volcanic evolutionary history, *Icarus*, *201*(1), 44–68, doi:10.1016/j.icarus.2008.12.019.

Wilson, M. J. (2014), The structure of opal-CT revisited, *Journal of Non-Crystalline Solids*, *405*, 68–75, doi:10.1016/j.jnoncrysol.2014.08.052.

Wiseman, S. M. et al. (2016), Characterization of artifacts introduced by the empirical volcano-scan atmospheric correction commonly applied to CRISM and OMEGA near-infrared spectra, *Icarus*, *269*, 111–121, doi:10.1016/j.icarus.2014.10.012.

Wray, J. J. et al. (2011), Columbus crater and other possible groundwater-fed paleolakes of Terra Sirenum, Mars, *Journal of Geophysical Research: Planets*, *116*(E1), n/a–n/a, doi:10.1029/2010JE003694.

Wray, J. J., S. T. Hansen, J. Dufek, G. A. Swayze, S. L. Murchie, F. P. Seelos, J. R. Skok, R. P. Irwin Iii, and M. S. Ghiorso (2013), Prolonged magmatic activity on Mars inferred from the detection of felsic rocks, *Nature Geosci*, *6*(12), 1013–1017, doi:10.1038/ngeo1994.

Zent, A. P., D. J. Howard, and R. C. Quinn (2001), H2O adsorption on smectites: Application to the diurnal variation of H2O in the Martian atmosphere, *J. Geophys. Res.*, *106*(E7), 14667–14674, doi:10.1029/2000JE001394.

Figures

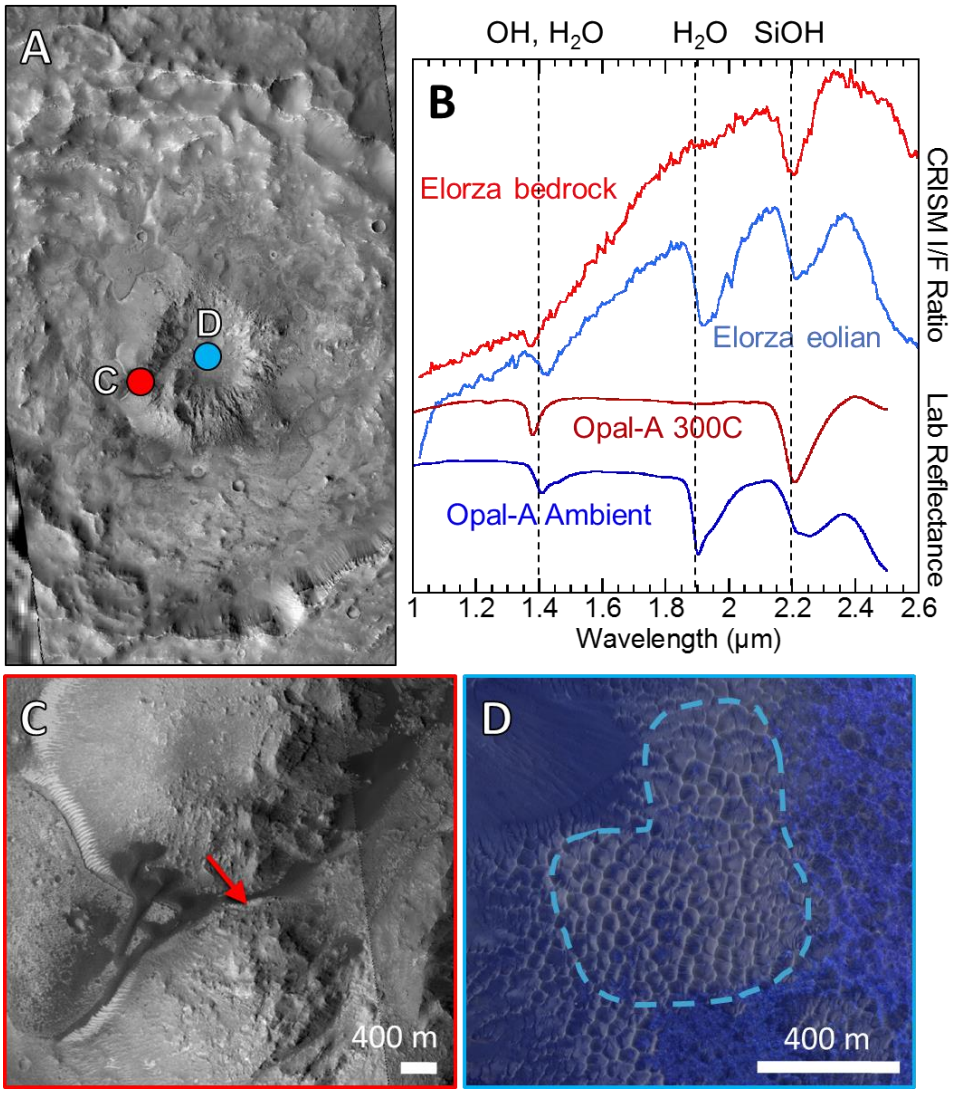

Figure 1. A) 40-km Elorza crater hosts **B)** two different types of hydrated silica spectra. **C)** Less hydrated silica, without a 1.9 μm feature, is hosted within a bedrock unit, while **D)** more hydrated silica is associated with eolian deposits at the central pit. Both detections are 4 km apart within the same CRISM image (FRT00008236).

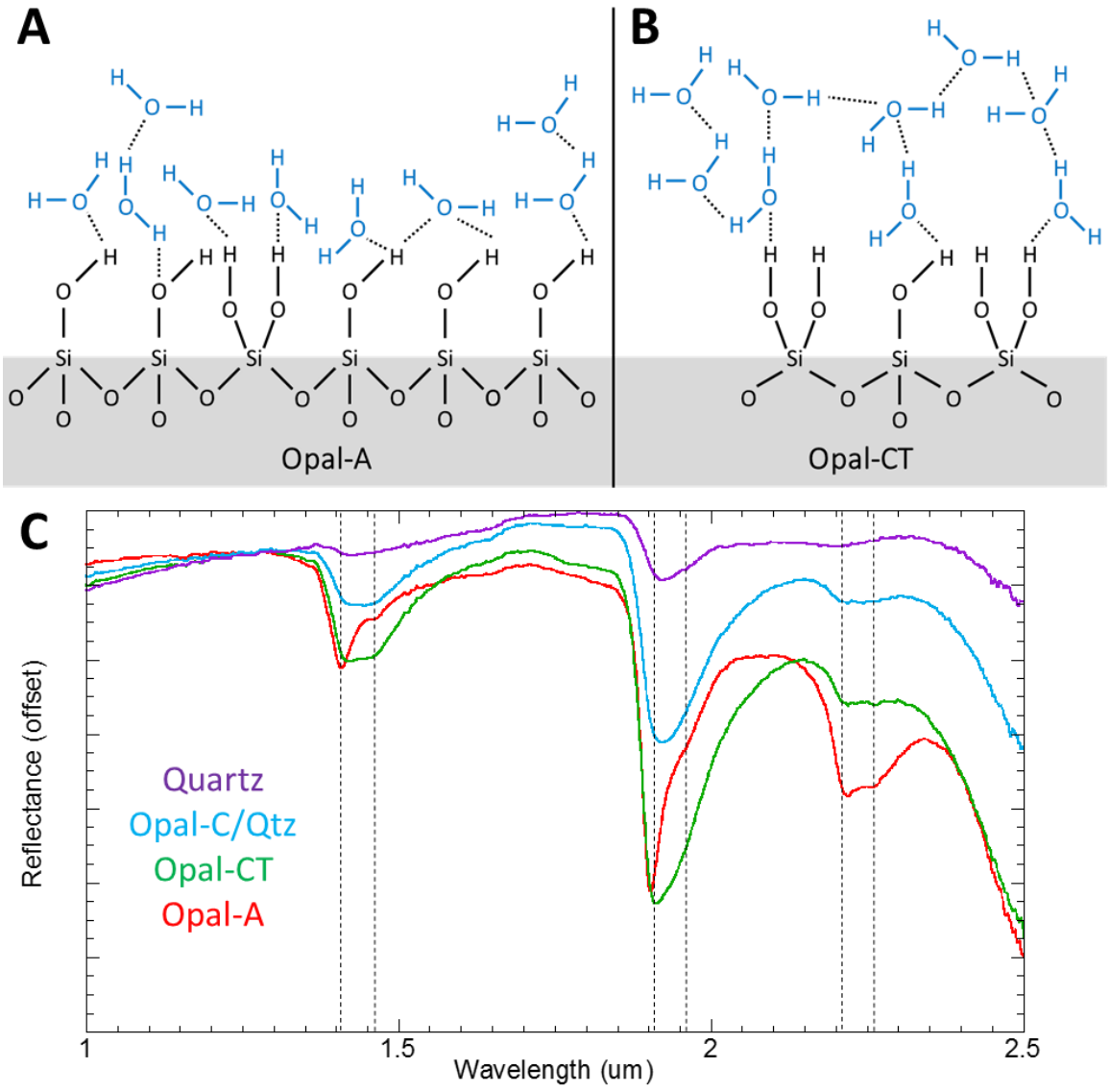

Figure 2. A) Depiction of the surface of opal-A and **B)** opal-CT with their associated populations of SiOH and H_2O groups. **C)** Offset laboratory spectra of opal-A, opal-CT, opal-C, and quartz. Vertical dashed lines indicate absorptions at 1.41, 1.46, 1.91, 1.96, 2.21, and 2.26 µm.

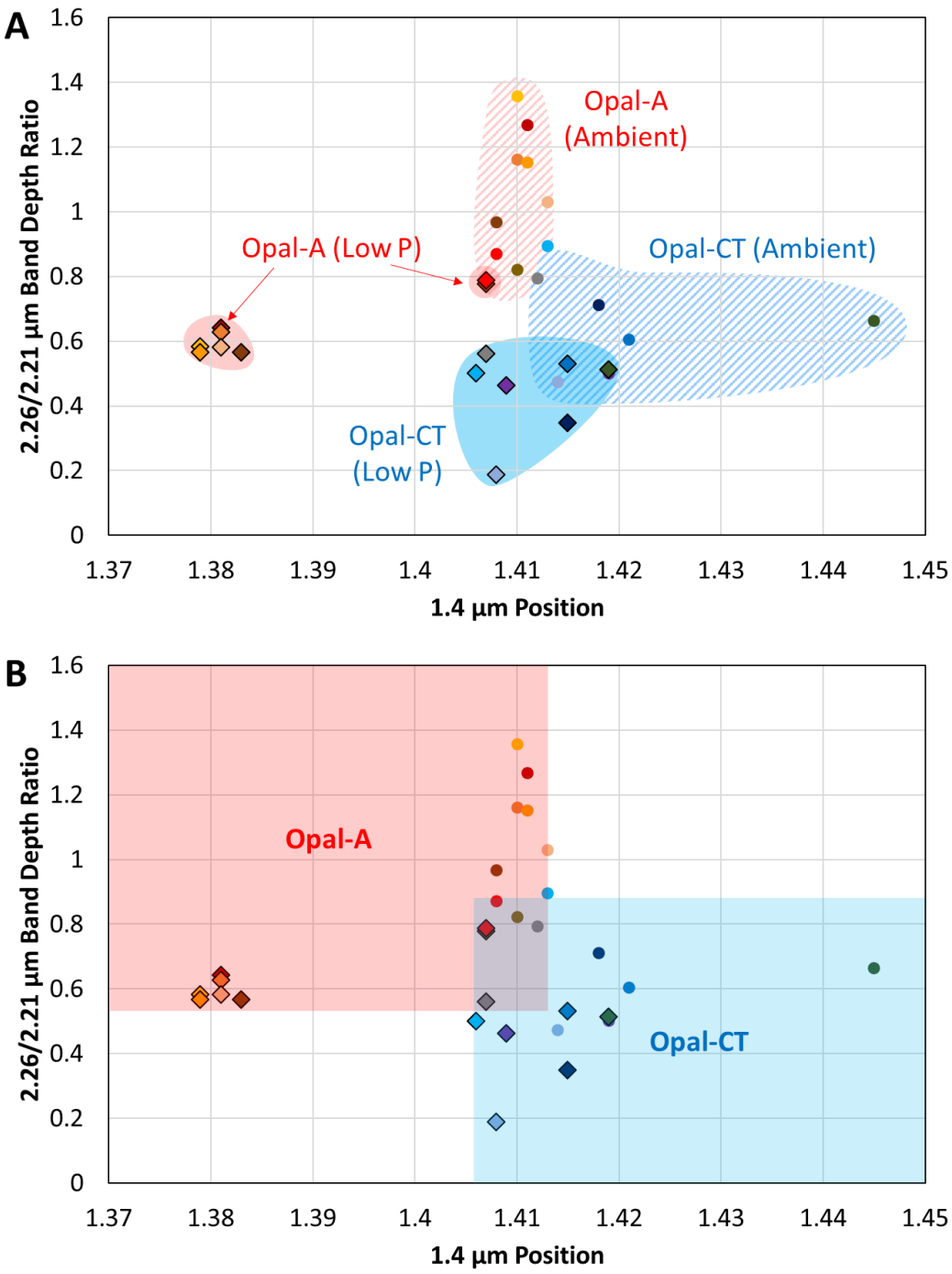

Figure 3. A) Opal-A and opal-CT are distinguishable from the position of the 1.4 µm absorption and the ratio of the band depths (or Gaussian amplitudes) at 2.26 µm relative to 2.21 µm [Sun et al., 2017bc]. The delineation between the two opal types is clear for spectra taken at ambient laboratory conditions (dots and hashed area) as well as for spectra taken at low pressure (0.016 mbar) to simulate opals exposed to Mars' drier atmosphere (diamonds and solid areas). **B)** These measurements at ambient and low pressure conditions bracket the possible areas in this parameter space where martian

opals are expected to plot. Ambient measurements represent the most hydrated state possible, whereas the low pressure measurements represent the least hydrated state possible.

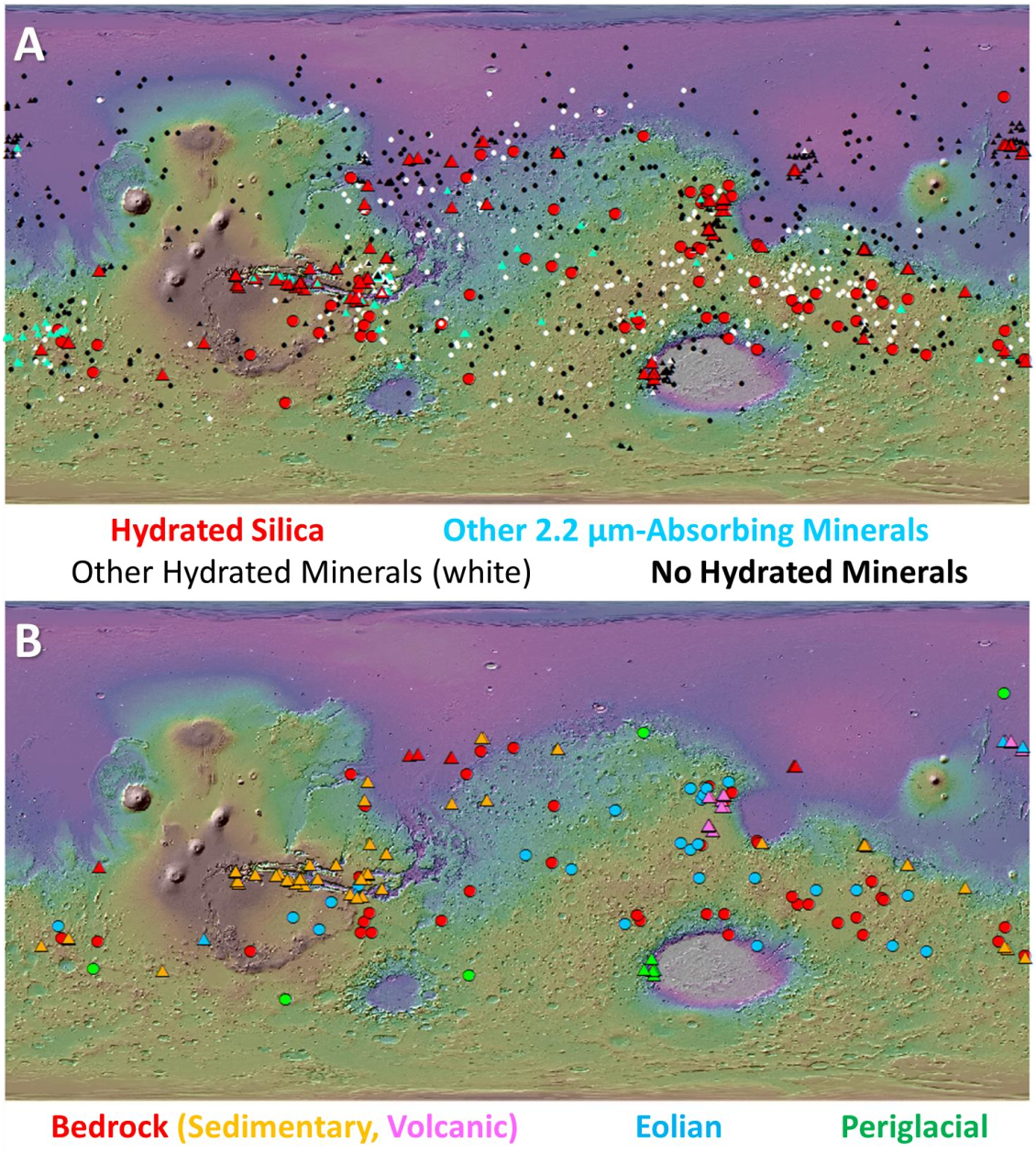

Figure 4. Mineral detections in this work, with circles indicating detections within impact craters [Sun and Milliken, 2015] and triangles indicating detections from intercrater regions. **A)** Hydrated silica is shown in red, while other 2.2 µm-absorbing minerals (e.g., Al clays, jarosite) are shown in blue. Also displayed are other hydrated mineral detections in white (e.g., Fe/Mg clays, zeolites, some sulfates) and images where no hydrated minerals were identified in black. **B)** Hydrated silica detections only, colored according to their categorization by geologic unit.

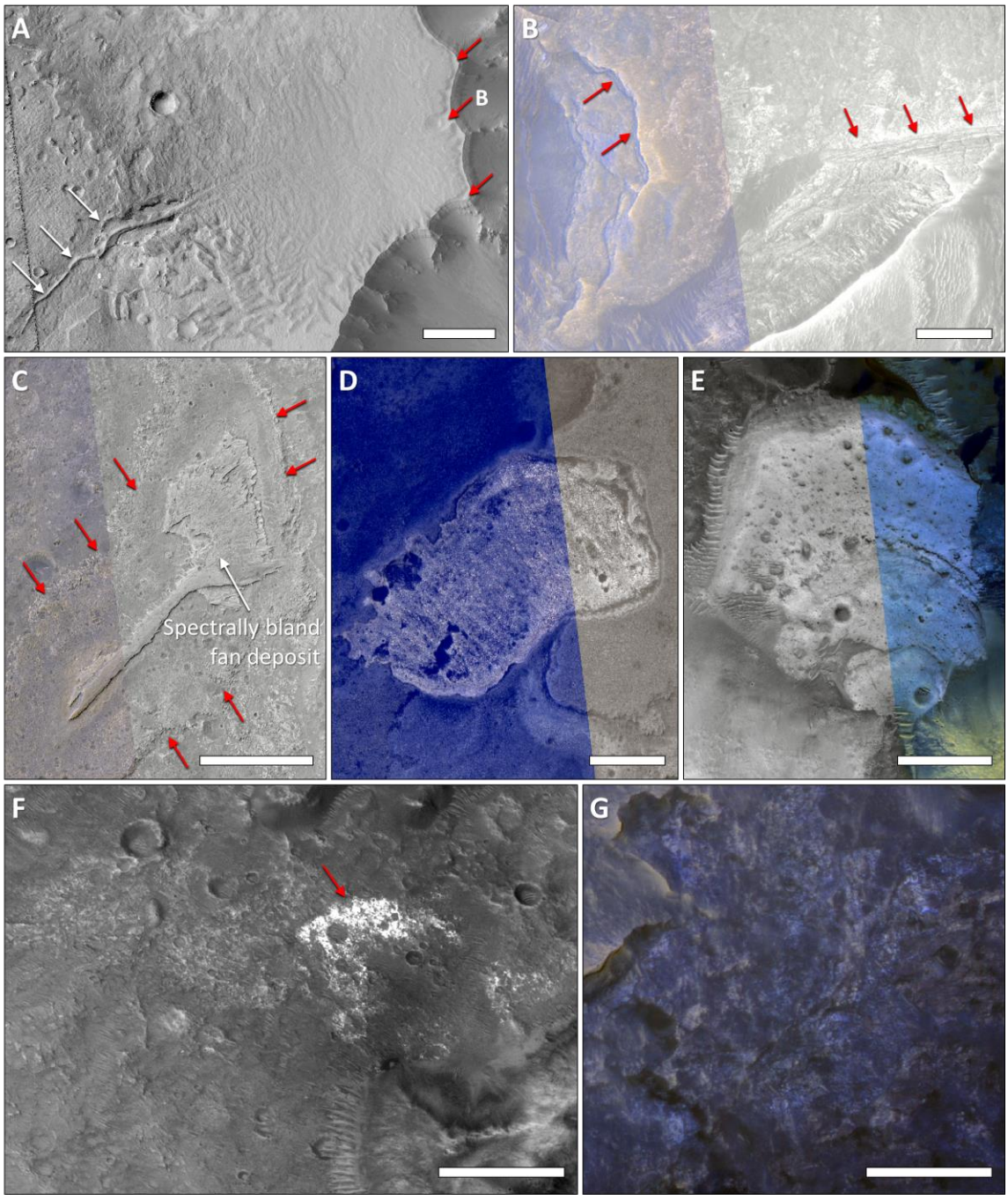

Figure 5. Hydrated silica, indicated by red arrows, in sedimentary bedrock of likely fluvial origins. **A)** Hydrated silica is identified in a light-toned bedrock layer exposed along the edges of Ganges Chasma from FRT00008949 and others. These layers may have a fluvial origin, as suggested by numerous inverted channels (white arrows) leading into these deposits. The scale bar indicates 3 km. **B)** Close-up view of hydrated silica-bearing bedrock, which exhibits meter-scale layering. Context for this image is given in A) and the scale bar indicates 100 m. **C)** Hydrated silica occurs within a single stratum lying below a spectrally bland fan deposit (white arrow) near Melas Chasma. Red arrows point out the margins of the hydrated silica-bearing stratum, observed in FRT000173AD.

The scale bar indicates 900 m. **D)** An example of hydrated silica in a light-toned stratum, also near Melas Chasma, observed in FRT000109B6. The scale bar indicates 250 m. **E)** Hydrated silica is found within a light-toned, massive fan deposit in the southern highlands, covered by FRT000086B7. The scale bar indicates 500m. **F)** Hydrated silica is associated with light-toned bedrock on the channel floor of Kasei Valles in FRT0000967E. The scale bar indicates 1500 m. **G)** Hydrated silica within light-toned bedrock at the base of Mount Sharp in Gale Crater, from ATO00038AA7 [Fraeman et al., 2016]. The scale bar indicates 100 m.

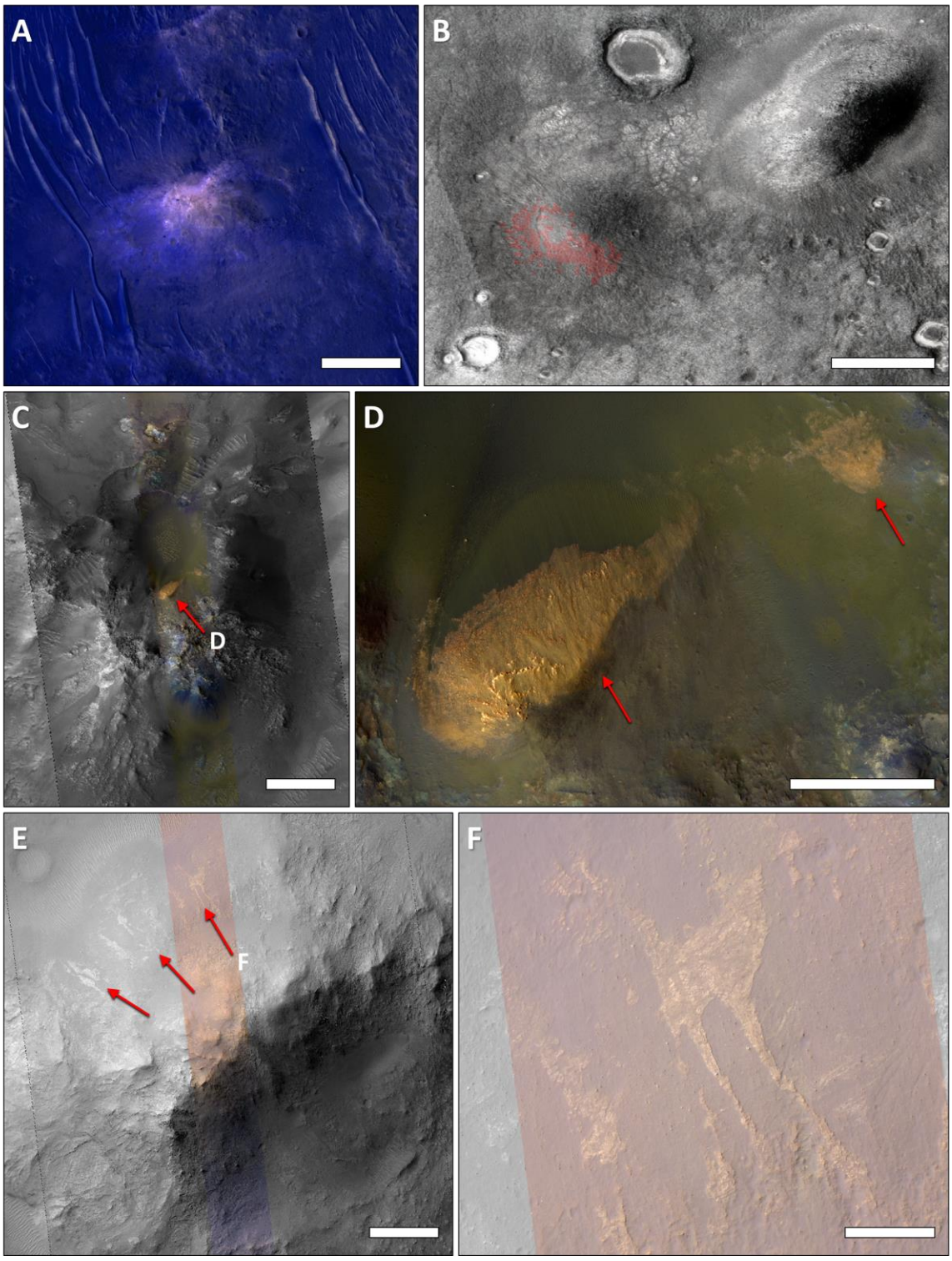

Figure 6. Hydrated silica, indicated by red arrows, is detected in bedrock in volcanic settings and within excavated bedrock and impact melt in craters. **A)** Dehydrated silica is found in high-relief bedrock near the cone of Nili Patera in FRT00010628. The scale bar indicates 150 m. **B)** Hydrated silica, overlain in red, occurs along the slopes of a dome-

like structure in Arcadia Planitia in FRT00008EE5. The scale bar indicates 2 km. **C)** Hydrated silica is uplifted at the central peak of an impact crater covered by FRT000129FA. The scale bar indicates 1 km. **D)** Close-up view of C) to show uplifted bedrock containing hydrated silica. Among examples of hydrated silica excavated at central peaks, this occurrence is particularly interesting because this bedrock unit is in high-relief whereas most other uplifted bedrock examples are superposed by other materials. The scale bar indicates 250 m. **E)** Hydrated silica occurs in light-toned bedrock that is interpreted as impact melt at a central peak covered by FRT000198FB. This lithified unit appears to have a downslope flow-like morphology away from the central peak and superposes the local bedrock. In the absence of clear fluvial features, these units are interpreted as impact melt. The scale bar indicates 1 km. **F)** Close-up view of E) to show the cohesiveness of the putative impact melt unit and its superposition above the local bedrock. The scale bar indicates 200 m.

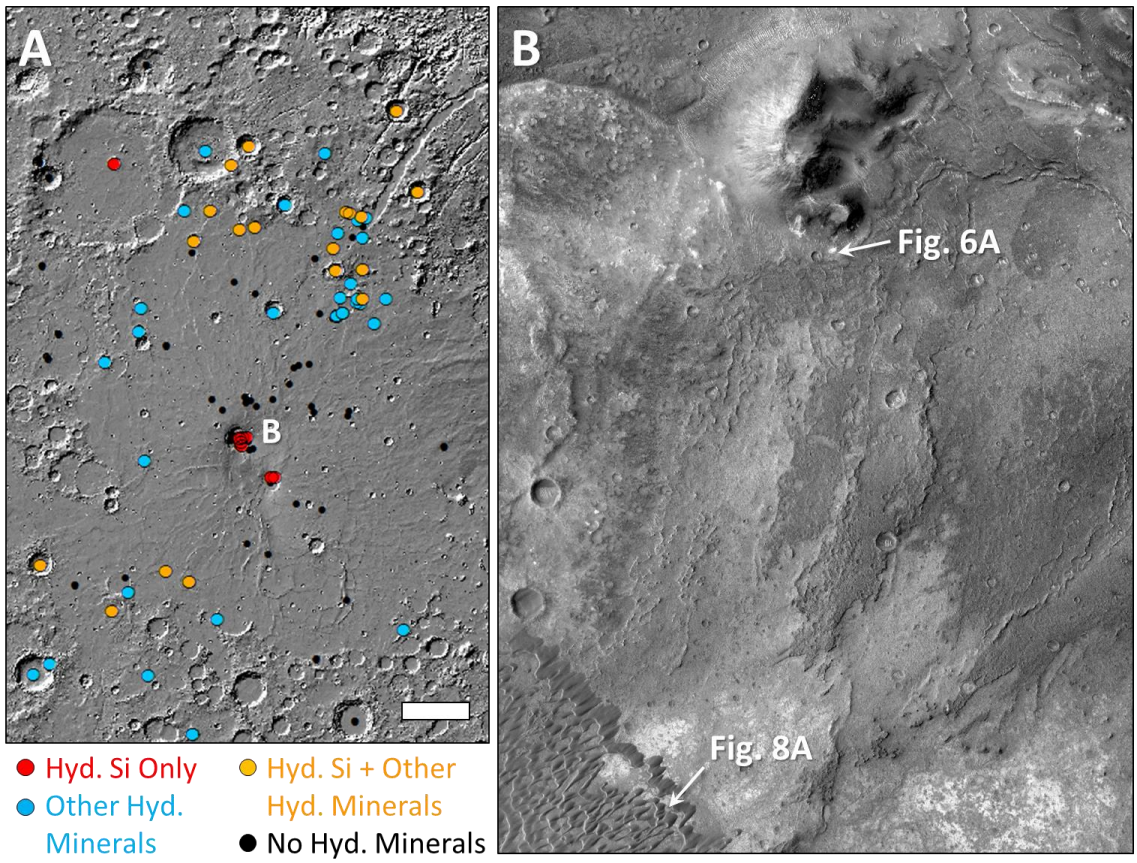

Figure 7. A) General context for hydrated silica detections in the Syrtis Major region. Hydrated silica is the sole hydrated phase (red) detected at Nili Patera proper, but in the greater Syrtis Major region it is detected alongside other hydrated minerals, either exposed within impact craters or along the edges of the Nili Patera lava flows. The scale bar indicates 200 km. **B)** Context at Nili Patera for a dehydrated silica detection in bedrock **(Figure 6A)** and a hydrated silica detection in active dunes **(Figure 8A)**, which are separated by 20 km of distance.

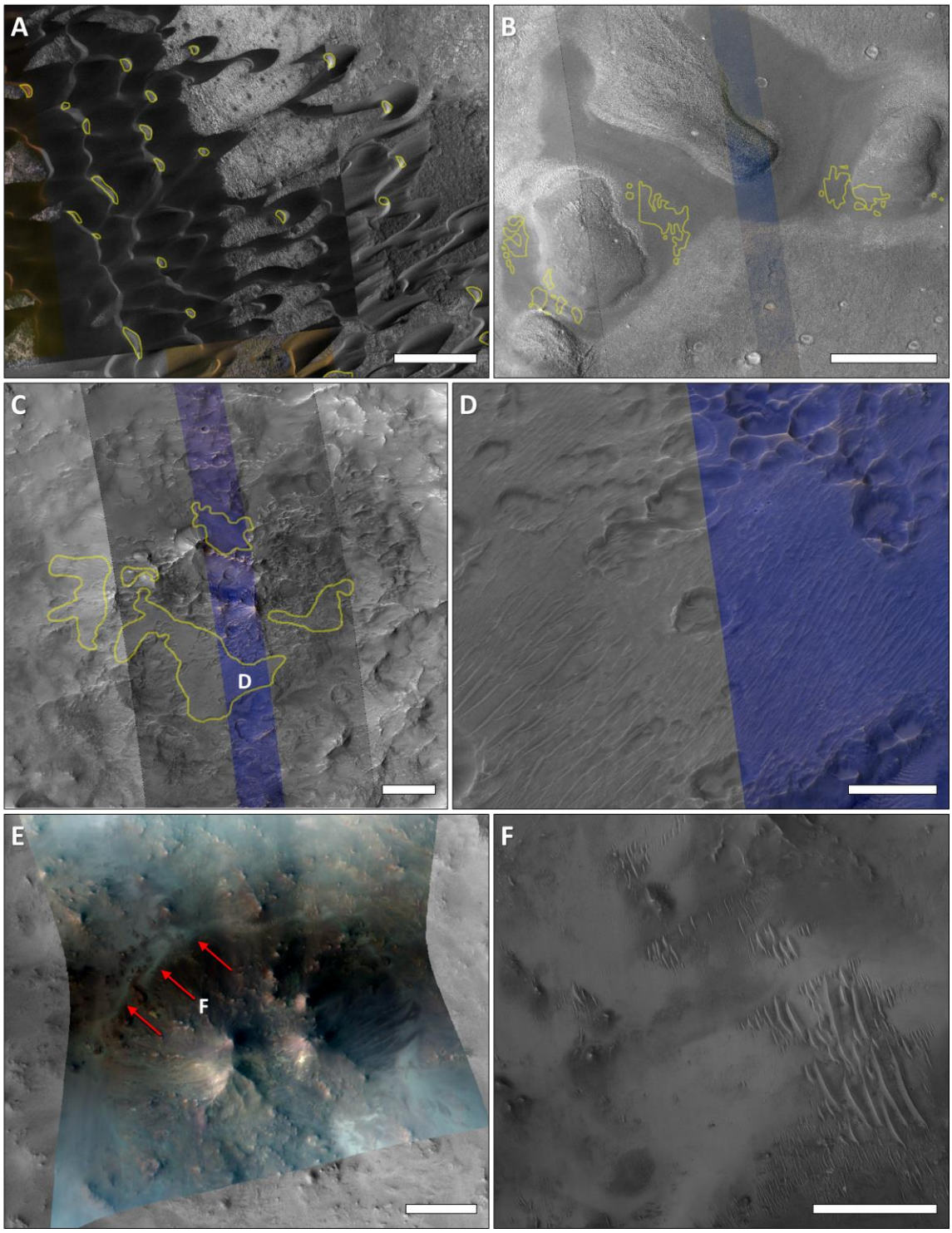

Figure 8. Hydrated silica, outlined in yellow, within eolian or unconsolidated deposits. **A)** Twenty kilometers south of Nili Patera, hydrated silica is found on the lee sides of dunes in FRT00004185. The scale bar indicates 500 m. **B)** Hydrated silica is detected in the debris aprons surrounding dome structures in Arcadia Planitia, in FRT0009A7D. The

scale bar indicates 2 km. **C)** Hydrated silica is found in deposits around the central peak of a crater in HRS00012428. The scale bar indicates 1 km. **D)** Close-up view of the deposits in C), showing the poor crater retention and eolian features on this unit. The scale bar indicates 250 m. **E)** In this CRISM false color stretch, hydrated silica occurs in the teal-toned swathes indicated by the red arrows at the base of the central peak in FRT000051EE. The scale bar indicates 2 km. **F)** Close-up view of E) showing these light-toned deposits with dunes present in areas. The scale bar indicates 1 km.

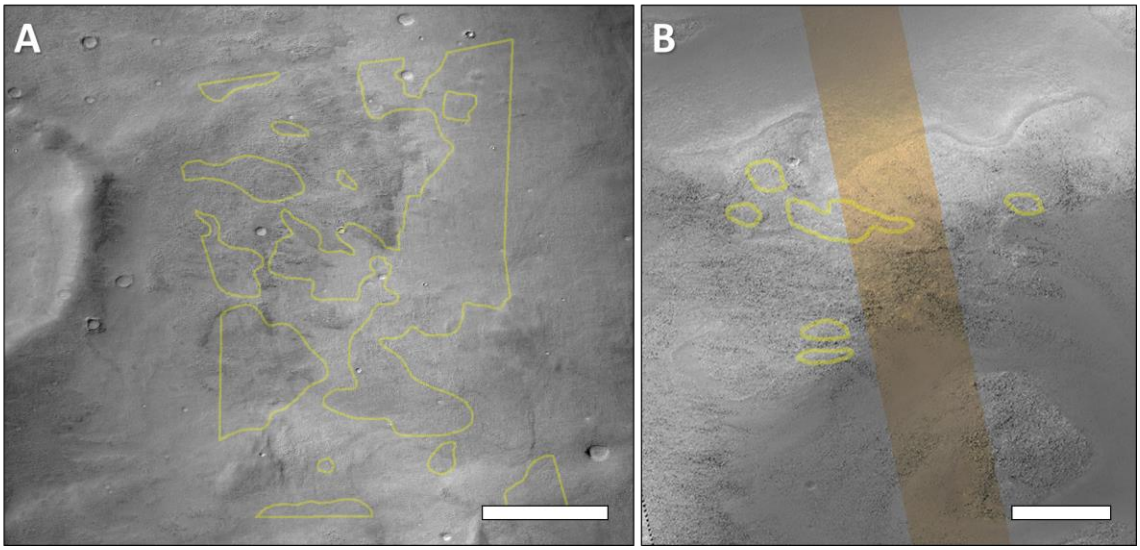

Figure 9. Hydrated silica, outlined in yellow, in periglacial deposits at **A)** Hellas Basin (HRL00013366) and **B)** Lowell crater (HRL0001FB53). The scale bar indicates 5 km and 1 km respectively.

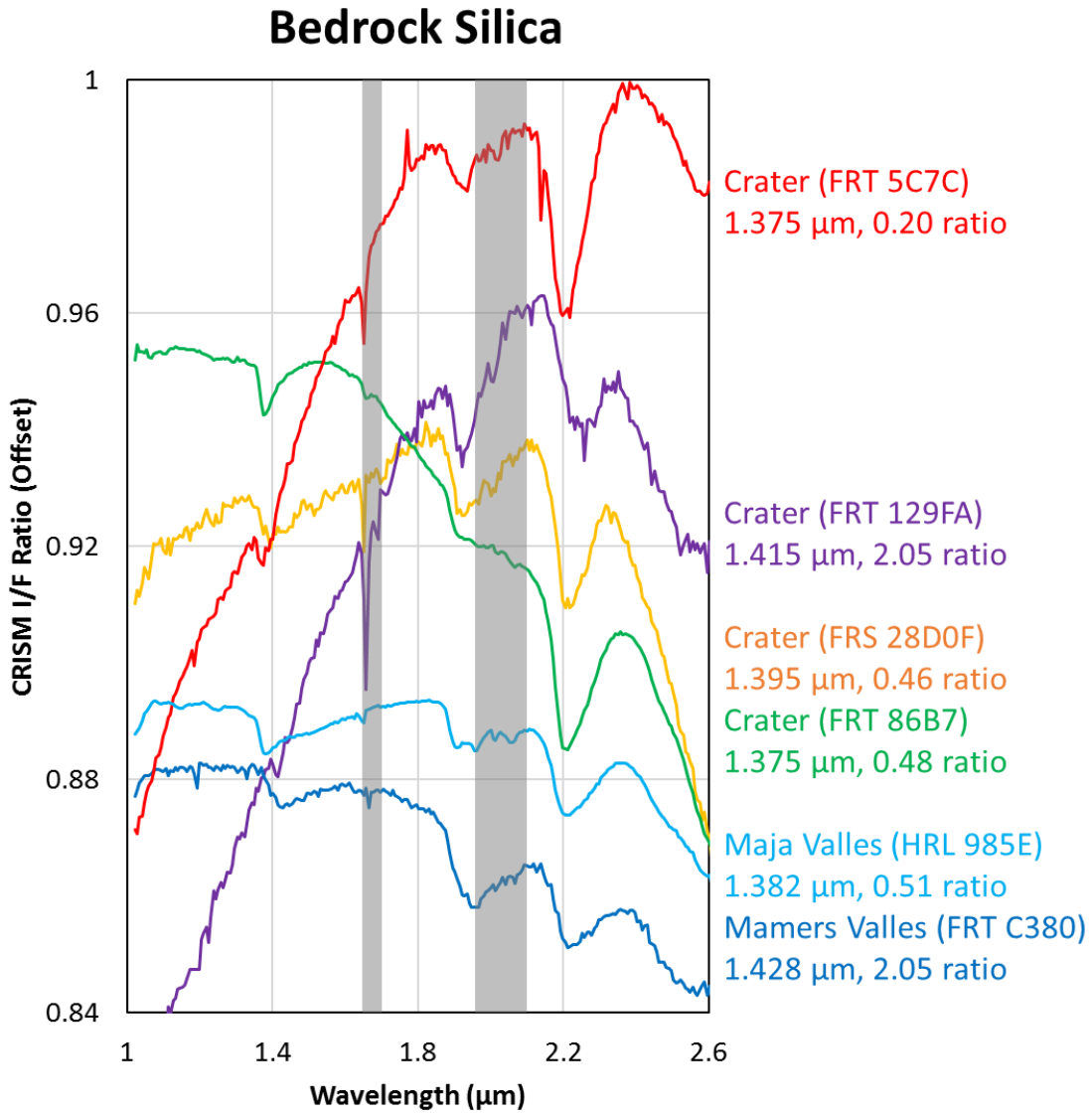

Figure 10. Hydrated silica spectra from bedrock units. Listed below each observation are the 1.4 µm band position and the 2.26/2.21 µm Gaussian amplitude ratio for that spectrum. Bedrock silica have 1.4 µm features centered at shorter wavelengths and generally low 2.26/2.21 µm ratio values, although silica from crater FRT 129FA **(Figure 6C, D**) have anomalously high parameter values. Grey regions at 1.6-1.7 µm and 1.95-2.1 µm mask wavelengths where a filter boundary and residual atmospheric absorptions are known to cause noise in CRISM data.

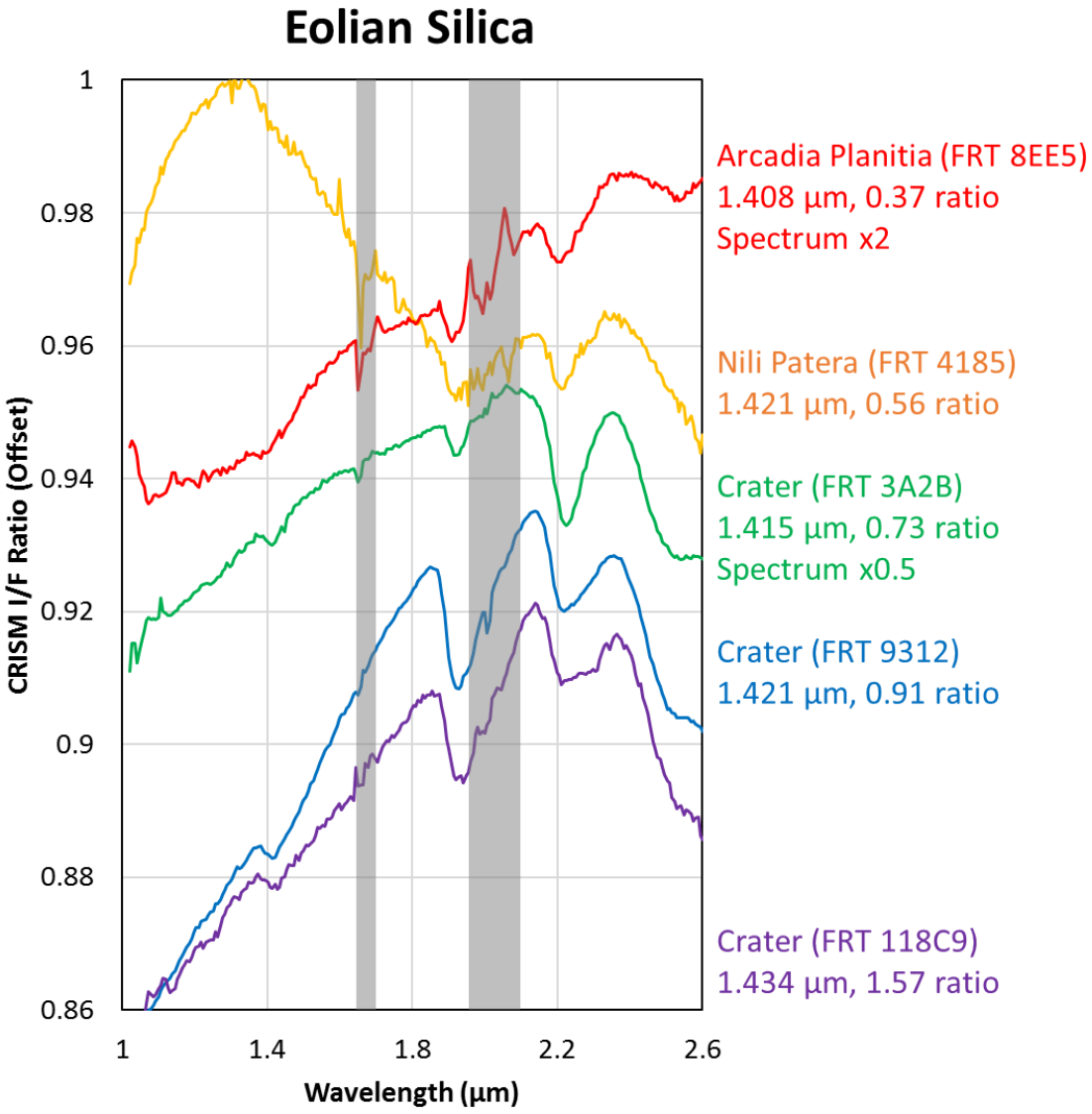

Figure 11. Hydrated silica spectra from eolian deposits. Images of the corresponding or analogous deposits are shown in **Figure 8A** for Nili Patera, **Figure 8B** for Arcadia Planitia, and Figure **8E-F** for crater FRT 9312. The spectra for Arcadia Planitia and crater FRT 3A2B have been scaled for clarity. Listed below each observation are the 1.4 µm band position and the 2.26/2.21 µm Gaussian amplitude ratio for that spectrum. Eolian silica have 1.4 µm features centered at longer wavelengths and moderate 2.26/2.21 µm ratio values. Grey regions at 1.6-1.7 µm and 1.95-2.1 µm mask wavelengths where a filter boundary and residual atmospheric absorptions are known to cause noise in CRISM data.

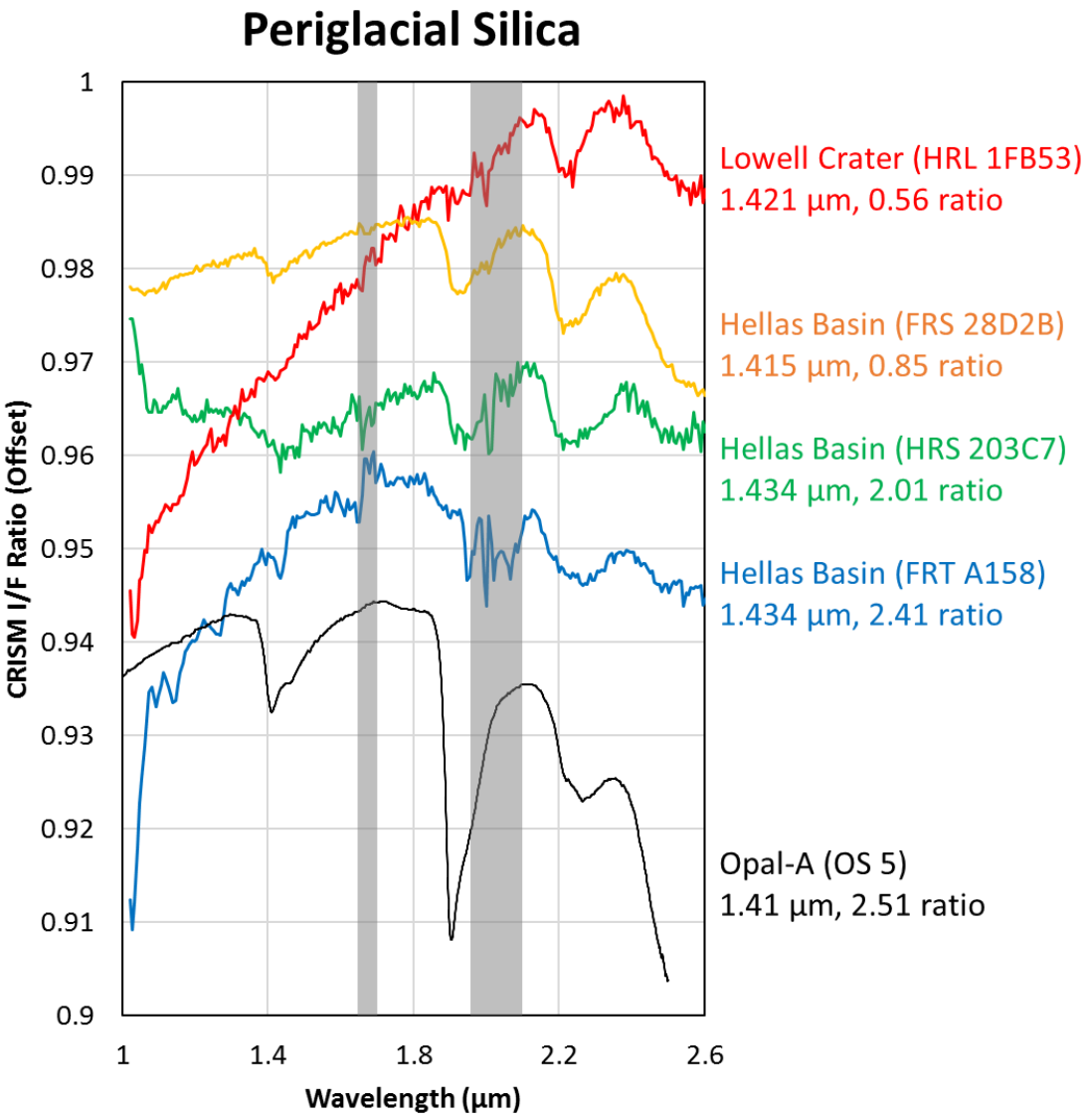

Figure 12. Hydrated silica spectra from periglacial deposits. Images of the corresponding or analogous deposits are shown in **Figure 9A** for Hellas Basin and **Figure 9B** for Lowell crater. Listed below each observation are the 1.4 µm band position and the 2.26/2.21 µm Gaussian amplitude ratio for that spectrum. Periglacial silica tend to have 1.4 µm features centered at longer wavelengths, as well as high 2.26/2.21 µm ratios. Shown for comparison is a laboratory spectrum of an opal-A sample with a similarly high 2.26/2.21 µm ratio. Grey regions at 1.6-1.7 µm and 1.95-2.1 µm mask wavelengths where a filter boundary and residual atmospheric absorptions are known to cause noise in CRISM data.

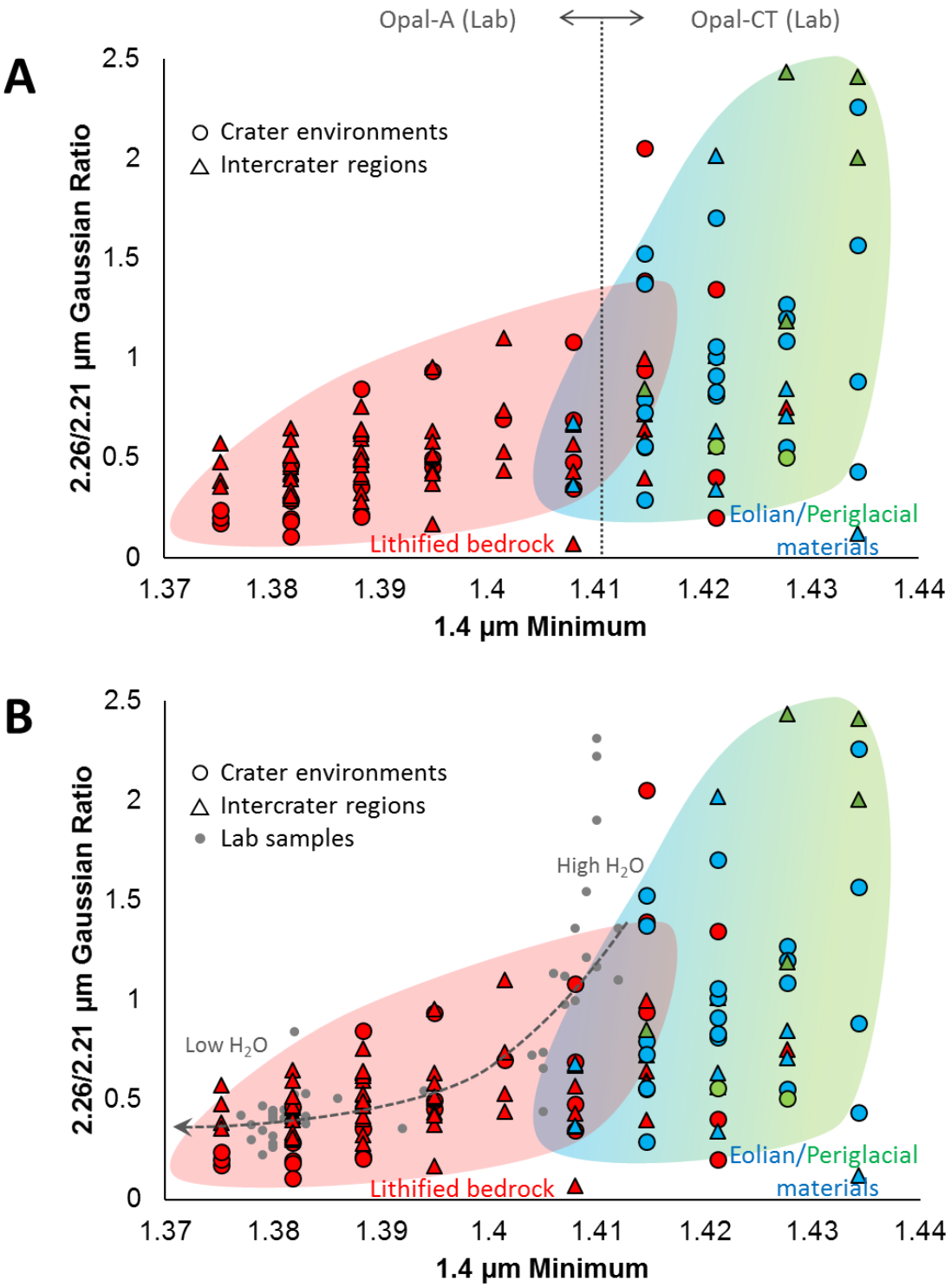

Figure 13. A) Hydrated silica in bedrock units appear spectrally distinct from silica found in eolian or periglacial materials. Eolian and periglacial silica have 1.4 µm positions at higher wavelengths, suggesting a composition similar to opal-CT by comparison with laboratory spectra of terrestrial opal samples. In contrast, bedrock silica

have 1.4 µm positions occurring at shorter wavelengths, indicating a composition similar to opal-A. The range of observed 1.4 µm positions in CRISM data is similar to the range of 1.4 µm positions predicted by laboratory measurements of opals at ambient and Mars-like conditions **(Figure 3B)**. **B)** The same CRISM data can be compared to laboratory opal-A that have been dehydrated through stepwise heating to 300°C (grey points). These laboratory data show trends expected of opals with varying hydration levels regardless of opal type.

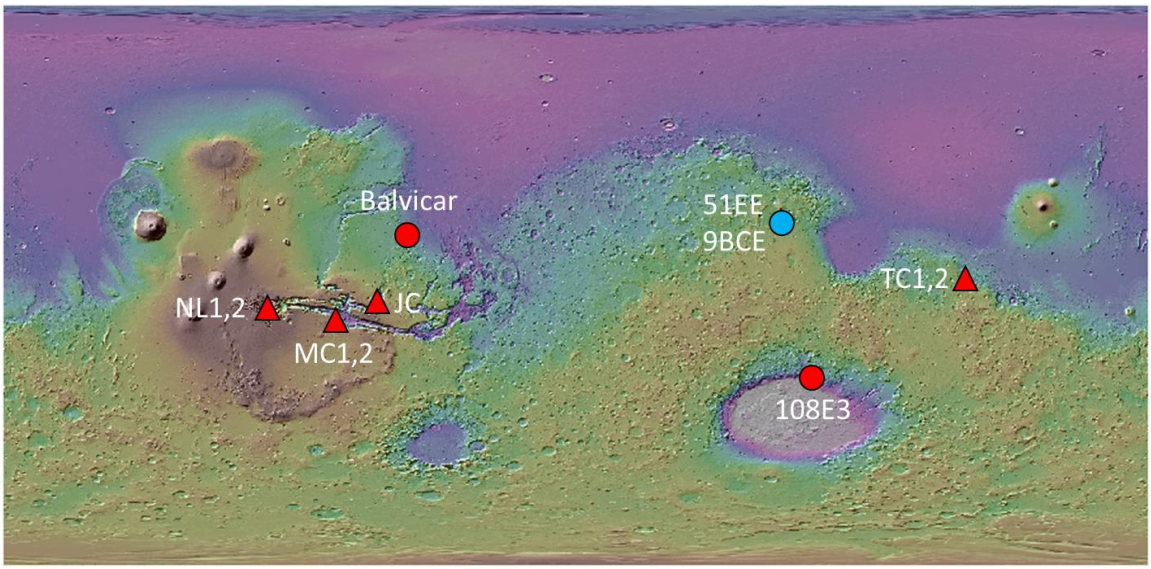

Figure 14. Sites where overlapping CRISM coverage allows for temporal study of the same hydrated silica units. Examples of specific sites are in **Figures 15 and 16**. Intercrater sites are indicated by triangles and abbreviated as follows: "NL" for two sites at Noctis Labyrinthus, "MC" for two sites at Melas Chasma, "JC" for Juventae Chasma, and "TC" for two sites at Terra Cimmeria. The remaining sites are within craters and indicated by circles; these are Balvicar crater and three unnamed craters that we refer to by their CRISM observations. Red indicates that the hydrated silica is found within bedrock units, while blue indicates that the silica is hosted in eolian material.

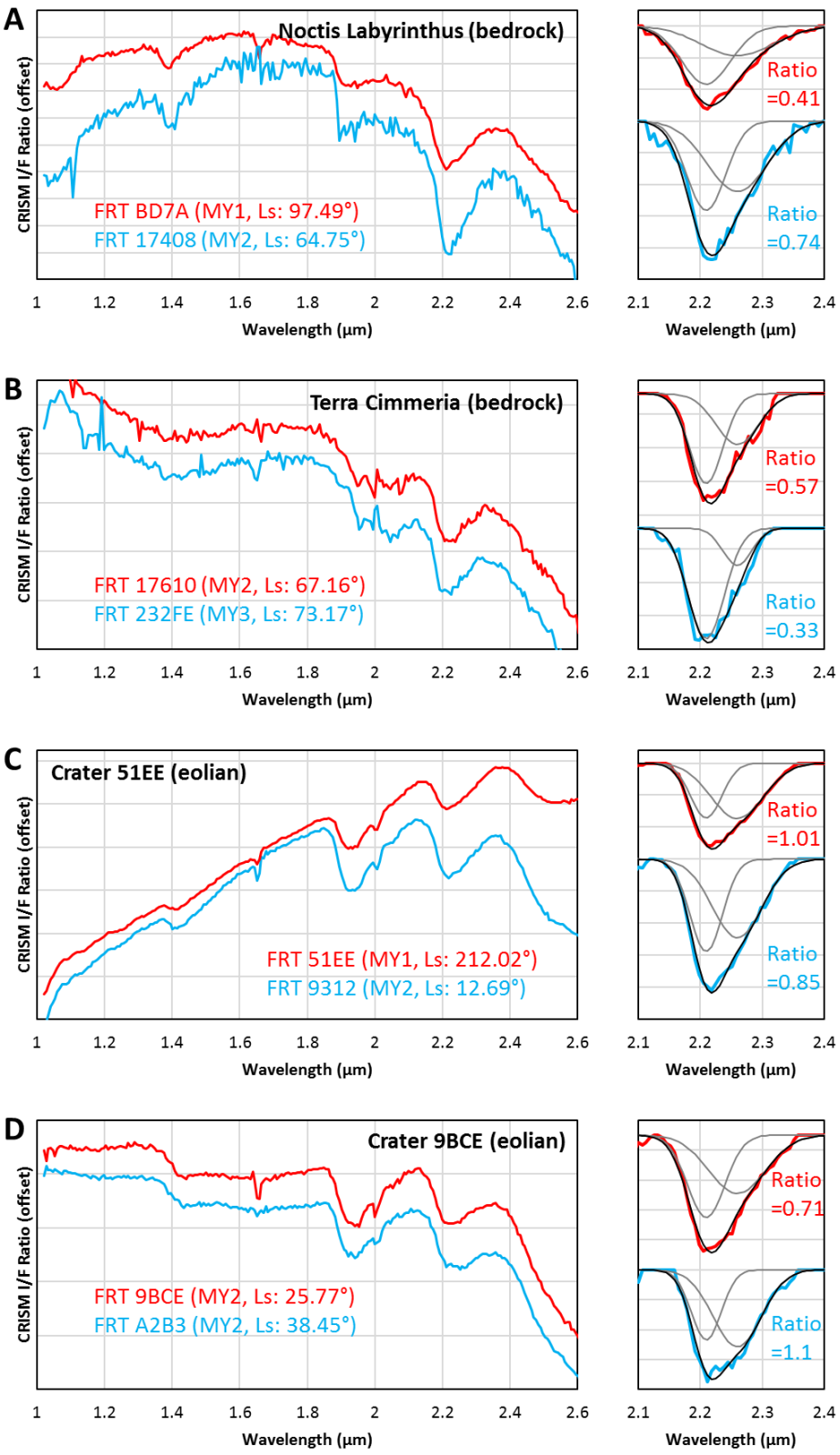
A
Noctis Labyrinthus (bedrock)
FRT BD7A (MY1, Ls: 97.49°)
FRT 17408 (MY2, Ls: 64.75°)
Ratio =0.41
Ratio =0.74
B
Terra Cimmeria (bedrock)
FRT 17610 (MY2, Ls: 67.16°)
FRT 232FE (MY3, Ls: 73.17°)
Ratio =0.57
Ratio =0.33
C
Crater 51EE (eolian)
FRT 51EE (MY1, Ls: 212.02°)
FRT 9312 (MY2, Ls: 12.69°)
Ratio =1.01
Ratio =0.85
D
Crater 9BCE (eolian)
FRT 9BCE (MY2, Ls: 25.77°)
FRT A2B3 (MY2, Ls: 38.45°)
Ratio =0.71
Ratio =1.1
CRISM I/F Ratio (offset)
Wavelength (μm)
1
1.2
1.4
1.6
1.8
2
2.2
2.4
2.6
2.1
2.3

Figure 15. CRISM spectra (left) and Gaussian modeling of the 2.2 μm feature (right) for the same hydrated silica deposit in overlapping CRISM images at the following sites: **A)** Noctis Labyrinthus, **B)** Terra Cimmeria, **C)** crater 51EE, and **D)** crater 9BCE.

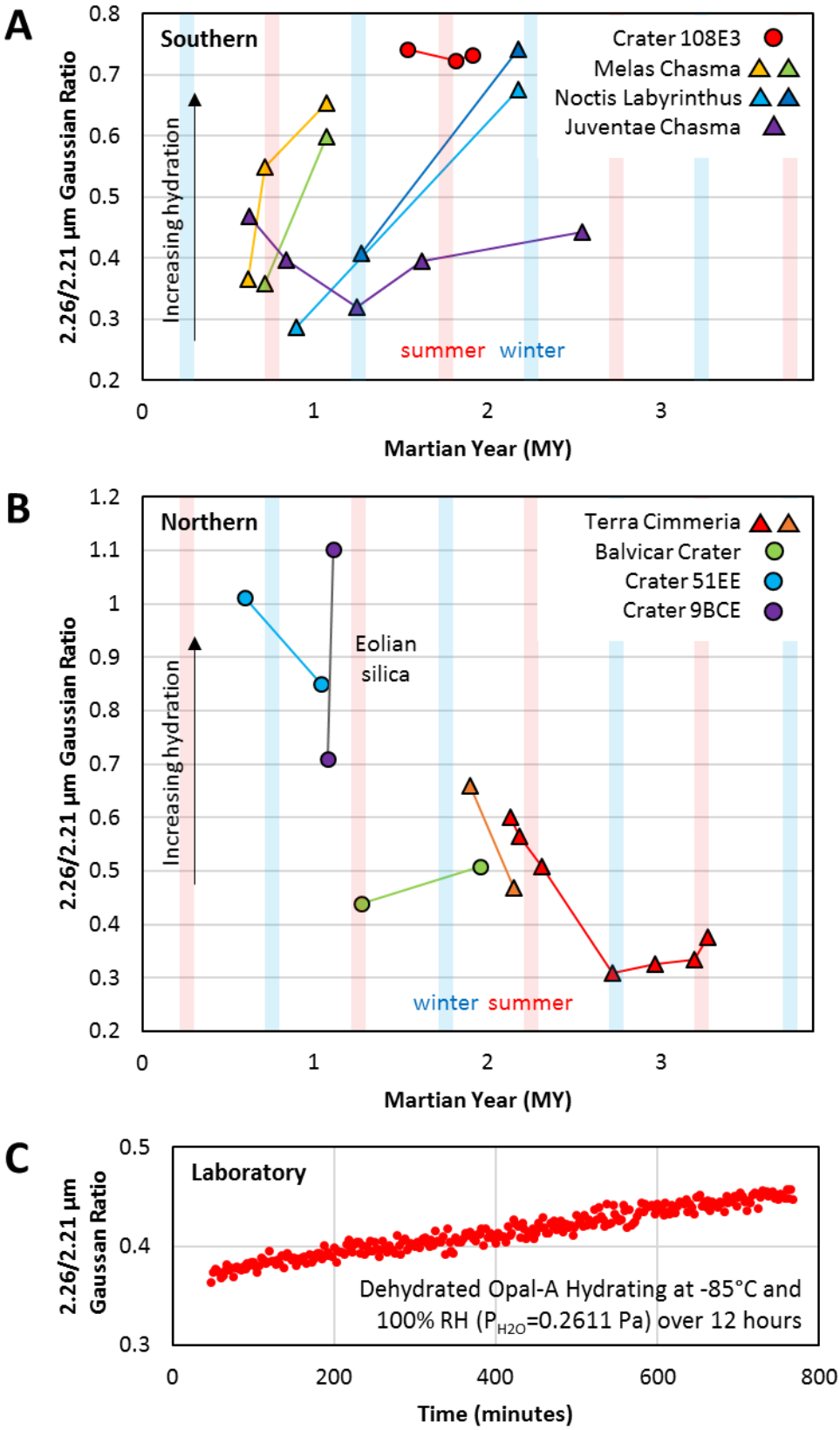
A
Southern
Crater 108E3
Melas Chasma
Noctis Labyrinthus
Juventae Chasma
Increasing hydration
summer winter
2.26/2.21 µm Gaussian Ratio
Martian Year (MY)
B
Northern
Terra Cimmeria
Balvicar Crater
Crater 51EE
Crater 9BCE
Eolian silica
Increasing hydration
winter summer
2.26/2.21 µm Gaussian Ratio
Martian Year (MY)
C
Laboratory
Dehydrated Opal-A Hydrating at -85°C and 100% RH (P_{H2O}=0.2611 Pa) over 12 hours
2.26/2.21 µm Gaussan Ratio
Time (minutes)

Figure 16. See **Figures 14 and 15** for context and spectra. **A)** 2.26/2.21 μm Gaussian ratio variations are observed in several locations in the southern hemisphere, plotted over martian year starting from the first CRISM image. Each marker color indicates a unique silica deposit with overlapping data. Connecting lines are drawn for clarity but are not meant to suggest immediate continuity. Vertical lines indicate southern summer and winter. **B)** The same plot for locations in the northern hemisphere, with vertical lines indicating northern summer and winter. Note that out of all the northern and southern locations shown in this figure, craters 51EE and 9BCE provide the only examples of eolian silica, which are spectrally consistent with an opal-CT composition **(Section 5.1)**. **C)** To demonstrate that such hydration changes are kinetically possible on Mars, laboratory data showing an increase in the 2.2 μm parameter as an opal-A sample is hydrated over 12 hours at Mars-like conditions of -85°C (>90% RH) and P_{H2O} of 0.2611 Pa [Sun et al., 2017c].

CHAPTER 7:

Our Current Understanding of the Timing of Aqueous Conditions on Mars from Observations of Clays and Opals

Vivian Z. Sun

Department of Earth, Environmental, and Planetary Sciences, Brown University,

Providence, RI 02912, USA

1. Introduction

This dissertation has explored the distribution of Fe/Mg clays and opals on Mars' surface in order to infer the nature and timing of the aqueous processes that formed them. Both mineral groups have a characteristic where varying exposure to water under certain aqueous conditions will produce different mineral forms. Fe/Mg smectites will alter to chlorite with exposure to water and heat, and amorphous opal-A will convert to more crystalline silica phases through quartz with just the presence of water [Tosca and Knoll, 2009]. The unique features of these two mineral groups therefore allow us to make inferences of water longevity when these different mineral phases can be distinguished.

In Chapter 2 we investigated Fe/Mg smectites and chlorites within impact craters to better constrain the timing of clay formation on Mars and the distribution of clays and diagenetic processes within the crust. In Chapters 3-6 we investigated the distribution and types of martian opals, which require comparatively more groundwork in laboratory analyses due to the spectral similarity of most hydrated silica species [e.g., Rice et al., 2013]. To that end we conducted a mineralogical and chemical study of terrestrial opal-rich samples (Chapter 3) and a spectral study of opal-A and opal-CT to determine their distinguishing spectral characteristics (Chapter 4). We also investigated how opal spectra may appear and behave when exposed to Mars-like atmospheric conditions (Chapter 5), and applied our laboratory results to CRISM data to determine the opal types present on Mars (Chapter 6). This dissertation has demonstrated that there is evidence for diagenetic processes acting on both Fe/Mg clays and opals on Mars, suggesting that aqueous conditions, though still limited compared to on Earth, were likely more extensive than previously thought [e.g., Tosca and Knoll, 2009].

2. Summary of Major Contributions

This dissertation makes the following contributions with respect to determining the spatial and temporal distribution and inferring the formation conditions of Fe/Mg clays (Chapter 2) and opaline silica (Chapters 3-6) on Mars.

2.1 Fe/Mg Clays

1. Fe/Mg clays primarily formed during the Noachian, but may have formed authigenically within crater environments during the Hesperian or Amazonian, implying that habitable conditions could have existed relatively recently in Mars' past.

The Noachian is commonly considered the primary period of Fe/Mg clay formation, and therefore the most habitable period of time on Mars [e.g., Bibring et al., 2006]. Much of this interpretation is based on Fe/Mg clay detections that are associated with impact craters and assumed to be excavated from depth [e.g., Mustard et al., 2008]. However, detailed correlation of these detections with geomorphology and stratigraphy show that some clays may have formed authigenically or were otherwise emplaced post-impact [Tornabene et al., 2009; Marzo et al., 2010; Mangold et al., 2012; Sun and Milliken, 2014; 2015], calling into question whether the paradigm of Noachian clay formation truly describes all clays on Mars.

In Chapter 2 we conducted a systematic survey of Fe/Mg clays at 633 central peaks to determine the true distribution of excavated crustal clays versus clays that were emplaced post-impact. Crater-count ages were used to constrain the oldest formation ages of possibly authigenic clays and the youngest formation ages of excavated clays. Our analysis confirmed that the majority (approximately two-thirds) of central peak clays are

excavated and likely formed during the Noachian or the Early Hesperian at the latest. However, the remaining clay population occurs in post-impact materials, with 25% of central peak clays possibly having formed authigenically in putative impact melt units. Based on the ages of the host craters, these authigenic clays could have formed as recently as the Hesperian or even the Amazonian. We concluded that although the Noachian was the primary period for clay formation, local environments within impact craters could have been capable of supporting habitable conditions during the Hesperian or Amazonian.

2. Chlorite occurrences increase with crater excavation depth, suggesting smectite-to-chlorite diagenesis and the presence of fluids within the martian crust.

The first indications of a smectite and chlorite gradient within the martian crust came from a global survey by Carter et al. [2013], who observed increasing occurrences of chlorite within the ejecta of large craters (>5-20 km) compared to small craters (<5 km). Our results from Chapter 2 confirmed this trend at a higher spatial resolution. We found that among excavated clays, chlorite occurrences systematically increase with excavation depth while smectites occurrences decrease. The transition from a smectite-dominated crust to a chlorite-dominated crust appears to occur at around 4 km depth. If this chloritization trend is the result of smectite diagenesis, this transitional depth may carry implications for determining the geothermal gradient within the crust, as this diagenetic process requires heat in addition to the presence of water [Chang et al., 1986; Inoue et al., 1991; Środoń, 1999]. Importantly, these results suggest that fluids were likely present within the crust in order to enable diagenesis. We observed uplifted clays at

depths up to 7 km and chlorites at possibly up to 17 km depth, which suggests the presence of fluids at significant crustal depths.

2.2 Opaline Silica

3. It is difficult to characterize opal-forming environments solely based on bulk measurements of mineralogy and chemistry.

Inferences of pH in opal-forming environments on Mars have long relied on bulk mineralogical and chemical measurements from rovers such as Spirit and Curiosity [Morris et al., 2008; Squyres et al., 2008; Morris et al., 2016; Rampe et al., 2017]. In Chapter 3 we studied the mineralogical and chemical characteristics of opal-bearing samples from several terrestrial analog sites in Hawaii, Yellowstone National Park, and New Zealand that span acid sulfate-leached basalts and acidic and neutral-alkaline hot spring sinters. Our mineralogical results were generally consistent with previous literature in that opals from acidic sites are generally accompanied by acidic minerals such jarosite, alunite, and kaolinite. However, chemical data were more difficult to interpret, as we observed few distinctions in chemistry between our sample groups, with only Ti and Mn exhibiting some correlation with environmental pH. In general, Ti in Hawaiian acid-leached basalts tends to be higher than in sinter samples. However, there is still significant overlap in Ti content between unaltered Hawaiian samples and acid-leached, opal-rich samples, possibly due to the fact that Hawaiian basalts are inherently enriched in Ti [Prytulak and Elliott, 2007]. As discussed by Preston et al. [2008] and Ruff et al. [2011], Ti content in sinter samples can also range up to 0.9 wt %, demonstrating that higher Ti levels are not necessarily unique to acid-leached basalts. These results

therefore suggest that chemical data must be interpreted in the context of other mineralogic, microtextural, and geologic observations.

4. Opal-A and opal-CT can be distinguished solely from NIR spectroscopy, owing to the different distribution and behavior of H_2O in these two phases.

In Chapter 4 we continued work by Langer and Florke [1974], Rice et al. [2013], and Robertson et al. [2013] to determine spectral parameters that are capable of distinguishing between different opal types. We found that opal-A and opal-CT are distinguishable from their 1.4 and 2.2 μm absorption features, where the position of the 1.4 μm feature occurs at longer wavelengths for opal-CT, and the ratio of the 2.26/2.21 μm absorption strengths is higher for opal-A. These results differ from those of Rice et al. [2013], who found no discernable difference between opal types at these wavelengths; it is possible that this discrepancy may be attributed to sample differences. An interesting outcome of this work is that H_2O adsorption properties are different for opal-A and opal-CT. Given the same H_2O content, H_2O will prefer to adsorb as a monolayer H-bonded to surficial SiOH in opal-A, whereas it will prefer to adsorb to other H_2O and form multilayers or networks of H_2O in opal-CT. In fact, opal-A is likely saturated at ambient conditions with respect to its adsorbed H_2O content, whereas opal-CT is still capable of adsorbing more H_2O if exposed to 100% relative humidity (RH; Chapter 5).

These 1.4 and 2.2 μm parameters are also capable of distinguishing opal-rich materials (>80 wt% opal) and are equally effective for rock and powder samples. Importantly, we are now able to distinguish between opal-A and opal-CT at both ambient (Chapter 4) and Mars-like conditions (Chapter 5), by characterizing the 1.4 and 2.2 μm

features, which are not obscured by the presence of most other H_2O-bearing minerals or residual atmospheric absorptions in the CRISM data.

5. Based on laboratory hydration experiments, opal-A and opal-CT will readily exchange H_2O with a Mars-like atmosphere and will exhibit spectral changes that are theoretically observable from CRISM data. There is possibly evidence for active water exchange between opals and the martian atmosphere based on analysis of overlapping CRISM images.

In Chapter 5 we documented hydration experiments at Mars-like temperatures (-85 to -10°C) to determine if opals are likely to change in hydration state as they exchange H_2O with a diurnally or seasonally changing martian atmosphere. Although the kinetics of this process are certainly slower at low temperatures, our experiments showed that opal-A can readily adsorb H_2O at -85°C and >90% RH and desorb H_2O at -55°C and 15% RH. These hydration changes occur over timescales as short as hours, and importantly, can be tracked from our spectral parameters (Chapter 4). With respect to CRISM-relevant absorptions, spectral changes are most obvious in the 2.26/2.21 μm ratio parameter and to a lesser degree in the position of the 1.4 μm position. Opal-CT also shows evidence for H_2O adsorption and desorption at low temperatures, though not to the degree of what is observed in opal-A. However, at temperatures below -45°C, opal-CT will start to exhibit ice-like spectra, particularly around 3 μm, as its multilayer H_2O freezes. Though opal-CT still adsorbs and desorbs H_2O under these conditions, the broader implications for martian opal-CT are that they may also have ice-like features in areas on Mars where temperatures are below -45°C.

To test if there is orbital evidence for opal-atmosphere H_2O exchange, in Chapter 6 we conducted a temporal study of overlapping CRISM images to track spectral changes in individual opal deposits over time. We observed temporal variations in the 2.26/2.21 μm ratio for many of the studied deposits, although they do not necessarily correlate with predicted trends in seasonal RH. These results may provide the first evidence for H_2O exchange between a specific mineral and the martian atmosphere, despite a similar previous study for sulfates in Valles Marineris [Roach et al., 2009]. This implies that opals and possibly other hydrated minerals could play a role in present-day atmospheric water cycling. However, much work remains to guarantee the robustness of these observations, although experimental results (Chapter 5) support opal-atmosphere H_2O exchange as a plausible phenomenon.

6. Opal-A and opal-CT are both present on Mars but appear correlated with geologic setting on a global scale. Opal-A tends to occur in bedrock units, while opal-CT is associated with loose, mobile unconsolidated deposits, suggesting differences in exposure age or facilitated opal maturation in unconsolidated deposits.

In Chapter 6, application of our lab-derived parameters (especially the 1.4 μm position) to orbital CRISM detections demonstrated that both opal-A and opal-CT are likely present on Mars. However, further classification by geologic setting showed that silica in bedrock units is more consistent with an opal-A composition, while silica in unconsolidated or periglacial deposits is more consistent with an opal-CT composition. This could represent differences in exposure age, where bedrock silica are younger and fresher exposures of opal-A and unconsolidated silica represent older opal-CT that could

have eroded from opal-bearing bedrock. Another explanation is that H_2O could be trapped within the particulates in unconsolidated deposits [Folk, 1978], and slow maturation to opal-CT could result from freeze-thaw events over time, similar to what has been proposed for carbonates in glacial settings [Fairchild et al., 1993]. Another attractive explanation for the spectral characteristics of unconsolidated silica deposits is mixing with other hydrated phases (particularly gypsum). Overall, the apparent correlation of opal crystallinity with geologic setting indicates that orbital silica detections require careful interpretation and geologic contextualization in order to make inferences about paleoenvironments on Mars.

3. Outstanding Questions and Future Directions

1. What is the true distribution of Fe/Mg smectites, chlorites, and mixed-layer clays and what are the implications for diagenetic processes and water in the crust?

Most Fe/Mg clays on Mars have been discussed in terms of smectites and chlorites, but there is evidence for mixed-layer clays that result from partial chloritization of smectites [Milliken et al., 2010]. Mixed-layer clays (MLC) are a compelling explanation for the spectral characteristics of many orbital clay detections. While some clay detections show narrow and defined absorptions resembling those spectrally pure saponite or nontronite, many detections are characterized by a broad 2.3 μm absorption whose shape is intermediate between those of smectite and chlorite (Chapter 2). Just as how chlorite may represent diagenesis under prolonged aqueous conditions (in addition to forming in higher-temperature environments, e.g., hydrothermal), MLC may also indicate moderately prolonged periods of aqueous conditions on Mars. Determining the

distribution of smectites, chlorites, and MLC is therefore an important task to undertake to assess the temporal and spatial distribution of Mars' water.

From Chapter 2, the current crustal distribution of Fe/Mg smectite and chlorite and the apparent trend of increasing chloritization with depth are very suggestive of diagenetic processes occurring within the crust, as surface smectites are buried and then altered at depth (alternatively, the chlorites may have formed from subsurface clay formation; Ehlmann et al., 2011). The presence of heat, in the form of a geothermal gradient in the crust, is a necessary component in smectite diagenesis. Unlike opals, which require only the presence of liquid water to propel their conversion to quartz, Fe/Mg smectites require both sufficient time and heat to convert to chlorite on planetary timescales [Tosca and Knoll, 2009]. If these MLC and chlorites are assumed to be the products of smectite diagenesis only, determining the distribution of smectite, chlorites, and MLC with depth can provide constraints on the water, temperature, and burial time/rates within the crust. This can be accomplished using just the central peak detections from Chapter 2 alone, but would require additional laboratory work to quantify the proportions of smectite, chlorite, and MLC:

1) Significant laboratory measurements are needed to constrain the spectral characteristics of smectite, chlorite, and MLC. Because the 2.3 μm absorption for MLC are intermediate between those of smectite and chlorite, one could imagine parameterizing this feature in a similar manner as we did for opals (Chapter 4) [e.g., Milliken et al., 2010]. For example, Gaussians can be used to model the sharp 2.3 μm feature in smectites, and multiple Gaussians can be used to model the complex 2.32-2.35 μm feature in chlorites and in MLC.

MLC samples would have to be characterized in detail using XRD to determine the relative proportions of smectite and chlorite and the effect on its spectral characteristics. This work would have to distinguish between the spectra of true MLC samples and simple physical mixtures of smectite and chlorite. This task is also complicated due to the inherent spectral variability in band position and band shape produced by smectites and chlorites of different compositions [King and Clark, 1989]. An additional aspect to consider is the effect of Mars-like atmospheric conditions on these spectra, as hydrated minerals are known to be less hydrated and have narrower absorptions at low pressures and temperatures (e.g., Chapter 5) [Bishop and Pieters, 1995]. This will be particularly relevant if the spectral parameters rely on quantifying absorption widths.

2) Once a spectral parameter to quantify the degree of chloritization in an MLC sample is identified, it can be applied to CRISM detections of Fe/Mg clays. These results will help quantify the proportion of smectite to chlorite in a CRISM clay detection, for example those in central peaks (Chapter 2). If these central peak clays truly represent diagenetic processes in the crust, we would expect to see an increasing chloritic component with excavation depth, even within the MLC detections alone. One could also imagine using the impact crater ages to constrain the timing of these diagenetic processes, burial depths/rates, and ancient geothermal gradients in the crust. For example, a 3 Ga crater that is excavating 50% chloritized MLC from 5 km depth can be compared to a 3 Ga crater excavating pure chlorite from 10 km depth.

Assuming no further alteration at the surface, these observations can constrain the geothermal heat gradient within the martian crust at 3 Ga.

2. What suite of chemical, mineralogical, and spectral properties is needed to fingerprint the type of opal-forming environments?

A longtime objective in the study of martian opals has been to determine the environmental conditions – pH, aqueous conditions, and water longevity – present at the time of opal formation or diagenesis. Even with the sophisticated instrument payloads onboard the Spirit and Curiosity rovers, it has been difficult to diagnose these formation conditions with certainty, as complex mineralogical and chemical signatures need to be carefully deconvolved in the context of geologic and stratigraphic context at the micro and macro-scales [e.g., Squyres et al., 2008; Ruff et al., 2011; Morris et al., 2016; Hurowitz et al., 2017].

As elaborated in Chapter 3, further terrestrial work at basaltic analog sites is necessary to provide a true comparison for observations from Mars rovers. The sample sites studied in Chapter 3 – Hawaii, Yellowstone National Park, and New Zealand – are commonly studied Mars analog sites, particularly for the study of volcanic fumarole environments (Hawaii) and hot spring settings (Yellowstone and New Zealand). However, Hawaiian basalts are inherently enriched in Ti [Prytulak and Elliott, 2007] and therefore comparisons of Ti content from Mars rovers to invoke acid sulfate weathering of basalt are not entirely analogous. Hot spring sites in Yellowstone and New Zealand are also hosted in rhyolitic country rock, which are inherently more silica-rich than the basalts that make up Mars' surface. Future work for determining the mineralogical and

chemical hallmarks of acidic versus alkaline opal-forming environments should therefore focus on analysis of samples from more analogous terrestrial sites, such as basaltic hot spring environments in Iceland, etc. [Preston et al., 2008].

Much work also remains to be done from the orbital perspective to determine how we can diagnose formation conditions using remote sensing datasets, which provide a more global view of martian environments but using a more limited suite of instruments. As with analyses of rover datasets, correlations of mineralogy, geomorphology, and stratigraphy are needed to produce meaningful interpretations of opal formation conditions (more details in the next section). Although chemistry is not obtainable from orbital measurements (at least not at fine spatial scales), accessory mineralogy has been used to infer environmental conditions such as pH [e.g., Milliken et al., 2008; Weitz et al., 2011].

With recent advances in distinguishing between opal types from NIR spectra [Rice et al., 2013; Chapters 4-5], it is now also possible to incorporate observations of opal type with accessory mineralogy to enhance inferences of environmental conditions. Smith et al. [2013] pioneered this concept by relating inferred opal crystallinity with accessory mineralogy for several silica-bearing sites across Mars, and found that low crystallinity silica were associated with sulfates, moderate crystallinity silica with Al clays, and high crystallinity silica with Fe/Mg clays. However, as we demonstrated in Chapters 2 and 6, many martian opals are associated with loose, mobile deposits [Ehlmann et al., 2009; Smith and Bandfield, 2012] that oftentimes cannot be traced back to a source region. The opals in these unconsolidated deposits also tend to be consistent with opal-CT, which may result from longer exposure ages or slow opal maturation

facilitated by the particulate nature of these deposits (Chapter 6). In such cases it may not be appropriate to draw correlations with accessory mineralogy, as the increased opal crystallinity may result from aqueous processes that are divorced from those that formed the accessory minerals, or the opal deposits may represent foreign materials lofted in from other locations. With these factors in mind, an analysis similar to that done by Smith et al. [2013] but using our data (Chapter 6) yielded no obvious correlations of opal crystallinity and accessory mineralogy. However, this does not preclude the possibility that correlations of silica crystallinity with accessory mineralogy are a very promising avenue forward in the study of opal-bearing environments, so long as the geologic contexts of these minerals are taken into consideration.

3. What are the ages of martian opal deposits and what does that imply for changes in environmental conditions during the Noachian to Hesperian transition, which resulted in the cessation of Fe/Mg clay formation and production of opaline silica?

In contrast to Fe/Mg clays, which are likely to have formed predominantly during the Noachian [Bibring et al., 2006; Chapter 2], many opal deposits on Mars appear to have formed during the more recent Hesperian period. Widespread deposits in Valles Marineris are superposed on Hesperian ridged plains [Milliken et al., 2008] and volcanic opal-bearing units are present within the Hesperian-age terrains at Nili Patera [Skok et al., 2010]. Many occurrences of hydrated silica are found within Hesperian impact craters (Chapter 2), and deposits at Noctis Labyrinthus [Weitz et al., 2011] and Acidalia Planitia [Pan and Ehlmann, 2014] are constrained to more recent alteration events that postdate Fe/Mg clay formation. Even in the ancient terrains at Mawrth Vallis, the observed

sequence of opals (and Al clays) overlying Fe/Mg clays has suggested opal formation possibly from pedogenesis of the Fe/Mg clay layer [Bishop et al., 2008]. The apparent end of widespread Fe/Mg clay formation and the apparent rise of opaline silica formation (amongst sulfates and Al clays) has many implications for the environmental transition between the Noachian and the Hesperian.

The ubiquity of opal is not surprising given its formation in diverse conditions, but the overall observations thus far suggest significant opal formation during the younger Hesperian period [Ehlmann and Edwards, 2014]. However, as we have seen, there are many complexities in inferring opal formation conditions, and detailed stratigraphic analyses are needed to constrain the timing of these opal-forming events [e.g., Milliken et al., 2008; Weitz et al., 2011; Pan and Ehlmann et al., 2014]. This is particularly difficult when a significant number of opals occur in loose, unconsolidated, and mobile materials that typically have uncertain origins (Chapters 2 and 6). Furthermore, stratigraphic relations can constrain the age of the host unit but not necessarily the age of the alteration event (Chapter 2). For example, the Valles Marineris deposits are Hesperian in age, but the opals could have formed as early as the Noachian if they are interpreted as detrital materials transported from a source region, or as recently as the Amazonian if they formed from post-depositional processes such as pedogenic leaching. Still, it is very much worth conducting detailed documentation of Mars' opal deposits and using stratigraphic relations, when appropriate (i.e. perhaps not in the case of loose, mobile deposits), to constrain their possible formation periods on Mars and obtain a better understanding of the changing martian environment over time.

In particular, the opal deposits in the plains around Valles Marineris are a prime target for this task, considering the widespread nature of these deposits and the wealth of CRISM, HiRISE, and CTX data available to study. Many of these opals seem to be hosted in geologic units of different tones and morphology, for example in light-toned layered bedrock around Ganges Chasma and in both dark and light-toned strata around Melas Chasma (Chapter 6). The geomorphologic diversity in the opal deposits at Valles Marineris alone suggests that there may have been several different, discrete episodes of opal formation within this single region. Further work in this area would require:

1) Determination of where these opal deposits are located and the presence of any accessory hydrated minerals (e.g., jarosite or Al clays; Milliken et al., 2008; Le Deit et al., 2012). These accessory phases would also have to be documented with regards to their stratigraphic position relative to opal to determine if inferences of their formation conditions should be connected or divorced.
2) Collection of CRISM spectra over these opal deposits, taking care to average enough pixels to produce higher signal-to-noise. Ideally, if the spatial resolution of CRISM allows, individual spectra may be collected from discrete strata (if present in the scene) to determine if there are compositional differences between different depositional events. Spectral parameterization, such as those performed in Chapter 6, can be one method of assessing these compositional differences.
3) Detailed geomorphologic and stratigraphic mapping of the entire Valles Marineris region. The distribution of these opal deposits (confirmed from CRISM) should be mapped, first from high-resolution HiRISE images where available and extrapolating to CTX images for more widespread coverage. Results will likely be

similar to mapping by Le Deit et al. [2012], but the emphasis in this work should be distinguishing between the different (e.g., dark versus light-toned) opal deposits. By mapping from HiRISE and CTX data on the basis of geomorphology, tone, and texture, we can assess the spatial distribution of these different opal deposits even in areas where there is no CRISM coverage. The end product for this task would be a regional stratigraphic column showing the relations between the different opal-bearing units and other mafic or hydrated units in the area [e.g., Viviano-Beck et al., 2017].

By producing detailed correlations between mineralogy, geomorphology, and stratigraphy, we may gain a better understanding of the number and timing of opal-forming events, as well as insight into the global environmental changes from the Noachian to the Hesperian, which transitioned from Fe/Mg clay formation to the formation of opaline silica, among other phases. This is perhaps most pertinent to the deposits around Valles Marineris, due to their widespread nature, but could be expanded to other areas with significant detections of opal (e.g., Terra Sirenum, Noachis Terra, Terra Cimmeria).

4. What are the spectral characteristics and water distributions of other hydrated silica phases, and how does that change our understanding of martian opals?

Although this dissertation work was able to distinguish between opal-A and opal-CT using NIR spectroscopy, there are many other hydrated silica phases that remain to be investigated, e.g., hydrated glass, opal-C, microcrystalline quartz. This was accomplished to a great degree by the seminal work of Rice et al. [2013], who identified spectral

differences between general silica groups (e.g., quartz versus opal). Although they were not able to determine differences in opal-A and opal-CT from the 1.4 and 2.2 μm absorptions from their samples, we found from our sample suite that both opal types were distinguishable in both absorption features. Given the differences between our findings and their results for opal-A and opal-CT alone, analysis of more samples is needed to determine if the other silica groups are similarly distinguishable. If a full suite of silica phases is characterized in this manner, we would be able to determine the types of hydrated silica that are present on Mars with more confidence, which would allow for more quantification of water longevity in opal-forming environments [Tosca and Knoll, 2009].

Another goal in this regard could be distinguishing between amorphous silica phases formed from different processes, as suggested by Rice et al. [2013] who suggested that silica formed from high-temperature processes may be spectrally distinct from those formed via low-temperature processes. For Mars, an important distinction that needs to be made is between hydrated glass (of volcanic or impact origins) and opal-A, which are both structurally similar as very amorphous silica. However, the geologic implications of each are very different, with the former representing high-temperature processes and the latter representing low-temperature aqueous alteration in environments with great biopreservation potential [e.g., Campbell et al., 2015]. As we found with opal-A and opal-CT (Chapter 4), it is possible that despite both being amorphous silica materials, hydrated glass and opal-A may have different surface structures and water adsorption properties that allow for their distinction in NIR spectra. Such work may also be coupled with data acquired from other laboratory measurements that have proven useful in

distinguishing silica phases [Wilson, 2014], such as nuclear magnetic resonance spectroscopy [Brown et al., 2003]. Experiments and measurements of these silica phases at simulated martian conditions (Chapter 5) may also reveal information about how they may be distinguished on Mars from orbital data, and also provide clues about the role of these phases in helping to regulate variations in atmospheric water content.

4. Final Thoughts

Through decades of research on Mars' geology and aqueous mineralogy, it is generally understood that aqueous conditions were relatively limited on Mars [e.g., Tosca and Knoll, 2009]. However, in recent years there has been increasing evidence for diagenetic alteration of both smectites and opaline silica that suggest more extensive aqueous processes. Chlorite occurrences are observed to increase with depth in the crust [Carter et al., 2013; Sun and Milliken, 2015] and more mature opal phases have been observed at both rover [Morris et al., 2016] and orbital scales [Smith et al., 2013]. This dissertation represents an effort to identify more of these geochemically mature phases on Mars, but further work is needed to use these detections to quantify the length of aqueous conditions on Mars. The nature of the environmental transition from the Noachian to the Hesperian is of particular interest and can be addressed by further study of Fe/Mg clays and opaline silica, which constitute the two largest groups of hydrated minerals and also appear to have formed during distinct periods in Mars' history. Future efforts should also be dedicated to correlating rover and orbital datasets and integrating these mineral detections with broader observations of accessory mineralogy and geomorphologic and stratigraphic setting. Though the longevity of aqueous conditions on Mars is yet unclear,

it is certain that there is plenty of work remaining with the wealth of datasets available for Mars research.

References

Bibring, J.-P. et al. (2006), Global Mineralogical and Aqueous Mars History Derived from OMEGA/Mars Express Data, *Science*, *312*(5772), 400–404, doi:10.1126/science.1122659.

Bishop, J. L., and C. M. Pieters (1995), Low-temperature and low atmospheric pressure infrared reflectance spectroscopy of Mars soil analog materials, *J. Geophys. Res.*, *100*(E3), 5369–5379, doi:10.1029/94JE03331.

Bishop, J. L. et al. (2008), Phyllosilicate Diversity and Past Aqueous Activity Revealed at Mawrth Vallis, Mars, *Science*, *321*(5890), 830–833, doi:10.1126/science.1159699.

Brown, L. D., A. S. Ray, and P. S. Thomas (2003), 29Si and 27Al NMR study of amorphous and paracrystalline opals from Australia, *Journal of Non-Crystalline Solids*, *332*(1–3), 242–248, doi:10.1016/j.jnoncrysol.2003.09.027.

Campbell, K. A., B. Y. Lynne, K. M. Handley, S. Jordan, J. D. Farmer, D. M. Guido, F. Foucher, S. Turner, and R. S. Perry (2015), Tracing Biosignature Preservation of Geothermally Silicified Microbial Textures into the Geological Record, *Astrobiology*, *15*(10), 858–882, doi:10.1089/ast.2015.1307.

Carter, J., F. Poulet, J.-P. Bibring, N. Mangold, and S. Murchie (2013), Hydrous minerals on Mars as seen by the CRISM and OMEGA imaging spectrometers: Updated global view, *J. Geophys. Res. Planets*, *118*(4), 831–858, doi:10.1029/2012JE004145.

Chang, H. K., F. T. MacKenzie, and J. Schoonmaker (1986), Comparisons between the diagenesis of dioctahedral and trioctahedral smectite, Brazilian offshore basins, *Clays and Clay Minerals*, *34*(4), 407–423.

Ehlmann, B. L., and C. S. Edwards (2014), Mineralogy of the Martian Surface, *Annual Review of Earth and Planetary Sciences*, *42*(1), 291–315, doi:10.1146/annurev-earth-060313-055024.

Ehlmann, B. L. et al. (2009), Identification of hydrated silicate minerals on Mars using MRO-CRISM: Geologic context near Nili Fossae and implications for aqueous alteration, *Journal of Geophysical Research: Planets*, *114*, E00D08, doi:10.1029/2009JE003339.

Ehlmann, B. L., J. F. Mustard, S. L. Murchie, J.-P. Bibring, A. Meunier, A. A. Fraeman, and Y. Langevin (2011), Subsurface water and clay mineral formation during the early history of Mars, *Nature*, *479*(7371), 53–60, doi:10.1038/nature10582.

Fairchild, I. J., L. Bradby, and B. Spiro (1993), Carbonate diagenesis in ice, *Geology*, *21*(10), 901–904, doi:10.1130/0091-7613(1993)021<0901:CDII>2.3.CO;2.

Folk, R. L. (1978), Angularity and Silica Coatings of Simpson Desert Sand Grains, Northern Territory, Australia, *Journal of Sedimentary Research*, *48*(2).

Hurowitz et al., J. A. (2017), Redox stratification of an ancient lake in Gale Crater, Mars, *in revision*.

Inoue, A., M. Utada, and K. Wakita (1992), Smectite-to-illite conversion in natural hydrothermal systems, *Applied Clay Science*, *7*(1–3), 131–145, doi:10.1016/0169-1317(92)90035-L.

King, T. V. V., and R. N. Clark (1989), Spectral characteristics of chlorites and Mg-serpentines using high-resolution reflectance spectroscopy, *J. Geophys. Res.*, *94*(B10), 13997–14008, doi:10.1029/JB094iB10p13997.

Langer, K., and O. W. Flörke (1974), Near infrared absorption spectra (4000–9000 cm− 1) of opals and the role of "water" in these SiO 2· nH 2 O minerals., *Fortschritte der Mineralogie*, *52*(1), 17–51.

Le Deit, L., J. Flahaut, C. Quantin, E. Hauber, D. Mège, O. Bourgeois, J. Gurgurewicz, M. Massé, and R. Jaumann (2012), Extensive surface pedogenic alteration of the Martian Noachian crust suggested by plateau phyllosilicates around Valles Marineris, *J. Geophys. Res.*, *117*(E11), E00J05, doi:10.1029/2011JE003983.

Mangold, N., J. Carter, F. Poulet, E. Dehouck, V. Ansan, and D. Loizeau (2012), Late Hesperian aqueous alteration at Majuro crater, Mars, *Planetary and Space Science*, *72*(1), 18–30, doi:10.1016/j.pss.2012.03.014.

Marzo, G. A., A. F. Davila, L. L. Tornabene, J. M. Dohm, A. G. Fairén, C. Gross, T. Kneissl, J. L. Bishop, T. L. Roush, and C. P. McKay (2010), Evidence for Hesperian impact-induced hydrothermalism on Mars, *Icarus*, *208*(2), 667–683, doi:10.1016/j.icarus.2010.03.013.

Milliken, R. E. et al. (2008), Opaline silica in young deposits on Mars, *Geology*, *36*(11), 847–850, doi:10.1130/G24967A.1.

Milliken, R. E., D. L. Bish, and T. Bristow (2010), The case for mixed-layered clays on Mars, *Lunar Planet. Sci. XLI*, Abstract 2030.

Morris, R. V. et al. (2008), Iron mineralogy and aqueous alteration from Husband Hill through Home Plate at Gusev Crater, Mars: Results from the Mössbauer instrument

on the Spirit Mars Exploration Rover, *J. Geophys. Res.*, *113*(E12), E12S42, doi:10.1029/2008JE003201.

Morris, R. V. et al. (2016), Silicic volcanism on Mars evidenced by tridymite in high-SiO2 sedimentary rock at Gale crater, *PNAS*, *113*(26), 7071–7076, doi:10.1073/pnas.1607098113.

Mustard, J. F. et al. (2008), Hydrated silicate minerals on Mars observed by the Mars Reconnaissance Orbiter CRISM instrument, *Nature*, *454*(7202), 305–309, doi:10.1038/nature07097.

Pan, L., and B. L. Ehlmann (2014), Phyllosilicate and hydrated silica detections in the knobby terrains of Acidalia Planitia, northern plains, Mars, *Geophys. Res. Lett.*, *41*(6), 1890–1898, doi:10.1002/2014GL059423.

Preston, L. J., G. K. Benedix, M. J. Genge, and M. A. Sephton (2008), A multidisciplinary study of silica sinter deposits with applications to silica identification and detection of fossil life on Mars, *Icarus*, *198*(2), 331–350, doi:10.1016/j.icarus.2008.08.006.

Prytulak, J., and T. Elliott (2007), TiO2 enrichment in ocean island basalts, *Earth and Planetary Science Letters*, *263*(3–4), 388–403, doi:10.1016/j.epsl.2007.09.015.

Rampe et al., E. B. (2017), Mineralogical trends in mudstone deposits from the Murray formation, Gale crater, Mars, *in revision at Earth and Planetary Science Letters*.

Rice, M. S., E. A. Cloutis, J. F. Bell III, D. L. Bish, B. H. Horgan, S. A. Mertzman, M. A. Craig, R. W. Renaut, B. Gautason, and B. Mountain (2013), Reflectance spectra diversity of silica-rich materials: Sensitivity to environment and implications for detections on Mars, *Icarus*, *223*(1), 499–533, doi:10.1016/j.icarus.2012.09.021.

Roach, L. H., J. F. Mustard, S. L. Murchie, J.-P. Bibring, F. Forget, K. W. Lewis, O. Aharonson, M. Vincendon, and J. L. Bishop (2009), Testing evidence of recent hydration state change in sulfates on Mars, *J. Geophys. Res.*, *114*(E2), E00D02, doi:10.1029/2008JE003245.

Robertson, K. M., R. E. Milliken, S. W. Ruff, J. D. Farmer, and E. L. Shock (2013), Can VIS-NIR reflectance spectra be used to assess formation environments of opaline silica on Mars?, *Lunar Planet. Sci., XLIV*, Abstract 1612.

Ruff, S. W. et al. (2011), Characteristics, distribution, origin, and significance of opaline silica observed by the Spirit rover in Gusev crater, Mars, *Journal of Geophysical Research: Planets*, *116*(E7), n/a–n/a, doi:10.1029/2010JE003767.

Skok, J. R., J. F. Mustard, B. L. Ehlmann, R. E. Milliken, and S. L. Murchie (2010), Silica deposits in the Nili Patera caldera on the Syrtis Major volcanic complex on Mars, *Nature Geosci*, *3*(12), 838–841, doi:10.1038/ngeo990.

Smith, M. R., and J. L. Bandfield (2012), Geology of quartz and hydrated silica-bearing deposits near Antoniadi Crater, Mars, *Journal of Geophysical Research: Planets*, *117*(E6), n/a–n/a, doi:10.1029/2011JE004038.

Smith, M. R., J. L. Bandfield, E. A. Cloutis, and M. S. Rice (2013), Hydrated silica on mars: combined analysis with near-infrared and thermal-infrared spectroscopy, *Icarus*, doi:10.1016/j.icarus.2013.01.024.

Squyres, S. W. et al. (2008), Detection of Silica-Rich Deposits on Mars, *Science*, *320*(5879), 1063–1067, doi:10.1126/science.1155429.

Środoń, J. (1999), Nature of Mixed-Layer Clays and Mechanisms of Their Formation and Alteration, *Annual Review of Earth and Planetary Sciences*, *27*(1), 19–53, doi:10.1146/annurev.earth.27.1.19.

Sun, V. Z., and R. E. Milliken (2014), The geology and mineralogy of Ritchey crater, Mars: Evidence for post-Noachian clay formation, *J. Geophys. Res. Planets*, *119*(4), 2013JE004602, doi:10.1002/2013JE004602.

Sun, V. Z., and R. E. Milliken (2015), Ancient and recent clay formation on Mars as revealed from a global survey of hydrous minerals in crater central peaks, *J. Geophys. Res. Planets*, *120*(12), 2015JE004918, doi:10.1002/2015JE004918.

Tornabene, L. L., G. R. Osinski, and McEwen, A. S. (2009), Parautochthonous Megabreccias and Possible Evidence of Impact-Induced Hydrothermal Alteration in Holden Crater, Mars., *Lunar Planet. Sci. XL*, Abstract 1766.

Tosca, N. J., and A. H. Knoll (2009), Juvenile chemical sediments and the long term persistence of water at the surface of Mars, *Earth and Planetary Science Letters*, *286*(3–4), 379–386, doi:10.1016/j.epsl.2009.07.004.

Viviano-Beck, C. E., S. L. Murchie, A. W. Beck, and J. M. Dohm (2017), Compositional and structural constraints on the geologic history of eastern Tharsis Rise, Mars, *Icarus*, *284*, 43–58, doi:10.1016/j.icarus.2016.09.005.

Weitz, C. M., J. L. Bishop, P. Thollot, N. Mangold, and L. H. Roach (2011), Diverse mineralogies in two troughs of Noctis Labyrinthus, Mars, *Geology*, *39*(10), 899–902, doi:10.1130/G32045.1.

Wilson, M. J. (2014), The structure of opal-CT revisited, *Journal of Non-Crystalline Solids*, *405*, 68–75, doi:10.1016/j.jnoncrysol.2014.08.052.

APPENDIX A:

Supplemental Information on Opaline Silica Formation, Microstructures, and Spectral Features at Thermal Wavelengths

Vivian Z. Sun

Department of Earth, Environmental, and Planetary Sciences, Brown University, Providence, RI 02912, USA

1. Formation and Diagenesis of Opals on Earth

Most of Earth's opaline silica is formed through biologic processes [Siever, 1962], but inorganic silica can be produced through a geologic "silica cycle" outlined by Siever [1957]. In this cycle, silicate minerals are aqueously weathered to liberate silica in solution. Upon saturation, typically at lower temperatures (<100-200°C), amorphous opal-A will precipitate out under both neutral-to-alkaline and acidic conditions due to the constant solubility of amorphous silica at pH<9 [Krauskopf, 1956]. As a result, opaline silica is found in a variety of aqueous settings, including soils [e.g., Tokashiki and Wada, 1975], marine environments [e.g., Kastner et al., 1977], hot spring sinters [e.g., Jones and Renaut, 2003], and residues, rinds, and coatings in fumarolic environments [e.g., Morris et al., 2000; Rodgers et al., 2002; Lynne et al., 2006; Minitti et al., 2007; Chemtob et al., 2010].

The precipitated opal-A then undergoes diagenesis through the Ostwald ripening process, as subsequent aqueous activity enables repeated dissolution and reprecipitation that forms progressively more crystalline varieties of silica such as opal-CT, opal-C, and finally microcrystalline quartz (e.g., chalcedony) [Siever, 1962]. The later stages of diagenesis favor preferential tridymite dissolution and cristobalite reprecipitation during the opal-CT to opal-C transition and ends with slow quartz precipitation on the basis of kinetics and thermodynamics [Williams et al., 1985; Williams and Crerar, 1985]. Under certain circumstances that alter silica solubility (e.g., higher temperatures and the presence of accessory minerals), more mature phases such as opal-CT/C or quartz may directly precipitate from solution without undergoing the full diagenetic sequence from opal-A [e.g., Greenwood, 1973; Williams et al., 1985; Spencer et al., 1992; Rondeau et al., 2004]. Metamorphism is the final stage of this cycle and regenerates the higher-temperature

silicate minerals that restart the "silica cycle" anew [more details found in Siever, 1957 and references therein].

Distinguishing between these different opal types can therefore provide significant insight into the aqueous history of an environment beyond just indicating the presence of water. Opal diagenesis requires a sufficient combination of both time and temperature under aqueous conditions [e.g., Mizutani, 1977; Herdianita et al., 2000], thus a particular type of opal can indicate the chemical maturity and extent of water-rock interactions in its formation environment. For instance, an environment that formed opal-C was likely subject to higher temperatures or more prolonged or intense aqueous alteration than an environment that only produced opal-A. These implications were applied to Mars by Tosca and Knoll [2009], who proposed that aqueous conditions were likely limited in Mars' history due to the prevalence of opal-A and the lack of more geochemically mature phases such as opal-CT and opal-C.

In the terrestrial literature, opal type has sometimes been linked to environmental setting, with opal-A corresponding to sedimentary environments and opal-CT/C to volcanic locations, although it is likely that they indicate formation temperature instead [Spencer et al., 1992; Rondeau et al., 2004 and references therein]. There is also some suggestion through experiments and observations that tridymite may be present only in opal-CT/C that formed through diagenesis, while opals with only cristobalite likely crystallized at high temperatures [Greenwood, 1973].

2. Opal Microstructures and Water Content

Techniques such as X-ray diffraction (XRD), scanning electron microscopy (SEM), transmission electron microscopy (TEM) and selected area electron diffraction (SAED), NIR and TIR/MIR spectroscopy, Raman spectroscopy, nuclear magnetic resonance (NMR) spectroscopy, and X-ray absorption spectroscopy (XANES) have also been able to distinguish between at least some opal types to varying degrees of success. These techniques all exploit the differences between opal structures and consequently their associated water content. This section provides an overview of the microtextures observed in opal specimens and the uncertainties in measuring water species in each opal type. This dissertation does not include a textural study of opaline silica because the majority of the work focuses on powdered samples rather than whole rocks. However, it is still important to note that information regarding opal type and even formation conditions can manifest at the micro- and macro-textural scales [e.g., Campbell et al., 2015]. Although it is convenient to separate the opal group into the familiar opal-A, opal-CT, and opal-C classes, the boundaries between these phases are blurred in reality and this is reflected in the difficulties in distinguishing them from laboratory measurements [e.g., Wilson, 2014]. The reader is directed to Gaillou et al. [2008] for a survey of SEM observations and Wilson [2014] for an excellent review of the other aforementioned techniques and their effectiveness in discerning opal-CT structures.

2.1 Opal Microstructures

Opal-A is the most amorphous of the opaline silica group and is often referred to as noncrystalline opal. It can be distinguished from hydrated silica glass on the basis of

their different tetrahedral networks and structures [Graetsch et al., 1990]. Opal-A can be further differentiated into "networked" opal-AN and opal-AG "gel." Opal-AN refers to hyalites which quench from high temperatures with a glass-like structure, and therefore will not be considered further in this work. Opal-AG, hereafter referred to as just opal-A, precipitates out in lower-temperature environments and are more relevant to the objectives of this work as they form the majority of opals found in nature. SEM imaging reveals that opal-A is characterized by regular spheres that are typically <1 μm in diameter, although they can grow to as large as ~10 μm. These spheres can have heterogeneous sizes within a sample and are closely packed together. Natural samples often contain secondary opal-A cementing these spheres [e.g., Jones and Renaut, 2003; Gaillou et al., 2008].

Opal-CT and opal-C are considerably more structured than opal-A and are sometimes referred to as "microcrystalline opal" as they are crystalline at microscopic scales [Jones and Segnit, 1971]. Opal-CT commonly consists of ~10^{-1} - 10^{1} μm lepispheres, which are spherical aggregates of silica blades or platelets that are an order of magnitude smaller. Less-ordered opal-CT abandons this lepisphere structure and appears as individual platelets or even smaller nanograins which are the building blocks for both opal-A and opal-CT [Gaillou et al., 2008]. The microstructure of opal-C is composed largely of platy crystals [Graetsch et al., 1985] and is sometimes referred to as lussatite [Jones and Segnit, 1971]. Finally, microcrystalline quartz (e.g., chalcedony) is the end product of the opal sequence and is nearly indistinguishable from quartz save for its finer grain size.

The common interpretation of opal-CT (and that gives it its name) is that it is composed of disordered interlayers of stacked cristobalite and around 30-50% stacked tridymite. Opal-C is even more structured than opal-CT and has a higher cristobalite

component with at most 20-30% tridymite stacking [Graetsch, 1994]. Evidence for this "microcrystalline" opal-CT model typically comes from studies using XRD or TEM [Graetsch et al., 1994; Guthrie et al., 1995; Elzea and Rice, 1996]. However, results from other techniques such as FTIR, Raman, NMR, and XANES spectroscopy seem to favor a "paracrystalline" opal-CT structure, which is dominated by an opal-A matrix with a small portion of stacked tridymite rather than cristobalite. This has led some workers to consider an opal-TC or opal-T endmember phase in place of opal-CT and opal-C [Ilieva et al., 2007; Eversull and Ferrell, 2008; Wilson, 2014], despite kinetic and thermodynamic arguments that cristobalite crystallization is favored over tridymite [Williams et al., 1985]. In this dissertation, interpretations are based on the conventional "microcrystalline" opal-CT structure, as our experimental methods (e.g., XRD) align most with those used to develop this model.

2.2 Uncertainties in Deriving Opal Water Content

It is not always clear in the literature whether water content is reported as structural water or the sum of structural (Type A) and adsorbed (Type B) water, nor whether water refers to molecular H_2O, SiOH, or both (see Chapter 4 for details on water speciation in opals). Structural and adsorbed water amounts can be estimated through heating (e.g., Penfield or thermogravimetric methods), while SiOH and H_2O groups can be observed through NIR spectroscopy. Most adsorbed water (typically H_2O) is removed at low temperatures <100-200°C while structural water (such as surface SiOH, H_2O released through annealing silanols, and H_2O in inclusions) is only lost at higher temperatures. Unless the structural and adsorbed SiOH and H_2O groups are specifically distinguished,

many works report a single value for opal water content which likely contains varying populations of all four water groups.

Several factors can also contribute to ambiguities in reported water contents, thus not all measurements can be compared equally. The amount of adsorbed water is a particularly unconstrained variable, as it can change with relative humidity and other lab conditions at the time of measurement [Dyar et al., 2010]. The temperature ranges required to remove structural and adsorbed water may also overlap and muddle the derived water contents. For instance, structural silanols may be removed at temperatures as low as 130°C and adsorbed H_2O can still be present up to 180°C [Gallego-Gomez et al., 2011]. There appears to be no unanimously defined temperature range that is used to standardize measurements between all studies, and even different methods can yield different water contents [Herdianita et al., 2000]. Organics and other volatiles in impure opal samples may also contribute to weight loss attributed to removed water [Graetsch et al., 1985; Jones and Renaut, 2004].

3. Features at Thermal or Mid-Infrared Wavelengths (TIR/MIR; 5-25 µm)

Spectral features at the TIR/MIR wavelengths are more indicative of Si-O bonds compared to near-infrared (NIR) hydration features. Opals have some features that are distinct from those of other silica polymorphs, and even opal-A and opal-CT can sometimes be distinguished. Complete references are as attributed in **Table A1**.

Opal absorptions at 5.01-5.03 and 5.32-5.35 µm are due to overtones and combinations of Si-O [Langer and Florke, 1974] or of H_2O and OH [Goryniuk et al., 2004]. The 5.35 µm feature is also a transparency feature and occurs as an emissivity peak in

particulate silica [Ruff et al., 2011]. Absorptions from 6.06-6.13 μm are due to the bending vibrations of molecular H_2O, and the 6.13 μm feature is observed in particulate sinter but not in solid opal-A [Ruff et al., 2011].

The Christiansen Feature (CF) is an emissivity maximum related to a rapid change in the refractive index and whose wavelength position is related to silicate polymerization. In opals, the CF occurs at 7.35 μm, which is notably shorter than for normal silicates [Goryniuk et al., 2004] but is only slightly shorter than the crystalline silica polymorphs [Michalski et al., 2003]. The Reststrahlen bands are the fundamental vibration bands due to Si-O stretching vibrations and occurs as a reflectivity maximum at 7.90 and 9.00 μm in opal. The latter band is nonunique and is also found in the other silica polymorphs at slightly higher wavelengths [Goryniuk et al., 2004]. A band at 8.51 μm may indicate cristobalite-like stacking in opal-CT [Michalski et al., 2003].

Opal-A and opal-CT also appear to have distinct absorptions. Additional Si-O stretch and bend frequencies for opal-A are found at 10.15, 11.50, 13.60, and 20.90 μm [Goryniuk et al., 2004]. The 13.60 μm band is a transparency feature, which is an emissivity minimum due to volume scattering in a normally transparent region. Transparency features can be amplified in particulate materials; for example, the 11.11 μm feature is present only in particulate silica [Ruff et al. 2011]. The 20.9 μm absorption is also a Reststrahlen band, and is most pronounced in polished quartz glass rather than particulate silica [Ruff et al., 2011]. Some of the opal-A features from 6-13 μm may vary by sample. Goryniuk et al. [2004] noted that consolidated samples contained a reflectance peak at 9 μm, while porous samples (that may not have secondary silica cement) had more uniform features in the 8-12 μm region. Opal-CT can be distinguished from opal-A by

having features at 18.18, 20, and 21.1-21.19 μm, with the 18.18 μm band being a secondary Christiansen feature [Ruff et al., 2011]. An absorption at 16.1 μm is noted to be present for cristobalite and opal-C, but is absent for opal-A and opal-CT [Graetsch et al., 1994; Rice et al., 1995].

Tables

Table A1. Compilation of opal and SiO_2 polymorph features in the 4-25 μm region. Non-opal features are greyed out but are included for comparison with opal features. References are numbered as follows: 1) Lippincott et al., 1958, 2) Langer and Florke, 1974, 3) Hair, 1975, 4) Stolper, 1982, 5) Graetsch et al., 1985, 6) Graetsch et al., 1994, 7) Rice et al., 1995, 8) Burneau and Carteret, 2000, 9) Michalski et al., 2003, 10) Goryniuk et al., 2004, 11) Dyar et al., 2010, 12) Ruff et al., 2011.

Abs (μm)	Molecule	Action	Si Phase	Ref. #
4.25-4.27	SiOH	H-bonding of SiOH to non-bridging O	silicate glass, chalcedony	4,5
5.01-5.03	OH, H_2O	overtone of H_2O and OH and Si-O fundamentals	opal	2,10
5.32-5.35	OH, H_2O	overtone of H_2O and OH and Si-O fundamentals	opal	2,10,12
6.06-6.13	H_2O	bending vibration	H2O	2,3,10-12
7.35	Si-O	Christiansen frequency	opal, SiO_2 polymorphs	9,10
7.9	Si-O	asymmetric Si-O stretch, Restrahlen band	opal-A	10
8.15-8.24	Si-O	Si-O asymmetric stretch	SiO_2 polymorphs	9
8.51	Si-O	cristobalite-like stacking in opal-CT	opal-CT	9
9-9.09	Si-O	asymmetric Si-O stretch, Restrahlen band	opal, SiO_2 polymorphs	1,9,10
9.55-9.63	Si-O	Si-O asymmetric stretch	SiO_2 polymorphs	9
10.15	Si-O	Si-O stretch	opal-A	10
11.11	Si-O	transparency feature	particulate silica	12
11.5	Si-O	Si-O stretch	opal-A	10
12.05-12.74	Si-O	Si-O symmetric stretch	SiO_2 polymorphs, silica glass	1,8,9
13.6	Si-O	transparency feature	opal-A	10
14.64	Si-O	Si-O symmetric stretch	SiO_2 polymorphs	9
16.05-16.1	Si-O	Si-O bend	opal-C, cristobalite	6,7,9
16.72-19.46	Si-O	Si-O bend	SiO_2 polymorphs	1,7,9
18.18	Si-O	secondary Christiansen frequency	opal-CT/C, SiO_2 polymorphs	12
20	Si-O	Si-O bend	opal-CT, cristobalite	7,9
20.62-20.75	Si-O	Si-O bend	SiO_2 polymorphs	1,7,9
20.9	Si-O	Si-O asymmetric bend, Restrahlen band	opal-A	10,12
21.01-21.05	Si-O	Si-O bend	SiO_2 polymorphs, silica glass	8,12
21.1-21.19	Si-O	Si-O bend	opal-CT	7,9,12
22.62-25	Si-O	Si-O bend	SiO_2 polymorphs	1,8,9

References

Burneau, A., and C. Carteret (2000), Near infrared and ab initio study of the vibrational modes of isolated silanol on silica, *Physical Chemistry Chemical Physics*, *2*(14), 3217–3226, doi:10.1039/b002863k.

Campbell, K. A., B. Y. Lynne, K. M. Handley, S. Jordan, J. D. Farmer, D. M. Guido, F. Foucher, S. Turner, and R. S. Perry (2015), Tracing Biosignature Preservation of Geothermally Silicified Microbial Textures into the Geological Record, *Astrobiology*, *15*(10), 858–882, doi:10.1089/ast.2015.1307.

Chemtob, S. M., B. L. Jolliff, G. R. Rossman, J. M. Eiler, and R. E. Arvidson (2010), Silica coatings in the Ka'u Desert, Hawaii, a Mars analog terrain: A micromorphological, spectral, chemical, and isotopic study, *J. Geophys. Res.*, *115*(E4), E04001, doi:10.1029/2009JE003473.

Dyar, M. D., C. A. Hibbitts, and T. M. Orlando (2010), Mechanisms for incorporation of hydrogen in and on terrestrial planetary surfaces, *Icarus*, *208*(1), 425–437, doi:10.1016/j.icarus.2010.02.014.

Elzea, J. M., and S. B. Rice (1996), TEM and X-ray diffraction evidence for cristobalite and tridymite stacking sequences in opal, *Clays and Clay Minerals*, *44*(4), 492–500.

Eversull, L. G., and R. E. Ferrell (2008), Disordered silica with tridymite-like structure in the Twiggs clay, *American Mineralogist*, *93*(4), 565–572, doi:10.2138/am.2008.2603.

Gaillou, E., E. Fritsch, B. Aguilar-Reyes, B. Rondeau, J. Post, A. Barreau, and M. Ostroumov (2008), Common gem opal: An investigation of micro- to nano-structure, *American Mineralogist*, *93*(11–12), 1865–1873, doi:10.2138/am.2008.2518.

Gallego-Gómez, F., A. Blanco, D. Golmayo, and C. López (2011), Three Regimes of Water Adsorption in Annealed Silica Opals and Optical Assessment, *Langmuir*, *27*(23), 13992–13995, doi:10.1021/la203529s.

Goryniuk, M. C., B. A. Rivard, and B. Jones (2004), The reflectance spectra of opal-A (0.5–25 μm) from the Taupo Volcanic Zone: Spectra that may identify hydrothermal systems on planetary surfaces, *Geophys. Res. Lett.*, *31*(24), L24701, doi:10.1029/2004GL021481.

Graetsch, H., O. W. Flörke, and G. Miehe (1985), The nature of water in chalcedony and opal-C from brazilian agate geodes, *Phys Chem Minerals*, *12*(5), 300–306, doi:10.1007/BF00310343.

Graetsch, H., A. Mosset, and H. Gies (1990), XRD and 29Si MAS-NMR study on some non-crystalline silica minerals, *Journal of Non-Crystalline Solids*, *119*(2), 173–180, doi:10.1016/0022-3093(90)90840-I.

Graetsch, H., H. Gies, and I. Topalović (1994), NMR, XRD and IR study on microcrystalline opals, *Phys Chem Minerals*, *21*(3), 166–175, doi:10.1007/BF00203147.

Greenwood, R. (1973), Cristobalite: Its Relationship to Chert Formation in Selected Samples from the Deep Sea Drilling Project, *Journal of Sedimentary Research*, *43*(3).

Guthrie, G. D., D. L. Dish, and R. C. Reynolds (1995), Modeling the X-ray diffraction pattern of opal-CT, *American Mineralogist*, *80*(7–8), 869–872, doi:10.2138/am-1995-7-834.

Hair, M. L. (1975), Hydroxyl groups on silica surface, *Journal of Non-Crystalline Solids*, *19*, 299–309, doi:10.1016/0022-3093(75)90095-2.

Herdianita, N. R., K. A. Rodgers, and P. R. L. Browne (2000), Routine instrumental procedures to characterise the mineralogy of modern and ancient silica sinters, *Geothermics*, *29*(1), 65–81, doi:10.1016/S0375-6505(99)00054-1.

Ilieva, A., B. Mihailova, Z. Tsintsov, and O. Petrov (2007), Structural state of microcrystalline opals: A Raman spectroscopic study, *American Mineralogist*, *92*(8–9), 1325–1333, doi:10.2138/am.2007.2482.

Jones, B., and R. W. Renaut (2003), Hot spring and geyser sinters: the integrated product of precipitation, replacement, and deposition, *Can. J. Earth Sci.*, *40*(11), 1549–1569, doi:10.1139/e03-078.

Jones, B., and R. W. Renaut (2004), Water Content of Opal-A: Implications for the Origin of Laminae in Geyserite and Sinter, *Journal of Sedimentary Research*, *74*(1), 117–128, doi:10.1306/052403740117.

Jones, J. B., and E. R. Segnit (1971), The nature of opal I. nomenclature and constituent phases, *Journal of the Geological Society of Australia*, *18*(1), 57–68, doi:10.1080/00167617108728743.

Kastner, M., J. B. Keene, and J. M. Gieskes (1977), Diagenesis of siliceous oozes—I. Chemical controls on the rate of opal-A to opal-CT transformation—an experimental study, *Geochimica et Cosmochimica Acta*, *41*(8), 1041–1059, doi:10.1016/0016-7037(77)90099-0.

Krauskopf, K. B. (1956), Dissolution and precipitation of silica at low temperatures, *Geochimica et Cosmochimica Acta*, *10*(1), 1–26, doi:10.1016/0016-7037(56)90009-6.

Langer, K., and O. W. Flörke (1974), Near infrared absorption spectra (4000–9000 cm− 1) of opals and the role of “water” in these SiO 2· nH 2 O minerals., *Fortschritte der Mineralogie*, *52*(1), 17–51.

Lippincott, E. R., A. Van Valkenburg, Weir, C. E, and E. Bunting (1958), Infrared studies on polymorphs of silicon dioxide and germanium dioxide, *Journal of research of the National Bureau of Standards*, *61*(1), 61–70.

Lynne, B. Y., K. A. Campbell, R. S. Perry, P. R. L. Browne, and J. N. Moore (2006), Acceleration of sinter diagenesis in an active fumarole, Taupo volcanic zone, New Zealand, *Geology*, *34*(9), 749–752, doi:10.1130/G22523.1.

Michalski, J. R., M. D. Kraft, T. Diedrich, T. G. Sharp, and P. R. Christensen (2003), Thermal emission spectroscopy of the silica polymorphs and considerations for remote sensing of Mars, *Geophys. Res. Lett.*, *30*(19), 2008, doi:10.1029/2003GL018354.

Minitti, M. E., C. M. Weitz, M. D. Lane, and J. L. Bishop (2007), Morphology, chemistry, and spectral properties of Hawaiian rock coatings and implications for Mars, *J. Geophys. Res.*, *112*(E5), E05015, doi:10.1029/2006JE002839.

Mizutani, S. (1977), Progressive ordering of cristobalitic silica in the early stage of diagenesis, *Contrib. Mineral. Petrol.*, *61*(2), 129–140, doi:10.1007/BF00374363.

Morris, R. V. et al. (2000), Mineralogy, composition, and alteration of Mars Pathfinder rocks and soils: Evidence from multispectral, elemental, and magnetic data on terrestrial analogue, SNC meteorite, and Pathfinder samples, *J. Geophys. Res.*, *105*(E1), 1757–1817, doi:10.1029/1999JE001059.

Rice, S. B., H. Freund, W.-L. Huang, J. A. Clouse, and C. M. Isaacs (1995), Application of Fourier Transform Infrared Spectroscopy to Silica Diagenesis: The Opal-A to Opal-Ct Transformation, *Journal of Sedimentary Research*, *65*(4).

Rodgers, K. A., K. L. Cook, P. R. L. Browne, and K. A. Campbell (2002), The mineralogy, texture and significance of silica derived from alteration by steam condensate in three New Zealand geothermal fields, *Clay Minerals*, *37*(2), 299–322, doi:10.1180/0009855023720035.

Rondeau, B., E. Fritsch, M. Guiraud, and C. Renac (2004), Opals from Slovakia ("Hungarian" opals), *European Journal of Mineralogy*, *16*(5), 789–799, doi:10.1127/0935-1221/2004/0016-0789.

Ruff, S. W. et al. (2011), Characteristics, distribution, origin, and significance of opaline silica observed by the Spirit rover in Gusev crater, Mars, *Journal of Geophysical Research: Planets*, *116*(E7), n/a–n/a, doi:10.1029/2010JE003767.

Siever, R. (1957), The silica budget in the sedimentary cycle, *The American mineralogist*, *42*(11–2), 821.

Siever, R. (1962), Silica Solubility, 0°-200° C., and the Diagenesis of Siliceous Sediments, *The Journal of Geology*, *70*(2), 127–150.

Spencer, R. J., A. A. Levinson, and J. I. Kolvula (1992), Opal from Queretaro, Mexico: Fluid inclusions study, *Gems and Gemology*, *28*(1), 28–34.

Stolper, E. (1982), Water in silicate glasses: An infrared spectroscopic study, *Contr. Mineral. and Petrol.*, *81*(1), 1–17, doi:10.1007/BF00371154.

Tokashiki, Y., and K. Wada (1975), Weathering implications of the mineralogy of clay fractions of two Ando soils, Kyushu, *Geoderma*, *14*(1), 47–62, doi:10.1016/0016-7061(75)90012-9.

Tosca, N. J., and A. H. Knoll (2009), Juvenile chemical sediments and the long term persistence of water at the surface of Mars, *Earth and Planetary Science Letters*, *286*(3–4), 379–386, doi:10.1016/j.epsl.2009.07.004.

Williams, L. A., and D. A. Crerar (1985), Silica Diagenesis, II. General Mechanisms, *Journal of Sedimentary Research*, *55*(3).

Williams, L. A., G. A. Parks, and D. A. Crerar (1985), Silica Diagenesis, I. Solubility Controls, *Journal of Sedimentary Research*, *55*(3).

Wilson, M. J. (2014), The structure of opal-CT revisited, *Journal of Non-Crystalline Solids*, *405*, 68–75, doi:10.1016/j.jnoncrysol.2014.08.052.

APPENDIX B:

Martian Central Peak Crater Database

Supplementary Material for Chapter 2

Vivian Z. Sun

and

Ralph E. Milliken

Department of Earth, Environmental, and Planetary Sciences, Brown University,

Providence, RI 02912, USA

Published in:

Journal of Geophysical Research – Planets, doi:10.1002/2015JE004918,

And also available in the Brown Digital Repository at:

https://doi.org/10.7301/Z0JW8BTX,

"Sun_Dissertation_AppendixB_CentralPeaksTable.xlsx"

Table B1. This supporting table lists all 633 central peak surveyed in our work and their various attributes: latitude, longitude, diameter, type of central structure, target rock (i.e. geologic unit as mapped by Tanaka et al., 2014), presence of fluvial landforms, and location of the crater in the Northern lowlands or Southern highlands. We include crater-count derived ages for hydrated central peaks, and their corresponding number in Figure 17. We also list previously published studies of individual craters that were referenced in the text (see Chapter 2 for the full references), and include a list of all the CRISM observations studied for each central peak region.

APPENDIX C:

Mineralogy and Chemistry of Opal-Bearing Samples

Supplementary Material for Chapters 3-5

Vivian Z. Sun

Department of Earth, Environmental, and Planetary Sciences, Brown University,

Providence, RI 02912, USA

Data available in the Brown Digital Repository at:

https://doi.org/10.7301/Z0JW8BTX,

"Sun_Dissertation_AppendixC_MinChemResults.xlsx"

Table C1. This table lists the opal-bearing samples referenced in Chapters 3-5 and provides information on their localities. Also listed are information regarding opal type, mineralogy, chemistry (from ICP-AES), and XRD parameter values for the samples studied in Chapter 3. Note that XRD parameters were not calculated for samples whose peaks due to igneous and other minerals overlapped with those of opals and precluded any meaningful calculation of the XRD parameters.

APPENDIX D:

Images of Opal-Bearing Samples

Supplementary Material for Chapters 3-5

Vivian Z. Sun

Department of Earth, Environmental, and Planetary Sciences, Brown University,

Providence, RI 02912, USA

Data available in the Brown Digital Repository at:

https://doi.org/10.7301/Z0JW8BTX,

"Sun_Dissertation_AppendixD_Sample_Images.docx"

Document D1. This document provides images of the opal-bearing samples studied in Chapters 3-5.

APPENDIX E:

XRD Data of Opal-Bearing Samples

Supplementary Material for Chapter 3

Vivian Z. Sun

Department of Earth, Environmental, and Planetary Sciences, Brown University,

Providence, RI 02912, USA

Data available in the Brown Digital Repository at:

https://doi.org/10.7301/Z0JW8BTX,

"Sun_Dissertation_AppendixE_XRDData.xlsx" and

"Sun_Dissertation_AppendixE_XRDData_Images.docx"

Document E1. The spreadsheet "Sun_Dissertation_AppendixE_XRDData.xlsx" provides the XRD pattern data for the opal-bearing samples studied in Chapter 3. For convenience, the document "Sun_Dissertation_AppendixE_XRDData_Images.docx" provides images of the aforementioned XRD patterns of opal-bearing samples.

APPENDIX F:

Spectral Data (0.4-25 μm) for Opal-Bearing Samples

Supplementary Material for Chapter 4

Vivian Z. Sun

Department of Earth, Environmental, and Planetary Sciences, Brown University,

Providence, RI 02912, USA

Data available in the Brown Digital Repository at:

https://doi.org/10.7301/Z0JW8BTX,

"Sun_Dissertation_AppendixF_SpectralData.xslx"

Spreadsheet F1. This spreadsheet provides the ASD and FTIR spectral data of opal samples (in powder and chip form) used in Chapter 4. Spectra were acquired at ambient laboratory conditions from 0.4-2.5 μm on the ASD and from 1-4.7 μm and 1.5-25 μm using a CaF2 and a KBr filter on the FTIR respectively.

APPENDIX G:

Low Pressure Spectra of Opal-A and Opal-CT

Supplementary Material for Chapter 5

Vivian Z. Sun

Department of Earth, Environmental, and Planetary Sciences, Brown University,

Providence, RI 02912, USA

Data available in the Brown Digital Repository at:

https://doi.org/10.7301/Z0JW8BTX,

"Sun_Dissertation_AppendixG_LowPressureSpectra.xlsx"

Spreadsheet G1. This spreadsheet provides the ASD spectral data of select opal-A and opal-CT samples measured at low pressures (0.016 mbar), used in Figure 2 and discussed in Section 4.1 of Chapter 5.

APPENDIX H:

High Temperature Spectra of Opal-A and Opal-CT

Supplementary Material for Chapter 5

Vivian Z. Sun

Department of Earth, Environmental, and Planetary Sciences, Brown University,

Providence, RI 02912, USA

Data available in the Brown Digital Repository at:

https://doi.org/10.7301/Z0JW8BTX,

"Sun_Dissertation_AppendixH_HeatingSpectra.xlsx"

Spreadsheet H1. This spreadsheet provides the spectral data from select opal-A and opal-CT samples as they are dehydrated through heating from 25°C to 500°C at a temperature ramp of 2°C/minute. Measurements are made from 1.7-16.7 μm on the Bruker LUMOS FTIR microscope. The data presented here are already continuum-removed using the default background removal function in the OPUS spectroscopy software, and are used in Figure 4 and Section 4.2 of Chapter 5.

APPENDIX I:

Spectra from Hydration and Dehydration Experiments on Opal-A and Opal-CT

Supplementary Material for Chapter 5

Vivian Z. Sun

Department of Earth, Environmental, and Planetary Sciences, Brown University,

Providence, RI 02912, USA

Data available in the Brown Digital Repository at:

https://doi.org/10.7301/Z0JW8BTX,

"Sun_Dissertation_AppendixI_RHSpectra.xlsx"

Spreadsheet I1. This spreadsheet provides the spectral data from select opal-A and opal-CT samples that were subjected to hydration and dehydration experiments at low temperatures (-85°C to -10°C). Measurements are made from 1.7-16.7 µm on the Bruker LUMOS FTIR microscope. The data presented here are already continuum-removed using the default background removal function in the OPUS spectroscopy software, and are used in Figures 5-8 and Section 5 of Chapter 5.

APPENDIX J:

List of CRISM Images Studied in a Survey of Hydrated Silica on Mars

Supplementary Material for Chapter 6

Vivian Z. Sun

Department of Earth, Environmental, and Planetary Sciences, Brown University,

Providence, RI 02912, USA

Data available in the Brown Digital Repository at:

https://doi.org/10.7301/Z0JW8BTX,

"Sun_Dissertation_AppendixJ_CRISMImages.xlsx"

Document J1. This document lists the CRISM images surveyed in Chapter 6. Images are categorized as containing hydrated silica, containing possible hydrated silica, or not containing hydrated silica (but may contain other hydrated phases within the CRISM scene). The images listed in this document are in addition to the images listed in the supplementary table for Chapter 2 ("Sun_Dissertation_AppendixB_CentralPeaksTable.xlsx").